The Preparation and Properties of $CuInSe_2$ Thin Films and $CuInSe_2$/CdS Thin Film Solar Cells

by

Henry Franklin Tiedje

A thesis
presented to the University of Waterloo
in fulfillment of the
thesis requirement for the degree of
Doctor of Philosophy
in
Physics

Waterloo, Ontario, Canada, 1997

The University of Waterloo requires the signatures of all persons using or photocopying this thesis. Please sign below, and give address and date.

Abstract

$CuInSe_2$ and the related I-III-VI_2 ternary chalcopyrite compounds and alloys are semiconductors suitable for use as absorbers in thin film solar cells. A three source co-evaporation system for the growth of $CuInSe_2$ films, a hot wall evaporation system for CdS films, and a radio frequency sputtering system for Mo films are described. Demonstration Mo/$CuInSe_2$/CdS solar cells are produced to verify that the Mo, $CuInSe_2$ and CdS films are of acceptable photovoltaic quality. $CuInSe_2$ film samples are deposited on Corning 7059 glass for a detailed study of their properties. The Se is evaporated at a rate about three times the rate required for stoichiometry, so that the films are fully selenized. The Cu and In sources are positioned so that the Cu/In ratio varies by about 10% across the film area. This allows many of the properties to be measured as a function of the Cu/In ratio, *on one substrate*. Most other parameters which can effect film properties, such as film thickness, substrate temperature during deposition, film growth rate, and impurity concentrations, are the same for a film on a given substrate.

$CuInSe_2$ films grown as a single layer at a substrate temperature of 350 °C with constant Cu and In deposition rates are compared with films grown by the two layer technique, in which the first layer is Cu-rich and deposited at 350 °C substrate temperature, and the second layer is In-rich and deposited at 450 °C. It is found that the measured film conductivity is much less sensitive to the incident Cu/In atomic flux ratio in the case of the two layer films. The two layer films also generally show greatly increased photoluminescence intensity and photoconductivity gain, when compared to the single layer films. Scanned beam specular reflectance imaging is a sensitive indicator of film surface roughness, which is affected by film composition and substrate material. It is shown by optical beam induced current (OBIC) imaging that solar cells made with two layer films have reduced sensitivity to variations in the Cu/In ratio, compared to those based on single layer films.

Sodium is introduced into some of the films by depositing a thin layer of NaOH on one half of a sodium-free 7059 glass substrate before starting the $CuInSe_2$ film growth. The other half of the substrate is used as an otherwise identical sodium-free reference film. The sodium has a significant effect on the x-ray diffraction pattern, specular reflectance, transmittance, photoluminescence, and photoconductivity of the films.

The properties of typical CdS window layer films and Mo electrode films are presented. The problems of poor Mo adhesion to the glass substrate and poor $CuInSe_2$ adhesion to the Mo are discussed. Argon ion beam bombardment during the $CuInSe_2$ film nucleation appears to improve adhesion to Mo.

The energy efficiency of the best solar cells is measured in bright sunlight. No attempt is made to select small high quality regions from a larger cell in order to obtain a higher maximum efficiency. The optical and electrical properties of some solar cells are presented.

Acknowledgments

I would like to thank my thesis supervisor, Dr. Don Brodie, for his support, helpful advice, patience and encouragement throughout this project.

I also thank Dr. Ted Dixon for the use of the scanning laser MACROscope and Mr. Alfonso Ribes and Dr. Savas Damaskinos for their assistance in acquiring the OBIC and specular reflectance images.

I thank Dr. Gary Dmitrienko and Dr. Gilles Lajoie, for allowing me to move the Cary 17 spectrophotometer from the chemistry building to the physics building, for use in this project. The spectrophotometer was essential for the measurement of thin film transmittance and photoconductivity spectra, and for measuring the spectral response of solar cells.

Mr. Ed Linton of the science student shop provided guidance and useful suggestions during the machining of many of the mechanical components for the experimental apparatus described.

Contents

Tables

Figures

Chapter 1
Introduction

1.1 Recent Progress in Photovoltaics

Direct photovoltaic conversion of sunlight into electricity has been actively studied since the demonstration of 6% efficient single crystal silicon solar cells in 1954 [1]. Today (1996) the record highest efficiency for a single crystal Si cell under AM1.5 sunlight is 24% [2]. This can be compared with the theoretical limit of about 30% for a Si cell, assuming unity quantum efficiency [3,4,5]. Despite the technical success of single crystal silicon solar cells, high capital cost continues to discourage their use as a large scale electric power source. In 1994, single crystal silicon modules were priced at about U.S. $5 per peak watt, or about $700 m^{-2}. This is expected to be reduced to about $2.5 per peak watt by the year 2010 [6]. To compete on a large scale with electricity produced from fossil fuels such as coal and natural gas, the price of photovoltaic modules must be further reduced to below about $0.5 per peak watt [7]. In many remote applications, however, photovoltaics is already competitive, because of its reliability and low maintenance requirements.

Along with the continuing effort to improve the conventional Si technology, much research effort has been directed toward potentially lower cost alternative technologies. Those presently (1996) in active development for flat panel solar cells include multicrystalline silicon, amorphous silicon thin films, and polycrystalline thin films. Concentrator systems where sunlight is focused with mirrors or lenses onto small high efficiency Si, GaAs or multiple junction devices are also being investigated .

Of the polycrystalline thin film solar cells, heterojunctions with absorbers made from CdTe or $CuInSe_2$ and its alloys with Ga and S, have achieved the best performance, with record efficiencies of 15.8% (CdTe, area 1.05 cm^2) and 17.7% ($Cu(In,Ga)Se_2$, area 0.41 cm^2)[2].

In 1993, of the 60.09 peak MW of terrestrial photovoltaic modules manufactured worldwide, 98.3% were based on silicon devices, either single crystal, multicrystalline or amorphous [6]. The world module production has been increasing at about a 16% annual rate, and 81 peak MW of modules were shipped in 1995 [8]. The only commercial polycrystalline thin film cells currently manufactured are based on CdTe. As of 1996 there was no commercial production of $CuInSe_2$-based cells [9,10].

1.2 History of $CuInSe_2$ Solar Cell Research

The first heterojunction $CuInSe_2$/CdS device was developed as an infra-red detector [11]. It consisted of a p-$CuInSe_2$ single crystal, onto which a 5-10 μm thick CdS layer was deposited by vacuum evaporation. With the addition of a SiO anti-reflection coating, a solar energy conversion efficiency of 12% was obtained for a device with 0.79 mm^2 active area [12]. Previously, only Si, GaAs/$Ga_xAl_{1-x}As$ and InP/CdS had demonstrated efficiencies above 10%.

Kazmerski reported the first all thin film $CuInSe_2$/CdS heterojunction solar cell, consisting of a p-$CuInSe_2$ absorber on Au coated glass and an n-CdS window, with both 6 μm thick semiconductor layers deposited, in situ, by vacuum evaporation. A 1.2 cm^2 device was 5.7% efficient [13]. The $CuInSe_2$ is deposited using a $CuInSe_2$ powder source and a separate Se source. A similar device with a 2 μm thick absorber layer was reported later with efficiency 6.6% [14].

Mickelsen [15] used three source evaporation for the $CuInSe_2$. The Cu and In sources are situated so as to minimize the variation in Cu/In ratio across the substrate. The Se evaporation rate was monitored with a quartz crystal microbalance, and the Cu and In fluxes monitored by electron impact emission spectroscopy. A Mo coated alumina substrate was used, with Mo serving as the contact to the p-$CuInSe_2$. A key innovation is the two layer process used to deposit the $CuInSe_2$. A Cu-rich layer is deposited at 350 ° C, followed by an In-rich layer at 450 °C, with inter-diffusion resulting in a nearly stoichiometric film. The original motivation for the two layer process was the elimination of copper nodules at the film surface, but additional benefits included improved adhesion to the Mo contact, a nearly ohmic Mo contact, and larger grain sizes. A CdS window layer is evaporated in-situ, onto the selenide, followed by a SiO anti-reflection coating. A 1 cm^2, 9.5% efficient solar cell was obtained using these methods. Later a wider bandgap mixed (Zn,Cd)S window layer increased the efficiency to 11% [16]. Mickelsen's work was pioneering, because three source evaporation, the Mo back contact, a high final substrate temperature (> 450 °C) and In-rich final deposition are features common to the $CuInSe_2$ absorbers in all of the highest efficiency devices made since.

The next major improvement was the $CuInSe_2$/CdS/ZnO structure [17]. A very thin (50 nm) CdS layer transmits light at photon energies greater than the CdS band gap. The short wavelength spectral response limit is therefore extended from 520 to about 390 nm, corresponding to the 2.4 eV (CdS) and 3.2 eV (ZnO) energy gaps, respectively. A significant increase in photocurrent is obtained, and the amount of Cd required is greatly reduced.

Further increases in efficiency have been obtained by using the mixed compound $CuIn_{1-x}Ga_xSe_2$ as an absorber. The bandgap increases from 1 to 1.7 eV as x increases from 0 to 1 [18]. The highest efficiency devices have the structure glass/Mo/Cu(In,Ga)Se_2/CdS/ZnO/MgF_2. The fabrication of a device with 17.7% efficiency, the highest ever reported for any polycrystalline thin film solar cell, is described in [19,20,21,22]. A brief summary of the process is as follows. First, a 1.5 μm thick Mo contact is sputter deposited onto a 2 mm thick soda-lime glass substrate. A 200 nm layer of stoichiometric $CuGaSe_2$ is then deposited on the Mo at 350 °C by evaporation from elemental sources. Next, Cu(In,Ga)Se_2 is deposited, with the Ga/(In+Ga) and Cu/(In+Ga) deposition ratios reduced as the film grows. The decreasing Ga/In ratio produces a graded band-gap so that the conduction band edge slopes down toward the heterojunction, in order to assist electron collection. The typical Cu(In,Ga)Se_2 absorber thickness is 2 μm, the substrate temperature is increased from 400 to 560 °C during deposition, the average Ga/(In+Ga) ratio is about 0.3, and the average copper content is in the range $0.86 < Cu/(In+Ga) < 0.96$. The CdS layer is 50 nm thick and is grown by chemical bath deposition using a solution of $CdSO_4$, NH_4OH and thiourea in water. A 50 nm thick high resistivity ZnO layer is sputter deposited onto the CdS, followed by a sputtered high conductivity Al doped n-ZnO transparent electrode about 300 nm thick. A Ni/Al contact grid 3 μm thick is evaporated onto the ZnO. A 100 nm thick MgF_2 anti-reflection coating is deposited by electron beam evaporation. Finally, the device is annealed in air for 2 minutes at 200 °C.

Besides co-evaporation of the elements, the only other absorber fabrication technique which has produced high efficiency devices is the two stage technique, where precursor films are deposited at low temperature on the Mo coated substrate, and the composite film is then reacted at high temperatures, usually in an excess Se environment. Solar cells with efficiencies of 14.6% have been fabricated using films formed from Cu+In+Ga+Se precursors, sputter deposited at less than 100 °C, then reacted at 550 °C in an inert atmosphere [23]. An efficiency of 14.9% has been reported for films made from co-evaporated Cu+In+Ga+Se precursors deposited at 150-200 °C, then selenized at 500 °C in an evaporated Se flux [24]. Devices made from electron beam evaporated Cu+In+Ga stacked precursor layers, selenized in 10% H_2Se + 90% N_2 atmosphere at 425 °C, then annealed at 575 °C in N_2, have reached 11.7% efficiency [25]. This two stage all metal stacked layer approach is of particular interest because, in principle, the metal precursors can be deposited by a low cost technique such as electro-deposition.

Other absorber fabrication techniques, which have yielded much lower efficiencies, include sputtering, electro-deposition, spray pyrolysis, and screen printing [9].

1.3 Overview of Thesis

Many issues remain to be addressed before the goal of low cost high performance solar cells can be realized [26]. Among these is the need to develop a more complete understanding of the relation between the method and conditions of $CuInSe_2$ film growth, and the properties of the resulting film This is a complex problem, because the semiconductor properties of the finished film are determined by intrinsic crystal point defects; stoichiometry; crystallite size and orientation; the presence of secondary crystal phases such as Cu_2Se , In_2Se_3, and $CuIn_3Se_5$; the presence of Ga and S as well as In and Se, in the case of alloys; film growth temperatures; impurities such as Na which diffuse into the film from the substrate; and other unidentified impurities which may reduce minority carrier lifetime [27] . Many of these factors are interdependent.

Accordingly, this project was intended to investigate the sensitivity of the semiconductor properties of $CuInSe_2$ to the film growth conditions and the film stoichiometry. An additional purpose was to evaluate the effect of ion beam assisted deposition on film quality, as very little work has been done in this area. Since the main potential use of thin film $CuInSe_2$ is as an absorber in solar cells, fabrication of reasonably efficient solar cells was seen as an important test of film quality. The plan was to first develop the means to produce films using the proven co-evaporation technique, and then to demonstrate good film quality by fabricating reasonably efficient solar cells. Once reproducible photovoltaic quality films could be routinely made, then experiments with the deposition conditions, including ion beam assisted deposition, could be carried out in a meaningful way.

The techniques and equipment used to deposit Mo, $CuInSe_2$, CdS and Al/Ni contacts were developed on an ongoing incremental basis, as film characteristics which limited the performance of diagnostic solar cells were identified. Three separate deposition systems were developed and maintained during the project.

The $CuInSe_2$ co-evaporation system was installed in a vacuum system pumped by an oil diffusion pump with a liquid nitrogen cold trap. A quartz crystal oscillator microbalance deposition rate monitor and source temperature controller were designed and constructed for controlling and monitoring the film deposition process. Thermal effusion sources were designed for the evaporation of Cu and In, and the Se was evaporated from an open boat source fabricated from thin Mo sheet. A thermal radiation substrate heater, and substrate temperature control electronics were designed and constructed. Thermocouple vacuum feed-throughs were installed. Later, because of concerns about possible impurity doping, the entire vacuum system was disassembled and cleaned, including the diffusion pump and all vacuum surfaces. The original substrate shutter and microbalance cooling block were removed and replaced. The $CuInSe_2$ deposition system is described in detail in chapter 2.

A radio frequency (RF) argon plasma sputtering system was used to deposit the Mo back contact on glass. A radiation heater was installed in the sputtering system to out-gas the glass substrates, and heaters were added to out-gas the vacuum chamber. Many experiments were carried out to determine the optimum argon pressure, RF power, and sputter mode (bias or normal). The Mo film deposition is described in detail in chapter 6.

A third vacuum chamber with an oil diffusion pump and liquid nitrogen cold trap was used for the vacuum deposition of the CdS window layer, and for deposition of the top contact grid for solar cells. The vacuum chamber was dis-assembled to repair a leak in the cold trap, and to install a rotary feed-through for a substrate shutter. Initial experiments with CdS evaporation showed that a hot wall system was necessary. A hot wall assembly was designed, as a removable insert in the vacuum chamber, so that the chamber could also be used for Al and Ni electrode deposition. Thermocouple feed-throughs were installed for source, substrate and wall temperature monitoring. A radiation heater was designed for the substrate. The source temperatures are manually controlled in the CdS system. Many experiments were carried out to determine optimum source, wall and substrate temperatures for CdS film growth. The CdS film deposition is described in detail in chapter 6.

The first solar cells had efficiencies below 0.05% (total area < 2 cm^2), and raising the efficiency to 4.8% (total area 14 cm^2) took about 19 months of intense effort (see appendix C). Even after optimizing the fabrication process, it takes about four days to make one solar cell. The detailed description of the fabrication and characterization of solar cells is the subject of chapter 7.

In 1993, evidence that sodium can have a significant influence on film properties was first published [28]. Some solar cells were therefore fabricated on soda-lime glass, and in fact, the best large area efficiency (4.8%) cell produced in this work is on a soda-lime glass substrate (cell number 951207). After good solar cells had been demonstrated, new photovoltaic quality (i.e. fully selenized, large grain, and grown as a thick double layer), as well as single layer thick $CuInSe_2$ films, were deposited on Corning 7059 glass for the purpose of film characterization. Some basic measurements, including x-ray diffraction, conductivity and transmittance had already been carried out on earlier lower quality films (data not shown), but the new films produced higher quality data, and allowed additional types of measurements to be made, all spanning a range of Cu/In ratio fixed by the Cu and In evaporation source locations and temperatures. For example, with the low quality films, photoconductivity and photoluminescence signals were too weak to allow spectral resolution, but with the photovoltaic quality films the spectra can be readily measured. To investigate the effects of sodium incorporation on film properties, some of the films were

deposited on 7059 glass substrates, on which half of the substrate area had been coated with evaporated NaOH. The uncoated half serves as a sodium-free reference sample. The properties of these films and some sodium-free films, all of which were deposited after the demonstration of good solar cells, are discussed in chapters 2,3,4, and 5. Where possible, an effort was made to maximize the number of measurements made on a single substrate, in order to show the variation of several properties over the same range of stoichiometry.

To investigate the effects of sodium incorporation on solar cells, Mo coated 7059 glass substrates were half-coated with NaOH. In each case, the uncoated half served as a sodium-free reference sample. Unfortunately, severe adhesion problems were encountered when depositing $CuInSe_2$ films on sodium-free Mo/7059 substrates. Typically the sodium-free half of the film would begin to peel off the substrate even before it had been removed from the vacuum chamber. Only one solar cell (#960316) survived with both halves intact. It was found that ion-beam assisted deposition during the film nucleation phase could be used to improve adhesion. It was also found that NaOH usually improves the adhesion of $CuInSe_2$ to Mo. The effect of adhesion failures is seen in the OBIC images of chapter 7.

For characterization of samples, new test equipment was assembled, existing equipment adapted, or commercial test equipment used. A Cary 17 spectrophotometer was borrowed from the department of chemistry and, with the addition of a spherical mirror, a current preamplifier, lock-in amplifier and data acquisition computer, it was adapted for the measurement of thin film photoconductivity spectra, and solar cell spectral response, as well as transmittance spectra. A liquid nitrogen cooled cold stage with a quartz glass window was constructed for photoluminescence and photoconductivity vs. temperature measurements. An enclosure was constructed to hermetically seal a germanium detector, thermoelectric cooler and a long pass filter, as the infrared detector package for the photoluminescence measurements. Differential amplifiers and an analog chart recorder were added to the Hall effect apparatus in order to more accurately discriminate weak Hall voltages from background noise. A current vs. voltage measurement system for solar cells was assembled using a power operational amplifier and voltage ramp generator. A single data acquisition computer was used for most characterization measurements and for the film deposition data records. A pre-existing system was used for the measurement of film conductivity vs. temperature.

In the following chapters, the deposition of $CuInSe_2$ polycrystalline films and the fabrication of $CuInSe_2$-based solar cells is described. Some of the electrical and optical properties of the films and solar cells are measured. The effect of sodium on the properties of the thin films is discussed.

1.4 References

1 D.M. Chapin, C.S. Fuller, and G.L. Pearson, "A new silicon p-n junction photocell for converting solar radiation into electrical power", J. Appl. Phys. **25**, 676 (1954)

2 M.A. Green, K. Emery, K. Bucher, D.L. King and S. Igari, "Solar Cell Efficiency Tables (Version 8)", Progr. Photovolt. **4**, 321 (1996)

3 W. Shockley and H.J. Queisser, "Detailed Balance Limit of Efficiency of p-n Junction Solar Cells, J. Appl. Phys. **32**, 510 (1961)

4 T. Tiedje, E. Yablonovitch, G.C. Cody and B.G. Brooks, "Limiting Efficiency of Silicon Solar Cells", IEEE Trans. Electron Dev. **ED-31**, 711 (1984)

5 R. Brendel, J.H. Werner, and H.J. Queisser, "Thermodynamic Efficiency Limits for Semiconductor Solar Cells with Carrier Multiplication", Sol. Energy Mater. Sol. Cells **41/42**, 419 (1996)

6 P.D. Maycock, "International photovoltaic markets, developments and trends forecast to 2010", *Proc. of 24th IEEE Photovoltaic Spec. Conf.*, p. 694 (IEEE, N.J. ,1994)

7 L.D. Danny Harvey, "Solar-hydrogen electricity generation in the context of global CO_2 emission reduction", Climatic Change, **29**, 53 (1995)

8 R. L. Mitchell, C. Edwin Witt, H. P. Thomas, L. O. Herwig, D. S. Ruby, C. C. Aldrich, "Benefits from the U.S. photovoltaic manufacturing technology project", *Proc. of 25th IEEE Photovoltaic Spec. Conf.*, p. 1215 (IEEE, N.J. , 1996)

9 A. Catalano, "Polycrystalline thin-film technologies: Status and prospects.", Sol. Energy Mater. Sol. Cells **41/42**, 205 (1996)

10 K. Zweibel, "Thin Films: Past, Present, Future", National Renewable Energy Laboratory, http://www.nrel.gov/research/pv/thinfilm.html

11 S. Wagner, J.L. Shay, P. Migliorato and H.M. Kasper, "$CuInSe_2$ heterojunction photovoltaic detectors", Appl. Phys. Lett. 25, 434 (1974)

12 J.L. Shay and S. Wagner, "Efficient $CuInSe_2$/CdS solar cells", Appl. Phys. Lett. **27**, 89 (1975)

13 L.L. Kazmerski, F.R. White, and G.K. Morgan, "Thin film $CuInSe_2$/CdS heterojunction solar cells", Appl. Phys. Lett. **29**, 268 (1976)

14 L.L. Kazmerski, *Ternary Compounds 1977*, Edited by G.D. Holah, p. 217, Inst. of Phys. Conf. Series no. 35 (1977)

15 R.A. Mickelsen and W.S. Chen, "Development of a 9.4% efficient thin -film $CuInSe_2$/CdS solar cell", *Proc. of the 15th Photovoltaic Specialist Conf.*, p. 800, (IEEE, New York, 1981)

16 R.A. Mickelsen, "Polycrystalline Thin-Film $CuInSe_2$/CdZnS Solar Cells", IEEE Trans. Electron Dev., ED-31, 542, (1984)

17 R.R. Potter, C. Eberspacher and L.B. Fabick, "Device Analysis of $CuInSe_2$/(Cd,Zn)S/ZnO Solar Cells", *Proc. of 18th IEEE Photovoltaic Specialists Conf.*, p.1659, (IEEE, New York, 1985)

18 W.S. Chen, J.M. Stewart, B.J. Stanbery, W.E. Devaney and R.A. Mickelsen, "Development of thin film polycrystalline $CuIn_{1-x}Ga_xSe_2$ solar dells", *Proc. of 19th IEEE Photovoltaic Spec. Conf.* p. 1445 (IEEE, N.J. 1987)

19 M.A. Contreras, J. Tuttle, A. Gabor, A. Tennant, K. Ramanathan, S. Asher, A. Franz, J. Keane, L. Wang, J. Scofield and R. Noufi, "High efficiency Cu(In,Ga)Se_2-based solar cells: processing of novel absorber structures", *Proc. of 24th Photovoltaic Spec. Conf.* p.68, (IEEE, New York, 1994)

20 J.R. Tuttle, J.S. Ward, A. Duda, T.A. Berens, M.A. Contreras, K.R. Ramanathan, A.L. Tennant, J. Keane, E.D. Cole, K. Emery and R. Noufi, "The Performance of Cu(In,Ga)Se_2 Based Solar Cells in Conventional and Concentrator Applications", *Thin Films for Photovoltaic and Related Device Applications*, Mat. Res. Soc. Symp. Proc. **426**, p. 143, (1996)

21 M.A. Contreras, J. Tuttle, A. Gabor, A. Tennant, K. Ramanathan, S. Asher, A. Franz, J. Keane, L. Wang and R. Noufi, "High efficiency graded bandgap thin-film polycrystalline Cu(In,Ga)Se_2-based solar cells", Sol. Energy Mater. Sol. Cells **41/42**, 231 (1996)

22 K. Ramanathan, M.A. Contreras, J.R. Tuttle, J. Keane, J. Webb, S. Asher, D. Niles, R. Dhere. A.L. Tennant, F.S. Hasoon, and R. Noufi, "Effect of Heat Treatments and Window Layer Processing on the Characteristics of $CuInGaSe_2$ Thin Film Solar Cells", Proc. of 25th IEEE Photovoltaic Spec. Conf., p.837 (IEEE, N.J., 1996)

23 V. Probst, F. Karg, J.Rimmasch, W. Reidl, W. Stetter, and H. Harms, "Advanced Stacked Elemental Layer Process for Cu(InGa)Se_2 Thin Film Photovoltaic Devices",*Thin Films for Photovoltaic and Related Device Applications*, Mat. Res. Soc. Symp. Proc. **426**, p. 165, (1996)

24 K. Kushiya, A. Shimizu, K. Saito, A. Yamada and M. Konagai, "Development of high-efficiency $CuIn_xGa_{1-x}Se_2$ Thin-Film Solar Cells by Selenization with Elemental Se Vapour in Vacuum", *Proc. of 24th IEEE Photovoltaics Spec. Conf.* p. 87 (1994)

25 B.M. Basol, V.K. Kapur, A. Halani, C.R. Leidholm, J. Sharp, J.R. Sites, A. Swartzlander, R. Matson, and H. Ullal, "Cu(In,Ga)Se_2 thin films and solar cells prepared by selenization of metallic precursors", J. Vac. Sci. Technol. A **14**, 2251 (1996)

26 J.R. Tuttle, J.R. Sites, A. Delahoy, W. Shafarman, B. Basol, S. Fonash, J. Gray, R. Menner, J. Phillips, A. Rockett, J. Scofield, F.R. Shapiro, P. Singh, V. Suntharalingam, D. Tarrant, T. Walker, S. Wiedeman and T.M. Peterson, "Characterization and Modeling of Cu(In,Ga)$(S,Se)_2$-based Photovoltaic Devices: A Laboratory and Industrial Perspective", Prog. Photovolt. **3**, 89 (1995)

27 A. Rockett, F. Abou-Elfotouh, D. Albin, M. Bode, J. Ermer, R. Klenk, T. Lommasson, T.W.F. Russell, R.D. Tomlinson, J. Tuttle, L. Stolt, T. Walter and T.M. Peterson, "Structure and chemistry of $CuInSe_2$ for solar cell technology: current understanding and recommendations", Thin Solid Films, **237**, 1 (1994)

28 J. Hedstrom, H. Ohlsen, M. Bodegard, A. Kylner, L. Stolt, D. Hariskos, M. Ruckh and H.W. Schock, "ZnO/CdS/Cu(In,Ga)Se_2 Thin Film Solar Cells with Improved Performance", *Proc. 23th IEEE Photovoltaics Spec. Conf.* p. 364 (1993)

Chapter 2

Growth and Stoichiometry of $CuInSe_2$ Films

2.1 Substrate Preparation

Corning 7059 barium borosilicate glass (1.929×1.929×0.048 inches) or Kodak CAT1413020 soda-lime slide cover glass (1.935×1.935×0.029 inches) were used as substrates. The substrates are thoroughly cleaned by the following procedure.

a) Wipe substrate with tissue soaked in detergent solution (ALCONOX in warm water).
b) Immerse in detergent solution and clean in ultrasonic bath for 5 minutes.
c) Rinse in water, immerse in acetone and clean in ultrasonic bath for 5 minutes.
d) Immerse in distilled water and clean in ultrasonic bath for 5 minutes.
e) Immerse in ethanol and clean in ultrasonic bath for 5 minutes.
f) Remove from ethanol and place under dust cover while ethanol evaporates.

2.2 Vacuum Deposition System

2.2.1 Overview of the Deposition Method

The $CuInSe_2$ films are deposited by co-evaporation (simultaneous vacuum evaporation) of the elements. Each of the elements (Cu, In, Se) is evaporated from an electrically heated source. Thermocouples monitor the source temperatures, and current to each source is automatically adjusted by a temperature controller, in order to hold each source at a particular temperature. The rate of change of frequency of a quartz crystal oscillator microbalance is used to measure the deposition rate for each element, and the temperature of each elemental source is calibrated to give the required deposition rate. The substrate is held at constant temperature by a radiation heater connected to a temperature controller. A mechanical shutter is used to cover the substrate during system bake-out and source calibration. A diagram of the vacuum evaporation system is shown in figure 2.1. Details of the temperature controller and deposition rate monitor are given below.

2.2.2 Evaporation Source Temperature Controller

A temperature controller was designed and constructed to independently control the temperature of each of the three sources. Average current flow to each source is determined by full wave adjustable phase control of the 115 VAC supply to the primary winding of a step down transformer. The secondary winding is connected to the source heater. An error amplifier compares the measured temperature to a reference temperature and automatically adjusts the turn-on phase in order to maintain the required source

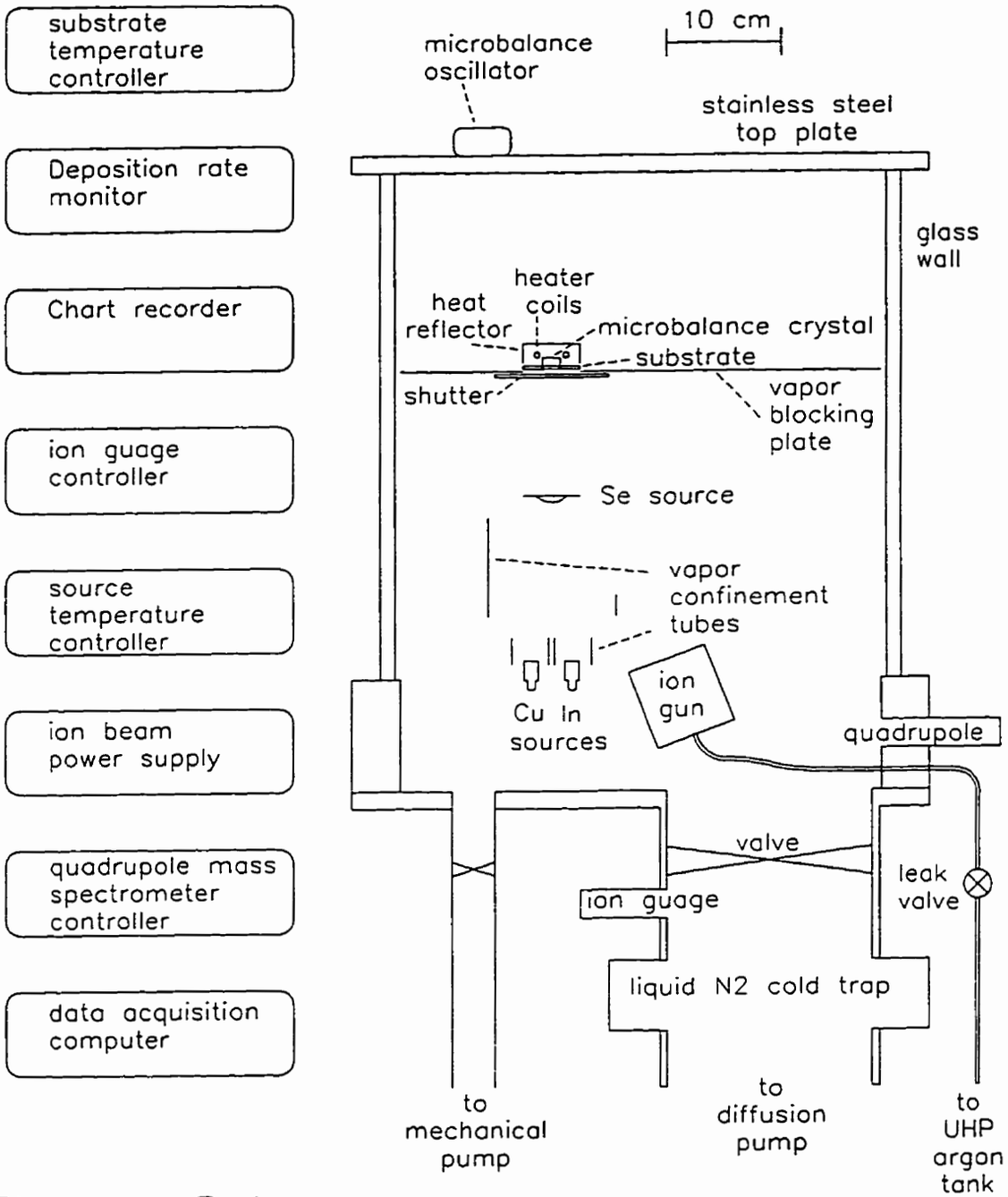

Figure 2.1

Simplified diagram of $CuInSe_2$ deposition system. Cu and In source heaters and wiring not shown. Thermocouples are located at the substrate and sources for temperature measurement and control. Vacuum base pressure 1E−7 Torr.

temperature. A simplified schematic of the temperature controller is shown in figure 2.2. Typical waveforms at several points are shown in figure 2.3 The operation of the phase controlled AC power supply is as follows.

Transformer T1 reduces the 115 VAC power line voltage to 6.3 VAC. This signal is attenuated and low pass filtered by R1, R2 and C1 (point A). Comparator U1, R3, R4 and gate U2 convert the signal to a 0-15 volt, 60 Hz square wave. R5,C2 and EX-OR gate U3 produce a 20 μS pulse at each transition of the square wave. These pulses trigger monostable U4 which then produces a precise 2 μS pulse train at 120 Hz (point B). Each pulse closes analog switch U5 which zeroes the integrator U6. Between pulses, the integrator output is a positive slope voltage ramp. The resulting waveform is a 0-10 volt saw-tooth at 120 Hz (point C).

Comparators U7-9 and solid state relays U10-12 serve control channels 1, 2 and 3, respectively. Each comparator outputs a variable width pulse train which determines the on time of the corresponding solid state relay. Since the channels function identically, only channel 1 is described in detail. The saw-tooth waveform connected to the non-inverting input of comparator U7 is compared to a control voltage (point D) connected to the inverting input. If the control voltage is less than the saw-tooth voltage, then the output (point E) of U7 is positive, U10 is on, and the step-down power transformer T2 is energized. Switch S1 selects as control voltage either an adjustable 0-10 volt DC level (R11; manual control) or the output from the error amplifier of the source 1 feedback network (U15; automatic control). As the control voltage is varied from 0 to 10 volts, the output voltage (point F) conduction angle θ changes linearly from 180 to 0 degrees. The transformer secondary current (point G) flowing through the evaporation source heater is a smoothed version of the output voltage, due to the low pass filtering effect of the transformer inductance.

When switch S1 is in the manual control setting, the conduction angle (and therefore the average output power to the source) can be set to any value by adjusting R11. There is no temperature feedback and this is an open loop control system.

With S1 in the automatic control position, a feedback network maintains a constant source temperature. A description of this closed loop control system is as follows: A thermocouple is located in the base of the source crucible. A DC differential amplifier U13 with gain 100 amplifies the thermocouple thermal voltage while rejecting any common mode signal. Capacitors C5, C6 and C7 filter out any AC differential signal. Error amplifier U14 amplifies the voltage difference between the thermocouple amplifier output and the reference voltage input which is selected with a 10 turn potentiometer (R23). The output from U14 is level shifted and attenuated by U15 to limit the voltage range to

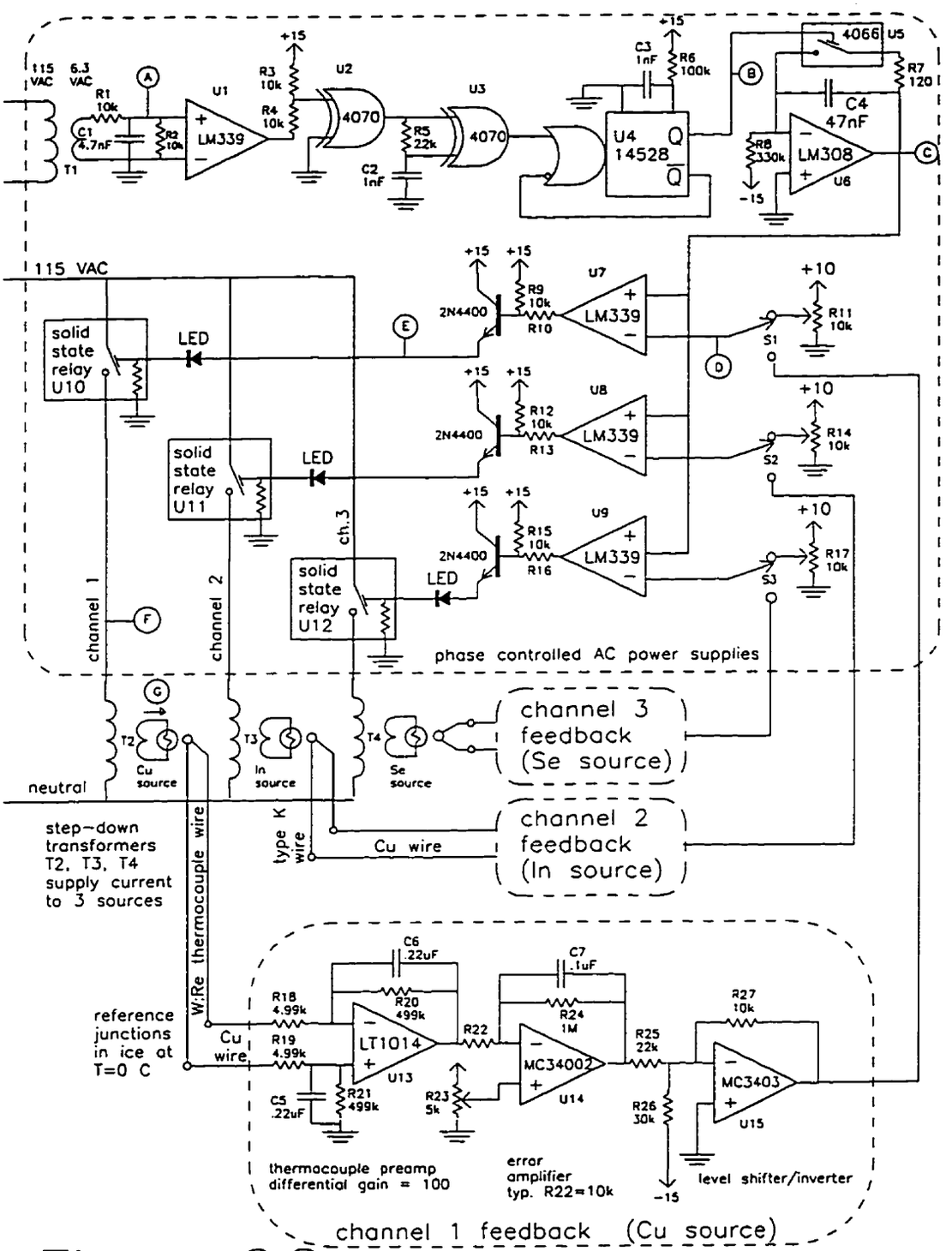

Figure 2.2

A simplified schematic of the 3 source temperature controller. Solid state relays control the conduction phase angle of the 110 volts AC at the primary of each step-down transformer. Thermocouples on sources provide temperature feedback.

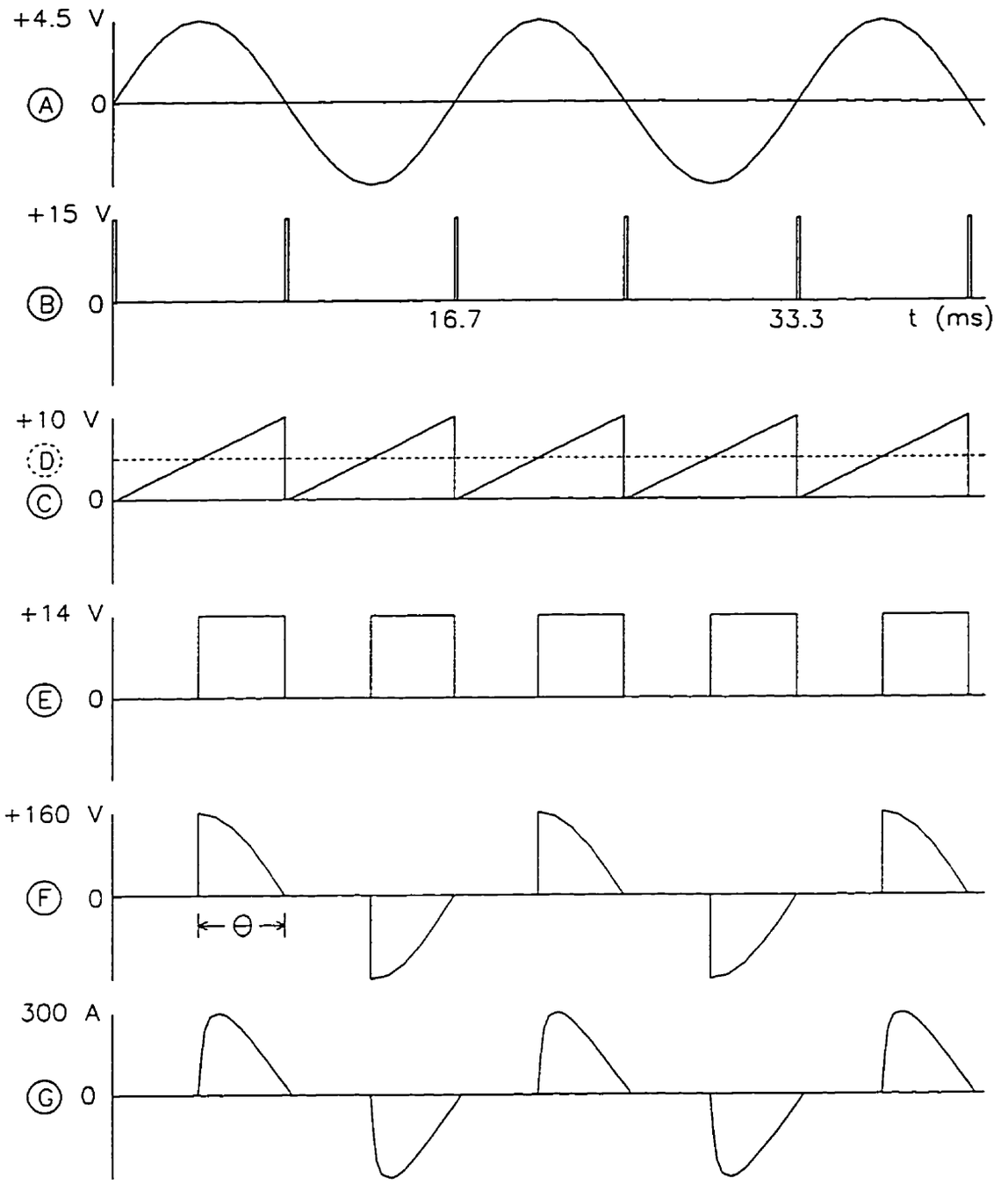

Figure 2.3

Typical waveforms at various test points in the source temperature controller electronics. Width of pulses at point B is 2 uS. Waveforms shown are for θ=90 degree conduction phase angle. Frequency is 60 Hz.

0 to 10 volts, as required for the phase control input. To minimize the error voltage, the error amplifier gain is set as high as possible without causing instability of the control system. This system is known as a proportional controller because the control signal is proportional to the error voltage.

2.2.3 Deposition Rate Measurement

The thickness of the growing film is monitored by a quartz crystal microbalance located near the substrate. This quartz disc has a fundamental mechanical resonance at $f_0 \cong 5MHz$, and controls the frequency of an electronic oscillator. Evaporated metal from the sources deposits on the exposed surface of the crystal. As metal accumulates on the crystal, the frequency of the crystal oscillator decreases by an amount Δf proportional to the thickness of deposited metal. The relationship can be expressed as

$$\Delta f = -c\rho t \qquad \text{Hz} \qquad (2.1)$$

where $c = 5.65 \times 10^7\ s^{-1}cm^2g^{-1}$, ρ is the density in gcm^{-3}, t is the film thickness in cm [1]. The rate of decrease in crystal oscillator frequency is proportional to the rate of growth of the film, and a desired growth rate and stoichiometry can be established by setting the appropriate evaporation source temperature for each element. Refer to figure 2.4 for the following description of the evaporation rate calibration system.

Transistor J1 and microbalance crystal X1 form a Colpitts oscillator [2] circuit. The electronics is located on the outside wall of the vacuum system in order to minimize the length of the connecting wires between the crystal and the electronics. Transistor J2 drives transformer T1 which superposes the 5 MHz oscillator signal onto the 5 volt power supply, so that only two conductors are required to connect the microbalance oscillator to the external circuits.

The rest of the electronics in figure 2.4 is rack-mounted beside the vacuum system. A tuned amplifier (J3, C6, T2) with center frequency 4.8 MHz and 3 dB bandwidth 500 kHz serves to de-couple the oscillator signal from the power supply, filter out noise, boost amplitude and remove harmonics. The sine wave is converted to a 5 volt square wave by J4 and Schmidt trigger U13. The square wave is counted by the binary counter U11, for a time interval of 1.024 seconds set by a timing pulse derived from the 4 MHz clock oscillator (X2, U1), followed by frequency dividers U3, U4, U5 and monostable U6. At the end of the count interval, the 10 least significant bits of the counter are loaded into the internal storage latch of a 10 bit digital to analog converter (DAC) U10, which holds the 10 bit binary number and converts this number to one of 1024 analog levels between 0 and 10 volts. The output voltage is proportional to modulo 1000 of the microbalance crystal oscillator frequency. This can be expressed as

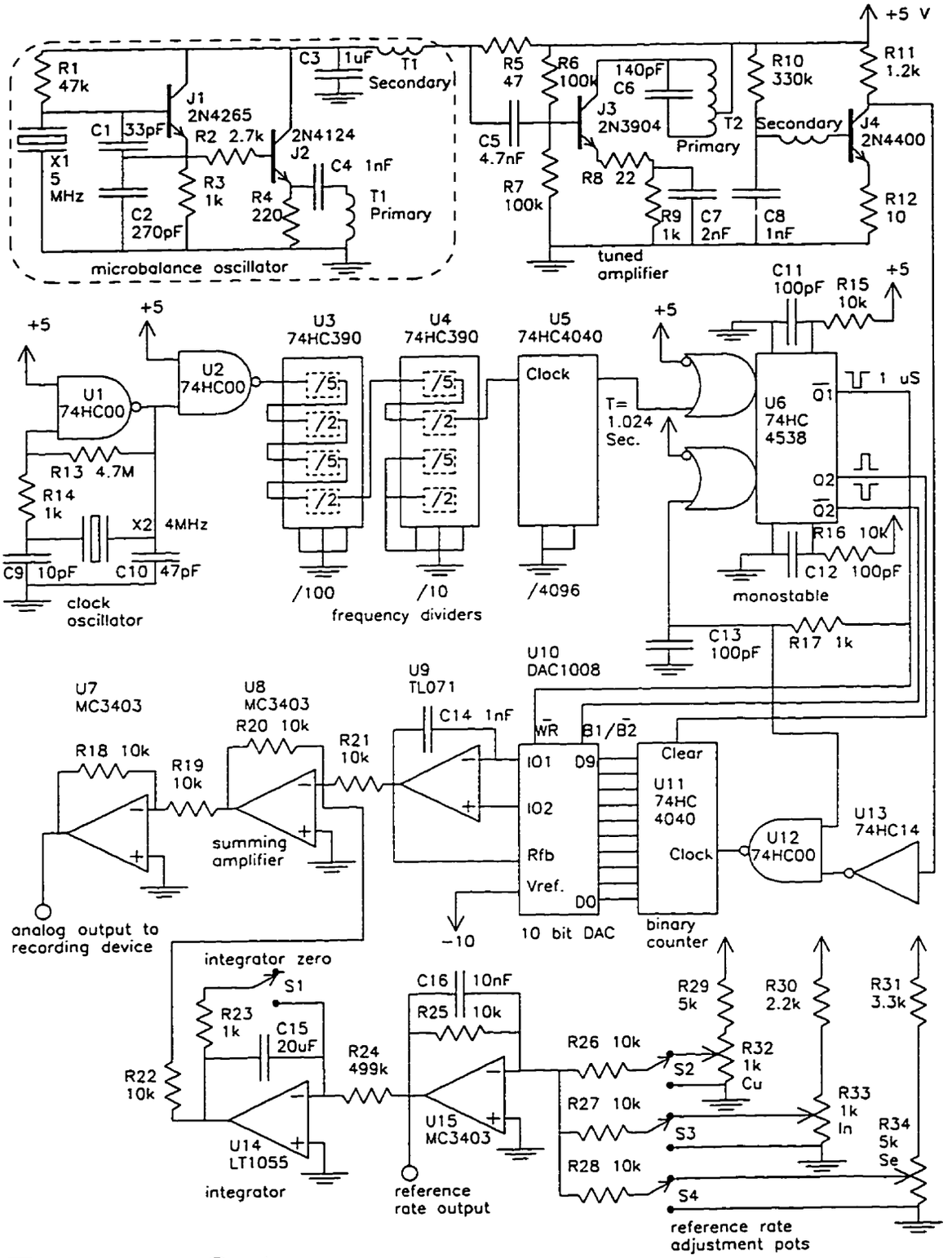

Figure 2.4

Film deposition rate monitor and rate calibration system

$$V = \frac{f - 1000n}{100} \quad \text{(volts)} \qquad (2.2)$$

where f is the microbalance frequency, V is the DAC output voltage and n is an integer chosen such that $0 < V < 10$. For a given n value, the output voltage changes by 1 volt for a 100 Hz change in the microbalance crystal frequency.

To facilitate the accurate setting of deposition rates, an analog reference ramp generator is included. Voltages proportional to the desired deposition rate for each of the three elements are selected with potentiometers (R32, R33, R34). Integrator U14 produces a voltage ramp with positive slope proportional to the sum of the switch (S2, S3, S4) selected input voltages provided by the calibration potentiometers. The reference ramp is then added to the output from the DAC by summing amplifier U8. Since the two input ramps to the summing amplifier have slopes of opposite sign, the output is a constant when the slopes have exactly equal magnitude. The output is connected to an analog chart recorder with 10 volts full scale and about 3 mm/minute chart speed. The chart record provides a very helpful visual indication of the calibration error, since zero error corresponds to a constant output.

2.3 Evaporation Source Design and Evaluation

A Mo boat source (similar to S9C-.010Mo from R.D. Mathis Company [3]) with a type K thermocouple fastened by a stainless steel bolt was used for the Se evaporation source. The design of the Cu and In sources was more difficult because higher temperatures and more precise deposition rate control are required. Initially, commercial crucible type sources (C9 Mo crucible and CH-10 heater from R. D. Mathis) were used. Various thermocouple-to-crucible thermal contacting schemes were tested, as indicated by the source types in figure 2.5. The In source calibration temperature and nominal deposition rate (shown as "+") for each $CuInSe_2$ film deposition is plotted in figure 2.6. For a given source type, points representing nominally identical calibration conditions are grouped together and the standard deviation (SD) from the mean group temperature is calculated. The SD is an indication of the repeatability of the calibration process, and includes other error sources unrelated to temperature measurement, such as variations in microbalance crystal sensitivity [1]. The radiation coupled thermocouple-in-a-well design (type (f) source, in figure 2.5) gave the lowest SD (SD $\cong$ 5 °C) and best overall performance. One notable failure of the type (f) source occurred when the thermocouple came into direct contact with the crucible. This point (marked "excluded" in figure 2.6) was excluded from the SD calculation. The last group of temperatures for the type (f) source shows a lower average temperature than the first group, despite the increased rate, because the source

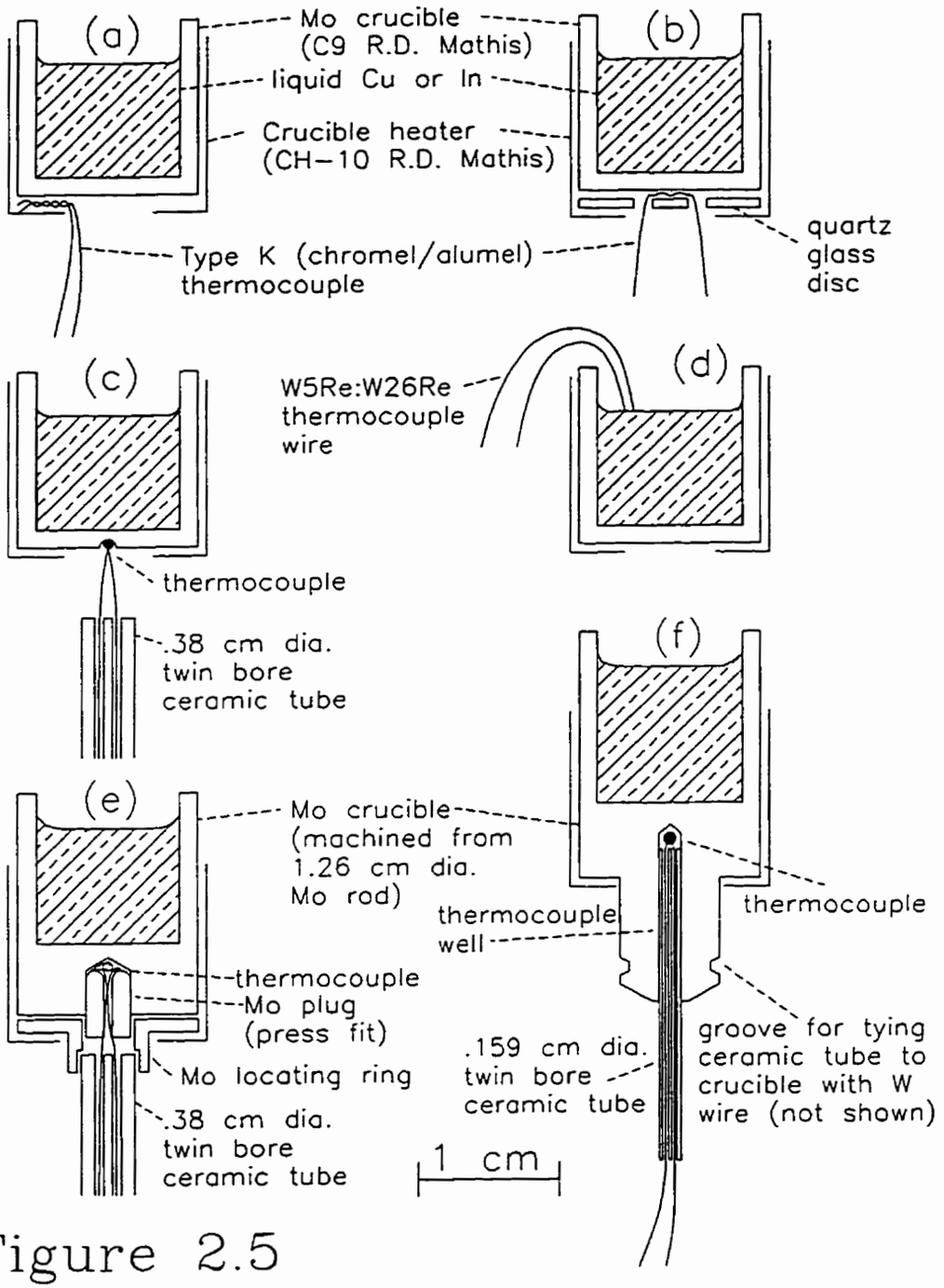

Figure 2.5

Source crucible temperature measurement schemes.
(a) Thermocouple between crucible and heater
(b) Thermocouple between crucible and quartz disc
(c) Thermocouple forced against crucible by spring
(d) Heated thermocouple in liquid metal (copper only)
(e) Thermocouple pressed into base of crucible
(f) Thermocouple in deep well; radiation heat transfer

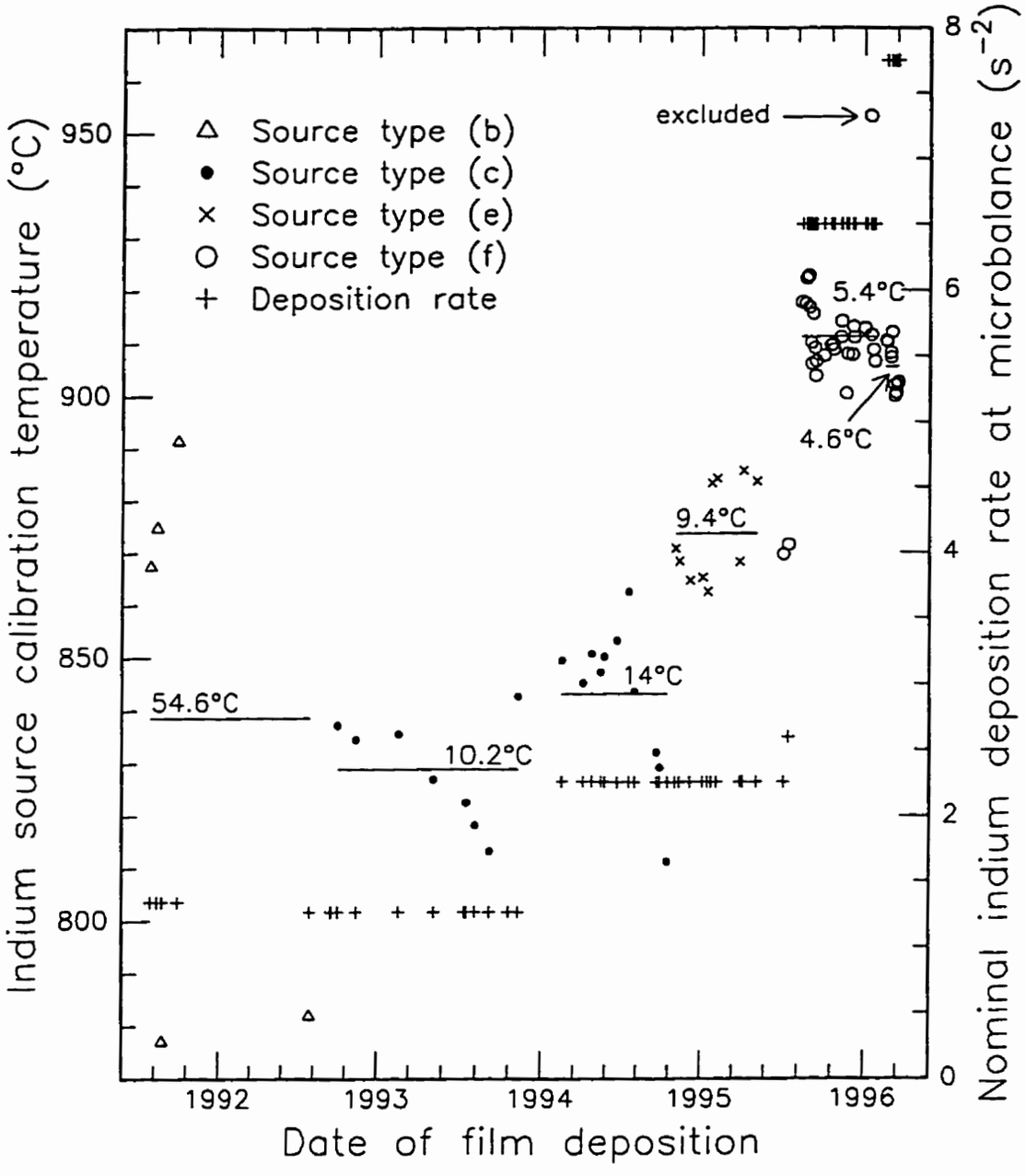

Figure 2.6

Indium calibration temperature history for the source types (b, c, e, f). The mean temperature for a similar group of points is represented by a horizontal line segment. The standard deviation is shown beside each line.

was moved closer to the crystal. Results (not shown) similar to those discussed above for In were obtained for the various Cu sources tested. Type (f) sources are used for all Cu, In and CdS evaporation described in this work, unless otherwise specified.

Deposition rate vs. temperature for the Cu, In and Se sources are shown on an Arrhenius plot in figure 2.7. The heats of vaporization for Cu and In and the sensitivity of the deposition rate to source temperature can be determined as follows.

The deposition rate temperature dependence is expected to be proportional to the mass evaporation rate. For a liquid metal [4], the mass evaporation rate is given by

$$G = CT^{-\frac{1}{2}} \exp\left(-\frac{\Delta H_v}{RT}\right) \qquad (gcm^{-2}s^{-1}) \qquad (2.3)$$

where ΔH_v is the heat of vaporization, R is the universal gas constant, and C is independent of temperature. Taking logarithms, we have

$$\ln(G) = \ln\left(T^{-\frac{1}{2}}\right) - \frac{\Delta H_v}{RT} + \ln(C) \qquad (2.4)$$

The slope of an Arrhenius plot is therefore

$$\text{Slope} = \frac{d[\ln(G)]}{d\left[\frac{1}{T}\right]} = \frac{T}{2} - \frac{\Delta H_v}{R} \qquad (2.5)$$

For the data of figure 2.7 the slopes obtained by least squares fits are

$(\text{slope})_{Cu} = -31412\ K$ at $T \cong 1500\ K$

$(\text{slope})_{In} = -21815\ K$ at $T \cong 1150\ K$

From these slope values we can calculate ΔH_v.

Experimental Values

$(\Delta H_v)_{Cu} = 63.94$ kcal/mol $\quad (\Delta H_v)_{In} = 44.51$ kcal/mol

Accepted Values [5]

$(\Delta H_v)_{Cu} = 72.8$ kcal/mol $\quad (\Delta H_v)_{In} = 53.8$ kcal/mol

The above simple analysis is not valid for the Se data of figure 2.7 because the Se melting point falls within the measured temperature range.

Differentiation of equation (2.3) yields

$$\frac{dG}{dT} = CT^{-\frac{1}{2}}\left(\frac{\Delta H_v}{RT^2} - \frac{1}{2T}\right)\exp\left(-\frac{\Delta H_v}{RT}\right)$$

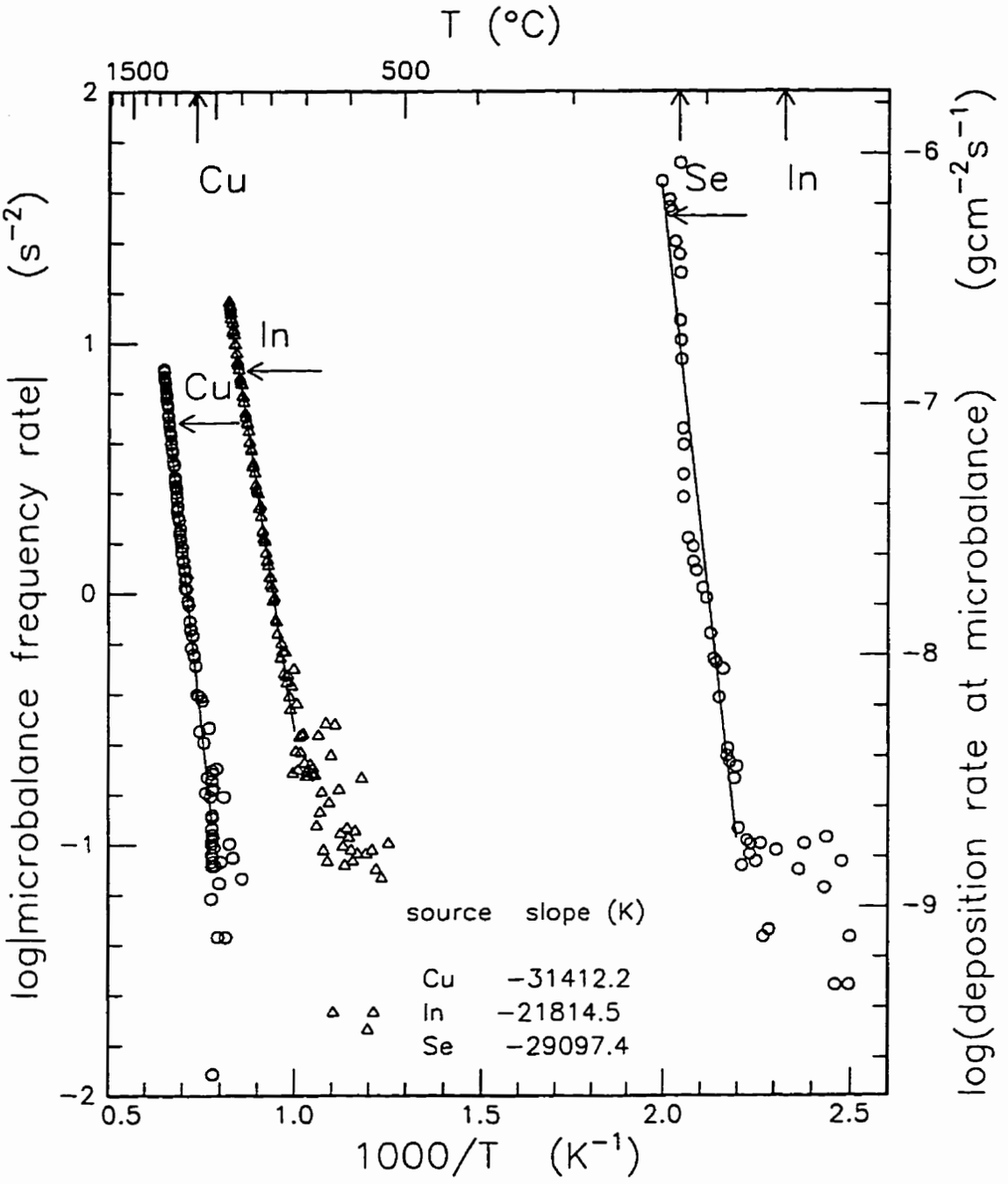

Figure 2.7

Typical deposition rates vs. source thermocouple temperature T. Horizontal arrows show operating points. Vertical arrows show melting temperatures. Slopes are calculated for ln(rate) vs. 1/T.

which can be written as

$$\frac{dG}{G} = \left(\frac{\Delta H_v}{RT} - \frac{1}{2}\right)\frac{dT}{T} = -\left(\frac{\text{Slope}}{T}\right)\frac{dT}{T} \qquad (2.6)$$

At typical source operating temperatures, we have

$\frac{dG}{G} = 20.9\frac{dT}{T}$ for the copper source at 1500 K, and

$\frac{dG}{G} = 18.9\frac{dT}{T}$ for the indium source at 1150 K.

These results show that the evaporation rate is extremely sensitive to the source temperature. A stability test record for the type (f) In source is shown in figure 2.8. The temperature controller set point was manually adjusted until a nominal 5 Hz/s (= 5 s^{-2}) deposition rate was measured by the crystal microbalance, at about 9 minutes after source current turn-on. No further adjustments were made to the controller until about 86 minutes, when the controller was switched off. The frequency rate of the microbalance oscillator, the source heater current, the 120 VAC supply to the controller, and the thermocouple temperature were recorded. The peak to peak relative noise in the deposition rate averaged over 3 minute intervals is about 1%. Therefore, the variation in the temperature of the In melt, averaged over 3 minute intervals, is less than or equal to

$$dT = \frac{T}{18.9}\frac{dG}{G} = \frac{1150}{18.9}\frac{1}{100} = 0.61\ \text{K}$$

Because the thermocouple is not in mechanical contact with the hot crucible, the thermocouple junction is at a lower temperature than the hot crucible. The temperature difference between the crucible and the thermocouple is the temperature offset δT. The results for two methods of δT measurement are shown in figure 2.9. In the first method, a stainless steel type (f) dummy crucible was constructed. A 0.01 inch (0.254 mm) diameter type K thermocouple was bolted directly to the crucible and another placed in the thermocouple well. The temperature of each thermocouple is recorded as the crucible is heated to operating temperature. In the second method, a Mo type (f) crucible with a 0.01 inch W5Re:W26Re thermocouple is used. The crucible contains Cu that was previously melted, then cooled, and the crucible is heated through the Cu melting temperature by increasing the heater current at a constant rate. The plateau in the thermocouple temperature vs. time curve corresponds with the Cu melting temperature (T_m = 1083.4 °C). As indicated in figure 2.9, the temperature offsets are $\delta T_1 \cong 44$ °C and $\delta T_2 \cong 76$ °C. Since the temperature offset cannot be easily determined in most cases, source temperatures quoted in this document are thermocouple temperatures, which are less than the actual crucible temperatures.

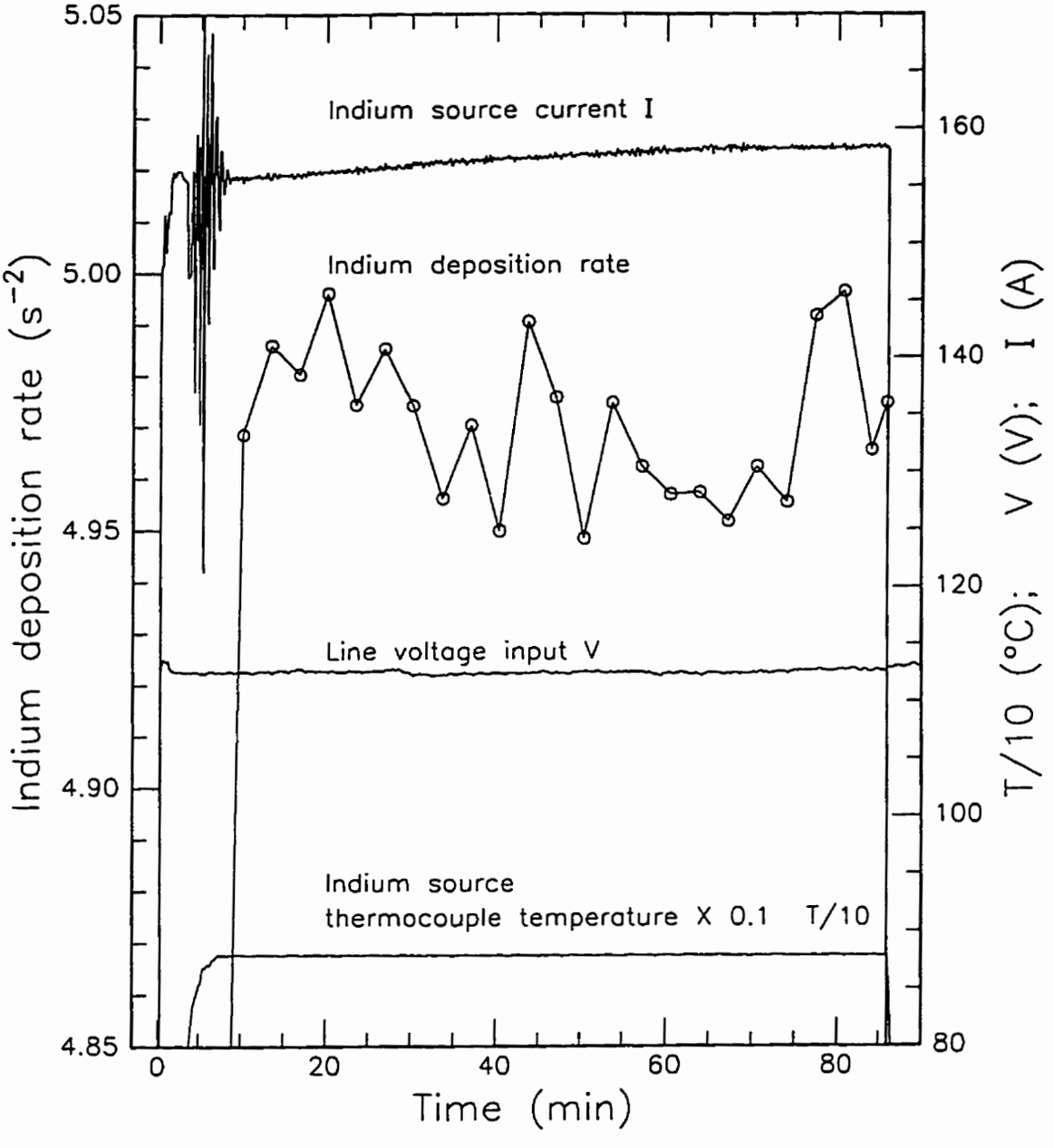

Figure 2.8

Stability test of indium source. The temperature controller is used to maintain constant source thermocouple temperature. The deposition rate is averaged over 3 minute intervals centered on the data points shown.

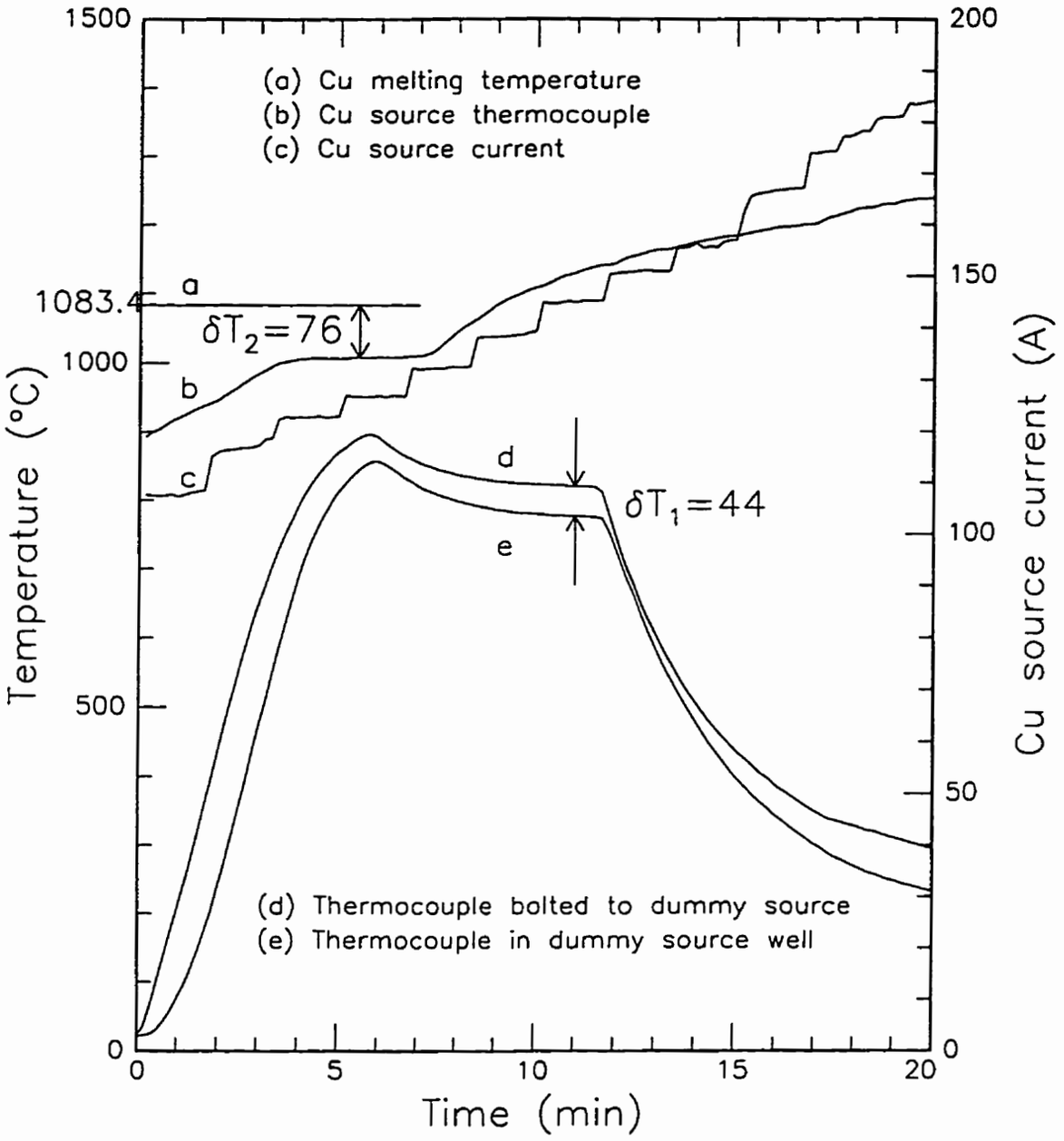

Figure 2.9

Source offset temperature δT determined by two methods. Curves (a, b, c) are for the Cu source with a W5Re:W26Re thermocouple. Curves (d) and (e) are for a stainless steel dummy crucible with type K thermocouples.

2.4 $CuInSe_2$ Film Deposition and Stoichiometry

2.4.1 Position Dependence of Deposition Rates

Because the evaporation sources are in different locations, relative to the substrate, the rate of deposition of each element on the substrate surface is a function of the position on the substrate. The expected deposition rates for each element, as well as the ratio of Cu rate to In rate, are calculated in this section. The calculation assumes a cosine distribution (source diameter much less than source to substrate distance [4]), and unity sticking coefficient for all elements. Referring to figure 2.10, the following points are specified, in cm units:

(0,0,0) = origin of coordinates, in the plane of the substrate
(x, y ,0) or (x, y) = any point in the substrate plane
(-a, 0, -h) = (-1.8 ,0, -26.3) = position of Cu source
(a, 0, -h) = (1.8 ,0, -26.3) = position of In source
(0, -4.53 , -11.5) = position of Se source
(0, 2.54 ,0) = position of microbalance crystal

In the plane (perpendicular to the source axis) of the substrate at a distance r from the source and at an angle θ from the source axis, the deposition rate D due to a small source with surface area A and mass evaporation rate G is

$$D = \frac{GA\cos^2\theta}{\pi r^2} \qquad (g\ cm^{-2}\ s^{-1}) \qquad (2.7)$$

After substituting for cosθ and r, the Cu and In rates are given by

$$D_{Cu}(x,y) = \frac{G_{Cu}Ah^2}{\pi\left((x+a)^2+y^2+h^2\right)^2} \qquad (2.8)$$

$$D_{In}(x,y) = \frac{G_{In}Ah^2}{\pi\left((x-a)^2+y^2+h^2\right)^2} \qquad (2.9)$$

The ratio of the Cu rate at (x, y) to the maximum Cu rate at (-a,0) is

$$B_{Cu} = \frac{D_{Cu}(x,y)}{D_{Cu}(-a,0)} = \frac{h^4}{\left((x+a)^2+y^2+h^2\right)^2} \qquad (2.10)$$

Circles of constant B_{Cu} are solutions of

$$(x+a)^2+y^2 = h^2\left(\frac{1}{\sqrt{B_{Cu}}}-1\right) \qquad (2.11)$$

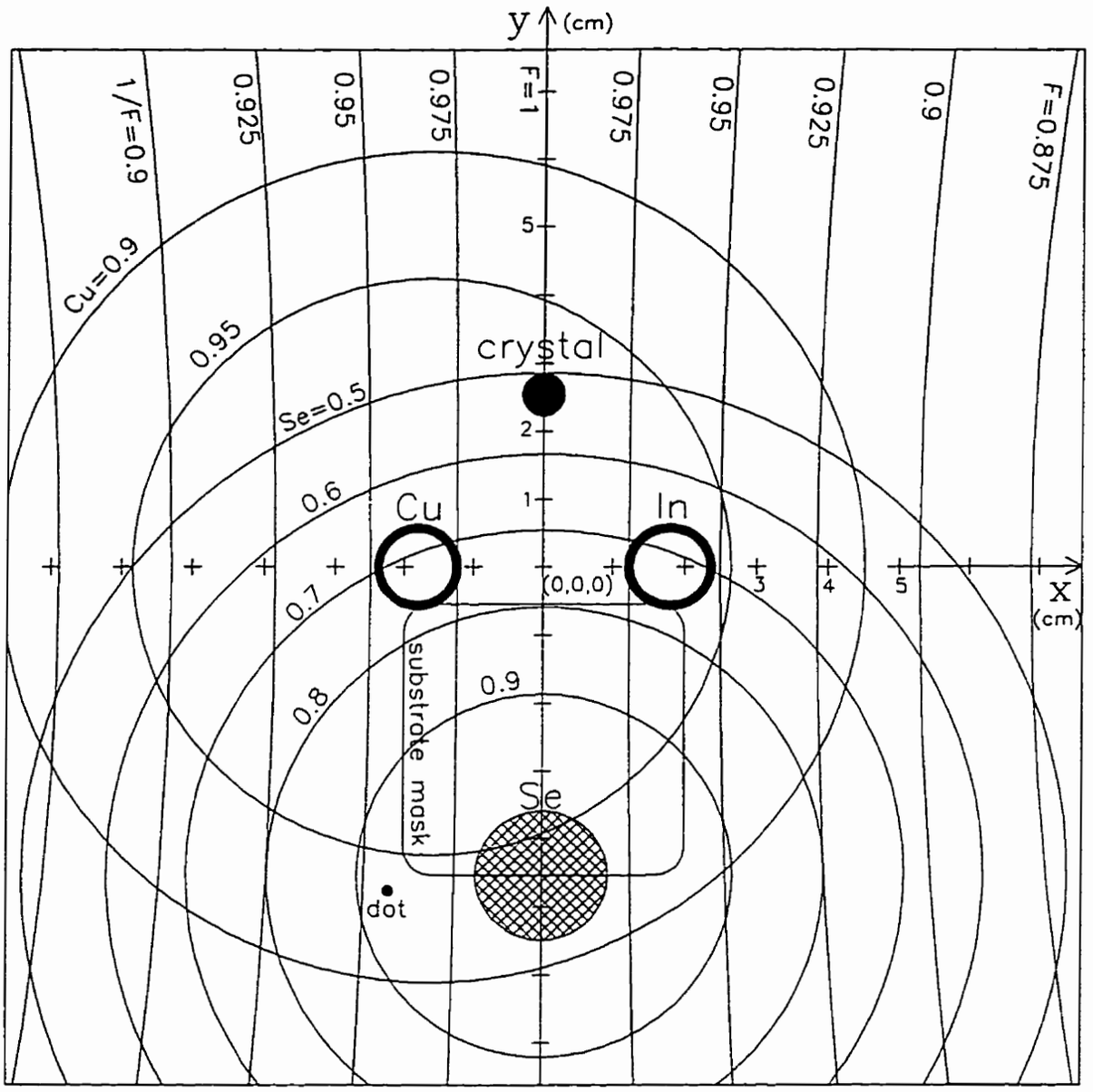

Figure 2.10

Computed deposition ratio F(x,y) and normalized Cu and Se rates, in the plane of the substrate. This is the top view, looking toward sources through the substrate. Lateral dimensions (x,y) are shown actual size, and the origin (0,0,0) is in the substrate plane as shown. The Cu and In sources are at z = −26.3 cm. The Se source is at z = −11.5 cm. This source configuration is used for films with serial number greater than 960221.

Circles of constant B_{In} and B_{Se} can be calculated in a similar way .

Let M_{Cu} and M_{In} be the atomic masses of Cu and In, respectively. The deposition ratio F(x, y) is defined as the expected ratio of the atomic Cu flux to the atomic In flux at the substrate position (x, y).

$$F(x,y) = \frac{D_{Cu}M_{In}}{D_{In}M_{Cu}} = \frac{G_{Cu}M_{In}}{G_{In}M_{Cu}}\left(\frac{(x-a)^2+y^2+h^2}{(x+a)^2+y^2+h^2}\right)^2 \qquad (2.12)$$

For equal atomic deposition rates we have $G_{Cu}/M_{Cu} = G_{In}/M_{In}$ and F(0,0) = 1. In this case, the curves of constant F are solutions of

$$x^2+y^2+h^2-2xa\left(\frac{1+\sqrt{F}}{1-\sqrt{F}}\right)=0 \qquad (2.13)$$

Figure 2.10 shows the substrate plane deposition map, computed using equations 2.11 and 2.13. Circles of constant B_{Se} and B_{Cu} are shown, as well as curves of constant F. Inspection of figure 2.10 shows that B_{Cu} and F(x, y) each vary by about 8% across the substrate, whereas B_{Se} varies by about 25%, because the selenium source is much closer to the substrate plane than the others. Circles of constant B_{In} (not shown) are similar to B_{Cu} but are centered on the In source. Note that F(x, y) varies only slightly with y, because $y << h$ in equation 2.12.

In subsequent chapters, some of the data is presented as a function of x at fixed y. In order to also provide an F(x, y) axis at a fixed y, the graphing software requires the inverse function x(F, y). Unfortunately, the inverse has a singularity at

$$F = \frac{G_{Cu}M_{In}}{G_{In}M_{Cu}}$$

To eliminate the singularity and to simplify the presentation of graphical data, F(x, y) is replaced by an approximate expression, y is fixed at $y_0 = -2.54$ cm and the result is defined as F(x), given by

$$F(x,y) \cong \frac{G_{Cu}M_{In}}{G_{In}M_{Cu}}\left(1-\frac{4xa}{y^2+h^2}\right)^2 \cong \frac{G_{Cu}M_{In}}{G_{In}M_{Cu}}\left(1-\frac{4xa}{y_0^2+h^2}\right)^2 = F(x) \qquad (2.14)$$

The relative error introduced by using the approximation F(x) is less than 0.1% for -2 cm $< x < 2$ cm and -3.56 cm $< y < -1.52$ cm. The approximation F(x) is used for calculations of auxiliary axis scales, or whenever the value of y is not explicitly defined. F(x, y) is used elsewhere. For rough calculations, one can use

$$F(x) \cong F(0)\left(1-\frac{8xa}{y_0^2+h^2}\right) = F(0)(1-0.021x)$$

and we see that F(x) decreases by about 2% per cm in the +x direction.

For film deposition with time dependent deposition rates D(t), such as in the case of two layer films, the average deposition ratio F_{av} is given by

$$F_{av} = \frac{M_{In}\int D_{Cu}(t)dt}{M_{Cu}\int D_{In}(t)dt} \qquad (2.15)$$

2.4.2 Typical Film Deposition Procedure

Figure 2.11 shows the deposition records for films 960229 and 960308. The deposition of a typical two layer film (960308) is described in the following. The day before deposition, a substrate is installed in the vacuum system, and the sources are filled with Cu, In (both 99.9999% pure) and Se (99.999% pure). The microbalance crystal is replaced if necessary (usually after completing two depositions). The vacuum system is pumped out, and heaters out-gas the vacuum chamber overnight. A small argon leak flushes the chamber. The morning of the day of deposition, the heaters and argon leak are switched off, the liquid nitrogen cold trap is filled, and the Cu, In and Se sources, and the substrate heater, are set to about one half of full operating power for out-gassing, while the chamber cools to room temperature. Next, the sources are briefly raised to full operating temperature, to melt the fresh charge of source material, and to complete the source out-gassing. The base pressure in the vacuum system is about 10^{-7} Torr. During the time interval 0 to 17.5 minutes (see figure 2.11, bottom), the source temperatures are adjusted to give the nominal microbalance frequency rates (in s^{-2}) shown in figure 2.11. The shutter is opened and the film is deposited from 17.5 to 89 minutes. At 69 minutes, the Cu rate is reduced and the substrate temperature increased, for the In-rich top layer. After the shutter is closed, the Cu and In sources are switched off, and the Se temperature is reduced slightly. Then the shutter is re-opened from 92 to 96 minutes, while the Se source is still on, to help minimize Se loss during the cool down to 300 °C. At 96 minutes the shutter is closed, and the substrate heater and Se source are switched off. By about 200 minutes, the substrate has cooled to about 70 °C. The high vacuum valve is then closed, the chamber filled to 5 Torr with UHP argon, and the substrate cools overnight to room temperature. Basic deposition data for all the $CuInSe_2$ films produced are listed in Appendix A. Deposition data for some films of interest are given in table 2.1 below.

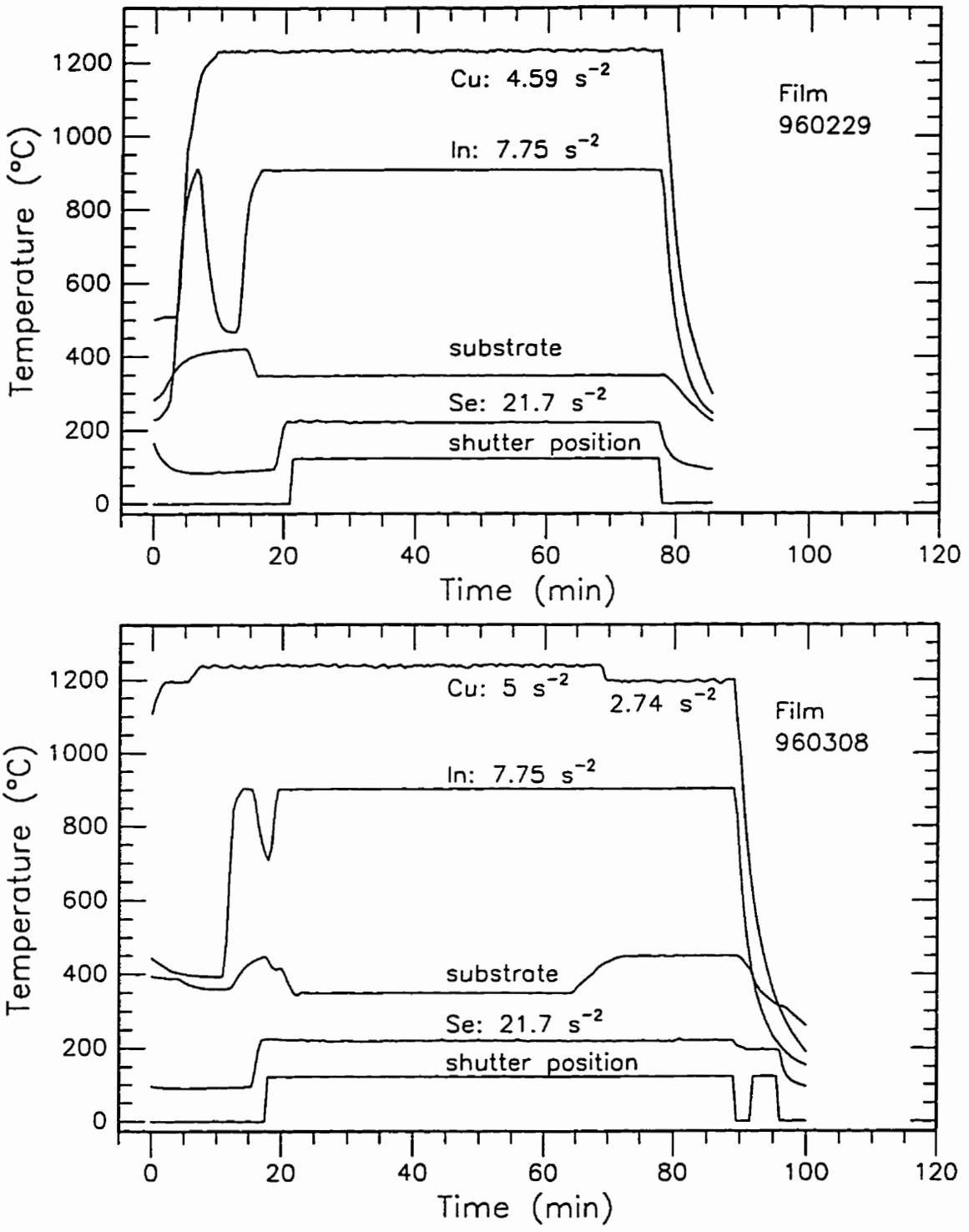

Figure 2.11

Film deposition records for two $CuInSe_2$ thin films. Top: film 960229; 2.57 μm thick, single layer. Bottom: film 960308; 2.95 μm thick, two layers.

Table 2.1: Film Deposition Data

Sample number	time (m) bottom/top	T_{sub} (°C) bottom/top	F(0, y) bottom/top	thickness d (μm)	substrate	comments
960228	44	350	1.02	1.99	7059 glass	
960229	56	350	1.07	2.566	7059 glass	
960309	52	350	1.166	2.288	7059 glass	1% NaOH for y>-2.54
960316	55	350	1.1145	2.588	Mo/7059	1% NaOH for y>-2.54
960308	51.5/20	350/450	1.186/.638 $F_{av.}$=1.032	2.95	7059 glass	1% NaOH for y>-2.54

2.4.3 Stoichiometry of $CuInSe_2$ Films

The actual concentration ratio of the metals in the finished film at position (x, y) is only approximately equal to F(x, y). The Cu and In sources are calibrated with the Se source off. Since high deposition rates are used, when the Se source is on there is a significant probability of collisions and possibly chemical interactions between the impinging Cu and In fluxes and the Se vapour. Not every evaporated metal atom leaving a source in the direction of the substrate will actually reach the substrate. Some may in fact be scattered in other directions by interaction with the Se vapour. Also, the sticking coefficients of both Cu and In are not necessarily exactly equal to one, and the flux from each source may deviate from a cosine distribution. As mentioned in section 2.3, source temperatures may drift slightly during the deposition.

The atomic concentrations of Cu, In and Se were measured at various points for each of four samples, using the EDX (electron probe energy dispersive x-ray analysis) accessory on a JEOL–840 scanning electron microscope. The results are shown in figure 2.12.

A ternary phase diagram and the $(Cu_2Se)_{1-x}(In_2Se_3)_x$ pseudo-binary line are shown in figure 2.13. All points on the pseudo-binary satisfy valence stoichiometry (Cu: +1, In: +3, Se: –2). The composition data of figure 2.12 are plotted on the diagram. All of the data points lie near the pseudo-binary. This indicates that sufficient Se is incorporated chemically, and that any excess Se not chemically bound re-evaporates at the high substrate temperatures used. The tendency of thin film compositions to lie near the pseudo-binary has been reported in [6].

All of the known ternary compounds in the Cu, In, Se system fall on the pseudo-binary. Of these, $CuInSe_2$ and the ordered vacancy compounds $Cu_2In_4Se_7$ and $CuIn_3Se_5$ [7,8] exist at room temperature. Studies of bulk polycrystalline samples [7,9] have shown that, at room

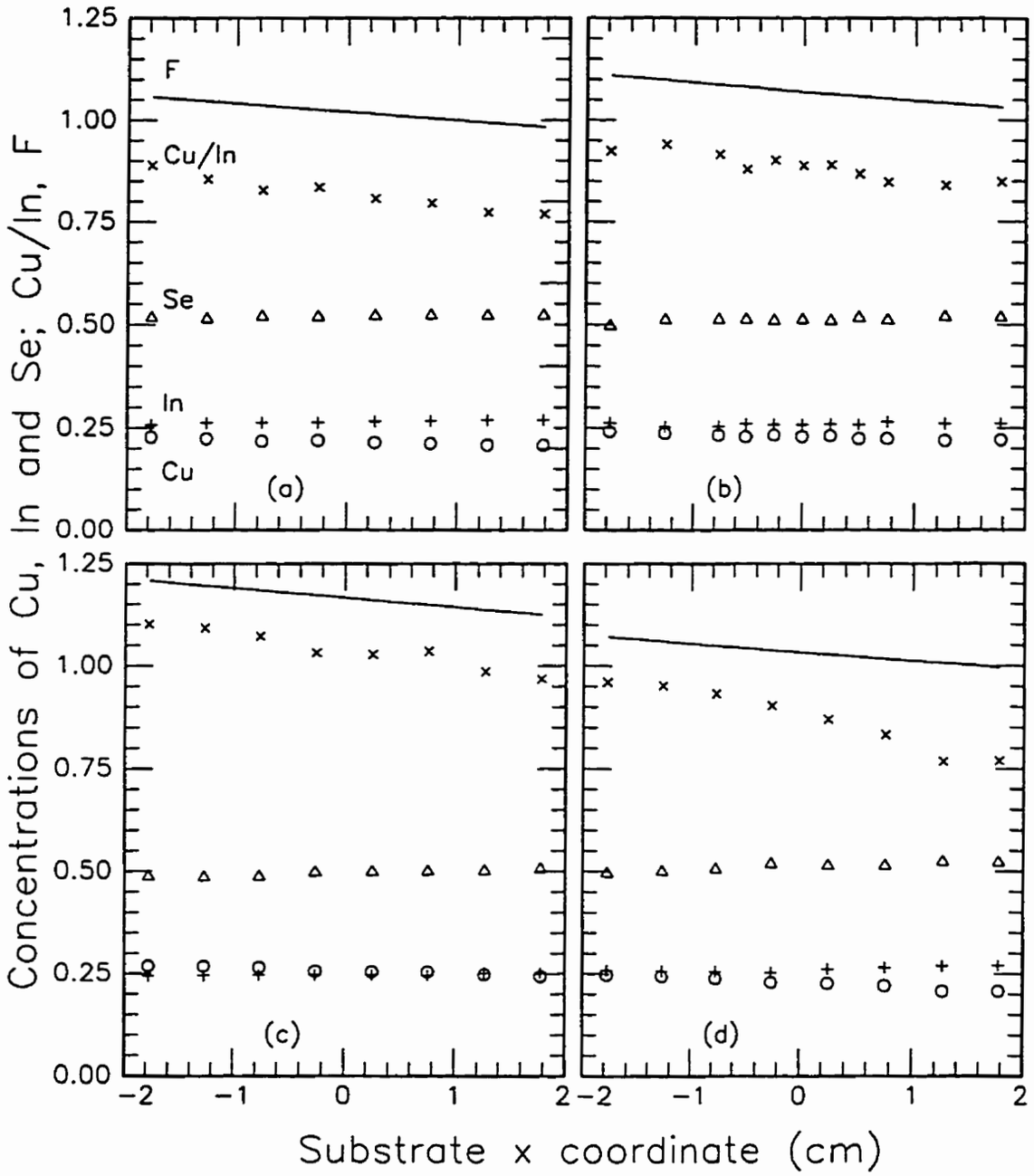

Figure 2.12

Elemental composition and Cu/In measured by EDX, and F, vs. position for $CuInSe_2$ films.
(a) 960228, y=−3 cm; (b) 960229, y=−1.52 cm
(c) 960309, y=−3.56 cm; (d) 960308 y=−3.56 cm

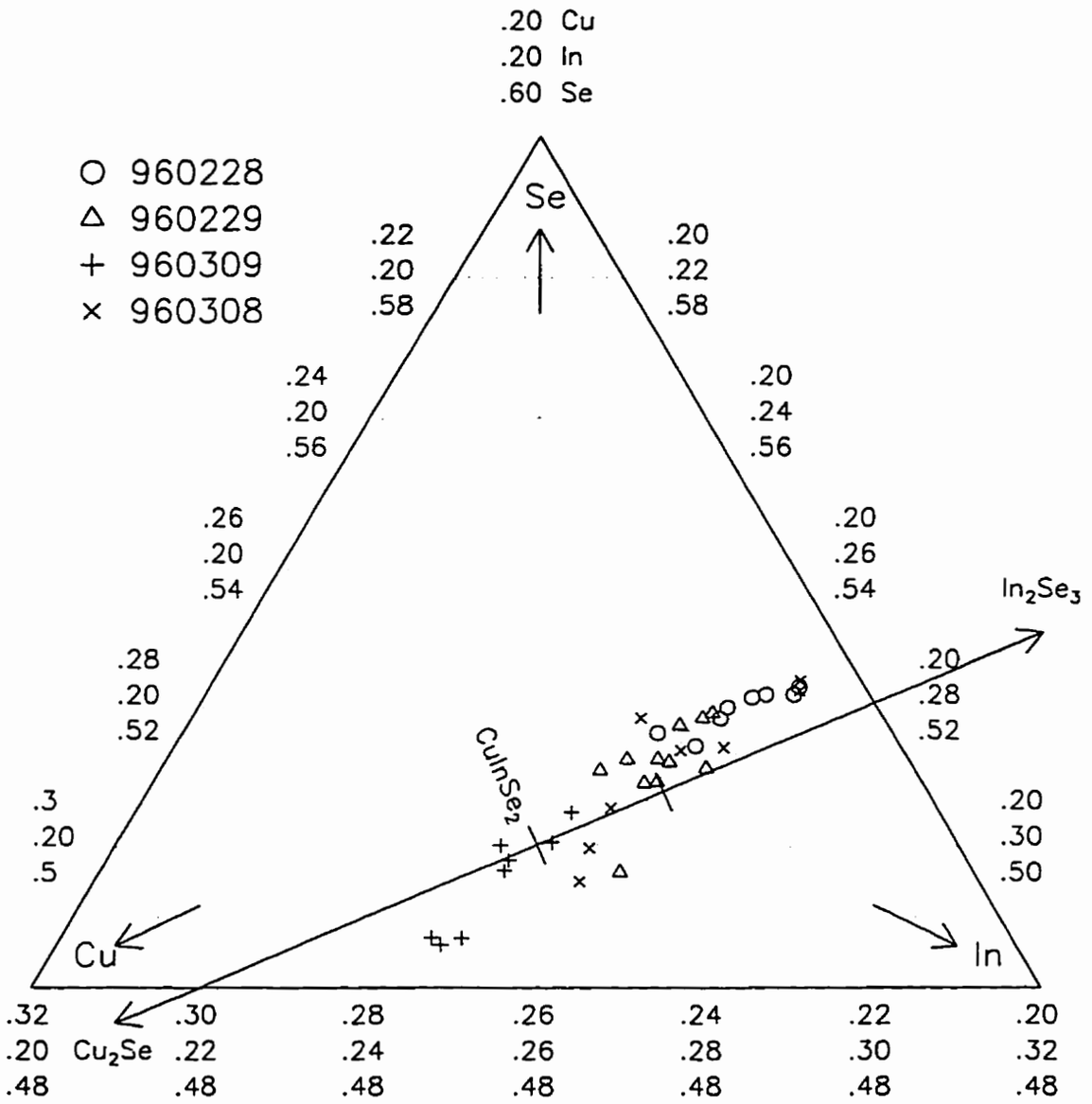

Figure 2.13

Atomic concentrations represented on the $CuInSe_2$ ternary phase field. The region of homogeneous chalcopyrite phase on the $(Cu_2Se)_{1-x}(In_2Se_3)_x$ pseudobinary line is between the tick marks.

temperature and thermal equilibrium, the homogeneous chalcopyrite phase exists for $0.53 \geq x \geq 0.5$. For copper rich mixtures ($x < 0.5$), the two phases $CuInSe_2$ and Cu_2Se are present. For $x > 0.53$, indium rich phases and $CuInSe_2$ are present. Differences observed in comparing the above results with those for thin films deposited by multiple source evaporation at 400 °C [9] suggest that the thin films do not reach complete thermal equilibrium under the deposition conditions.

The "two layer" film growth method, pioneered at Boeing [**10, 11**] is used for some of the films grown in this work. A brief description follows. According to the pseudo-binary phase diagram, for $x < 0.5$, only the phases $CuInSe_2$ and Cu_2Se are present in Cu-rich films [7]. Therefore, a Cu-rich layer ($d \cong 2.5$ μm) is deposited first, at sufficiently high temperatures ($T_{sub} = 350$ °C used here) to promote the growth of large grains of $CuInSe_2$. The resulting film is highly conducting and of poor photovoltaic quality due to the presence of excess Cu_2Se. To convert the Cu_2Se, the substrate temperature is raised to $T_{sub} = 450$ °C and an In-rich layer is deposited. The excess Cu_2Se reacts with the depositing In-rich mixture and growth of the $CuInSe_2$ grains continues. The deposition is stopped when all Cu_2Se is consumed and the overall composition is nearly stoichiometric. A recent article [**12**] describes an improved two stage technique where both layers are deposited at $T_{sub} > 500$ °C, the bottom layer is highly Cu-rich and the top layer is deposited without Cu. At the high temperature, Cu_2Se is a liquid, which facilitates transport of the $CuInSe_2$, formed from the reaction of Cu_2Se with depositing In and Se, to the existing $CuInSe_2$ crystals. The finished film is large grain, stoichiometric $CuInSe_2$, possibly with a thin surface layer of $CuIn_3Se_5$.

In figure 2.14, the measured Cu/In ratio is plotted as a function of the deposition ratio F. For the single layer films, a linear function of F approximating the measured Cu/In is determined by a least squares fit. This function $\beta_1(F)$, called the linearized Cu/In ratio, is used to predict the expected Cu/In ratio at other positions (x, y) on a substrate or for other single layer films deposited at $T_{sub} = 350$ °C, for which EDX measurements were not made. For the two layer film, the measured Cu/In ratio varies over a wider range than for the single layer films. This is probably due to a difference in the amount of free Cu_2Se available in the Cu-rich layer, at different (x, y) positions on the film. At $x \cong 1.8$ cm, the bottom Cu-rich layer is perhaps stoichiometric so that there is no excess Cu_2Se available and the top layer stays In-rich. At $x \cong -1.8$ cm, excess Cu_2Se in the bottom layer reacts with In and Se from the top layer to cause additional growth of the bottom $CuInSe_2$ grains and increase the top Cu/In ratio. Therefore, the bottom layer is approximately stoichiometric across the whole substrate and all of the composition variation due to F(x) is confined to the top layer. Since EDX measures only the near surface concentrations (depth < 0.1 μm), then a wider range in Cu/In is measured for the two layer film, than if

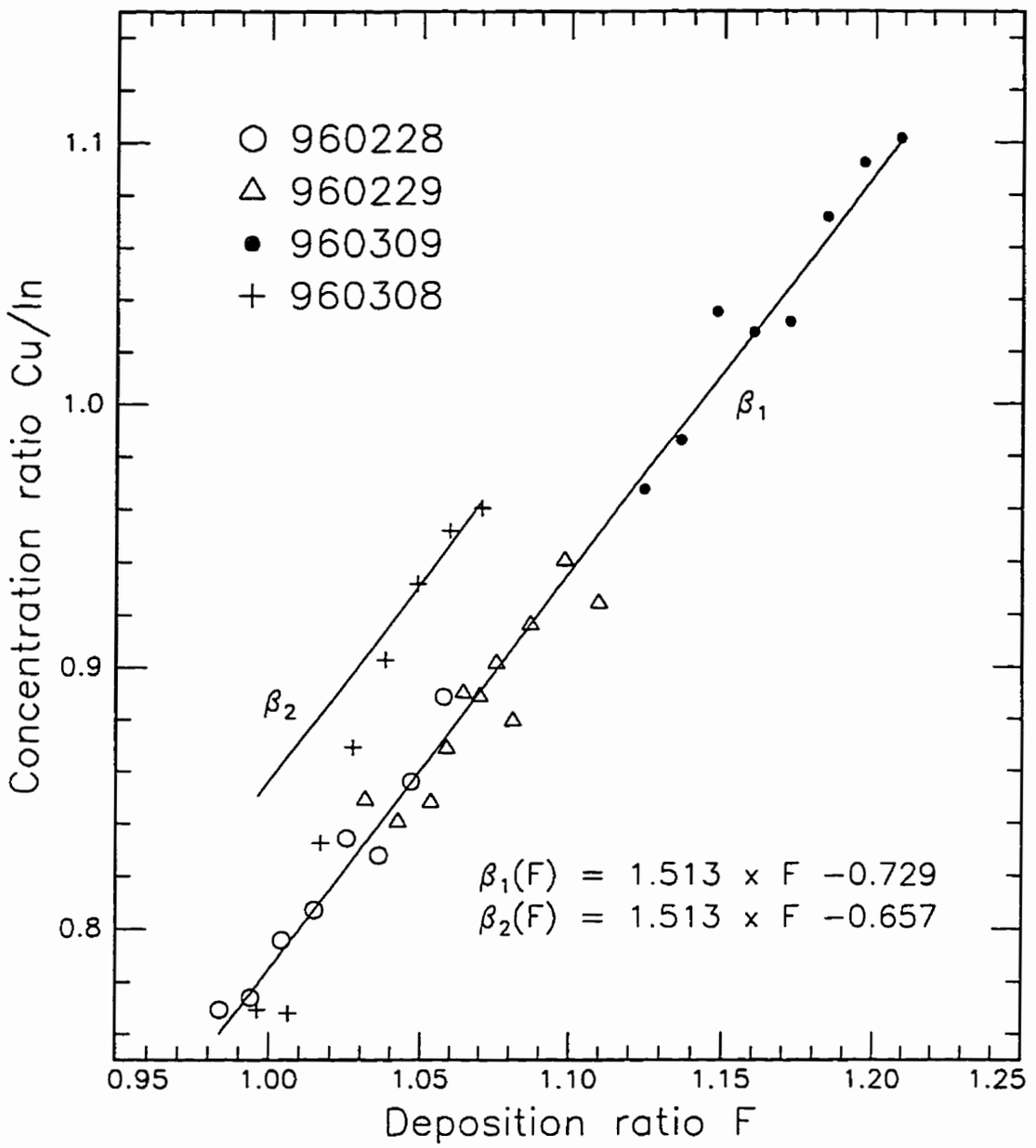

Figure 2.14

Cu/In concentration ratio as a function of deposition flux ratio F for three single layer $CuInSe_2$ films and a two layer film (960308). β_1 is least squares fit to single layer data. β_2 is estimated Cu/In, for two mixed layers.

the two layers were completely mixed. Assuming that the two layers are completely mixed near F(-1.8, y), then an estimate of the bulk $\beta_2(F)$ is a line passing through the point F=1.07, Cu/In=0.96 with the same slope as $\beta_1(F)$. From figure 2.14, the linearized concentration ratios are

$$\beta_1(x,y) = 1.513 \times F(x,y) - 0.729 \qquad (2.16a)$$

$$\beta_2(x,y) = 1.513 \times F(x,y) - 0.657 \qquad (2.16b)$$

Equations 2.16 are used to compute the $\beta(x)$ axis from the F(x) axis provided with some of the figures in the following chapters.

The accuracy of the EDX technique is limited by the uncertainties associated with the x-ray counting statistics, the uncertainties in the stoichiometry of the $CuInSe_2$ reference sample and the possible existence of segregated surface layers with substantially different composition than the bulk film. Indium rich surface layers about 30 nm thick have been measured by SIMS (secondary ion mass spectrometry) in films deposited at T_{sub}= 350 °C by Cu and In sputtering with Se co-evaporation [13]. X-ray photoelectron spectroscopy measurements on polycyrstalline films deposited by physical vapor deposition have shown that the surface Cu/In varies from 0.33 to 2.4 as the bulk Cu/In varies from 0.85 to 1.1 [14]. Since EDX probes only the near surface composition, the presence of an In rich surface layer could explain the lower than expected (based on F calculations) Cu/In ratios measured here by EDX and presented in figures 2.12-2.14.

2.5 Sodium Doping

Experiments were conducted to determine the effect of sodium on film properties and solar cell performance. Sodium was incorporated either by using soda-lime glass substrates, or by depositing a layer of NaOH on a sodium free substrate (7059 glass or Mo/7059) prior to $CuInSe_2$ deposition. Two different methods were developed to deposit the NaOH layer. In the solution method, the substrate was inserted in 0.1 molar NaOH in ethanol solution and then removed. After the ethanol evaporates, a polycrystalline layer of NaOH remains. The second method is vacuum evaporation of NaOH, using the same vacuum chamber as used for the CdS depositions. NaOH is placed in a Mo boat source (R.D. Mathis S8A-.005Mo) inside a Pyrex glass cylinder. The substrate and a microbalance crystal are placed at the mouth of the cylinder. The source temperature is slowly increased to out-gas the NaOH. The NaOH is evaporated until the microbalance indicates a deposited mass of NaOH sufficient to dope the $CuInSe_2$ film with the required molar concentration of Na (1% NaOH means 1 Na per 100 $CuInSe_2$). The actual Na concentration in the finished film could be significantly different, because it has been assumed that NaOH does not dissociate upon evaporation and that no NaOH or Na

evaporates from the film during deposition of $CuInSe_2$. Vacuum evaporation produced the best results (smaller crystallites, more uniform coverage) and was used for all sodium doped samples except solar cell 960113, which was dipped.

2.6 Film Coordinates

Most of the properties of the $CuInSe_2$ films are sensitive to composition via F(x, y). Therefore the x and y coordinates of the measurement point, or the center of the measurement region, are specified. Because the Cu/In ratio is the most important parameter, and since its gradient is in the -x direction, the largest property changes are observed as the x position is changed. Thus, where convenient, measurements are made over a range of x values. In the case of NaOH doped films, one half of the film (y > -2.54 cm) is doped and the other not, so that the same range of x is available for testing, either doped or undoped.

For electrical characterization, it is necessary to isolate small rectangular zones (figure 2.15) from the larger film and assume that elemental concentration variations within the zone can be neglected. The zones are isolated by mechanically removing the film immediately surrounding the zone with a scribe. A small contact bridge to the adjacent zone is left as a Hall contact. Gold is evaporated through a mask, to form ohmic contact dots at the ends of each zone. Since the glass substrate is too large to fit into the Hall test chamber, the substrate is broken in half along the y = -2.54 cm line. Small indium wires are press bonded to the gold dots for connection to external circuits. Obviously, measurements requiring a large continuous film (X-ray diffraction, reflectance maps, etc.) must be made before the film is sectioned into zones for the electrical measurements.

The configuration described in section 2.4.1 and shown in figure 2.10, is the most recent arrangement of evaporation sources, substrate and microbalance crystal. This arrangement was used for all films fabricated after February 21, 1996 (sample numbers greater than 960221). The projection of these source positions onto the film plane is shown in figure 2.16 (b). The view is of the film coated side of the substrate, as seen from the sources, looking in the +z direction. Contours of constant F are shown for the case F(0,y)=1. The point labeled "dot" is a circular patch of film due to deposition through a small hole in the mask. The dot serves as an indicator of film orientation with respect to the evaporation sources.

For sample numbers in the range 950708 to 960123 inclusive, a different arrangement of evaporation sources was used, and substrate positions are given in a coordinate system (u, w, z). The position (0,0,0) is at the center of the film surface. The projection of the source positions onto the film plane (z = 0) is shown in figure 2.16 (a). The view is of the

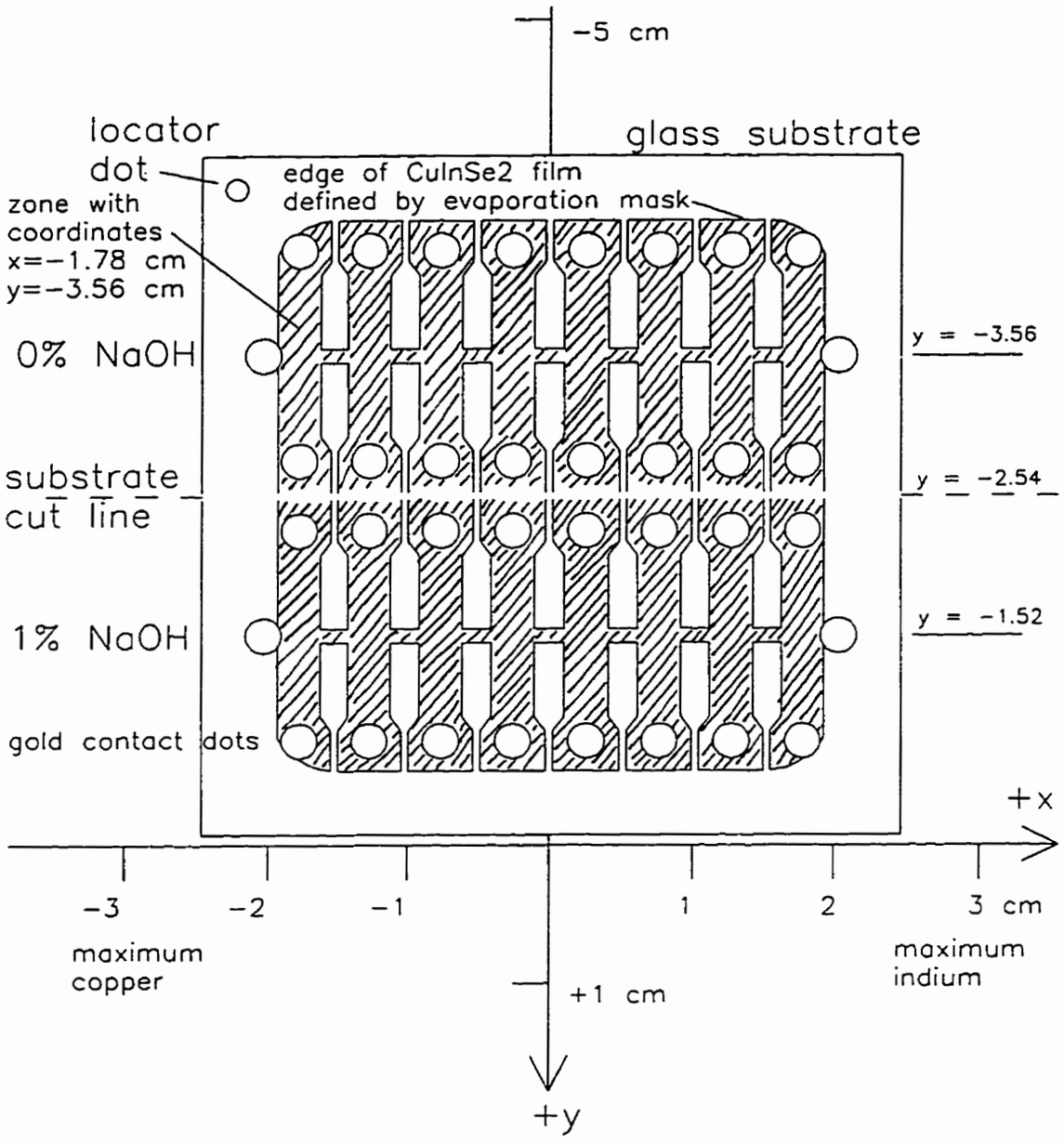

Figure 2.15

Layout of film 960308 after evaporation of gold contact dots and sectioning of film into zones. The half $y > -2.54$ is doped with 1% NaOH. The view is of the film side of the substrate, so that the y−axis and substrate positions shown in figure 2.10 are reflected about the x−axis in this figure.

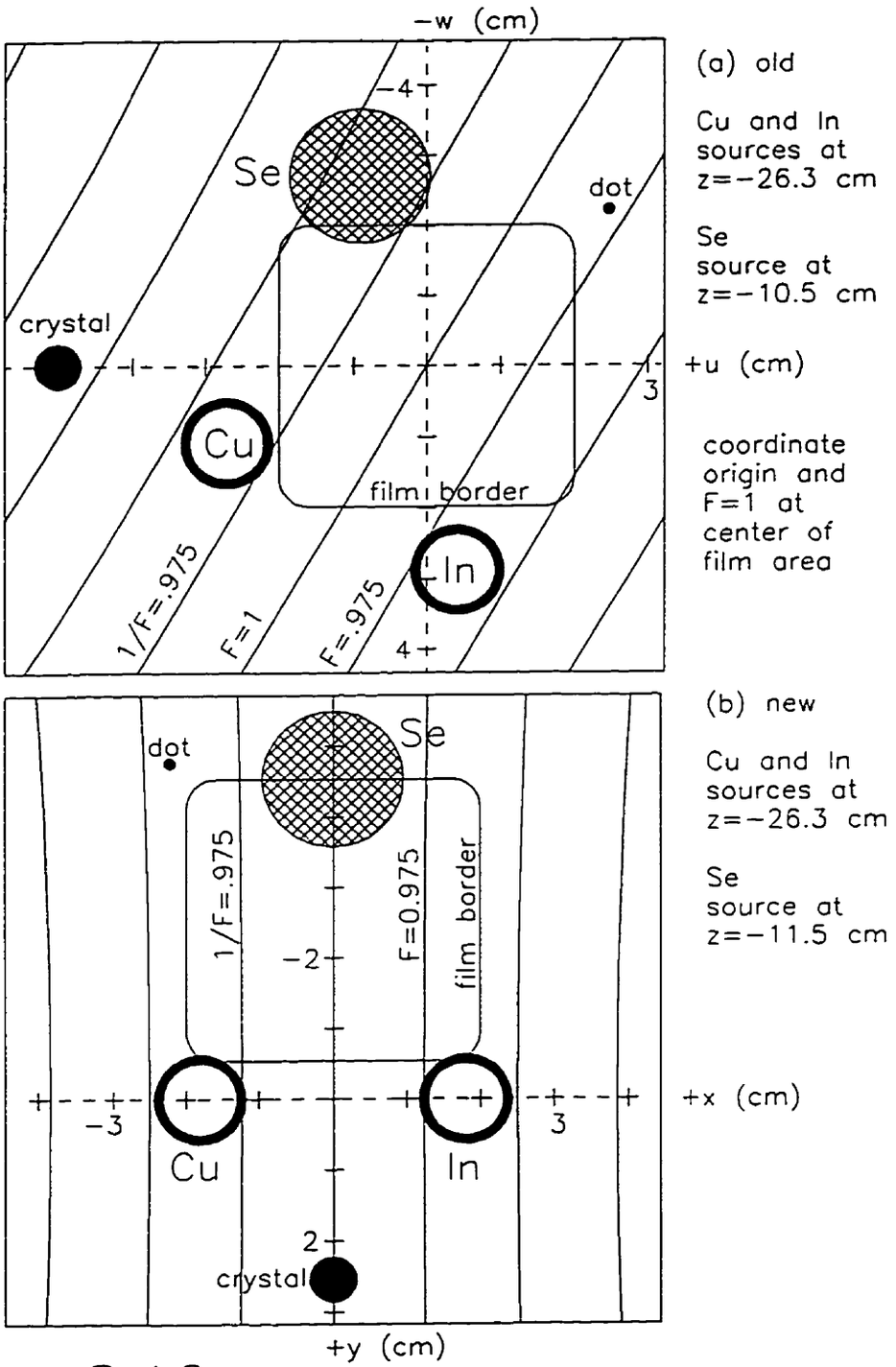

Figure 2.16

Projection of source positions onto the plane of the film, as seen from the film side of the substrate. Source postions (a) were used for sample numbers 950708 to 960123. Source positions (b), corresponding to figure 2.10, are used for numbers greater than 960221. F and 1/F contours are shown at intervals of 0.025.

film coated side of the substrate, looking from the sources in the +z direction. Contour lines of constant F are shown for F = 1 on the mirror symmetry line between the Cu and In sources.

Inspection of figure 2.16 shows that arrangement (b) has the advantage of increased symmetry when compared to (a). In arrangement (b) the microbalance crystal and the substrate center are on the same F, B_{Cu} and B_{In} contours. This means that the respective deposition rates of Cu and In at the microbalance crystal and substrate center are identical.

2.7 References

1 *Applications of Piezoelectric Quartz Crystal Microbalances*, edited by C. Lu and A.W. Czanderna (Elsevier, Amsterdam, 1984)

2 R. J. Matthys, *Crystal Oscillator Circuits*, (Wiley, New York, 1989)

3 *Vacuum Evaporation Sources Catalog*, The R.D. Mathis Company, P.O. Box 92916, Long Beach, CA 90809-2916

4 *Handbook of Thin Film Technology*, edited by L. Maissel and R. Glang (McGraw Hill, New York, 1970)

5 *Handbook of Chemistry and Physics*, edited by R.C. Weast (CRC press, Boca Raton 1989)

6 A. Rockett, R. W. Birkmire, "$CuInSe_2$ for photovoltaic applications", J. Appl. Phys. **70**, (7), R81 (1991)

7 M. L. Fearheiley, "The phase relations in the Cu,In,Se system and the growth of $CuInSe_2$ single crystals", Solar Cells, **16**, 91 (1986)

8 M. H. Bode, J. Tuttle, and M.M. Al-Jassim, "TEM investigations on ordered phases in $CuInSe_2$", *American Institute of Physics, Conference Proceedings 306, 12th NREL Photovoltaic Program Review*, edited by R. Noufi and H. S. Ullal, 421 (AIP press, New York, 1994), p. 421

9 J. C. W. Folmer, J. A. Turner, R. Noufi, and D. Cahen, "Structural and solar conversion characteristics of the $(Cu_2Se)x(In_2Se_3)1\text{-}x$ system", J. Electrochem. Soc.,**132**,1319, (1985)

10 R. A. Mickelsen, W. S. Chen, "Development of a 9.4% efficient thin film $CuInSe_2$/CdS solar cell", *Proc. 15th IEEE Photovoltaics Specialists Conf.* (IEEE, New York, 1981) p. 800

11 R. A. Mickelsen, W.S. Chen, Y.R. Hsiao, V. E. Lowe, "Polycrystalline thin film $CuInSe_2$/CdZnS solar cells", IEEE Transactions on Electron Devices, **31**, 543, (1984)

12 J.R. Tuttle, M. Contreras, A. Tennant, D. Albin, and R. Noufi,"High efficiency thin film $Cu(In,Ga)Se_2$ based photovoltaic devices: Towards a universal approach to absorber fabrication", *Proc. 23rd IEEE Photovoltaics Specialists Conf.* (IEEE, New York, 1993), p. 415

13 A. Rockett, T.C. Lommasson, L.C. Yang, H. Talieh, P. Campos, J.A. Thornton, "Deposition of $CuInSe_2$ by the hybrid sputtering and evaporation method", *Proc. 20th IEEE Photovoltaics Specialists Conf.* (IEEE, New York, 1988), p. 1505.

14 A. Rockett, F. Abou-Elfotouh, D. Albin, M. Bode, J. Ermer, R. Klenk, T. Lommasson, T.W.F. Russell, R.D. Tomlinson, J. Tuttle, L. Stolt, T. Walter, T.M. Peterson,"Structure and chemistry of $CuInSe_2$ for solar cell technology: current understanding and recommendations", Thin Solid Films, **237**, 1, (1994).

Chapter 3

Structure and Optical Properties of $CuInSe_2$ Films

3.1 Structure of $CuInSe_2$

3.1.1 Crystal Structure of Chalcopyrite Semiconductors

The ABX_2 ternary compound semiconductors form two major subgroups. Group (1) consists of the $A^{I}B^{III}X_2^{VI}$ compounds where A = Cu, Ag; B = Al, Ga, In, Tl and X = S, Se, Te. Group (2) consists of the $A^{II}B^{IV}X_2^{V}$ compounds where A = Zn, Cd, Mg; B = Si, Ge, Sn; X = P, As, Sb. Of the possible ABX combinations of the above elements, 17 group (1) and 15 group (2) compounds are listed in a recent reference [1]. The groups (1) and (2) ternary compounds are isoelectronic analogs of the binary II-VI and III-V compounds, respectively. The binary and ternary compounds have a valence electron to atom ratio of 4, the same as the group IV semiconductors Si and Ge. The ternary compounds have the chalcopyrite structure (space group symmetry $I\bar{4}2d$). The chalcopyrite structure can be derived from the diamond structure, as shown in figure 3.1. The Si diamond structure is equivalent to two face centered cubic sublattices displaced by 1/4 body diagonal. If one Si sublattice is replaced with Zn and the other replaced with S, the zincblende structure of ZnS is produced. Here each Zn atom is tetrahedrally coordinated with four S atoms and vice-versa. If the Zn sublattice is replaced alternately with A and B and the S sublattice replaced with X, then the chalcopyrite structure of ABX_2 is produced. In this structure, each cation (A or B atom) is tetrahedrally coordinated with 4 anions (X atoms), and each X is tetrahedrally coordinated with two A and two B atoms. The conventional tetragonal unit cell [2, 3] has 4 formula units per cell, volume a^2c and is defined as follows.

Tetragonal unit cell vectors are $\bar{a} = a\hat{x}$; $\bar{b} = b\hat{y}$; $\bar{c} = c\hat{z}$

In the tetragonal unit cell vector basis system, the atomic coordinates are given by

4 A atoms in (a) positions, $0\ 0\ 0$; $0\ \frac{1}{2}\ \frac{1}{4}$

4 B atoms in (b) positions, $0\ 0\ \frac{1}{2}$, $0\ \frac{1}{2}\ \frac{3}{4}$

8 X atoms in (d) positions, $g\ \frac{1}{4}\ \frac{1}{8}$; $\bar{g}\ \frac{3}{4}\ \frac{1}{8}$; $\frac{3}{4}\ g\ \frac{7}{8}$; $\frac{1}{4}\ \bar{g}\ \frac{7}{8}$ where $g \cong \frac{1}{4}$

Positions $0\ 0\ 0$ and $\frac{1}{2}\ \frac{1}{2}\ \frac{1}{2}$ are equivalent. To obtain all 16 positions of the conventional unit cell, add the coordinates of the equivalent positions to the above coordinates and

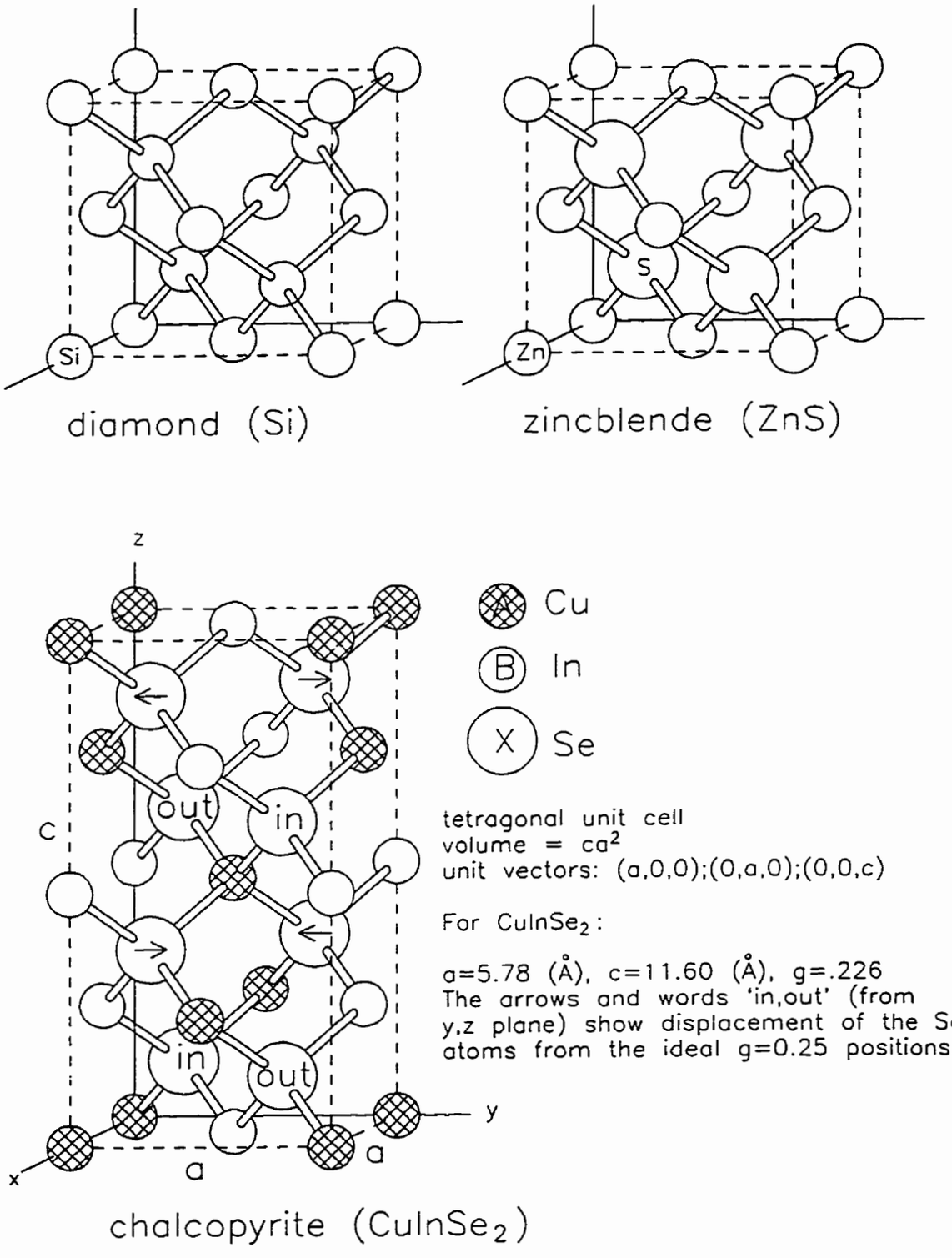

Figure 3.1
Diamond, zincblende and chalcopyrite structures.

translate by the unit cell vectors, as necessary, to bring the coordinates inside the tetragonal cell volume. The anion displacement parameter g specifies the position of the X atom. The tetragonal distortion parameter is $\gamma = c/2a$. To obtain ordinary Cartesian coordinates (x, y, z) from the atomic coordinates, multiply the $\bar{a}$ and $\bar{b}$ components by a and the $\bar{c}$ component by $2\gamma a$.

Expressions for the bond lengths R_{AX} and R_{BX} can be obtained [4] directly from the Cartesian coordinates. The results are

$$R_{AX} = a\left(g^2 + \left(\frac{1+\gamma^2}{16}\right)\right)^{\frac{1}{2}} \quad \text{where } \gamma = \frac{c}{2a} \qquad (3.1)$$

$$R_{BX} = a\left(\left(\frac{1}{2} - g\right)^2 + \left(\frac{1+\gamma^2}{16}\right)\right)^{\frac{1}{2}} \qquad (3.2)$$

The bond angles are determined by using the cosine law for the triangle containing the two bonds. For example, the angle θ_{AXB} between bonds AX and BX at atom X is given by

$$\cos(\theta_{AXB}) = \frac{\bar{R}_{AX} \bullet \bar{R}_{BX}}{R_{AX}\, R_{BX}} \qquad (3.3)$$

The parameters g and γ determine the amount by which the conventional chalcopyrite unit cell atomic coordinates differ from the ideal ($g = 1/4$, $\gamma = 1$) case where both A and B atoms occupy geometrically regular tetrahedra. It has been shown [5] that a simple relationship exists between g and γ if one assumes a regular tetrahedral location of the X atoms about the B sites. This result is obtained by forming a cube containing the tetrahedron and requiring that any edge parallel to the z axis be the same length as any edge perpendicular to the z axis.

$$\frac{\gamma a}{2} = a\sqrt{\left(g - \frac{1}{4}\right)^2 + \left(g - \frac{3}{4}\right)^2}$$

which reduces to

$$g = \frac{1}{2} - \frac{1}{4}\sqrt{2\gamma^2 - 1} \qquad (3.4)$$

For the group (2) chalcopyrites, experimentally determined values of g and γ are found to be in close agreement with equation 3.4. This is not surprising since the Group IV atoms have a strong tendency to form four sp^3 hybrid bonds. For the group (1) chalcopyrites, equation 3.4 is not usually applicable [2]. The g values can be determined by x-ray diffraction measurements. The measured set of h k l reflection intensities is compared to a computed set which uses an initial g estimate in the structure factor calculation. The

value of g is then adjusted and the intensity calculations repeated until a minimum least squares fit to the measured intensities is obtained.

3.1.2 Crystal Parameters for $CuInSe_2$

Table 3.1 shows published values of the lattice constants and anion displacement parameter of $CuInSe_2$ determined by x-ray diffraction using single crystal or powder samples. Differences in values may be partly due to variations in the degree of ordering of the cation sublattice among the different $CuInSe_2$ samples. A random arrangement of the Cu and In atoms reduces the structure from chalcopyrite to zincblende [6].

Table 3.1: Published Crystal Data for $CuInSe_2$

a (Å)	c (Å)	$\gamma = c/2a$	g	x-ray sample	Reference
5.785	11.57	1	.22	powder	[7]
5.77	11.54	1	—	?	[8]
5.782	11.62	1.0048	.235	powder	[9]
5.78399	11.6142	1.004	.224	?	[10]
5.7810	11.6103	1.0042	.2258	?	[11]
5.7810	11.6422	1.0069	.226	crystal	[12]
5.78	11.55	0.9991	—	?	[1]

Typical values obtained from table 3.1 are a = 5.78 Å , c = 11.60 Å , g = 0.226. Using these values in equations 3.1 and 3.2, the bond lengths are $R_{CuSe} = 0.42a = 2.428$ Å and $R_{InSe} = .448a = 2.588$ Å. The angles calculated with equation 3.3 are given in table 3.2. The z coordinate difference between the two outer atoms in the triplet is $z_3 - z_1$.

Table 3.2: $CuInSe_2$ Bond Angles

Bonds 1–2–3	Bond angle (degrees)	$z_3 - z_1$
Se–Cu–Se	106.67	0
Se–Cu–Se	110.89	$\gamma a/2$
Se–In–Se	111.86	0
Se–In–Se	108.29	$\gamma a/2$
Cu–Se–Cu	114.91	$\gamma a/2$
In–Se–In	104.55	$\gamma a/2$
Cu–Se–In	109.08	0
Cu–Se–In	109.36	$\gamma a/2$

3.2 X-ray Diffraction Patterns of $CuInSe_2$ Films

3.2.1 Diffraction Plane Spacing and Structure Factors

Polycrystalline thin films of $CuInSe_2$ were deposited on Corning 7059 glass, as described in chapter 2. X-ray diffraction patterns were taken using a Siemens D500 automatic θ-2θ powder diffractometer. For the tetragonal lattice, the spacing for planes with Miller indices h k l is given by

$$\text{plane spacing} = \frac{a}{\sqrt{h^2 + k^2 + \frac{l^2}{4\gamma^2}}} \qquad (3.5)$$

For the chalcopyrite space group $I\bar{4}2d$, reflections are present (structure factor non-zero) for h k l with $h + k + l = 2n$ and for h h l with $2h + l = 4n$ [3].

The structure factors can be separated into groups [4] according to whether they are characteristic of both chalcopyrite and zincblende (zincblende-like) or chalcopyrite only (chalcopyrite-only). The zincblende-like structure factors are non-zero for planes h k 2l where h k l are all even or all odd. The zincblende-like reflections would continue to exist if the anion sublattice were replaced with a single group II element, for example Zn, whereas the other reflections would vanish. They are the dominant features in all of the diffraction patterns.

3.2.2 Effect of Deposition Ratio F on Diffraction Pattern

Figure 3.2 shows x-ray diffraction patterns for three single layer films grown with different Cu/In deposition ratios F. As F increases, the diffraction peaks increase in height and become somewhat narrower. This corresponds to the increase in crystallite size which occurs as the film changes from In-rich to Cu-rich. Also, the crystallites are highly oriented with the 112 plane parallel to the substrate. Only zincblende-like reflections are observed with these films.

3.2.3 Two Layer Films and Sodium Doped Films

Figure 3.3 shows diffraction patterns for a single layer Na doped $CuInSe_2$ film and for two layer $CuInSe_2$ films, with and without Na doping. The single layer film (a) shows a pattern very similar to the undoped half of the same substrate (Fig. 3.2 c). However, the 213,105 and 211 chalcopyrite-only reflections are more intense in the Na doped film. The two layer films (Fig. 3.3 b, c) show additional chalcopyrite-only reflections, namely 101 and 103. The Na doped half of film 960308 appears to be more highly 112 oriented, with stronger 112 and 336 reflections. A similar effect of sodium on the orientation of two

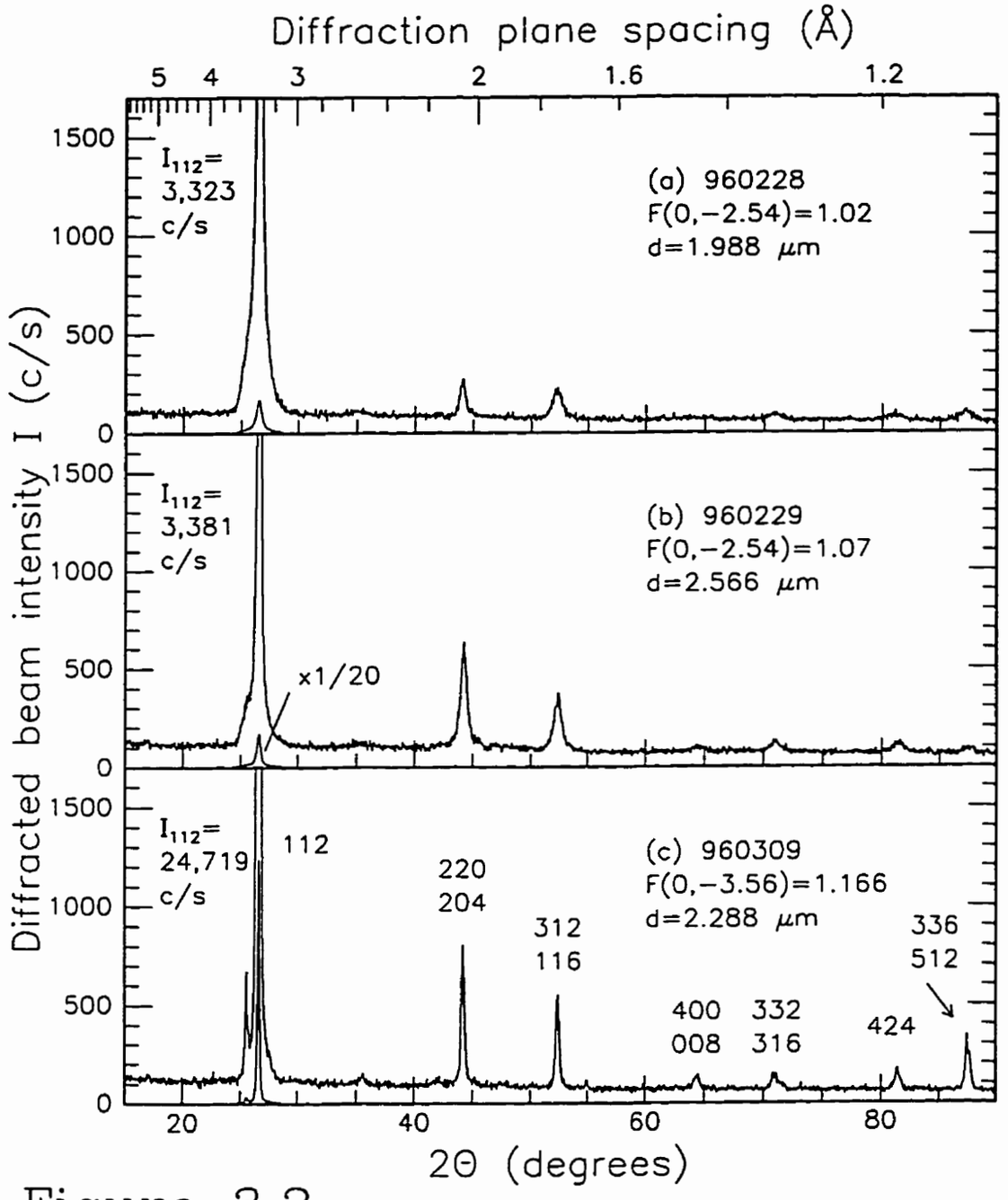

Figure 3.2

X−ray diffraction patterns of single layer $CuInSe_2$ films deposited at T_{sub}=350°C on 7059 glass, for three different F values. Cu Kα (λ=1.541838 Å), 0.05° angle step, 1 second count interval. 112 peaks also shown x1/20 with each plot

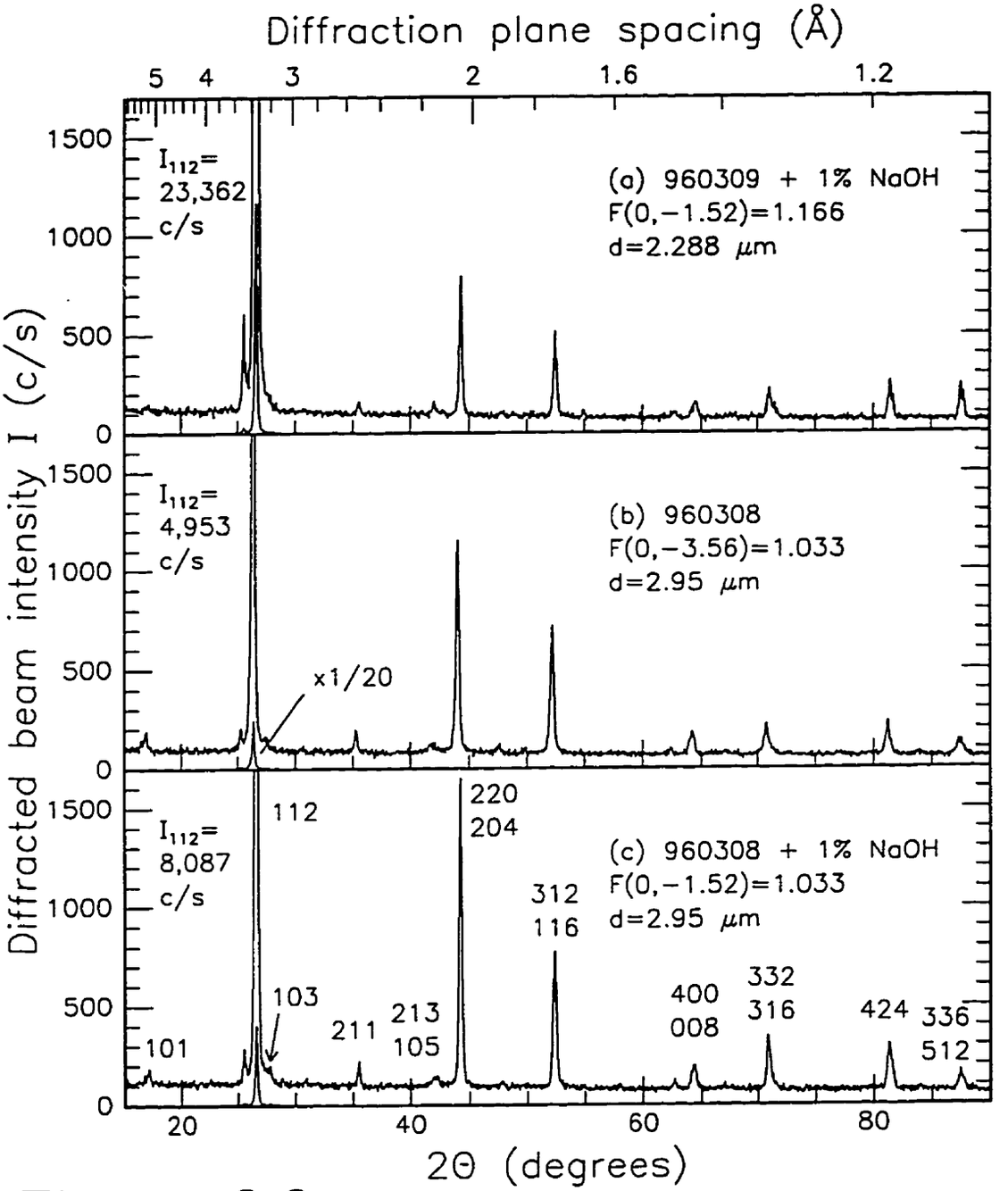

Figure 3.3

X−ray diffraction patterns of $CuInSe_2$ films on 7059 glass, showing weak chalcopyrite lines. (a) single layer with 1% NaOH, (b) two layer (c) two layer with 1% NaOH

112 peaks also shown x1/20 with each plot

layer films has been reported in [13]. Sodium has also been incorporated by growing $CuInSe_2$ films on sodium rich substrates such as soda-lime glass [13] and by controlled incorporation of sodium selenide (Na_2Se) [14].

3.3 Electron Microscope Images of Films

The film surfaces were studied with an Hitachi S–570 scanning electron microscope (SEM). The surface texture and crystallite (grain) size of single layer films deposited at 350 °C at different deposition ratios F, are shown in a series of five SEM images. The Cu-rich film 960309 at F = 1.151 is shown in figure 3.5 (a), and in figures 3.4 (a) to (d), film 960229 is shown at four zones, with F(x) decreasing from 1.11 to 1.043. At the largest F (figure 3.5 a) the grains are about 0.2 μm in size, and the film has a rough surface texture due to the fact that the grains cluster together to form "lumps" about 1.5 μm across. As F decreases, the sizes of the grains and lumps decrease until in figure 3.4 (d) the grains are barely resolved (grain size < 0.1 μm), and the film surface is relatively smooth. The x-ray diffraction data of figure 3.2 also indicate that grain size decreases as F decreases. The general variation of the film surface roughness with F can be observed with a good quality optical microscope.

Comparison of figures 3.5 (a) and (b) shows the effect of sodium doping on the single layer Cu-rich film 960309. In the sodium doped film, no lumps are present, and the grains appear somewhat larger (0.2 to 0.3 μm) than in the sodium free film.

The two layer film 960308 (figure 3.5 c, d) has larger grains than any of the single layer films. The sodium free two layer film (figure 3.5 c) has ≈ 0.4 μm grains, 2 to 3 μm lumps, and a rough surface, whereas the sodium doped film (figure 3.5 d) has more densely packed ≈ 0.5 μm grains, no lumps, and a relatively smooth surface. The dense packing of the sodium doped film is consistent with the increased 112 orientation of the grains noted in section 3.2.3. The generally larger grain size of the two layer films helps to explain their superior semiconductor properties, as compared to the smaller grain, single layer films.

3.4 Specular Reflectance

3.4.1 Specular Reflectance Measurement

The specular reflectance R_{sp} of the films is sensitive to surface texture, and the optical constants n, k (complex index of refraction: N = n + ik). The surface texture is a function of film morphology, which varies with Cu/In ratio, film growth conditions (i.e. substrate temperature), substrate material, sodium content, and film thickness. Experiments show that stoichiometry of the film (a function of F) and sodium content each have a strong influence on R_{sp}.

(a) x = –1.78 cm, F(x) = 1.11

(b) x = –0.76 cm, F(x) = 1.087

(c) x = +0.25 cm, F(x) = 1.064

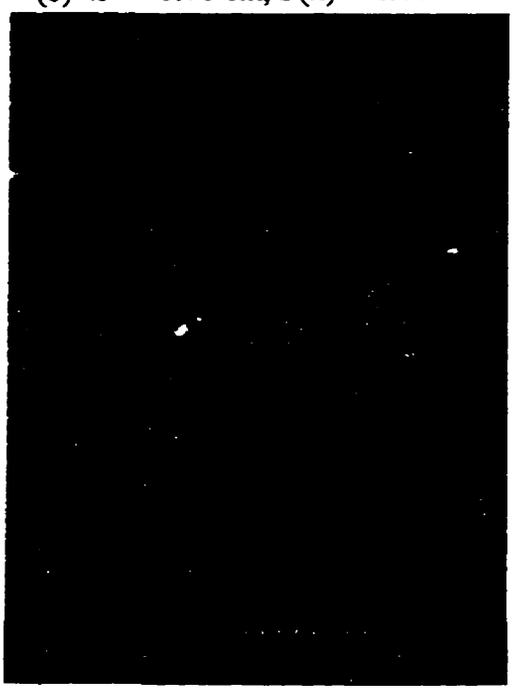

(d) x = 1.27 cm, F(x) = 1.043

Figure 3.4

Scanning electron microscope images of the surface of the 2.57 μm thick single layer film 960229 deposited on 7059 glass at 350 °C. The photographs were taken on the substrate line y = –1.52 cm, at the x positions indicated. The crystallite size decreases and the film surface becomes more smooth as the Cu/In ratio decreases.

(a) 960309, 0% Na, y = –2.74 cm

(b) 960309, 1% Na, y = –2.34 cm

(c) 960308, 0% Na, y = –2.64 cm

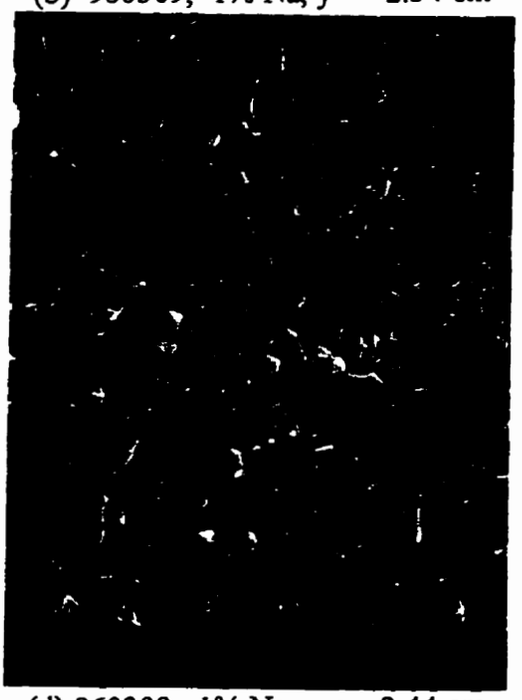

(d) 960308, 1% Na, y = – 2.44 cm

Figure 3.5

SEM images of $CuInSe_2$ films on 7059 glass, showing the effect of 1% Na doping. The 2.23 μm thick Cu-rich single layer film 960309 is shown at x = 0.6 cm, F(x) = 1.151. The 2.95 μm thick two layer film 960308 is shown at x = –0.76 cm, F(x) = 1.048.

Specular reflectance maps of the films were obtained using a scanning laser beam confocal imaging system (MACROscope) developed by Dr. A.E. Dixon at the University of Waterloo [15]. Reflectance images of 512x512 pixels and 8 bit gray scale spanning a sample area 3.92 × 3.92 cm^2 were obtained. Each gray scale image was converted to a reflectance map by calibration to a reference mirror with reflectance 0.828. Reflectance maps for $CuInSe_2$ films 960229 and 960308 are shown in figures 3.6 and 3.7. Line scans representing the variation of R_{sp} with x at constant y were extracted from several reflectance maps. They are shown in figures 3.8 and 3.9.

3.4.2 Effect of Deposition Ratio F on Specular Reflectance

Curves (a) (b) and (c) of figure 3.8 are for single layer films (d ≅ 2 - 2.6 μm) grown at T_s = 350 °C on 7059 glass. They show that the specular reflectance reaches a maximum of $R_{sp} \cong 0.16$ at F ≅ 1.035. For F > 1.055, the R_{sp} decreases rapidly, passes through a local maximum at F = 1.073 and then goes to zero. This corresponds with a transition in film visual appearance from a smooth (specular) gray surface to a darker gray matte (diffusing) surface. This change in film texture near Cu/In ≅ 1 has been reported elsewhere [16, 21] and is consistently observed. It is a useful marker for checking F, and can be seen through the glass wall of the vacuum chamber during film growth. In two layer films, the texture of the first layer is maintained during the growth of the second layer, so that the first layer determines the resulting morphology of the film.

3.4.3 Effect of Sodium Doping on Specular Reflectance

Figure 3.9 shows the effects of sodium doping on R_{sp} for films deposited on 7059 glass and Mo coated 7059 glass. Before the $CuInSe_2$ deposition, one half (y > −2.54 cm) of each of the three substrates was coated with NaOH. The specular reflectance of the sodium doped half is much greater than that of the sodium free half for both the single layer Cu-rich film on glass (960309) and the two layer film on glass (960308). The single layer film on Mo coated glass (960316) showed little change due to sodium doping, perhaps because the sodium diffuses into the Mo instead of the $CuInSe_2$ film.

3.4.4 Relation Between Surface Roughness and Specular Reflectance

In the data of figures 3.6 to 3.9, the specular reflectance seems to be a function of surface texture, i.e. smoother surfaces show higher specular reflectance. The relation between specular reflectance and surface texture can be quantified using a theory of the reflection of electromagnetic radiation from rough surfaces originally developed [17] in connection with the scattering of radar waves from sea water and later adapted to optics [18]. For a parallel beam of light of wavelength λ at normal incidence to a surface of

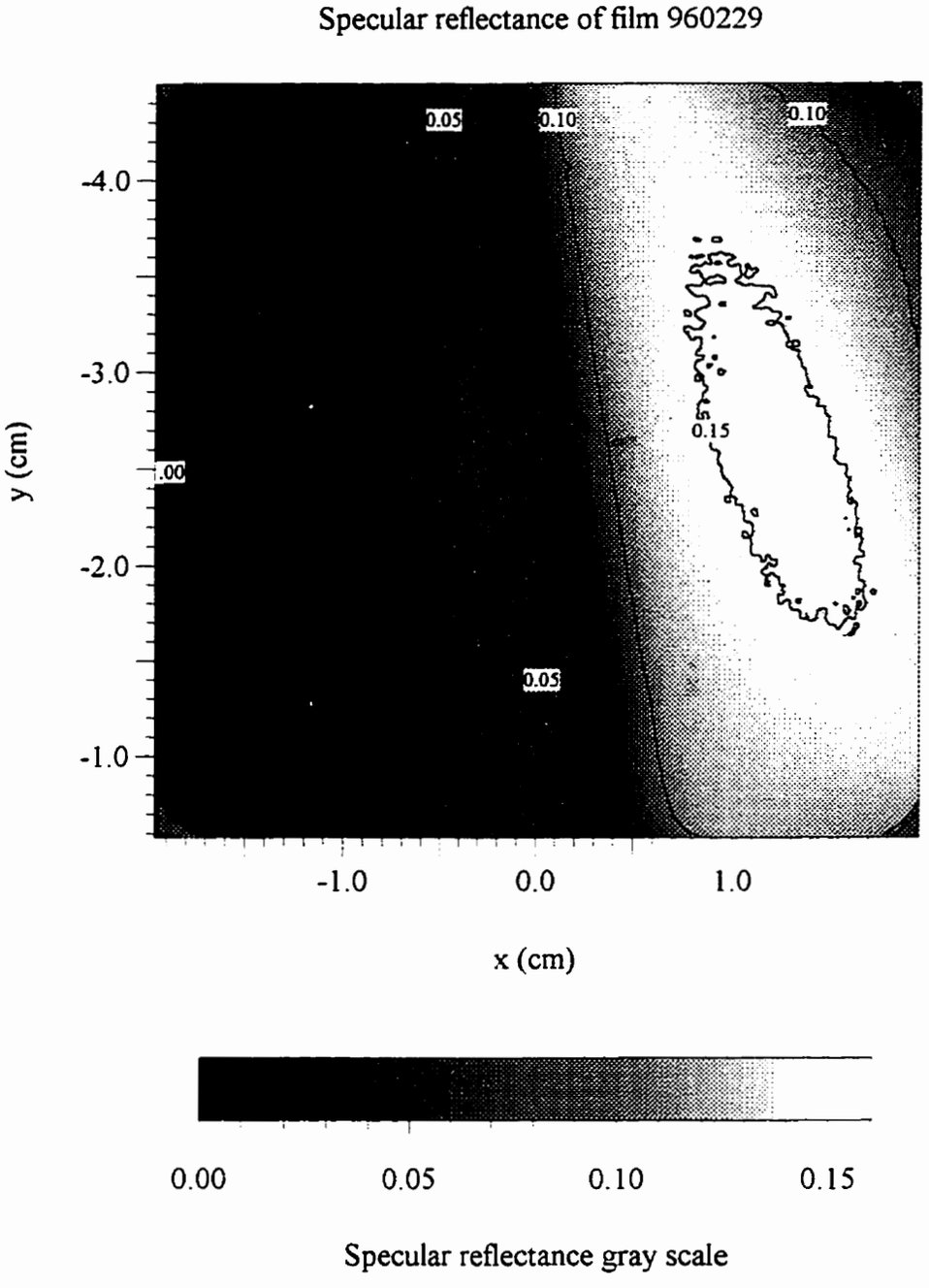

Figure 3.6

A specular reflectance map of single layer $CuInSe_2$ film 960229 deposited on 7059 glass, obtained using the scanning laser imaging system at 633 nm wavelength. Iso-reflectance contours at intervals of 0.05 are shown. The Cu/In ratio decreases as x increases.

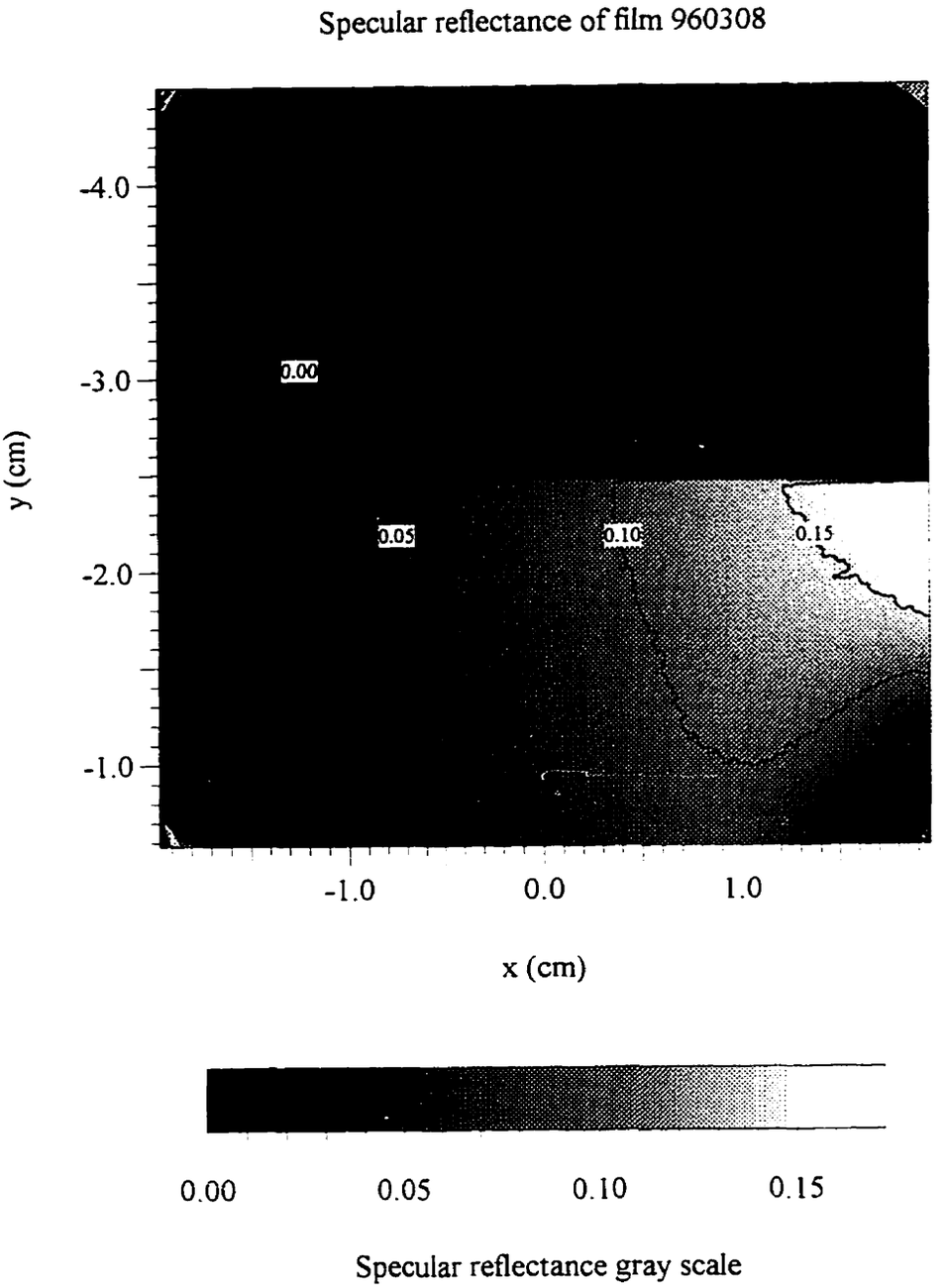

Figure 3.7

A specular reflectance map of two layer $CuInSe_2$ film 960308 deposited on 7059 glass, obtained using the scanning laser imaging system at 633 nm wavelength. Iso-reflectance contours at intervals of 0.05 are shown. The lower half (y > -2.54 cm) of film area is doped with 1% sodium.

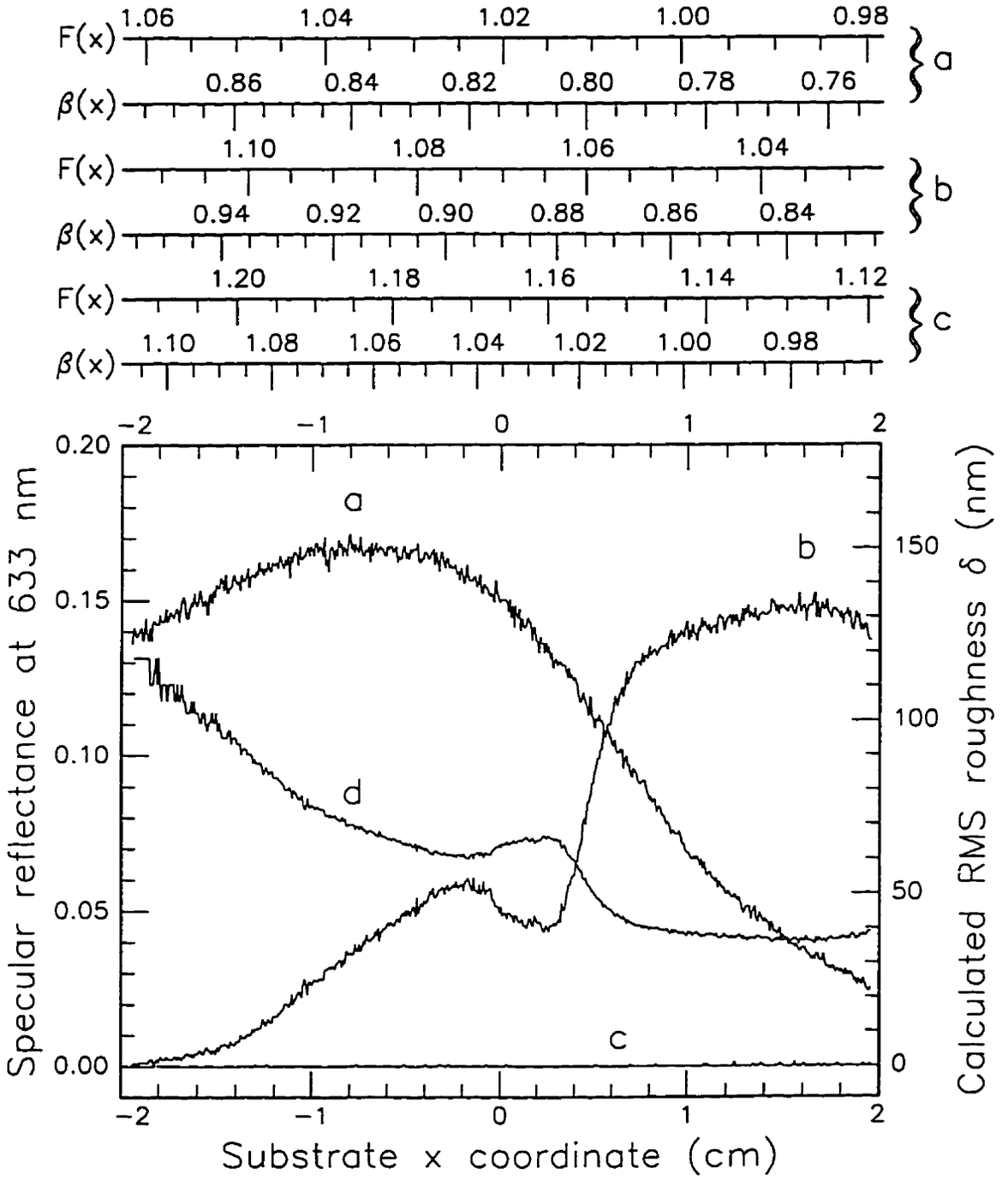

Figure 3.8

Specular reflectance of single layer $CuInSe_2$ films on 7059 glass. (a) 960228, y = −1.56 cm; (b) 960229, y = −1.56; (c) 960309, y = −2.62 (d) RMS surface roughness calculated from (b)

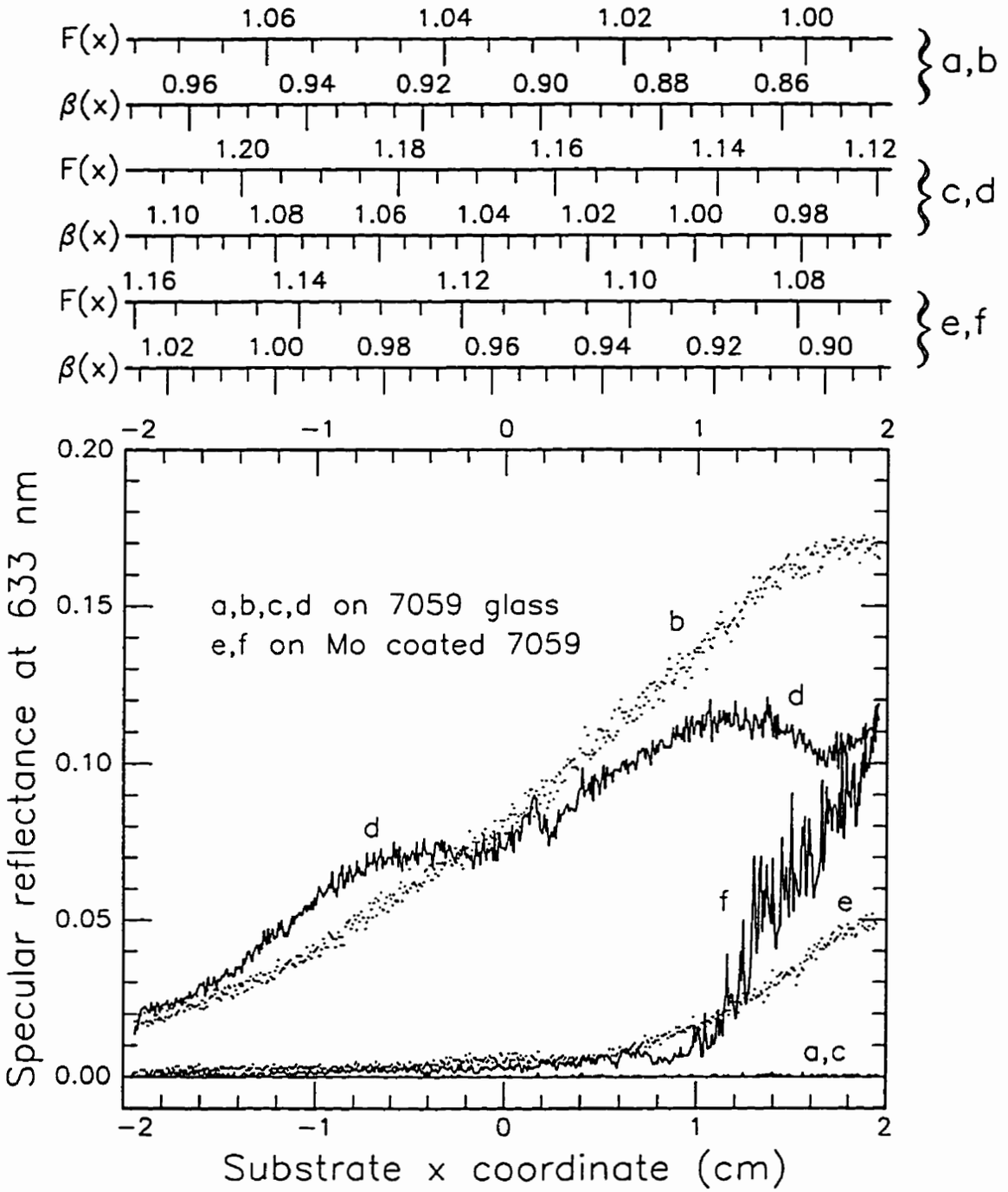

Figure 3.9

The effect of NaOH on the specular reflectance.
960308: (a) 0% Na, y=−2.64; (b) 1% Na, y=−2.37
960309: (c) 0% Na, y=−2.62; (d) 1% Na, y=−2.41
960316: (e) 0% Na, y=−2.64; (f) 1% Na, y=−2.0

root mean square (rms) roughness δ , the specular reflectance R_{sp} is given by

$$R_{sp} = \mathrm{Re}\,xp\left(-\left(\frac{4\pi\delta}{\lambda}\right)^2\right) \qquad (3.6)$$

where where $\delta << \lambda$ and R is the reflectance of a perfectly smooth surface of the same material. As an example, in figure 3.8 (d) the calculated rms surface roughness δ as a function of x is shown for the reflectance data of figure 3.8 (b), assuming R = 0.25 at 633 nm [19, 20] for polished $CuInSe_2$ single crystals. The effects of surface texture on reflectance and transmittance of $CuInSe_2$ films is also discussed in [21].

3.5 Transmittance Spectra of $CuInSe_2$ Films

3.5.1 Transmittance Spectrum Measurement Technique

The optical transmission spectra of several films were measured using a Cary 17 spectrophotometer with sample and reference channel AC outputs connected to the data acquisition computer. With both signal and reference beam paths clear, the reference channel gain was adjusted so that sample and reference output amplitudes were equal (defined as unity transmittance). Thus the spectra presented below represent the transmittance of the combination of film and substrate, with no attempt made to remove the contribution of the substrate.

3.5.2 Observed Transmittance Spectra

Figure 3.10 shows the transmittance spectra for films with different F. For all films, the transmittance approaches zero as the energy exceeds about 1 eV, which is the expected $CuInSe_2$ bandgap. For photon energies less than the band-gap energy E_g, the transmittance spectra depend strongly on the F value. At low F the films are quite transparent and interference fringes are clearly visible (a, b). At high F the interference effects disappear and the films are less transparent (d).

Figure 3.11 shows the transmittance spectra for films with and without sodium doping. A dramatic increase in transmittance is observed for single layer and double layer films when sodium is added to the film.

If the transmittance data of figure 3.10 are compared with the specular reflectance data (figure 3.8) at the same F values, it is apparent that films with high transmittance also have high specular reflectance, while films with low transmittance have near zero specular reflectance. This trend is particularly clear with sample 960229. Curve (b) of figure 3.8 shows the specular reflectance variation with x, and curves (a, b, c) of figure 3.10 are the transmittance spectra at three points within the same x and F ranges.

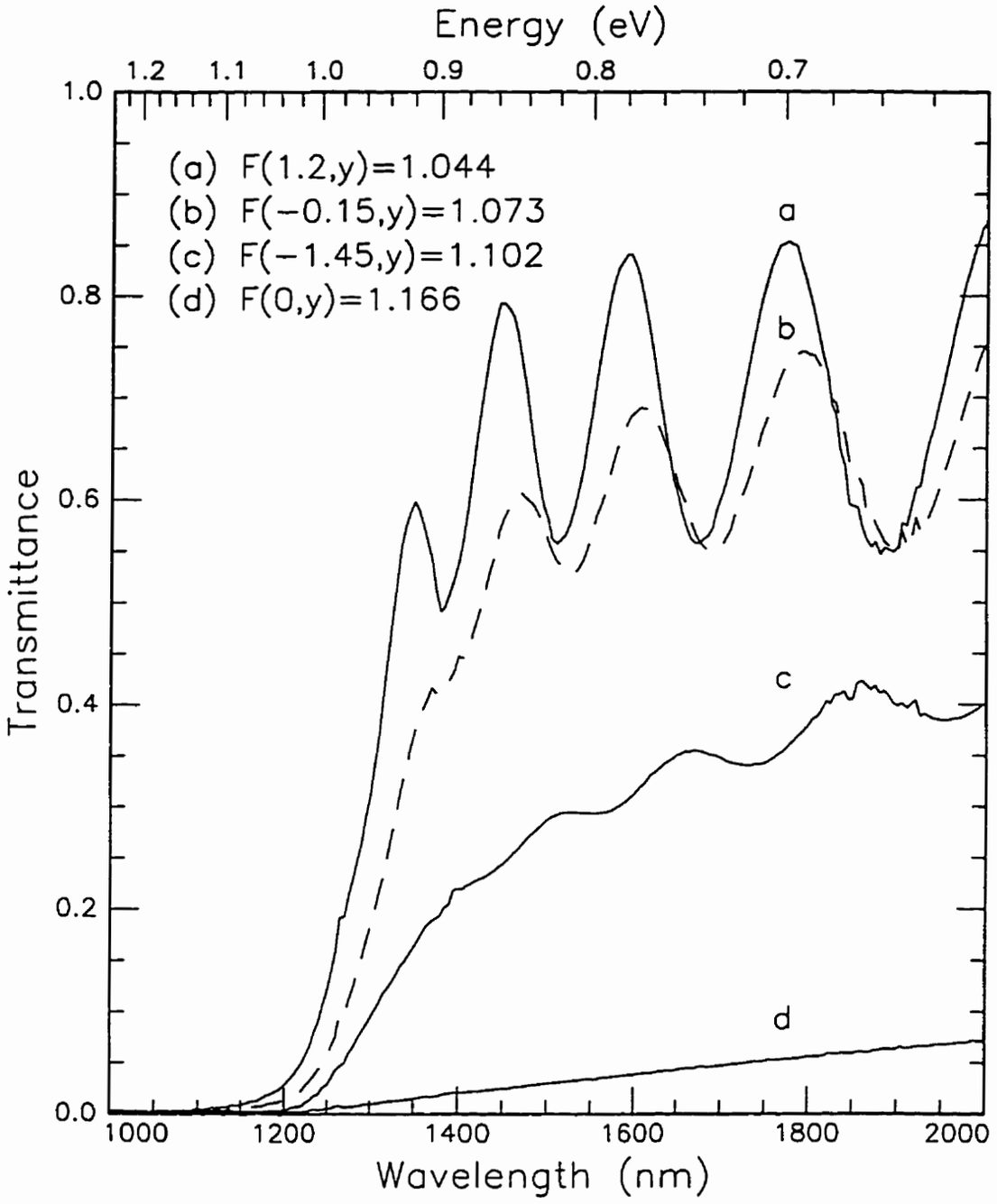

Figure 3.10

Transmittance spectra at different F(x,y) for single layer $CuInSe_2$ films. Bandwidth=1 nm.
(a),(b),(c) 960229, d=2.57 μm, y=−2.54 cm
(d) 960309, d=2.29 μm, y=−3.56 cm

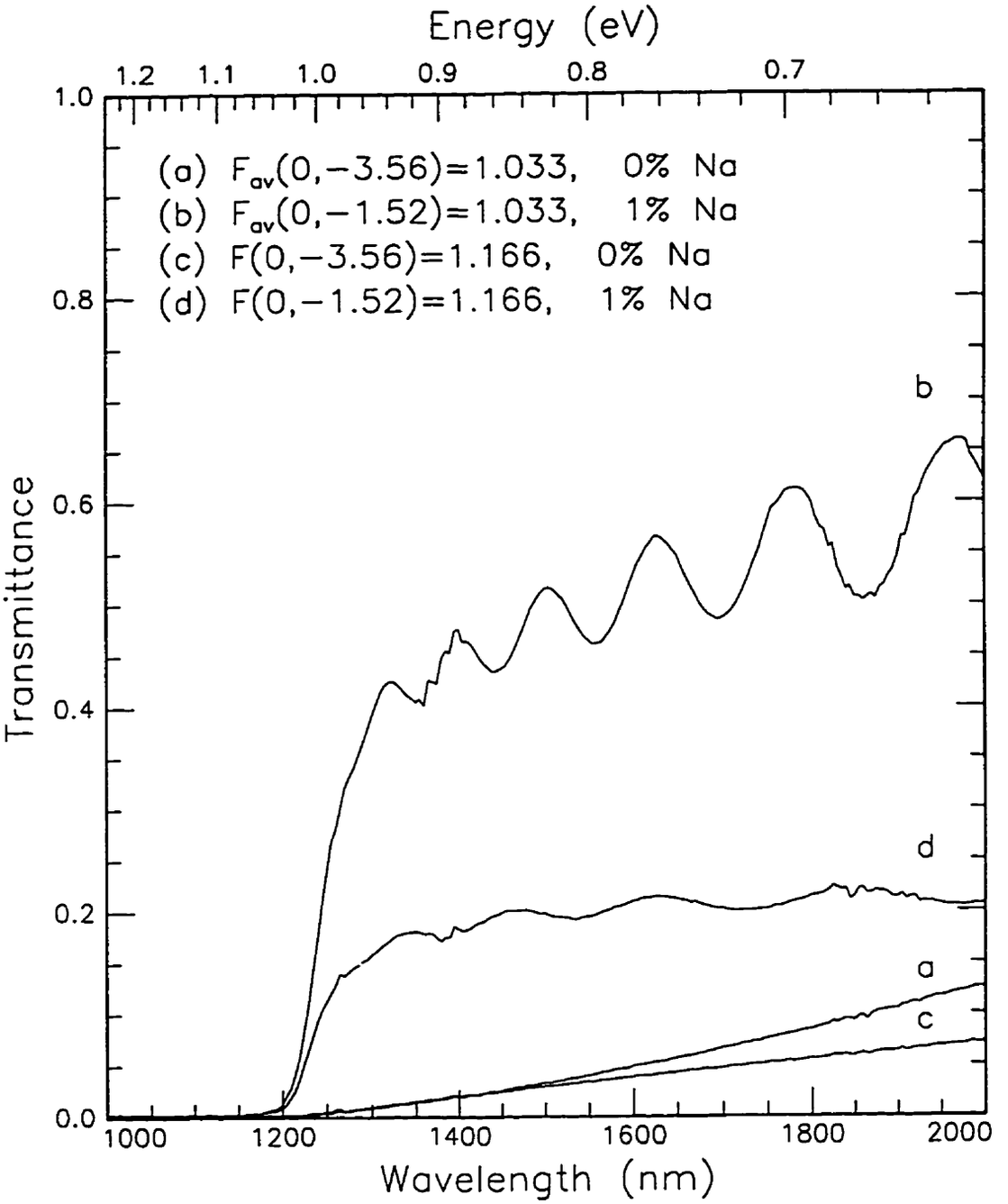

Figure 3.11

The effect of sodium on the transmission spectra of $CuInSe_2$ films. Bandwidth=1 nm.
(a),(b): 960308, two layer film, d=2.95 μm
(c),(d): 960309, single layer, d=2.29 μm

The reason for the observed relation between the specular reflectance and transmittance for $E_{photon} < E_g$ may be that the low reflectance films have rough surfaces which act as optical diffusers so that although the light is transmitted, it is scattered out of the spectrophotometer beam path and is therefore not detected.

3.5.3 Evaluation of Energy Gap from Transmittance Spectra

$CuInSe_2$ is a direct bandgap semiconductor. Therefore the expected relation between the absorption coefficient α and the photon energy $\hbar\omega$, for $\hbar\omega \geq E_g$, is given by

$$\alpha = \frac{C}{\hbar\omega}\left(\hbar\omega - E_g\right)^{\frac{1}{2}} \qquad (3.7)$$

where C is a constant [22]. For $\hbar\omega \geq E_g$, a plot of $(\alpha\hbar\omega)^2$ vs. $\hbar\omega$ should be a straight line with intercept E_g and slope C. The absorption coefficient is related to the imaginary part k of the complex index of refraction by

$$\alpha = \frac{4\pi k}{\lambda} \qquad (3.8)$$

One approach for determining (n, k) of an absorbing film on a substrate is to calculate transmittance and reflectance (T, R) as functions of n, k, λ, measure the experimental values of transmittance and reflectance (T_{exp}, R_{exp}) as functions of λ, and solve the system of nonlinear equations for (n, k) at each wavelength

$$T(n,k,\lambda) - T_{exp}(\lambda) = 0 \qquad (3.9a)$$

$$R(n,k,\lambda) - R_{exp}(\lambda) = 0 \qquad (3.9b)$$

There are difficulties with this technique. The equations which give R and T explicitly in terms of n and k are very complicated and require numerical solution. Furthermore, multiple solutions often occur at a particular $R_{exp}(\lambda)$ and $T_{exp}(\lambda)$. Expressions for R and T of an absorbing film on a transparent substrate are given in [23, 24].

Since only $T_{exp}(\lambda)$ data was measured for the $CuInSe_2$ films, it is not possible to apply the full solution outlined above. However, by using an approximation for T in the high absorption region, one can obtain useful estimates of the absorption coefficient α.

The method used is to ignore the substrate and model the film as an unsupported thick plate [25, 26, 27]. If the plate thickness d is assumed to be greater than the optical coherence length, then interference effects can be ignored and the intensities rather than the amplitudes of the multiply reflected beams are summed. For the thick plate model, the transmittance is given by

$$T = \frac{(1-R)^2 \exp(-\alpha d)}{1-R^2 \exp(-2\alpha d)} \qquad (3.10)$$

where R is the reflectance at a plate/air interface, and T is the transmittance of the plate. The second term in the denominator of equation 3.10 is the contribution due to multiple reflection. This term is negligible for strong absorption. Equation (3.10) can be solved for the absorption coefficient α.

$$\alpha = \frac{1}{d} \ln\left(\frac{(1-R)^2}{2T} + \sqrt{\frac{(1-R)^4}{4T^2} + R^2} \right) \qquad (3.11)$$

The R value must be obtained from additional data or estimated. If we ignore interference effects and assume that the absorption coefficient is zero at a wavelength below the bandgap, then we can use equation 3.10 to determine R at that wavelength. For $\alpha = 0$, equation 3.10 becomes

$$T_0 = \frac{1-R}{1+R} \qquad (3.12)$$

Using the data of figure 3.10 (a), let $T_0 = T_{exp}(1350\text{nm}) = 0.6$, then from equation 3.12 we obtain $R = 0.25$. Assuming that R is constant over the range of wavelengths near the band gap energy, we can use equation 3.11 to determine α. For consistency, the same R value is used for all of the absorption coefficient calculations. The data of figures 3.10 and 3.11 are used to calculate the $(\alpha\hbar\omega)^2$ vs. $\hbar\omega$ plots of figures 3.12 and 3.13, respectively.

As mentioned in section 3.5.2 above, films with rough surfaces scatter much of the light out of the spectrophotometer beam path. Scattering is not included in the thick plate model which was used to derive equation 3.11. The reduction in measured transmittance due to scattering causes an anomalous increase in the absorption coefficient, as calculated using equation 3.11. Therefore films with rough surfaces show significant absorption below E_g, as seen in figures 3.12 (d) and 3.13 (a, c), and equation 3.7 cannot be used to obtain a meaningful estimate of E_g.

For the relatively smooth, non-scattering films, equation 3.7 is used to estimate E_g by extrapolating the linear portion of the $(\alpha\hbar\omega)^2$ vs. $\hbar\omega$ data (for $\hbar\omega \geq E_g$) to the intercept at the axis $(\alpha\hbar\omega)^2 = 0$, as shown in figures 3.12 (a, b, c) and 3.13 (b, d). In each case, the energy gap is determined to be approximately 1 eV.

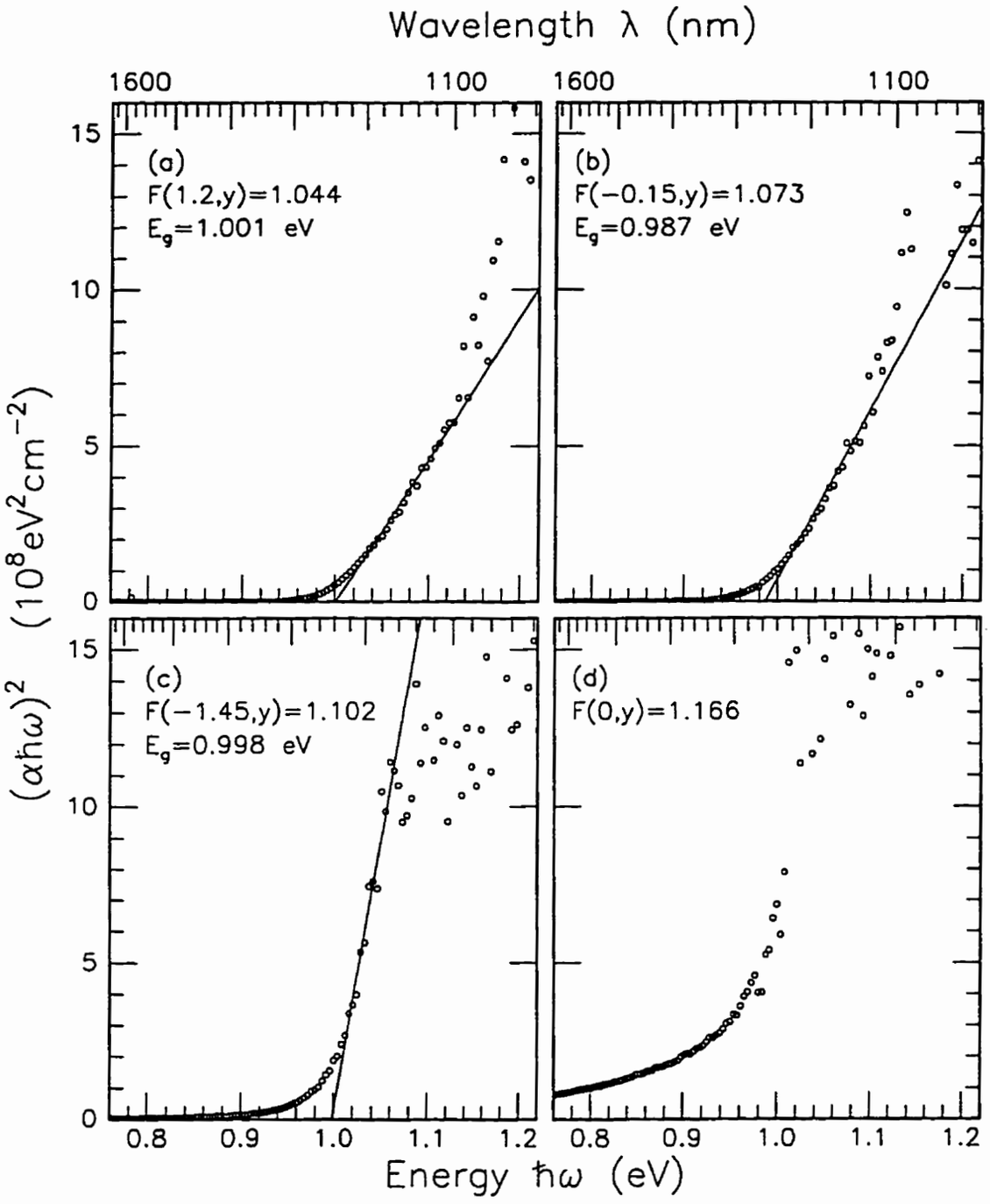

Figure 3.12

Plots of $(\alpha\hbar\omega)^2$ vs. $\hbar\omega$ at different F(x,y) for single layer $CuInSe_2$ films.
(a),(b),(c) 960229, d=2.57 μm, y=−2.54 cm
(d) 960309, d=2.29 μm, y=−3.56 cm

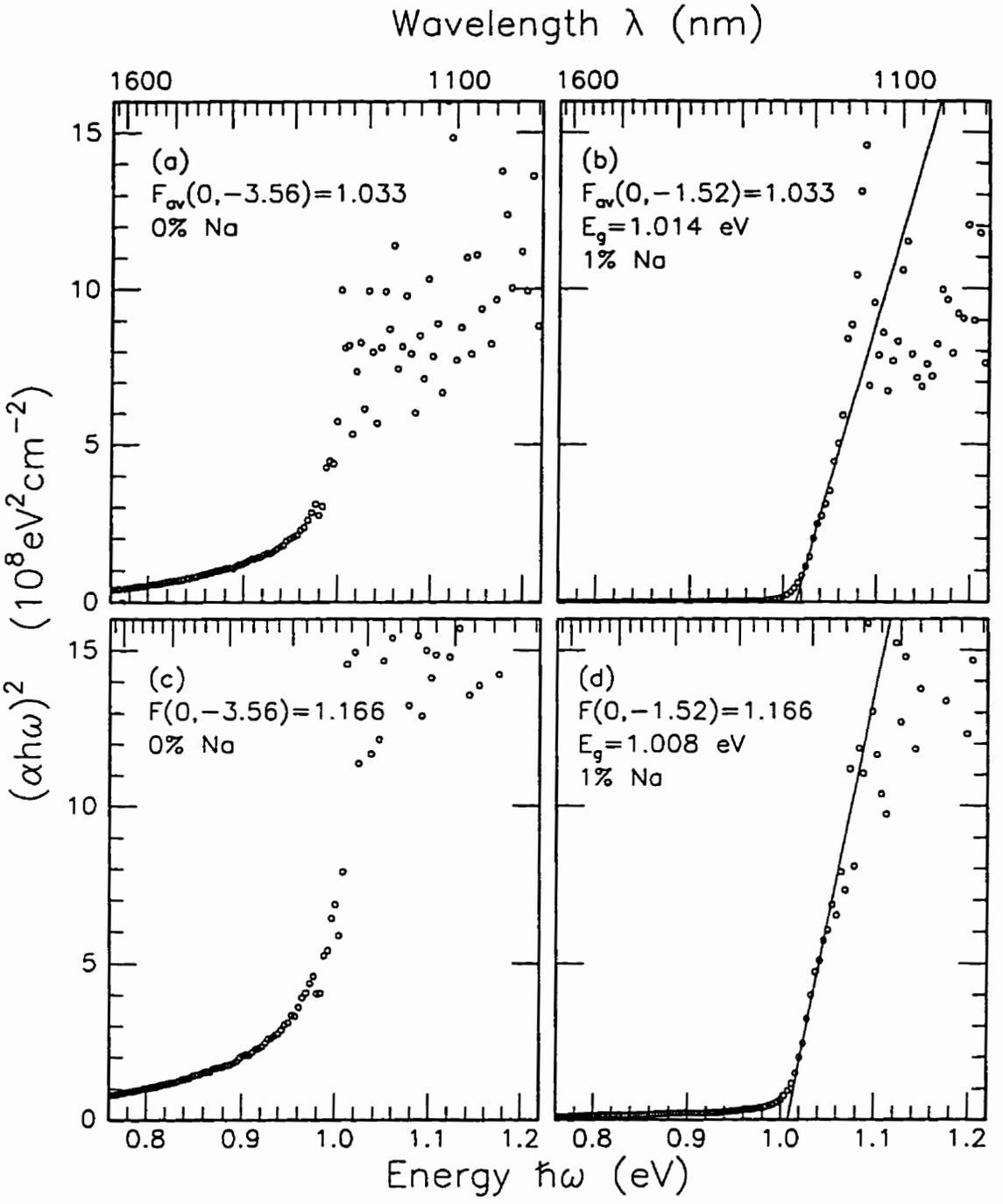

Figure 3.13

Plot of $(\alpha\hbar\omega)^2$ vs. $\hbar\omega$ for $CuInSe_2$ films with 0% Na and with 1% Na, for the same F.
(a),(b) 960308, d=2.95 μm, two layer
(c),(d) 960309, d=2.288 μm, single layer

3.5.4 Evaluation of the Index of Refraction

The real part n of the index of refraction for $CuInSe_2$ can be estimated from those transmittance spectra which show interference fringes by using the relation

$$n(\lambda_{av}) \cong \frac{1}{2d}\left(\frac{\lambda_m \lambda_{m+1}}{\lambda_m - \lambda_{m+1}}\right) \qquad (3.13)$$

where λ_m and λ_{m+1} are the wavelengths of two adjacent interference fringes, differing by 1 order, and λ_{av} is their average. The results are shown in figure 3.14 (a, b). In other published studies, n is determined for polycrystalline thin films by solving a system of equations similar to equations 3.9 [21, 24, 28] (figure 3.14 c, d, e), and, for single crystals at energy well below the band-gap, by assuming no absorption and using reflectance data only (Use R = 0.257 at 0.5 eV from [20], calculate n = 3.056, as shown in figure 3.14 f). Transmittance spectra for single crystals at energies well above the band-gap are not reported in the literature, probably because it would be difficult to prepare the required thin specimens. As seen in figure 3.14, there are considerable discrepancies between the various data sets, which may relate to differences in stoichiometry, method of computation, crystallite size and orientation, film porosity, substrate material, etc.

3.6 Photoluminescence

3.6.1 Description of the Photoluminescence Spectrometer

A photoluminescence spectrometer was constructed, as indicated in figure 3.15. The sample under study is placed inside a heat shield on a liquid nitrogen cooled copper platform in an evacuated chamber with a glass window. The output from a 633 nm HeNe laser is short pass filtered, chopped and brought through a slot in the heat shield to a focus on the sample surface. Luminescence radiation is collected and focused to a real image at the entrance slit of a grating monochromator. Two long pass filters at the exit slit strongly attenuate any 633 nm light which is reflected from the sample and diffracted through the monochromator in the second or third order. Following the filters, a thermo-electrically cooled germanium photodiode detects the luminescence radiation. The combination of Ge photodiode with long pass filters is the IR (infrared) detector. The spectral response of the IR detector was measured using the apparatus of figure 5.3, with the IR detector illuminated by the probe beam, immediately following the chopper mirror. The IR detector response is shown in figure 3.16 (a). The monochromator passbands at 1266 nm and 1899 nm are shown in figure 3.16 (b, c).

The photodiode signal current is amplified by a low noise preamplifier, followed by a lock-in amplifier. A data acquisition computer records the data output from the

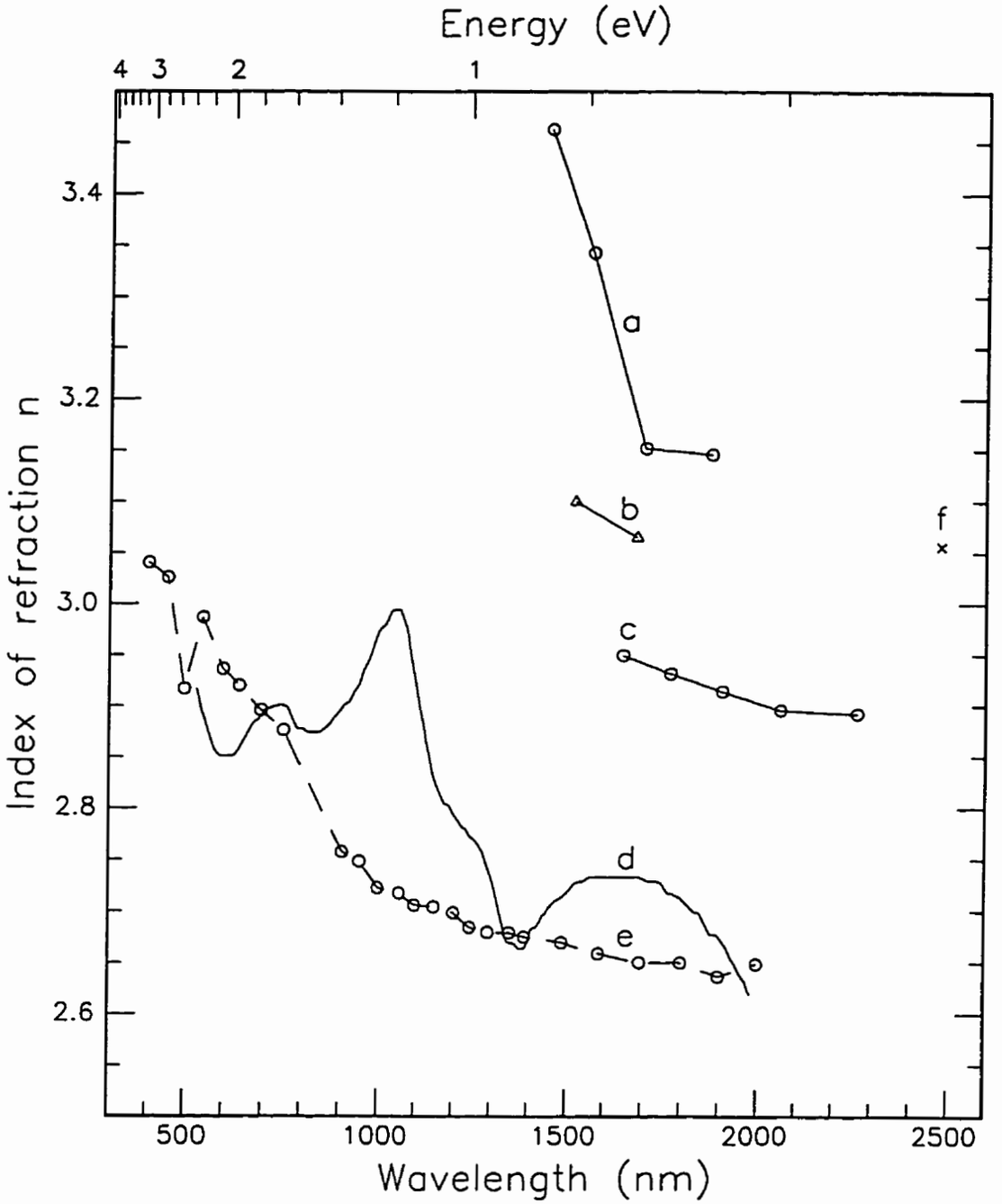

Figure 3.14

$CuInSe_2$ refraction index n. Films: (a) 960229, d=2.566 μm; (b) 960308, d=2.95 μm; (c) Ref. [28], d<0.355 μm; (d) [21], d=0.291 μm; (e) [24] d<0.2 μm; Single crystal: (f) [20]

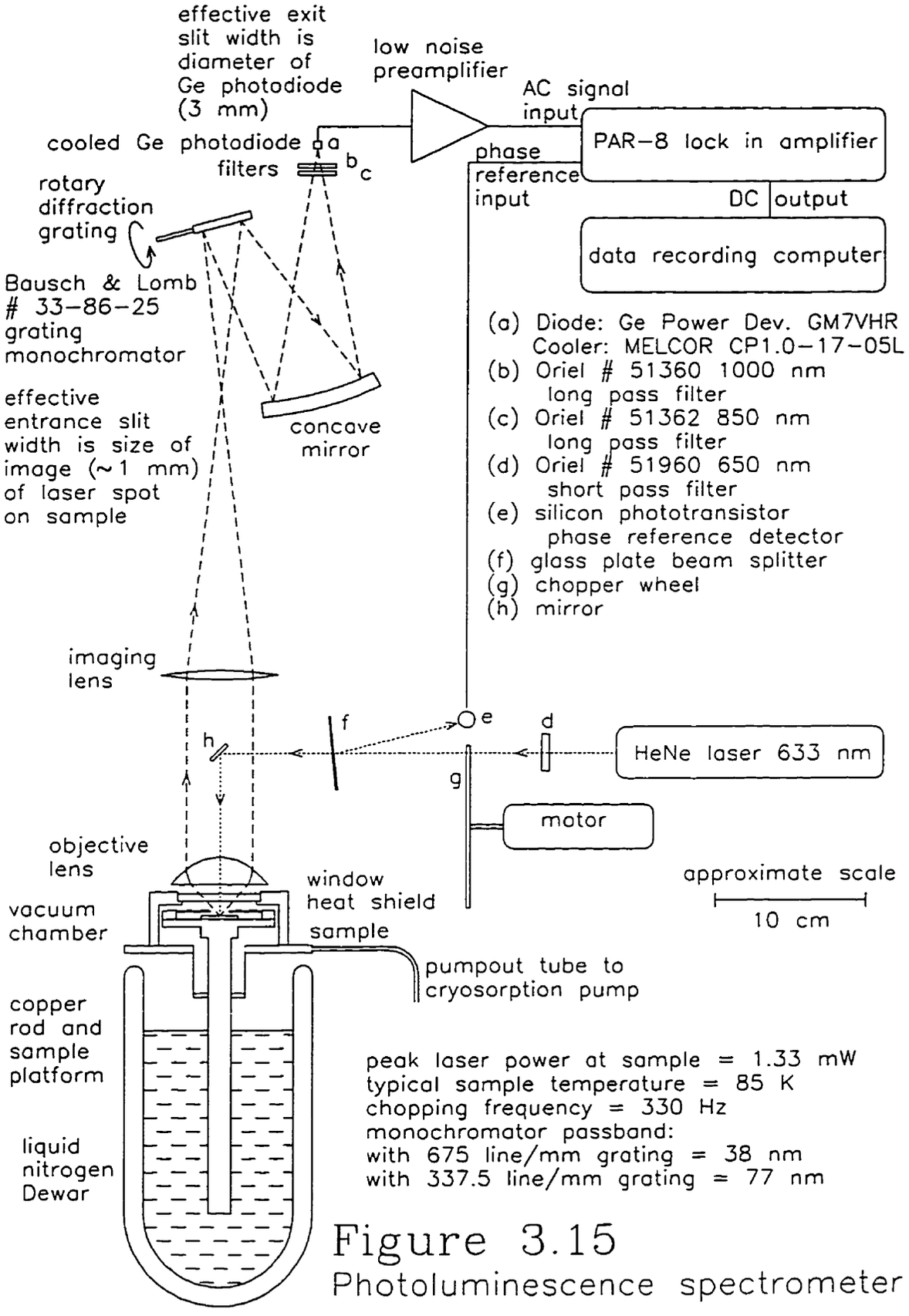

Figure 3.15
Photoluminescence spectrometer

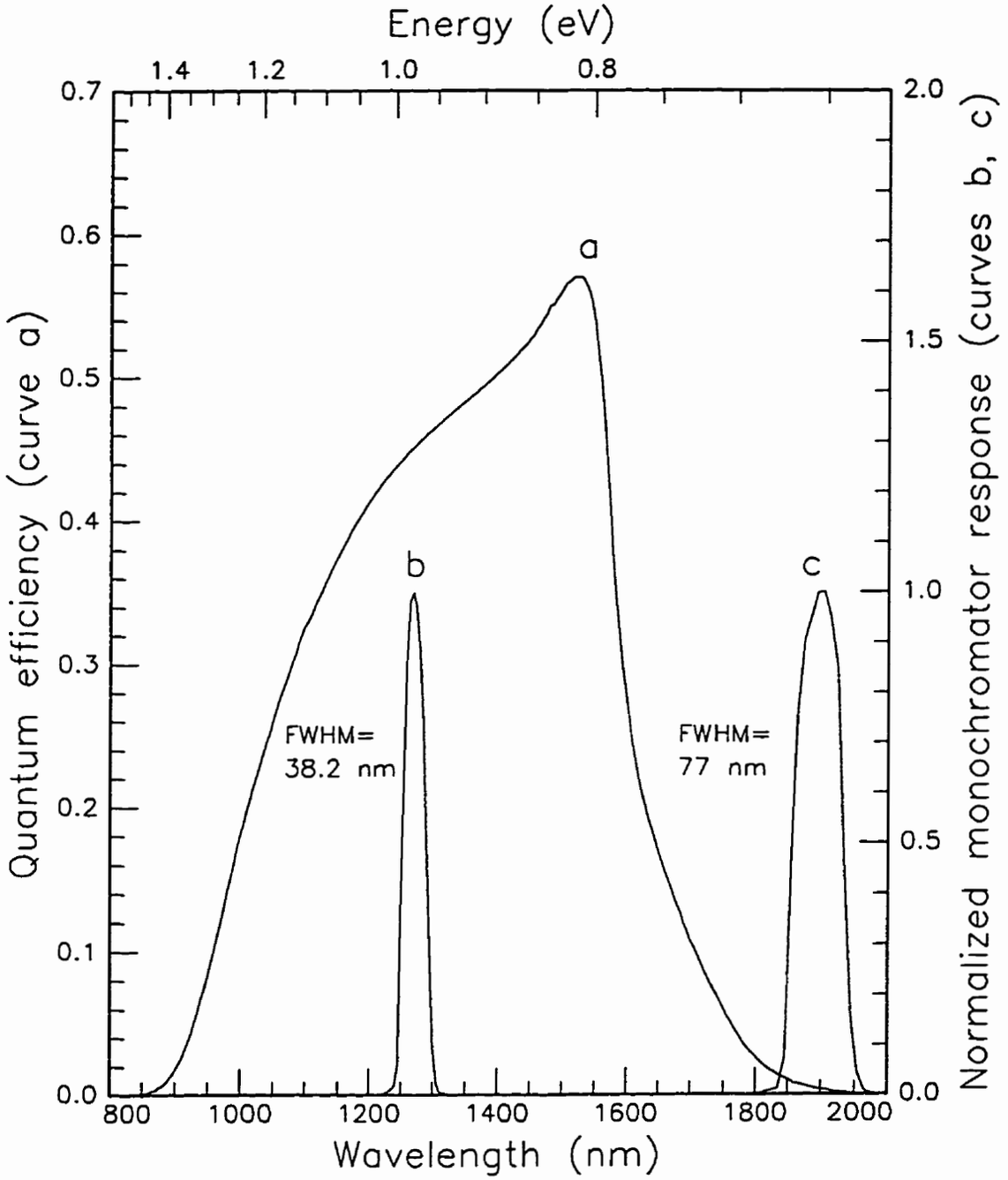

Figure 3.16

(a) Spectral response of Ge photodiode with Oriel #51362 1000 nm and #51360 850 nm long pass filters. (b) Monochromator passband at 2x633 nm with 675 lines/mm grating; (c) Monochromator passband at 3x633 nm with 337.5 lines/mm grating

monochromator. The monochromator wavelength setting (i.e. grating angle) is advanced manually by the experimenter after an audible prompt from the computer.

The photoluminescence efficiency of the $CuInSe_2$ films is generally very low, so that any means available to increase the signal to noise ratio must be applied. The sample is kept as cold as possible ($T \cong 85$ K), since the luminescence intensity increases with decreasing temperature. The laser excitation is chopped at 330 Hz, so that AC amplification can be used, in order to take advantage of the lower detector and amplifier noise spectral densities at higher (i.e. non-zero) frequencies. The Ge detector (Germanium Power Devices GM7VHR) is mounted on a thermoelectric cooler (MELCOR CP1.0-17-05L), and a low noise operational amplifier is used (Analog Devices AD743, 4 $nV/\sqrt{Hz}$ input noise). Typically the lock-in amplifier DC output filter time constant is 1 to 10 seconds, depending on signal strength. Cooling the Ge detector halves the output noise voltage.

The output power from the HeNe laser is 4.8 mW, but this is reduced by losses in the optical system to 1.33 mW (peak power, without chopping) at the sample surface. The diameter of the laser focal spot is about 50 μm, so that the power density at the sample surface is about 65 W/cm^2 (without chopping).

3.6.2 Total Detected Emission vs. Position on Substrate

The photoluminescence total detected emission (TDE) is measured by removing the monochromator from the system and placing the IR detector at the image point of the collecting lens system. Since the photodiode current is proportional to the detected photon flux, the TDE is given in units of photodiode current. Because the incident laser power is known, the signal is also given in units of total detected yield defined as

$$\text{total detected yield} = \frac{\#\text{ detected IR photons}}{\#\text{ photons at 633 nm incident on sample}}$$

The total detected photoluminescence emission vs. position x on the substrate is given for single layer and two layer films in figure 3.17. Large changes in TDE are observed as the position of the measurement point is changed. This is due to the variation of film composition with position. Also, note that the maximum TDE is much larger for the two layer film (960308) than for the single layer films.

3.6.3 Photoluminescence Spectra

Using the diffraction grating monochromator, photoluminescence emission spectra were recorded at different positions on each sample. The spectra were normalized by the IR detector response function of figure 3.16 (a) so that the spectral emission is given in units of normalized photodiode current for a hypothetical IR detector with a quantum efficiency

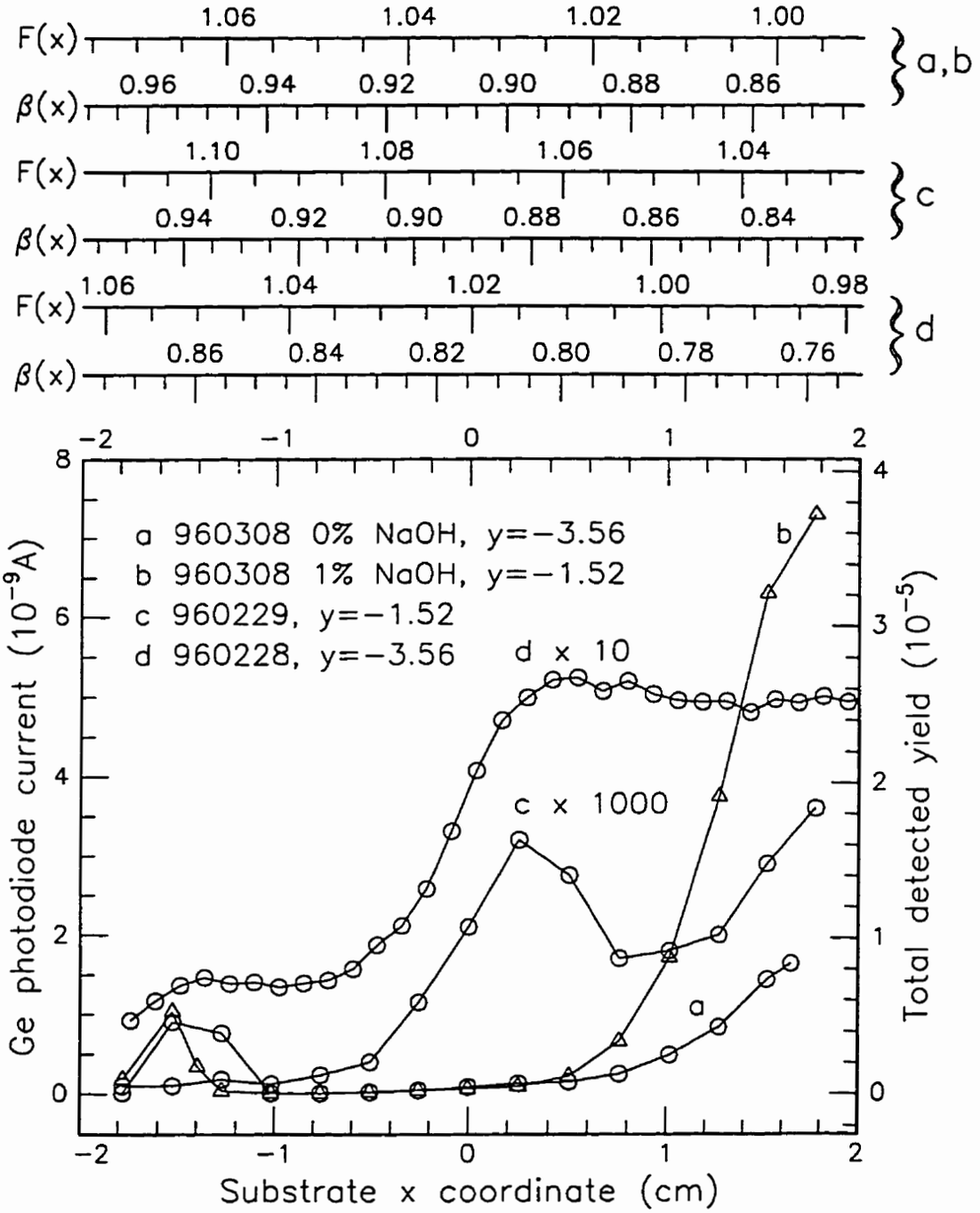

Figure 3.17

Total detected photoluminescence emission vs. position for one and two layer $CuInSe_2$ films. IR detector response as indicated in figure 3.16 F(x) and $\beta(x)$ scales particular to each film.

of 0.59, independent of wavelength. To minimize error during normalization, the wavelength of the monochromator must be correctly matched with the wavelength of the IR detector response, since the IR detector response decreases rapidly with wavelength above about 1500 nm. Dimensionless units of spectral yield are also provided, where

$$\text{spectral yield}(\lambda) = \frac{\#\text{photons in passband centered on } \lambda \text{ arriving at IR detector}}{\#\text{ photons at 633 nm incident on sample}}$$

In figure 3.18 the photoluminescence emission spectra for single layer films 960229 at one position (e) and 960228 at 4 substrate positions (a, b, c, d) are shown. Since these films are fine grained and In-rich at all the positions indicated, the TDE was expected to be very weak. The relatively strong emission and insensitivity to F(x) of 960228 was surprising. Strong emission was expected only from films having large crystallites, whereas the x-ray diffraction data (figure 3.2 a) indicate only small crystallites. The energy of peak emission is 0.74 eV, well below the $CuInSe_2$ band-gap.

Figure 3.19 shows the photoluminescence emission spectra at 8 different positions on the sodium free half of the two layer film 960308. For clarity of presentation, the spectra are grouped into weak and strong, and plotted on separate axis. Comparison of (a, b, c) shows a large increase in peak intensity at 0.81 eV followed by a similar decrease, as x varies from −1.78 to −0.76 cm. As x increases further, the intensity increases, and, in (f), a second emission peak appears at about 0.915 eV. The intensity of the 0.915 eV peak increases as x increases to 1.78 cm (g, h).

In figure 3.20, the photoluminescence emission spectra at 8 different positions on 960308 with 1% NaOH are shown. In (a), the emission maximum appears to be below the lowest photon energy measured. As x increases, an emission maximum appears at 0.83 eV (b). With further increase in x, new peaks appear at 0.9 eV and 0.93 eV (e), and these increase in intensity as x increases to 1.78 cm (f, g, h). A local TDE maximum occurs at x = −1.52 cm, as shown in figure 3.17 (b), but a spectrum was not recorded at this point.

The above results for 960308 show that the TDE and the emission energy distribution are highly sensitive to F(x). For example, as shown in figure 3.20 (c-h), the relative change in F(x) for x = −0.76 to x = 1.78 cm is only about 5%, yet the peak emission intensity increases by about 600 times over this range.

The results also show that the addition of 1% NaOH causes an increase in the emission intensity by a factor of 5 for the maximum emission observed at x = 1.78 cm (compare figures 3.19 (h) and 3.20 (h)). Also, the sodium doping appears to split the high intensity peak at 0.915 eV seen in figure 3.19 (h) into two peaks at 0.9 and 0.93 eV in figure 3.20 (h). These peaks are probably broadened by the poor monochromator resolution (38 nm).

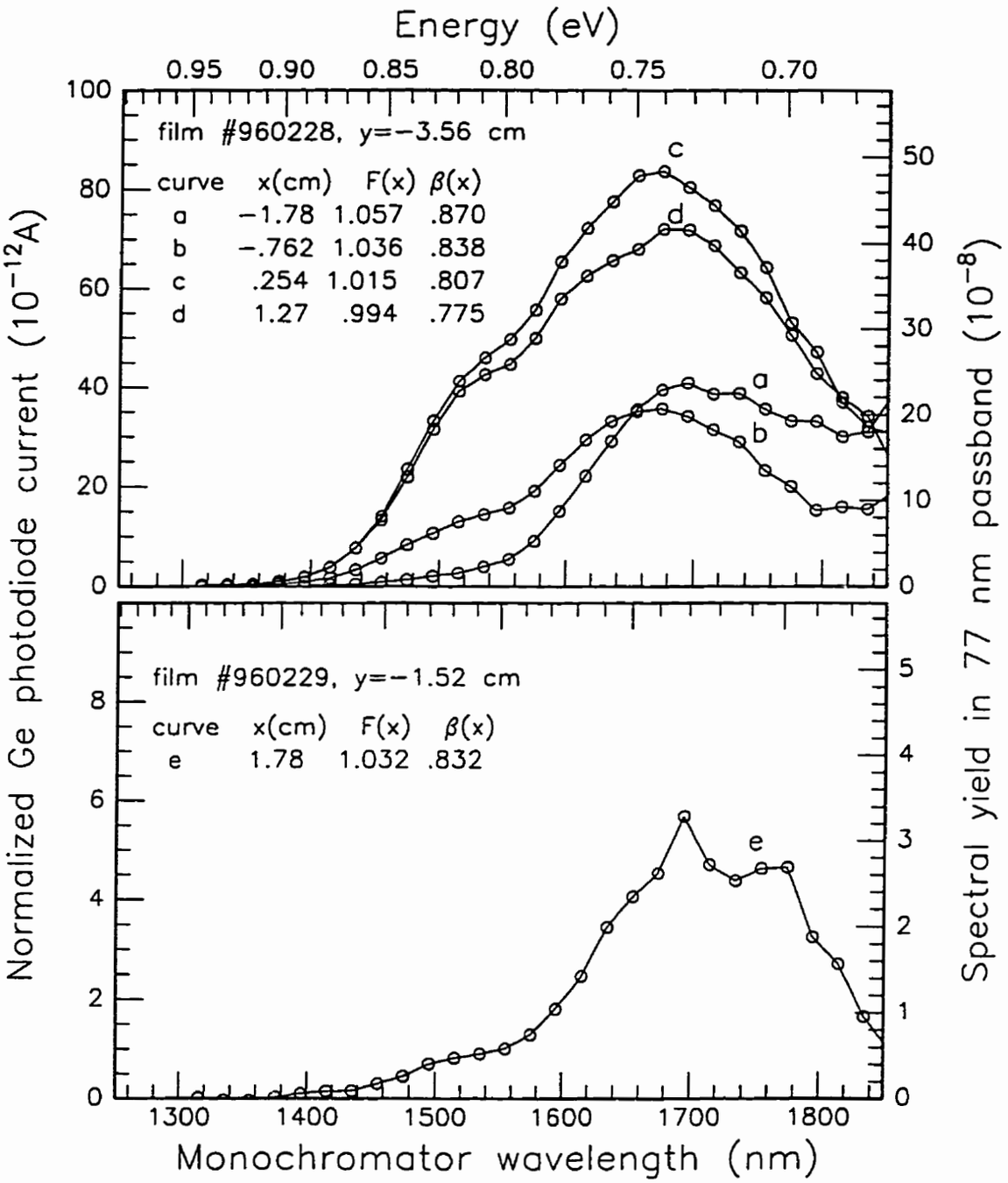

Figure 3.18

Photoluminescence spectra at different positions x for single layer $CuInSe_2$ films. Monochromator grating 337.5 lines/mm. Temperature 85 K Excitation 1.33 mW at 633 nm, chopped at 330Hz.

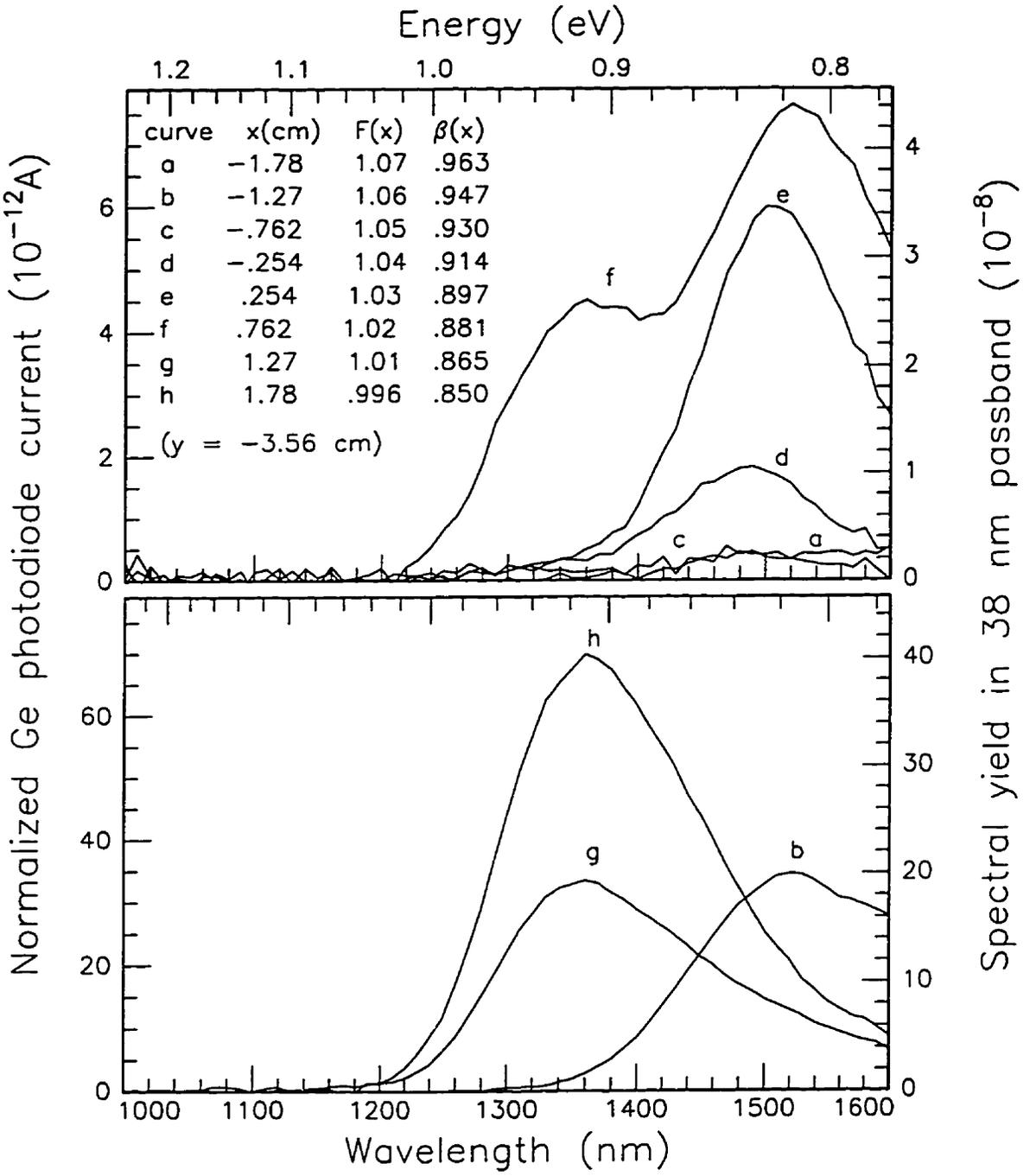

Figure 3.19

Photoluminescence spectra at different x positions for the two layer $CuInSe_2$ film 960308 with 0% Na. Grating has 675 lines/mm. Temperature 85 K. Excitation 1.33 mW at 633 nm, chopped at 330Hz.

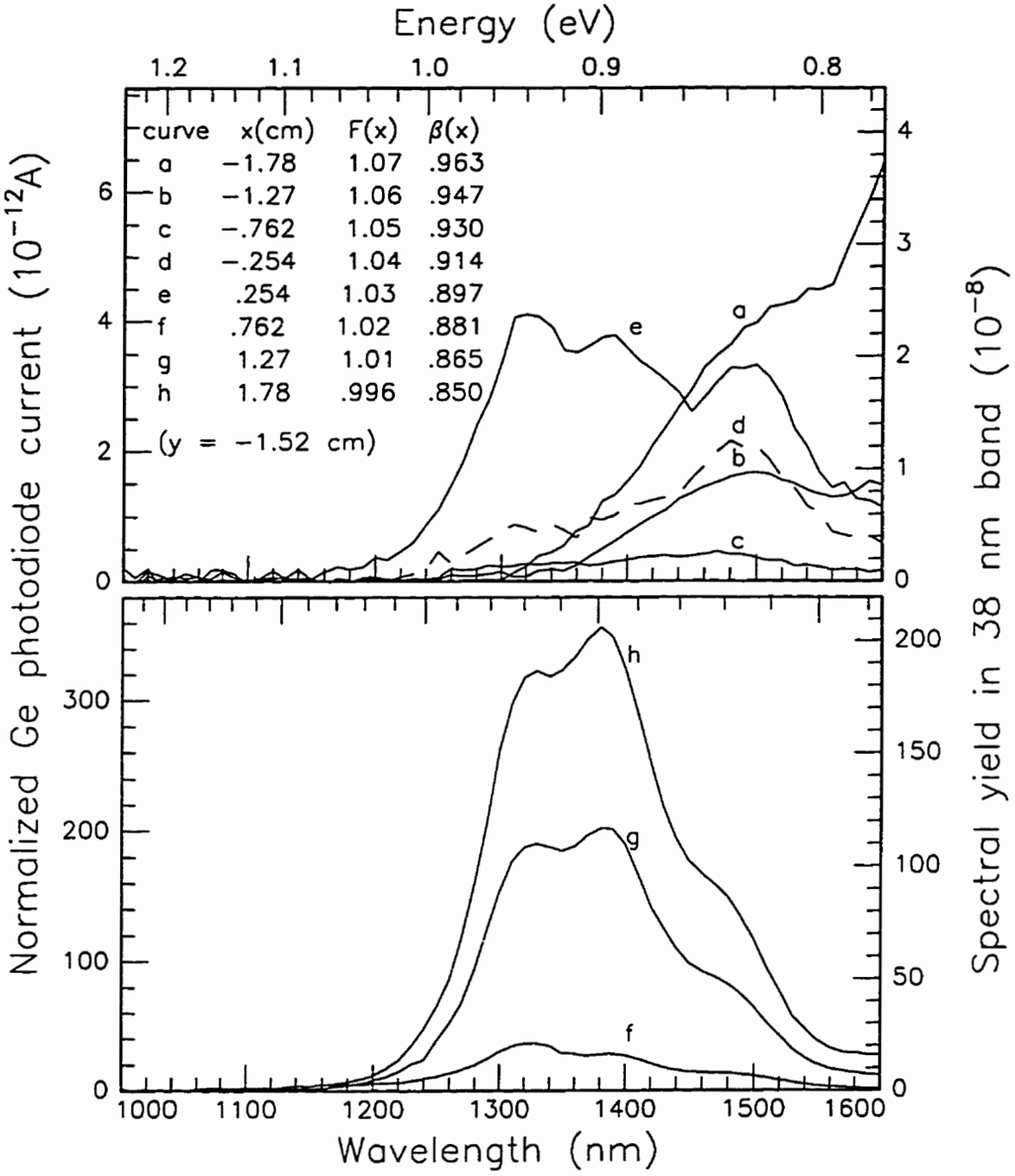

Figure 3.20

Photoluminescence spectra at different positions x for the two layer $CuInSe_2$ film 960308 with 1% Na. Grating has 675 lines/mm. Temperature is 85 K. Excitation: 1.33 mW at 633 nm, chopped at 330Hz.

3.6.4 Photoluminescence Intensity vs. Temperature

For all the $CuInSe_2$ films tested, the luminescence emission was found to be strongly temperature dependent. The maximum TDE for all samples tested occurs at the lowest temperatures accessible ($T \cong 85$ K) with the apparatus of figure 3.15. The temperature dependence of the TDE for sample 960308 is shown in figure 3.21, with positions and sodium content as indicated. For the two strongest emission positions (a, b), the TDE is seen to decrease slowly as the film is warmed, until a critical temperature ($T_c \cong 150$ K) is reached, above which the TDE is rapidly quenched. In the case of the two weaker emission positions (c, d), there is rapid quenching of TDE starting from the lowest temperature. For single layer $CuInSe_2$ films described in [31], thermal quenching begins at $T_c \cong 50$ K.

3.6.5 Interpretation of the Photoluminescence Data

Band to band radiative recombination has been observed in low temperature photoluminescence measurements of pure stoichiometric single crystals [2] (peak emission at 0.99 eV, T = 2 °K). However, typical single crystals, and polycrystalline thin films, have high intrinsic defect densities, so that the luminescence spectra are dominated by radiative transitions between defects, usually assumed to be donor-acceptor pairs. A simple model [29] of radiative recombination between a well separated (defined below) donor-acceptor pair predicts that the emitted photon energy $\hbar\omega$ is given by

$$\hbar\omega = E_g - (E_A + E_D) + \frac{q^2}{4\pi\varepsilon r} \qquad (3.14)$$

The last term in equation 3.14 accounts for the fact that the electrostatic interaction between an ionized donor and ionized acceptor is neutralized at the instant before the radiative recombination takes place. Assume that the ionization energies of an isolated donor and isolated acceptor are given by E_D and E_A respectively. Now consider a donor-acceptor pair separated by a distance r large enough that their Bohr radii do not overlap. Take the case where both donor and acceptor are ionized as the zero energy initial state of the system. Energy E_g is added to create an additional free hole and free electron. When the donor and acceptor are both neutralized by capture of a free hole and a free electron, the energy of the system is reduced by $E_D + E_A - q^2 / 4\pi\varepsilon r$. The subsequent radiative recombination of the captured electron-hole pair returns the system to the initial state while releasing the remaining energy as a photon of energy given by equation 3.14. Several predictions follow from equation 3.14.

For substitutional impurities and defects, the donors and acceptors must be on lattice sites and the separation r takes on discrete values. A series of sharp luminescence emission

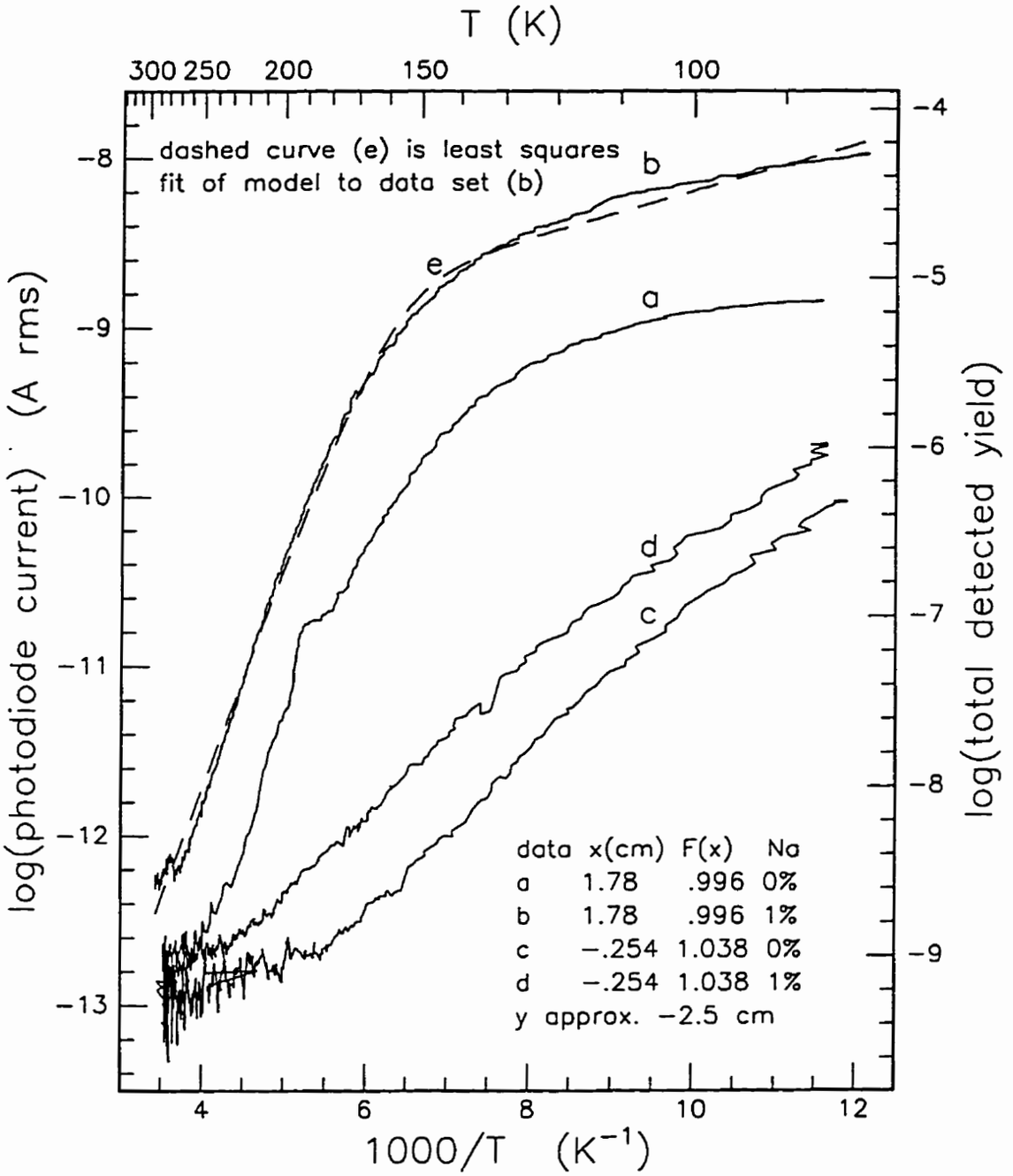

Figure 3.21

Total detected photoluminescence emission vs. temperature for the two layer $CuInSe_2$ film 960308
Detector response as indicated in figure 3.16
Excitation: 1.33 mW, 633 nm, chopped at 330 Hz.

lines has been observed in GaP at low temperatures [29], where each line corresponds to a particular r value.

As the excitation intensity increases, the steady state electron-hole pair density increases and the average distance r between neutralized donor-acceptor pairs decreases. The emission energy therefore increases as the excitation energy increases, and the magnitude of the increase is ultimately limited by the total density of donors and acceptors. This increase in emission energy has been observed in $CuInSe_2$ films [30,31].

Since the radiative transition rate depends on the density of neutral donors and acceptors, as the temperature is increased, captured carriers are more likely to be released to the bands before recombining, causing a reduction in the number of neutral donors and acceptors. This results in a decrease in luminescence emission with increasing temperature, as seen in figure 3.21, and an increase in non-radiative recombination.

Figure 3.22 shows a very simple $CuInSe_2$ energy level diagram which is used to develop a model where the radiative recombination produces a luminescence intensity vs. temperature dependence similar to that of figure 3.21 (b). The various parameters used in the model are defined in figure 3.22. The capture coefficient is the product of the free carrier thermal velocity and the carrier capture cross section at the localized state. The Coulomb interaction between charged acceptors and donors is neglected. Hole capture at neutral donors is neglected, as is electron capture at neutral acceptors. Thermal release of captured electrons or holes from the recombination centers is neglected. For this simple model the rate equations are

$$\frac{dn}{dt} = g - nC_n(N_D - n_1) + n_1N_CC_n\exp\left(-\frac{E_D}{kT}\right) - B_n(N_R - n_2)n \qquad (3.15)$$

$$\frac{dn_1}{dt} = nC_n(N_D - n_1) - n_1N_CC_n\exp\left(-\frac{E_D}{kT}\right) - Wn_1p_1 \qquad (3.16)$$

$$\frac{dn_2}{dt} = B_n(N_R - n_2)n - B_pn_2p \qquad (3.17)$$

$$\frac{dp_1}{dt} = pC_p(N_A - p_1) - p_1N_VC_p\exp\left(-\frac{E_A}{kT}\right) - Wn_1p_1 \qquad (3.18)$$

$$\frac{dp}{dt} = g - pC_p(N_A - p_1) + p_1N_VC_p\exp\left(-\frac{E_A}{kT}\right) - B_pn_2p \qquad (3.19)$$

The charge neutrality condition is

$$p + N_D - n_1 = n + N_A + n_2 - p_1 \qquad (3.20)$$

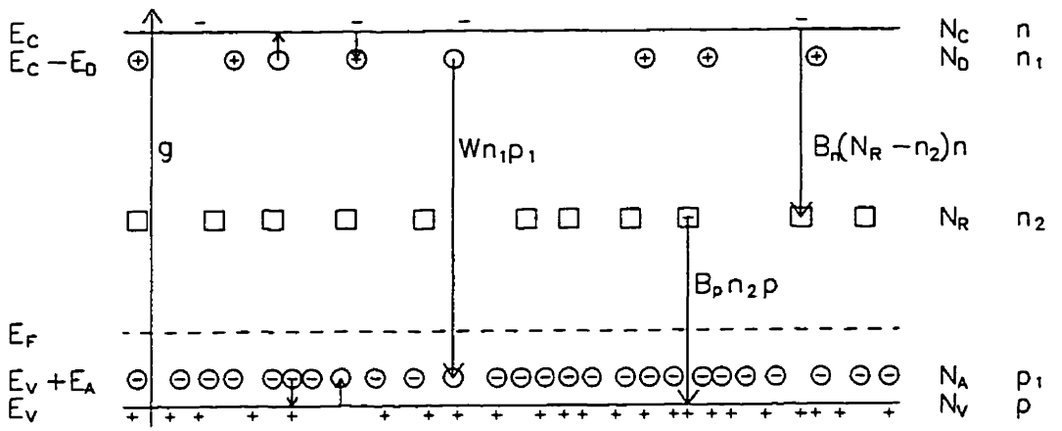

Circles represent donor and acceptor levels. Squares represent recombination centers. Arrows show electron transitions between states. Charges shown before transitions.

N_C is the conduction band density of states referred to conduction band minimum at E_C

N_D is the donor density at energy E_C-E_D

N_R is the non-radiative recombination center density at approximately $(E_V + E_C)/2$

N_A is the acceptor density at energy $E_V + E_A$

N_V is the valence band density of states referred to valence band maximum at energy E_V

n is the free electron density

n_1 is the density of neutral donors

n_2 is the density of electrons in the non-radiative recombination centers

p_1 is the density of neutral acceptors

p is the free hole density

C_n is the capture coefficient for free electrons at ionized donors

B_n is the capture coefficient for free electrons at neutral recombination centers

B_p is the capture coefficient for free holes at electron occupied recombination centers

C_p is the capture coefficient for free holes at ionized acceptors

W is the radiative recombination coefficient for captured electrons and holes

$N_C C_n$ is the "attempt to escape frequency" to the c. band of electrons at donor levels

$N_V C_p$ is the "attempt to escape frequency" to the v. band of holes at acceptor levels

g is the rate of optical generation of electron hole pairs by the laser excitation

E_F is the Fermi energy level for g = 0

Figure 3.22

A simplified $CuInSe_2$ energy-level diagram, used to explain the temperature dependence of the photoluminescence intensity.

Assume that the acceptors are shallow and mostly ionized, and assume that $N_A >> N_D$ and $N_A >> N_R$. Therefore at low levels of illumination the sample is p type with $N_D >> n_1$, $N_A >> p_1$, and $p >> n$. Assume $B_p \geq B_n$ and since $p >> n$, equation 3.17 shows that in steady state $N_R >> n_2$. Therefore equation 3.20 becomes $p \cong N_A$. Under steady state conditions, with the above assumptions, equations 3.15, 3.16 and 3.18 become

$$0 = g - nC_nN_D + n_1N_CC_n \exp\left(-\frac{E_D}{kT}\right) - B_nnN_R \qquad (3.21)$$

$$0 = nC_nN_D - n_1N_CC_n \exp\left(-\frac{E_D}{kT}\right) - Wn_1p_1 \qquad (3.22)$$

$$0 = C_pN_A^2 - p_1N_VC_p \exp\left(-\frac{E_A}{kT}\right) - Wn_1p_1 \qquad (3.23)$$

Solve equation 3.22 for n and substitute in equation 3.21, then solve equation 3.21 for n_1 and then multiply both sides by Wp_1 to obtain Wn_1p_1. Neglect the last term in equation 3.23, solve for p_1 and substitute in the right side of the new version of equation 3.21. The radiative recombination rate is then given by

$$Wn_1p_1 = \frac{g}{1 + \frac{B_nN_R}{C_nN_D} + \frac{B_nN_RN_CN_V}{WN_DN_A^2}\exp\left(-\frac{E_A + E_D}{kT}\right)} \qquad (3.24)$$

A better fit to the experimental data can be obtained if we assume that the recombination center electron capture coefficient is thermally activated, i.e. $B_n = B_0\exp(-E_B/kT)$. This form of B_n would occur, for example, if the electron must be thermally excited over a small Coulomb-repulsive energy barrier E_B before capture. Then the quantum efficiency (Q.E.) of the photoluminescence process is given by

$$Q.E. = \frac{Wn_1p_1}{g} = \frac{1}{1 + \frac{B_0N_R}{C_nN_D}\exp\left(-\frac{E_B}{kT}\right) + \frac{B_0N_RN_CN_V}{WN_DN_A^2}\exp\left(-\frac{E_A + E_D + E_B}{kT}\right)} \qquad (3.25)$$

If we estimate that 10% of the emitted photons are detected in the measurements of figure 3.21, a least squares fit of equation 3.25 to the experimental data of figure 3.21 (b) can be obtained. The fit is shown in figure 3.21 as curve (e), with the following values

$$1 + \frac{B_0N_R}{C_nN_D} = 7.32\text{x}10^4$$

$$\frac{B_0N_RN_CN_V}{WN_DN_A^2} = 1.55\text{x}10^{12}$$

$E_A+E_D = 0.230$ eV and $E_B = 0.027$ eV

Although a reasonably good fit to the experimental data is obtained, the model of figure 3.22 is clearly incomplete, because in reality a variety of donor, acceptor, recombination and trapping defects occur over a range of levels in the energy gap. According to the model, the emission should be monochromatic, at energy $\hbar\omega = E_g - (E_D + E_A) \cong 0.784$ eV (using E_g = 1.014 from figure 3.13 (b)). As seen in figure 3.20 (h) the actual emission occurs over a range of about 0.85 to 0.95 eV, with a peak at 0.9 eV.

The higher peak energy could be partly due to the fact that the average r value in equation 3.14 decreases as the excitation intensity increases. According to [**31**] the peak emission energy from a single layer film increases from 0.925 to 0.940 eV as the excitation intensity at 840 nm increases from 0.1 to 100 Wcm^{-2}, whereas in [**30**] the peak emission energy from a two layer film increases from 0.90 eV to 0.96 eV as the laser intensity at 514 nm is increased from 30 to 300 Wcm^{-2}.

An experimentally observed temperature dependence of photoluminescence emission intensity of a form similar to that of equation 3.24 has been reported elsewhere for $CuInSe_2$ [**31**], for GaAs [**29**] and for (Cd,Zn)S:Ag phosphors [**32**], although the details of the energy structure and recombination kinetics differ for each material.

The experimental results show that the intensity, spectrum and temperature dependence of luminescence emission are very sensitive to the stoichiometry, film growth method and sodium content of the films. Since luminescence is related to factors which also affect solar cell performance, such as the doping density and minority carrier lifetime, one can appreciate the process control difficulties faced by a prospective manufacturer of high efficiency $CuInSe_2$ based solar cells.

3.7 References

1 *Semiconductors: Other Than Group IV Elements and III-V Compounds*, edited by O. Madelung (Springer-Verlag, Berlin, 1992).

2 J. L. Shay and J. H. Wernick, *Ternary Chalcopyrite Semiconductors: Growth, Electronic Properties and Applications* (Pergamon, Oxford, 1974).

3 International Tables for X-ray Crystallography, Vol. 1 (Kynoch Press, Birmingham, 1969).

4 J. E. Jaffe and A. Zunger, "Electronic structure of the ternary chalcopyrite semiconductors $CuAlS_2$, $CuGaS_2$, $CuInS_2$,$CuAlSe_2$,$CuGaSe_2$,$CuInSe_2$" Phys. Rev. B **28**, 5822 (1983).

5 S. C. Abrahams and J. L. Bernstein, "Luminescent Piezoelectric $CdSiP_2$: Normal Probability Plot Analysis, Crystal Structure, and Generalized Structure of the II-IV-V_2 Family", J. Chem. Phys. **55**, 796 (1971).

6 S. C. Abrahams and J. L. Bernstein, "Crystal Structure of Luminescent $ZnSiP_2$", J. Chem. Phys. **52**, 5607 (1970)

7 H. Hahn, G. Frank, W. Klinger, A. D. Meyer and G. Storger, Zeits. Anorg. Allgem. Chem. **271**, 153 (1953) (as referenced in [**11**])

8 N. A. Goryunova, *The Chemistry of Diamond-like Semiconductors*, edited by J. C. Anderson (MIT Press, Cambridge, Mass. 1965), p.142 (as referenced in [**2**])

9 J. Parkes, R. D. Tomlinson, and M. J. Hampshire, "Crystal data for $CuInSe_2$", J. Appl. Crystallography **6**, 414 (1973)

10 H. W. Spiess, U. Haeberlen, G. Brandt, A. Rauber and J. Schneider, Phys. Status Solidi B **62**, 183 (1974) (as referenced in [**4**])

11 K. Nagata, Y. Miyamato and K. Takarabe, "Refinement of the crystal structure of copper indium selenide ($CuInSe_2$)", Fukuoka Daigaku Rigaku Shuho **19**, 103 (1989) (from Chem. Abs. **113**, p. 631 (1990))

12 K. S. Knight, "The crystal structures of $CuInSe_2$ and $CuInTe_2$", Materials Research Bulletin, **27**, 161 (1992)

13 J. Hedstrom, H. Ohlsen, M. Bodegard, A. Kylner, L. Stolt, D. Hariskos, M. Ruckh, H. W. Schock, "ZnO/CdS/Cu(In,Ga)Se_2 thin film solar cells with improved performance", *Proc. 23rd IEEE Photovoltaic Specialists Conf.* (IEEE, New York, 1993), p. 364

14 V. Probst, J. Rimmasch, W. Riedl, W. Stetter, J. Holz, H. Harms. F. Karg, H. W. Schock, "The impact of controlled sodium incorporation on rapid thermal processed Cu(InGa)Se_2 thin films and devices", *Proc. 24th IEEE Photovoltaics Specialists Conf.* (IEEE, New York, 1994), p.144

15 A.C. Ribes, S. Damaskinos, H.F. Tiedje, A.E. Dixon, D.E. Brodie, "Reflected-light, photoluminescence and OBIC imaging of solar cells using a confocal scanning laser MACROscope/microscope", Solar Energy Materials and Solar Cells, **44**, 439 (1996)

16 B. E. McCandless and R. W. Birkmire, "Control of Deposition and Surface Properties of $CuInSe_2$ Thin Films for Solar Cells", *Proc. 20th IEEE Photovoltaics Specialists Conf.* (IEEE, New York, 1988), p. 1510

17 H. Davies, Proc. Inst. Elec. Engrs. **101**, 209 (1954) (as referenced in [**18**])

18 H. E. Bennett and J. O. Porteus, "Relation Between Surface Roughness and Specular Reflectance at Normal Incidence", J. Opt. Soc. Am. **51**, 123 (1961)

19 J. C. Rife, R. N. Dexter, P. M. Bridenbaugh, "Optical properties of the chalcopyrite semiconductors $ZnGeP_2$, $ZnGeAs_2$, $CuGaS_2$, $CuAlS_2$, $CuInSe_2$, and $AgInSe_2$", Phys. Rev. B **16**, 4491 (1977)

20 J. N. Gan, J. Tauc, V. G. Lambrecht, Jr., M. Robbins, "Optical properties of the $(CuInSe_2)_{1-x}(2ZnSe)_x$ system", Phys. Rev. B **12**, 5797 (1975)

21 J. R. Tuttle, D. Albin, R. J. Matson, R. Noufi, "A comprehensive study of the optical properties of thin-film $CuInSe_2$ as a function of composition and substrate temperature", J. Appl. Phys. **66**, 4408 (1989)

22 O. Madelung, *Introduction to Solid State Theory*, (Springer-Verlag, New York, 1978)

23 R. T. Philips, "A numerical method for determining the complex refractive index from reflectance and transmittance of supported thin films", J. Phys. D: Appl. Phys., **16**, 489 (1983)

24 J. L. Hernandez-Rojas, M. L. Lucia, I. Martil, G. Gonzalez-Diaz, J. Santamaria and F. Sanchez-Quesada, "Optical analysis of absorbing thin films: applications to ternary chalcopyrite semiconductors", Applied Optics, **31**,1606 (1992)

25 J. Schmidt, H.H. Roscher, R. Labusch, "Preparation and properties of $CuInSe_2$ thin films produced by selenization of co-sputtered Cu-In films", Thin Solid Films, **251**, 116 (1994)

26 H. Neumann, R.D. Tomlinson, "Band-gap narrowing in n-type $CuInSe_2$ single crystals", Solid state communications, **57**, 591 (1986)

27 J. Herrero and C. Guillen, "Study of the optical transitions in electrodeposited $CuInSe_2$ thin films", J. Appl. Phys. **69**, 429 (1991)

28 W. Horig, H. Neumann, V. Savelev, and J. Lagzdonis, "Refractive indices of $CuInSe_2$, $CuInTe_2$ and $CuGaTe_2$", Physics Letters, **78A**, 189 (1980)

29 H. B. Bebb and E.W. Williams, *Semiconductors and Semimetals, Vol. 8, Transport and Optical Phenomena*, edited by R.K. Willardson and A.C. Beer, (Academic Press, New York, 1972), p. 313

30 R.E. Hollingsworth and J.R. Sites, "Annealing temperature effects on $CuInSe_2$/CdS solar cells", Solar Cells, **16**, 457 (1986)

31 S. Zott, K. Leo, M. Ruckh and H.W. Schock, "Photoluminescence of polycrystalline $CuInSe_2$ thin films", Appl. Phys. Lett. **68**, 1144 (1996)

32 F. E. Williams and H. Eyring, "The mechanism of the luminescence of solids", J. Chem. Phys.,**15**, 289 (1947)

Chapter 4

Transport Properties of $CuInSe_2$ Films

4.1 Intrinsic Defect Model for $CuInSe_2$

Early experiments with chalcopyrite single crystals ABX_2 (A= Cu, Ag; B = Al, Ga, In; X= S, Se) showed that the conductivity can be altered significantly by annealing under maximum or minimum chalcogen (X) pressure [1]. The copper compounds (A = Cu) are made p-type by annealing under maximum chalcogen pressure at 600-800 °C for 24 hours. Annealing under vacuum renders the crystals highly resistive (wide band gap members, B = Al, Ga) or n-type (narrow band gap members B = In). In particular, $CuInSe_2$ initially having $p = 10^{18}\ cm^{-3}$, $\sigma = 2\ \Omega^{-1}cm^{-1}$ and $\mu_p = 10\ cm^2V^{-1}s^{-1}$ changes to $n = 4x10^{17}\ cm^{-3}$, $\sigma = 20\ \Omega^{-1}cm^{-1}$ and $\mu_n = 320\ cm^2V^{-1}s^{-1}$ after annealing in vacuum.

An intrinsic point defect model [2,3,4] has been developed which attempts to explain the electrical characteristics of intrinsic $CuInSe_2$ by assuming that point defects (vacancies, interstitials and antisite defects) are the electrically active species. In this model, a small deviation from molecularity Δm and a small deviation from valence stoichiometry Δs are defined as follows:

$$\Delta m = \frac{[Cu]}{[In]} - 1 \quad \text{and} \quad \Delta s = \frac{2[Se]}{[Cu]+3[In]} - 1 \quad \text{where } |\Delta m| << 1 \text{ and } |\Delta s| << 1$$

Depending on the signs of Δm and Δs, different electrically active defects are most likely to occur. The possible intrinsic defects and their formation energies are given in table 4.1 below. Defects with a high formation energy have low probability, and therefore have a much smaller concentration than the defects with low formation energies .

For example, low energy defects consistent with $\Delta m < 0$ and $\Delta s < 0$ would be In_{Cu} and V_{Se}. Smaller numbers of acceptor defects could also be present, but they would be compensated by the donors, resulting in an n-type material. For $\Delta m > 0$, $\Delta s > 0$ the defect Cu_{In} would produce a p-type material. In the case $\Delta m > 0$, $\Delta s < 0$, Cu_{In} acceptors exist, and the carrier type depends on the density of compensating V_{Se} donors.

A study of as-grown $CuInSe_2$ single crystals [5] confirmed the above predictions of conductivity type for $|\Delta m| < 0.08$ and $|\Delta s| < 0.06$. The carrier concentrations varied over only a relatively small range ($n = 1.8x10^{15} - 5x10^{17}\ cm^{-3}$ and $p = 1.5x10^{16} - 3x10^{17}\ cm^{-3}$) and showed no correlation with $|\Delta m|$ and $|\Delta s|$. This was probably due to the high degree of compensation observed for all the samples in the study. Donor ionization energies were determined to be $E_D < 20$ meV (assigned to V_{Se} and In_{Cu}) and $E_A = 20$-30 meV (assigned to Cu_{In}). However, another study [6] of $CuInSe_2$ crystals with controlled deviation from

stoichiometry produced n-type crystals only for a range $-0.127 < \Delta m < 0.02$ and $-0.089 < \Delta s < -0.015$. Outside of this range the crystals were p-type.

Table 4.1: Intrinsic Point Defects in $CuInSe_2$

Defect	Formation energy (eV)		Type (Ionic model)
	Ref. [7]	Ref. [8]	
In_{Cu}	1.6	1.4	donor
Cu_{In}	1.9	1.5	acceptor
V_{Se}	2.2	2.4	donor
V_{Cu}	3.2	2.6	acceptor
V_{In}	2.4	2.8	acceptor
Cu_i		4.4	donor
In_{Se}	5.0	5.0	donor
Se_{In}	5.2	5.5	acceptor
Cu_{Se}	5.4	7.5	donor
Se_{Cu}	6.0	7.5	acceptor
In_i		9.1	donor
Se_i		22.4	acceptor

4.2 Electrical Properties of Single Layer $CuInSe_2$ Films

4.2.1 Conductivity of Single Layer $CuInSe_2$ Thin Films

The variation of conductivity with the Cu/In ratio only, is most often reported for thin films. This is because during high temperature processing in an excess Se environment, for any Cu/In ratio selected, the chemical requirement of valence stoichiometry will naturally tend to fix the Se content so that the film composition lies near the $(Cu_2Se)_{1-x}(In_2Se_3)_x$ pseudo-binary line ($\Delta s \equiv 0$). Furthermore, the exact value of Δs is usually hidden by the measurement uncertainty of the analytical technique used to determine composition, so that one can be confident of Se excess or deficiency only by an annealing process similar to the one described in section 4.1. Typically, the films are high conductivity p-type for Cu/In > 1 (usually as measured by EDX) and low conductivity n-type for Cu/In < 0.8, with a fairly rapid transition region between these values [**9, 10, 11**].

As described in section 2.6, measurement zones are defined on films 960229 and 960309. A schematic of the conductivity and Hall effect measurement apparatus is shown in figure 4.1. A thermocouple is bonded to the substrate surface and the sample is placed in a small evacuated sample chamber on a variable temperature stage. The chamber is placed between the poles of a large electromagnet, with the field turned off (the field is turned on briefly for Hall measurements, described next). A fixed potential V is applied across the

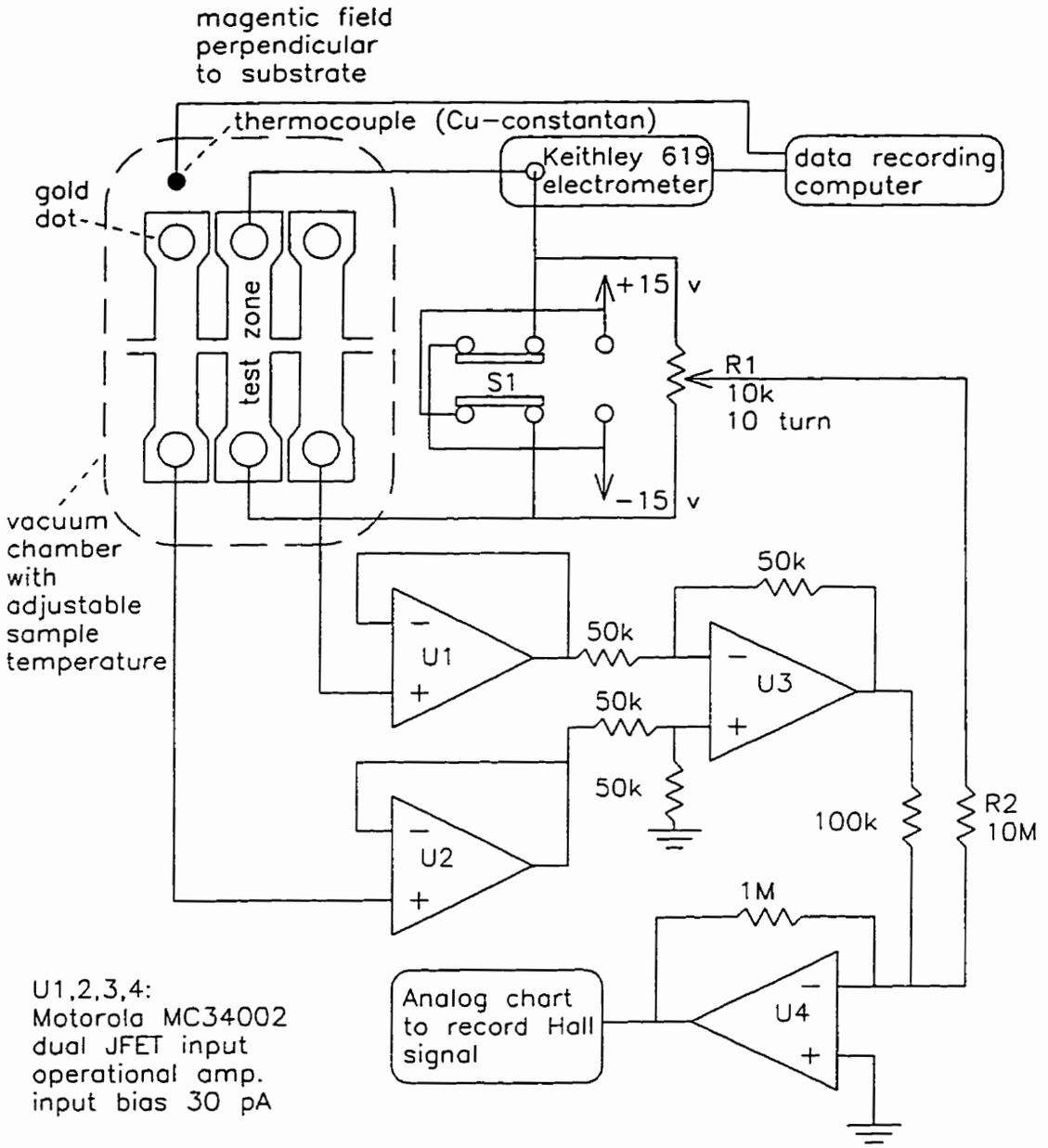

Figure 4.1

Apparatus for measurement of conductivity and Hall voltage as a function of temperature. Sample current measured every 0.1 mV of thermocouple. B field on briefly to record Hall voltage at fields B = +/– 0.964 T.

sample through the contact dots, and the current I is recorded by the computer over a range of temperatures. The contacts are considered ohmic, since no significant voltage drop exists at the contacts, and the sample current varies linearly with applied voltage. The conductivity σ is calculated using

$$\sigma = \frac{I L_y}{V L_x d} \qquad (4.1)$$

Units: σ ($\Omega^{-1}cm^{-1}$), I current (A); V applied voltage (V); L_y length (cm); L_x width (cm); d thickness (cm). Typical values are $I = 10^{-6}$, $V = 30$, $L_y = 1.3$, $L_x = 0.27$, $d = 2.5 \times 10^{-4}$.

Figure 4.2 shows the conductivity vs. temperature for 8 zones on sample 960229, and 5 zones of sample 960309, including 2 with 1% NaOH doping, covering a range in F of 1.032 to 1.136. For each film, the conductivity varies monotonically with x and F(x). Although the nominal F(x) ranges do not overlap, the conductivity ranges of the two films do overlap, as shown by curves (e, f). This overlap could be because the true bulk Cu/In ranges overlap, despite the fact that the EDX measurements of figure 2.14 show no overlap. Another possibility is that Δs differs significantly between the two samples, due to differences in Se concentration. The EDX measurements shown in figures 2.12 and 2.13 seem to indicate a slightly higher Se concentration for 960229 than for 960309, although the difference is opposite to what one would expect, since the Se source is closer to the measurement zones of sample 960309 (see figure 2.16 (b) and compare y values for 960229 and 960309).

In the high temperature region the conductivity is modeled as

$$\sigma(T) = \sigma_\infty \exp\left(-\frac{E_a}{kT}\right)$$

The conductivity thermal activation energy E_a is determined from the slope of a linear fit to data in the temperature range $294\ K < T < 343\ K$. The activation energies are tabulated in figure 4.2. The infinite temperature conductivity σ_∞ is the intercept of the linear fit at the (1000/T) = 0 axis. The activation energy E_a, σ_∞, and the room temperature conductivity for 8 zones of film 960229 are presented in figure 4.5.

The room temperature conductivities for 8 sodium-free and 8 sodium-doped zones of the Cu-rich sample 960309 are shown in figure 4.6 (e, f). The presence of sodium results in a higher conductivity at all F(x), and a conductivity more than ten times higher for the four zones in the positions $x > 0$.

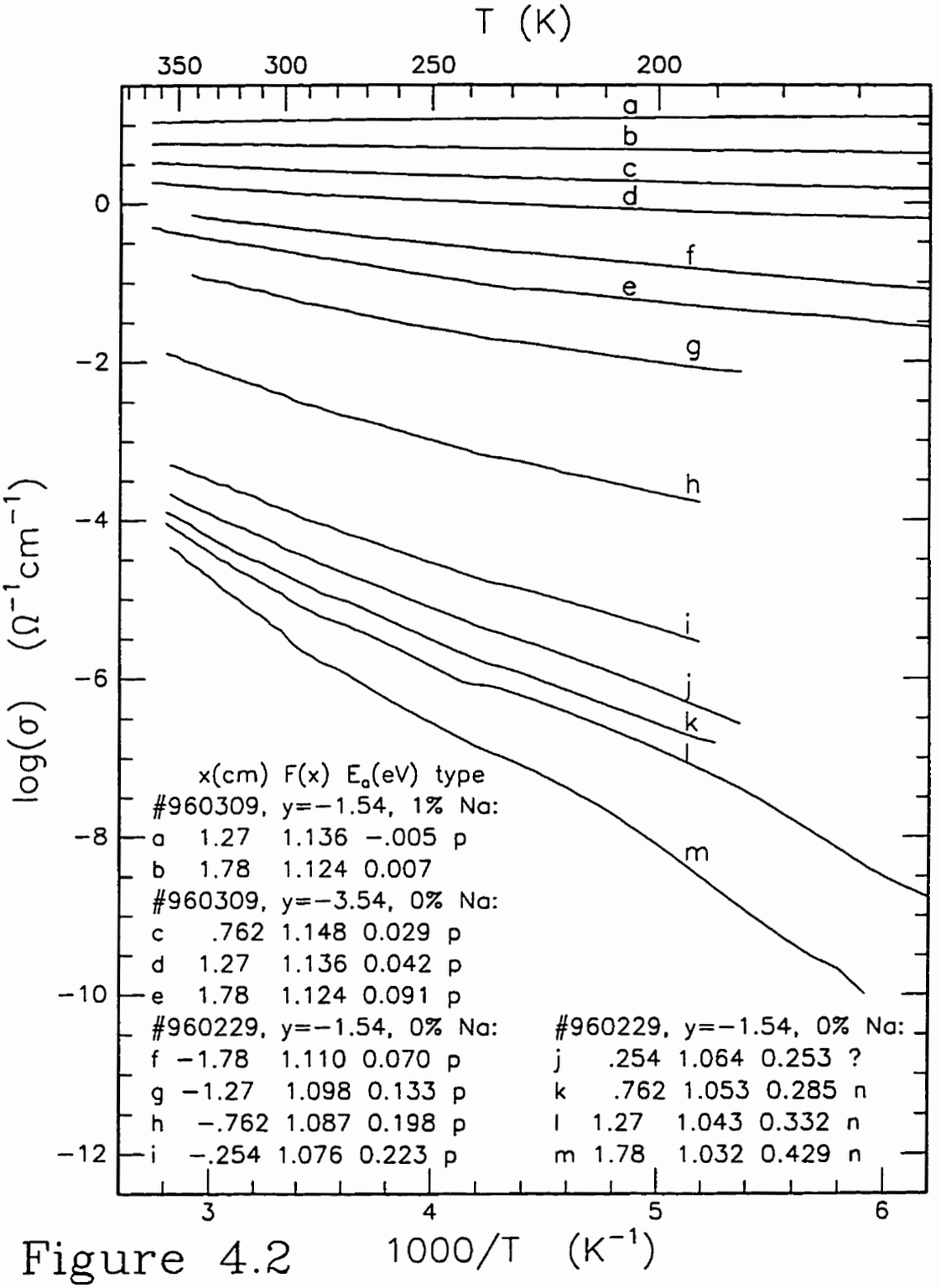

Figure 4.2

Conductivity vs. temperature for single layer $CuInSe_2$ films deposited on 7059 glass @ 350 °C. Beside each letter, x, F(x), activation energy E_a, and carrier type are specified.

4.2.2 Hall Coefficient and Carrier Density for Single Layer Films

The Hall effect measurements were taken at various temperatures during the conductivity measurement procedure described above. The Hall apparatus is shown in figure 4.1. The sample contacts are connected to +15 and −15 volt power supplies (lower voltages used for high conductivity samples) through a polarity switch S1, which controls the direction of current through the sample. Unity gain, low input bias current buffer amplifiers U1 and U2 bring the voltages at the Hall electrodes to the differential amplifier U3. Due to conductivity gradients in the plane of the film, a substantial offset potential difference V_0 (typical $V_0 \cong 1$ volt) exists between the Hall contacts at zero field. Most of the output offset of amplifier U3 due to V_0 is subtracted by means of a proportional current at the inverting input of U4, brought through R2 from potentiometer R1. The output from U4 is connected to a chart recorder. Since the residual output offset drifts as the sample temperature changes, the Hall voltage V_H is detected as the change in the slowly drifting output voltage during a brief ($\cong$ 20 s, long enough for decay of induced EMF's) application of the magnetic field. The Hall voltage is calculated as the average of voltage measurements taken at the four possible combinations of zone current and field directions.

The Hall coefficient is defined as

$$R_H = \frac{E_y}{J_x B_z} \qquad (cm^3C^{-1}) \qquad (4.2)$$

where the current density J_x (Acm^{-2}) is in the +x direction, the magnetic field B_z (G) is in the +z direction, and E_y (Vcm^{-1}) is the Hall electric field. (This is the conventional choice of x, y, z for descriptions of the Hall effect, and should not be confused with the x, y, z substrate coordinates defined in figures 2.10 and 2.15.)

If the Hall voltage is taken as positive when the Hall electric field is in the +y direction, then with film thickness d, and current I, we have

$$R_H = \frac{V_H d}{B_z I} \qquad (4.3)$$

Assume a p-type sample, and let the scattering correction factor be equal to one. The electric field E_y (due to accumulated charge displaced by the Lorentz force) must balance the Lorentz force. Therefore, $qE_y - qv_xB_z = 0$, and since $J_x = qv_xp$, we obtain

$$E_y = \frac{J_x B_z}{qp}.$$

Combining the above result with equation 4.2, we obtain

$$R_H = \frac{1}{qp} \qquad (4.4)$$

Using $\sigma = q\mu_p p$ in equation 4.4, we get the Hall mobility

$$\mu_p = \sigma R_H \qquad (4.5)$$

A similar analysis applies when n >> p, for which we obtain

$$R_H = -\frac{1}{qn} \qquad (4.6)$$

and

$$\mu_n = \sigma R_H \qquad (4.7)$$

For the case where neither carrier type dominates, one can show that the Hall coefficient is

$$R_H = \frac{\mu_p^2 p - \mu_n^2 n}{q\left(\mu_p p - \mu_n n\right)^2} \qquad (4.8)$$

Figure 4.3 shows the Hall coefficient vs. temperature for 8 zones of film 960229, and 5 zones of film 960309, including 2 with 1% NaOH doping, covering a range in F of 1.032 to 1.136. The set of zones is the same as shown in figure 4.2, and the same identifying letter is assigned to the data for each zone. Data sets (a to i) are for p-type conductivity zones, and data (k, l, m) are for n-type zones. No Hall voltage can be detected for the zone x = 0.254 cm of 960229 which falls in the transition region between p-type and n-type. This can be explained in terms of equation 4.8, if we assume that

$$p = \frac{\mu_n^2}{\mu_p^2} n$$

The carrier density, as indicated by the right hand axis of figure 4.3, is approximately determined using equations 4.4 and 4.6. For each film, a steady decrease in free carrier density is seen as the F(x) value decreases. There is some overlap (see data e, f) of the carrier density ranges for films 960229 and 960309, despite the fact that the corresponding F(x) ranges do not overlap. This is consistent with the overlap in the conductivity ranges for the same films, as noted in section 4.2.1. The two sodium doped zones of 960309 (a, b) show a higher carrier density than the corresponding sodium free zones (d, e). This suggests that sodium acts as an acceptor in $CuInSe_2$, or that it somehow reduces the density of electrically active donor defects.

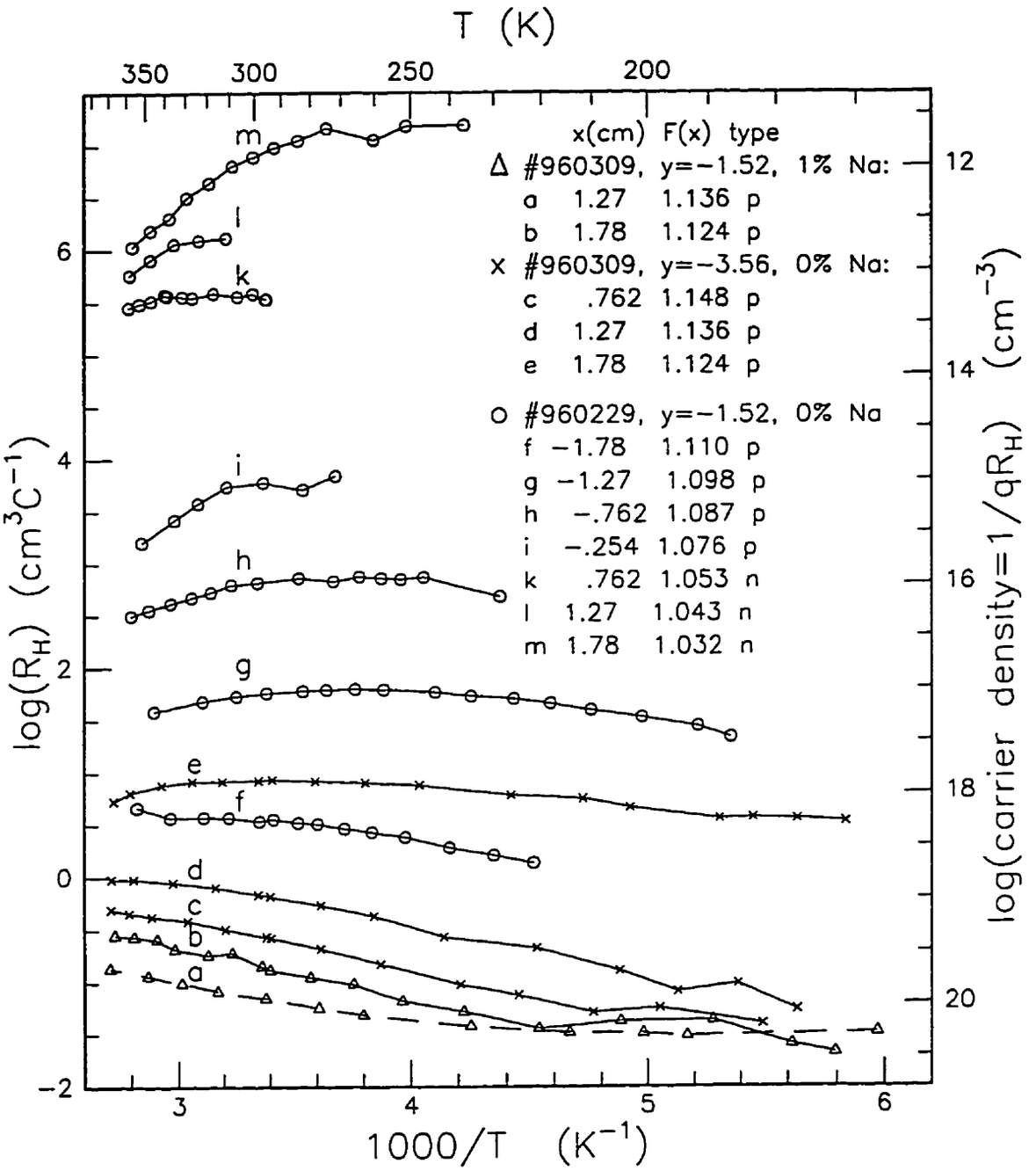

Figure 4.3

Hall coefficient vs. temperature for single layer $CuInSe_2$ films deposited on 7059 glass at 350 °C. x(cm), F(x), and carrier type (n or p) follow each letter listed above.

4.2.3 Hall Mobility Data for Single Layer Films

Using equations 4.5 and 4.7, the hole and electron mobilities can be determined. Data for the same zones as figures 4.2 and 4.3, with the same identifying letters, are shown in figure 4.4.

As expected, the effective mobilities measured here for polycrystalline films are substantially less than the bulk mobility of single crystals. Referring to figures 4.4 or 4.5, we have μ_p = 0.8 - 3.5 $cm^2V^{-1}s^{-1}$ and μ_n = 7.8 - 29 $cm^2V^{-1}s^{-1}$ at room temperature. These can be compared with μ_p = 15 - 50 $cm^2V^{-1}s^{-1}$ and μ_n = 90 - 900 $cm^2V^{-1}s^{-1}$ for single crystal specimens with small deviations from stoichiometry [5].

For polycrystalline thin films, carrier mobility for transport in the film plane is less than the bulk single crystal mobility μ_b because of scattering at intergrain boundaries and film surfaces. If typical grain dimensions are much greater than the carrier mean free path λ, then internal grain mobility can be assumed equal to μ_b . Then one need consider only the effect of intergranular boundary potentials on carrier transport in the film. The mean free path for bulk $CuInSe_2$ can be estimated using

$$\lambda = v\tau_b = \left(\frac{2kT}{m^*}\right)^{\frac{1}{2}}\left(\frac{\mu_b m^*}{q}\right) = 5.42\times10^{-2}\left(\frac{m^*}{m_0}\right)^{\frac{1}{2}}\mu_b \qquad \text{(nm at T= 300 K)}$$

where v is the carrier thermal velocity, τ_b is the mean time between collisions and μ_b is in $cm^2V^{-1}s^{-1}$ for λ in nm. Taking $m^* = 0.1m_0$ and μ_b = 900 $cm^2V^{-1}s^{-1}$ for n-type $CuInSe_2$, we obtain λ = 15 nm, which is much less than a typical grain size. A similar calculation for p-type material would result in a smaller λ, because of the lower hole mobilities.

A simple model [12] for the effective film mobility μ_f in the presence of grain boundary potential barriers of height ϕ gives

$$\mu_f = \mu_b \exp\left(-\frac{q\phi}{kT}\right)$$

The film mobility data of figure 4.4 show thermal activation, with $\phi \cong 0.1$V for the p-type films and $\phi \cong 0.2$ V for the n-type films. The bulk mobility μ_b also depends on temperature. According to [5], $\mu_{b,p}$ decreases slowly and $\mu_{b,n}$ stays constant or decreases slowly for T increasing from 200-300 K. The temperature dependent μ_b could explain the slight negative curvature of some of the curves in figure 4.4.

The mobilities of the two Na doped zones of film 960309 (figure 4.4 a, b) are slightly less than the corresponding sodium-free zones (d, e) at room temperature. However, at lower temperatures the Na doped zones have higher mobilities. The room temperature carrier densities and Hall mobilities at 7 zones of film 960229 are shown in figure 4.5.

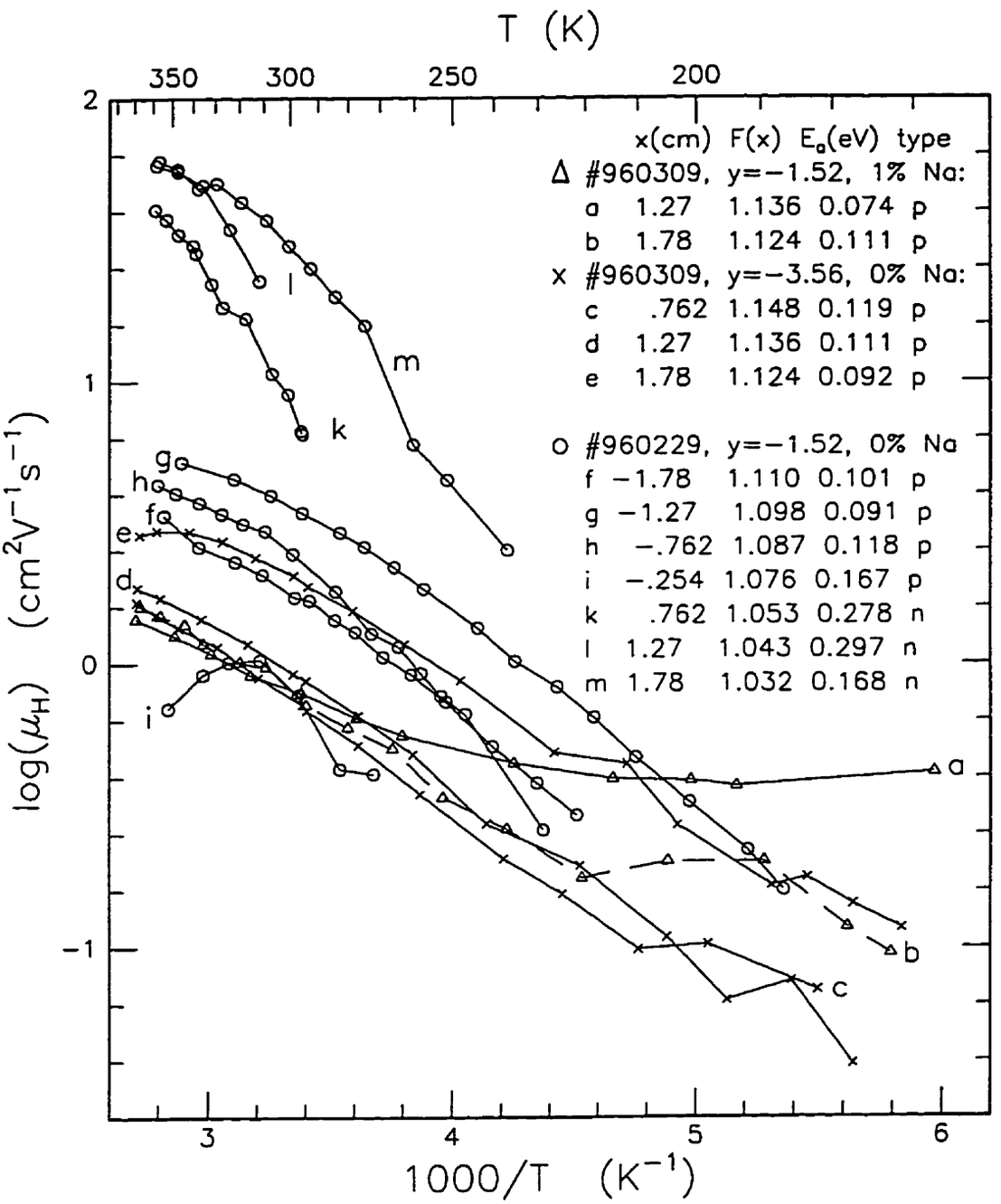

Figure 4.4

Hall mobility vs. temperature for single layer $CuInSe_2$ films deposited on 7059 glass at 350 °C. x (cm), F(x), E_a (eV) and carrier type (n or p) follow each letter listed above.

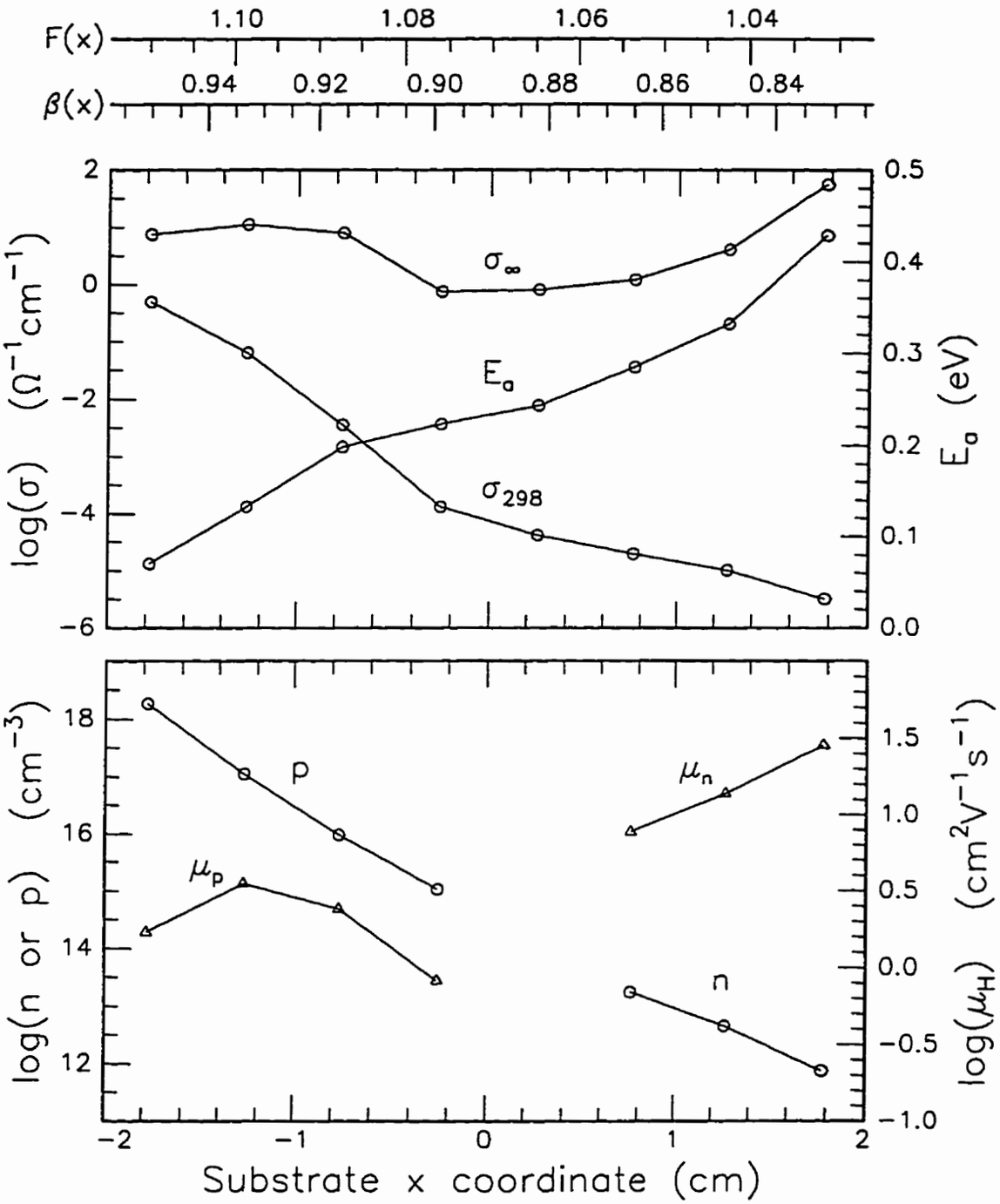

Figure 4.5

Electrical properties vs. x of film 960229 at T=298 K. σ_{298}: conductivity ; σ_{∞}: conductivity extrapolated to T=∞ E_a activation energy of σ_{298}; n, p: carrier concentration μ_p, μ_n: Hall mobility. No Hall data for x=.254 cm

4.3 Electrical Properties of Two Layer $CuInSe_2$ Films

The two layer film 960308 was deposited with one half of the film 1% sodium doped, and the other half sodium free. After storing for about 50 days in room temperature air, the conductivity of all zones was measured at room temperature. The results are shown in figure 4.6 (a, b). The measurements were repeated (figure 4.6 c, d) after an additional 40 days in air, during which time the films were subjected to a series of photoconductivity tests involving repeated exposure to an intense light from a Xe flash lamp (see section 5.2.5). Note that after the 40 days, the conductivity of the zones in positions $-1 < x < 1$ decreases, and that the decrease for the sodium free zones (about 10 fold) is much greater. This may be evidence of a photoelectronic instability (see section 5.2.4, final paragraph) . However, the shift in conductivity was not anticipated, so it is possible that other unknown effects (i.e. humidity, oxidation, etc.) during the 40 day storage period are responsible for the observed drop in conductivity.

The conductivity vs. temperature (measured after the flash tests described above) for a sodium doped and a sodium free zone at position $x = -0.762$ cm, is shown in figure 4.7 (a, b). Hall measurements could be obtained only for the sodium doped zone, with the result $p \cong 10^{15}$ cm^{-3} and $\mu_p \cong 2.5$ $cm^2V^{-1}s^{-1}$ at T=300 K. The mobility is similar to that of the single layer p-type films.

The conductivity of the two layer films (figure 4.6 a, b) shows much less dependence on x than the single layer film (figure 4.6 g) which encompasses the same conductivity range. Over the range -1.3 cm $< x < +1.3$ cm, (a) varies by 2.3 times, (b) by 1.7 times, and (g) by 6000 times. The explanation may be that, as described in section 2.4.3, the two layer film has segregated into a stoichiometric layer and an indium rich layer. Since the two layers are electrically in parallel, and the indium rich films have very low conductivity, the effective conductivity of the film is determined by the higher conductivity bottom stoichiometric layer. The two layer technique allows for the formation of a stoichiometric layer over a much larger F range than can be achieved with a single layer film. The intersection of curves (g) and (a) occurs at $x \cong -0.43$ cm, where $\sigma \cong 6 \times 10^{-4}$ $\Omega^{-1}cm^{-1}$ for both films. Assuming that the films have the same hole mobility ($\mu_p \cong 2.5$ $cm^2V^{-1}s^{-1}$), then $p \cong 1.5 \times 10^{15}$ cm^{-3} for both films. According to [5], stoichiometric single crystals have $p = 1.5 \times 10^{16}$ to 2×10^{17} cm^{-3} and $n = 1.8 \times 10^{15}$ to 5×10^{17} cm^{-3}. Thus it is reasonable to conclude that in the range -1.3 cm $< x < 1.3$ cm, the two layer film includes a bottom approximately stoichiometric layer, and that most of the variations in overall average film composition are incorporated into an indium rich top layer of varying composition and thickness. For $x < -1.3$ cm, the bottom layer becomes Cu-rich, so that the conductivity increases dramatically.

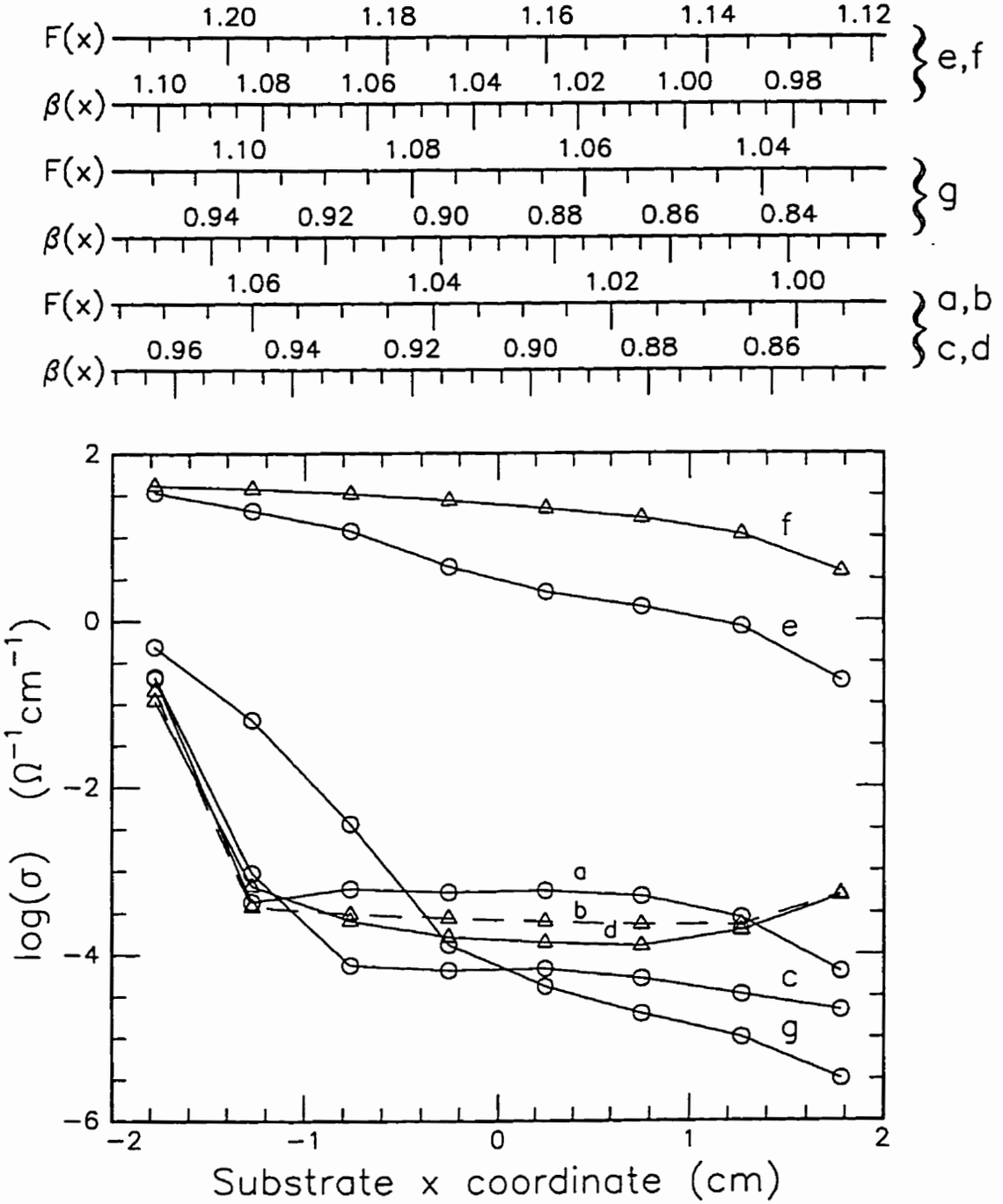

Figure 4.6

Conductivity vs. x of $CuInSe_2$ films on 7059 glass.

(a) 960308 y=−3.56
(b) 960308 y=−1.52 1% Na
(c) 960308 y=−3.56, *
(d) 960308 y=−1.52 1%Na, *
(e) 960309 y=−3.56
(f) 960309 y=−1.52 1% Na
(g) 960229 y=−1.52
(*: after flash test)

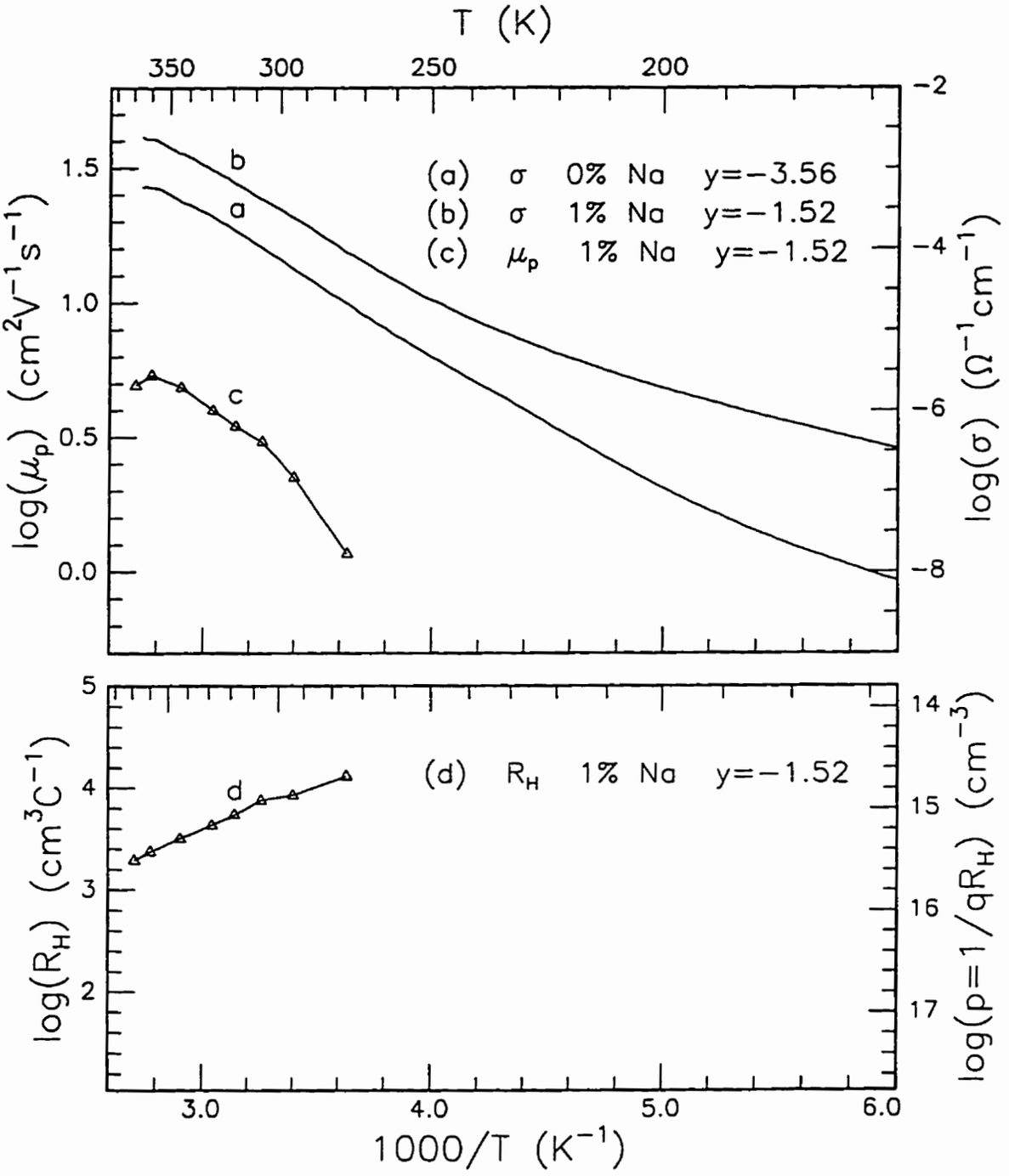

Figure 4.7

Electrical properties vs. temperature for two layer $CuInSe_2$ film 960308, x=−0.762 cm, F(x)=1.049. No Hall data for 0% Na, y=−3.56 cm, because the signal to noise ratio was too low.

4.4 References

1 B. Tell, J. L. Shay and H. M. Kasper, "Room temperature electrical properties of ten I-III-IV_2 semiconductors", J. Appl. Phys., **43**, 2469 (1972)

2 J. A. Groenink and P. H. Janse, "A generalized approach to the defect chemistry of ternary compounds", Z. Phys. Chem. N. F. **110**, 17 (1978)

3 H. J. Von Bardeleben, "The chemistry of structural defects in $CuInSe_2$", Solar Cells, **16**, 381 (1986)

4 H.Y. Ueng, H.L. Wang, "Defect structure of the nonstoichiometric Cu-III-VI_2 chalcopyrite semiconductors", *Non-Stoichiometry in Semiconductors*, edited by K.J. Bachmann, H.L. Hwang, C.Schwab (Elsevier, New York, 1992)

5 H. Neumann and R. D. Tomlinson, "Relation between electrical properties and composition in $CuInSe_2$ single crystals", Solar Cells, **28**, 301 (1990)

6 L.S. Yip, W.S. Weng, Z.A. Shukri, I. Shih and C.H. Champness,"Crystals of $CuInSe_2$ with controlled deviations from stoichiometry", *Non-Stoichiometry in Semiconductors*, edited by K.J. Bachmann, H.L. Hwang, C.Schwab (Elsevier, New York, 1992)

7 H. J. Koller, "Structure and defect chemistry of grain boundaries in $CuInSe_2$", Solar Cells, **31**, 77 (1991)

8 S. M. Wasim, "Transport properties of $CuInSe_2$", Solar Cells, **16**, 289 (1986)

9 R. Noufi, R. Axton, C. Herrington, and S. K. Deb,"Electronic properties vs. composition of thin films of $CuInSe_2$", Appl. Phys. Lett. **45**, 668 (1984)

10 T. Datta, S. Noufi and S. K. Dab, "Electrical conductivity of p-type $CuInSe_2$ thin films", Appl. Phys. Lett. **47**, 1102 (1985)

11 M. Verela, J. L. Morenza, J. Esteve and J.M. Codina, "Electrical conductivity of polycrystalline $CuInSe_2$ thin films", J. Phys. D: Appl. Phys., **17**, 2423 (1984)

12 L.L. Kazmerski, *Polycrystalline and Amorphous Thin Films and Devices*, (Academic Press, New York, 1980)

Chapter 5

Photoconductivity of $CuInSe_2$ Films

5.1 Thermal Effects

A preliminary test of the photoconductivity of film 960229 was carried out with 633 nm HeNe laser light, using the apparatus of figure 5.1 (a). It was observed that the higher conductivity zones do not rapidly reach a steady state current if the incident radiation is continuous. The current continues to increase, but at a decreasing rate. The current decays in a similar manner when the light is switched off The frequency response is determined by measuring the root mean square (RMS) value of the fundamental Fourier component of the current while varying the laser chopping frequency. Results are shown in the log-log plot of figure 5.2. The slopes of (a, b) and the low frequency portion of (c) are $-1/2$, so that the frequency dependence is of the form

$$I_p(\omega) \propto \omega^{-\frac{1}{2}}$$

None of the simple models of photoconductivity predict the observed form of the frequency dependence. The possibility that film conductivity is modulated by temperature variations due to film heating by the laser light was investigated.

In the simplest thermal model, the substrate and film are lumped together as a single thermal mass at uniform temperature with thermal capacitance C. The heat flow from the mass is proportional to the temperature difference between the substrate and the surroundings, and the constant of proportionality is the thermal conductance G.

$$\Delta T(\omega) \propto \frac{P}{G + j\omega C} \qquad (5.1)$$

This is the frequency response of a simple infra-red bolometer detector [1] with thermal time constant $\tau = C/G$ and incident power density P. At high frequencies, $\omega >> 1/\tau$, the model predicts that the temperature varies inversely with frequency. Therefore we need a different thermal model to explain the results of figure 5.2 (a, b, c).

We instead model the substrate as a semi-infinite solid occupying the half space $x > 0$, with the surface at $x = 0$. The one dimensional heat diffusion equation is

$$\frac{\partial^2 T}{\partial x^2} = \frac{1}{\kappa}\frac{\partial T}{\partial t} \qquad (5.2)$$

where $\kappa = K/\rho c$ (cm^2s^{-1}) is the thermal diffusivity , K ($WK^{-1}cm^{-1}$) is the thermal conductivity, ρ (gcm^{-3}) is the density and c ($JK^{-1}g^{-1}$) is the heat capacity. Solutions to

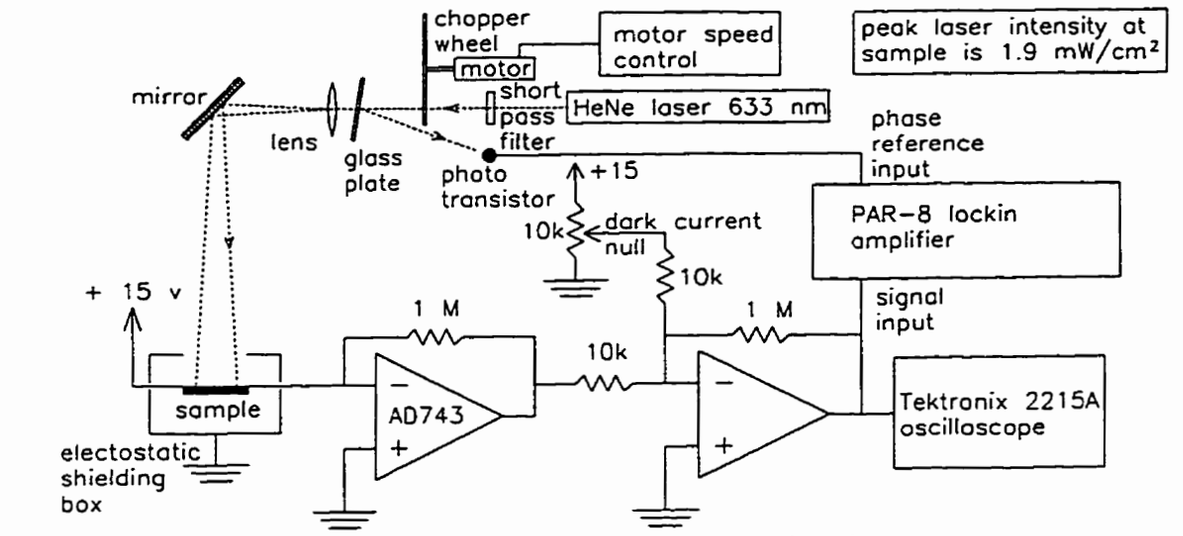

(a) Illumination of sample with light at variable chopping frequency

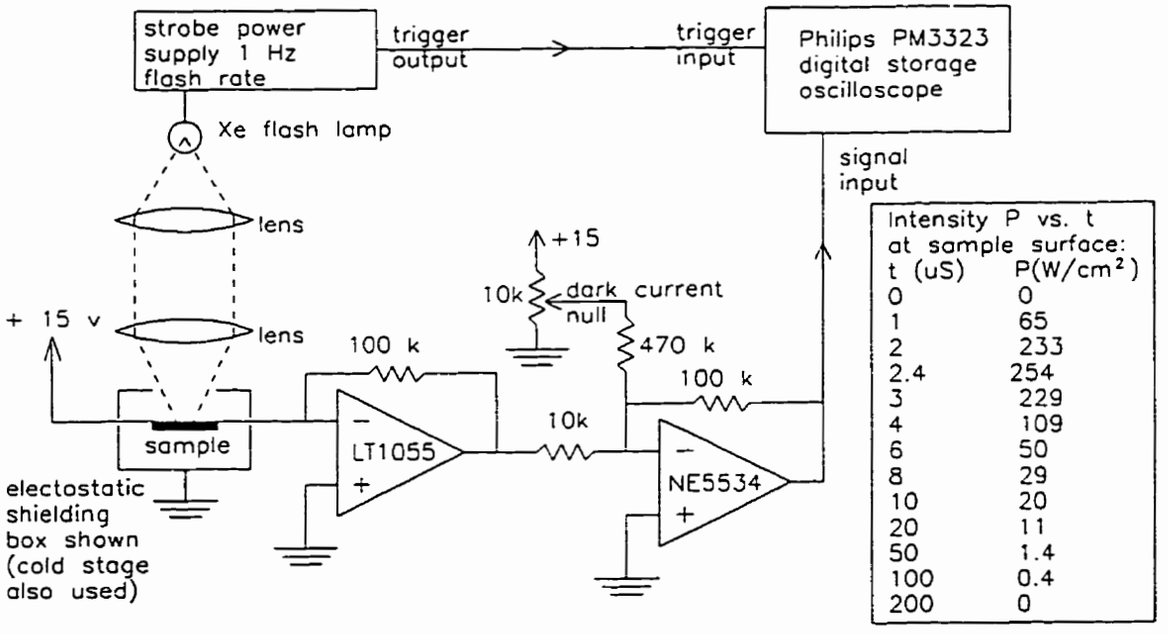

(b) Sample illuminated with Xe flash lamp, transient photocurrent recorded.

Figure 5.1

Photoconductivity tests:
(a) Apparatus for testing frequency response of CuInSe thin film photoconductivity. Variable chopper frequency. Lockin amplifier used for f > 2Hz, oscilloscope f < 2Hz
(b) Apparatus for measuring photoconductivity transient response. Xe flash lamp triggered at t=0. Laser and flash intensities as listed above right.

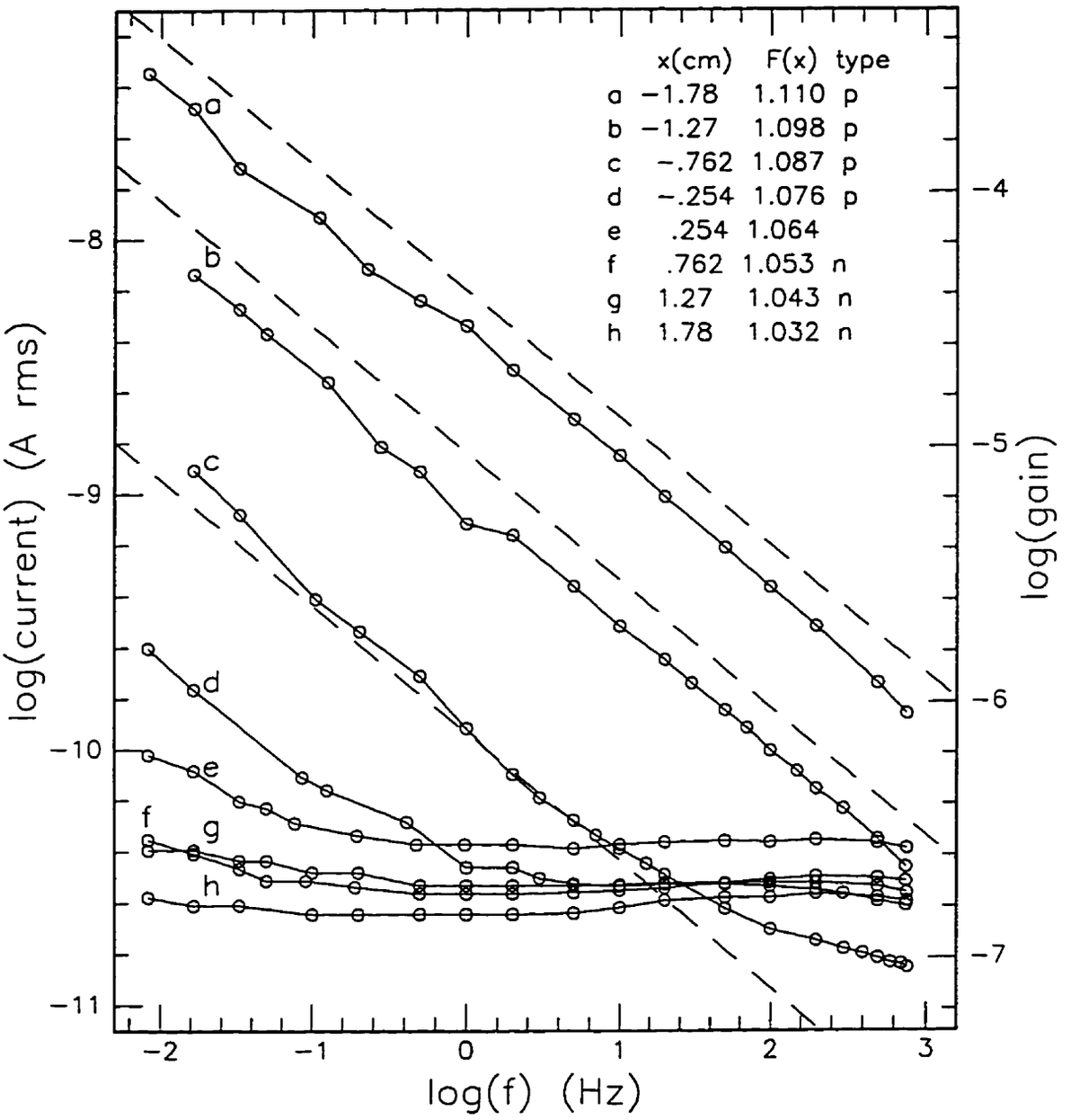

Figure 5.2

AC photocurrent vs. chopping frequency for single layer $CuInSe_2$ film 960229 at y=−1.52 cm. Laser intensity at 633 nm is P_0=1.9 mW/cm^2 (peak) Dashed lines are thermal calculations for a,b,c

equation 5.2 are presented in [2] for various boundary conditions at $x = 0$, assuming that $T(x \geq 0, t < 0) = T_0$. Define $\Delta T(x, t) = T(x, t) - T_0$ and consider the following cases.

Case 1

Boundary condition:

Instantaneous heat pulse input of energy per unit area U (Jcm^{-2}) at $x = 0$, $t = 0$.

Solution:

$$\Delta T(x,t) = \frac{U}{K}\sqrt{\frac{\kappa}{\pi t}}\exp\left(-\frac{x^2}{4\kappa t}\right) \qquad (5.3)$$

Case 2

Boundary condition:

Constant input power per unit area p at $x = 0$ for $t > 0$.

$$-K\frac{\partial T}{\partial x} = p \qquad \text{at } x = 0,\ t > 0$$

Solution:

$$\Delta T(x,t) = \frac{2p}{K}\left(\sqrt{\frac{\kappa t}{\pi}}\exp\left(-\frac{x^2}{4\kappa t}\right) - \frac{x}{2}\operatorname{erfc}\left(\frac{x}{2\sqrt{\kappa t}}\right)\right) \qquad (5.4)$$

Case 3

Boundary condition:

Input power per unit area p(t) at $x = 0$ for $t > 0$.

$$-K\frac{\partial T}{\partial x} = p(t) \qquad \text{at } x = 0,\ t > 0$$

Steady state solution (transient term not shown) for $p(t) = P\sin(\omega t)$ and $t > 0$:

$$\Delta T(x,t) = \frac{P}{K}\sqrt{\frac{\kappa}{\omega}}\exp\left(-x\sqrt{\frac{\omega}{2\kappa}}\right)\sin\left(\omega t - \frac{\pi}{4} - x\sqrt{\frac{\omega}{2\kappa}}\right) \qquad (5.5)$$

Case 4

Boundary condition:

Heat flow into the surface is proportional to the temperature difference between the region $x < 0$ at temperature g(t) and the surface at temperature T(0, t).

$$-K\frac{\partial T}{\partial x} = H(g(t) - T) \qquad \text{at } x = 0,\ t > 0$$

Steady state solution (transient term not shown) for $g(t) = T_0 + \Theta\sin(\omega t)$, $t > 0$:

$$\Delta T(x,t) = \frac{\Theta h}{\sqrt{(h+\Omega)^2 + \Omega^2}} \exp(-\Omega x)\sin\left(\omega t - \Omega x - \tan^{-1}\left(\frac{\Omega}{h+\Omega}\right)\right) \qquad (5.6)$$

Where $h = \frac{H}{K}$, $\Omega = \sqrt{\frac{\omega}{2\kappa}}$ and H ($Wcm^{-2}K^{-1}$) is the surface heat transfer coefficient.

Case 4 can be used to determine the film temperature during laser irradiation. Consider the glass substrate as a semi-infinite solid ($x > 0$, film surface in the $x = 0$ plane) initially at a uniform temperature T_0. The $CuInSe_2$ film is an absorbing surface layer with reflectance R at the laser wavelength, and negligible thickness. If the absorbed power per unit area from the laser is p(t), and the ambient temperature is T_A then the boundary condition is

$$-K\frac{\partial T}{\partial x} = H(T_A - T) + p(t) = H\left(T_A + \frac{p(t)}{H} - T\right) \qquad \text{at } x = 0,\ t > 0$$

Thus, the contribution of the laser is modeled as an equivalent temperature variation of the medium in the $x < 0$ half space.

The power per unit area absorbed on a surface of reflectance R due to the chopped laser beam (square wave, minimum 0, maximum intensity P_0) can be represented as a Fourier series:

$$p(t) = \frac{(1-R)P_0}{2}\left(1 + \frac{4}{\pi}\sum_{\substack{n \\ odd}}\frac{1}{n}\sin(n\omega t)\right)$$

The boundary condition becomes

$$-K\frac{\partial T}{\partial x} = H\left(T_A + \frac{(1-R)P_0}{2H} + \frac{2(1-R)P_0}{\pi H}\sum_{\substack{n \\ odd}}\frac{1}{n}\sin(n\omega t) - T\right) \qquad \text{at } x = 0,\ t > 0$$

Therefore the combination of the time dependent power input from the laser, and the heat flow due to the temperature difference between the surface $x = 0$ at temperature $T(0,t)$ and the region $x < 0$ at temperature T_A, can be represented as an equivalent time varying temperature g(t) of the region $x < 0$ given by

$$g(t) = T_0 + \frac{2(1-R)P_0}{\pi H}\sum_{\substack{n \\ odd}}\frac{1}{n}\sin(n\omega t)$$

where T_0 has been chosen such that

$$T_0 = T_A + \frac{(1-R)P_0}{2H}$$

Since the heat diffusion equation is linear, the complete steady state solution to the equation is the sum of the steady state solutions for each Fourier component of g(t).

$$\Delta T(x,t) = \frac{2(1-R)P_0}{\pi K}\sum_{\substack{n \\ odd}} \frac{1}{n\sqrt{\left(h+\sqrt{n\Omega}\right)^2 + n\Omega^2}} \exp(-\sqrt{n\Omega}x)\sin\left(n\omega t - \sqrt{n\Omega}x - \tan^{-1}\left(\frac{\sqrt{n\Omega}}{h+\sqrt{n\Omega}}\right)\right)$$

The small temperature oscillation at x = 0 causes a variation in the film conductivity, and a corresponding modulation of the current flowing through the film. The film conductivity, and its temperature derivative, can be written as

$$\sigma(T) = \sigma_\infty \exp\left(-\frac{E_a}{k_B T}\right)$$

$$\frac{d\sigma}{dT} = \frac{\sigma E_a}{k_B T^2}$$

Therefore, at temperature $T(t) = T_0 + \Delta T(0, t)$, the conductivity of the film is

$$\sigma(t) = \sigma(T_0)\left(1 + \frac{E_a}{k_B T_0^2}\Delta T(0,t)\right)$$

The current flowing through the film of thickness d, width L_x, length L_y, and with applied voltage V is

$$I(t) = \frac{VdL_x\sigma(T_0)}{L_y}\left(1 + \frac{E_a}{k_B T_0^2}\Delta T(0,t)\right)$$

The RMS current component at ω due to the film temperature variation is

$$I_{RMS}(\omega) = \frac{\sqrt{2}dL_x V E_a (1-R)P_0\sigma(T_0)}{\pi k_B T_0^2 L_y K\sqrt{(h+\Omega)^2+\Omega^2}} \qquad (5.8)$$

For the case where $\Omega >> h$, or equivalently $\omega >> 2\kappa h^2$ the current is

$$I_{RMS}(\omega) \cong \frac{\sqrt{2}dL_x V E_a (1-R)P_0\sigma(T_0)}{\pi k_B T_0^2 L_y K}\sqrt{\frac{\kappa}{\omega}} \qquad (5.9)$$

Equation 5.9 can also be obtained from equation 5.5 by using just the time dependent (AC) component of the laser power as the boundary condition in case 3 above.

Corning 7059 barium borosilicate glass has the following thermal properties.

$K = 9.95\text{x}10^{-3}$ $Wcm^{-1}K^{-1}$ [3]

$\rho = 2.76$ gcm^{-3} [3]

$c = 0.753$ $Jg^{-1}K^{-1}$ [4]

From the above quantities, the thermal diffusivity can be calculated.

$$\kappa = \frac{K}{\rho c} = 4.79 \times 10^{-3} \quad cm^2 s^{-1}$$

When the surface $x = 0$ is in air, heat transfer is by radiation and convection. The radiation heat transfer per unit time per unit area for a body at T surrounded by a black body at T_0 is given by

$$s\varepsilon(T^4 - T_0^4)$$

where s is the Stefan-Boltzmann constant and ε is the emissivity of the surface. For small temperature differences, this can be approximated by a linear relationship given by

$$s\varepsilon(T^4 - T_0^4) \cong 4s\varepsilon T_0^3 (T - T_0) = H_r (T - T_0)$$

For $T_0 = 293$ K and $\varepsilon = 1$, we have

$H_r = 5.7 \times 10^{-4}$ $Wcm^{-2}°C^{-1}$

The heat transfer coefficient by free convection with air is

$H_c \cong 2\text{–}4 \times 10^{-4}$ $Wcm^{-2}°C^{-1}$ [2,5]

The combined heat transfer coefficient is $H = H_c + H_r$, approximated by

$H \cong 10^{-3}$ $Wcm^{-2}°C^{-1}$

Therefore,

$$h = \frac{H}{K} \cong 0.1 \text{ cm}^{-1}$$

The other parameters are

$d = 2.566 \times 10^{-4}$ cm; $L_x = 0.27$ cm; $L_y = 1.3$ cm; $V = 15$ volts; $R = 0.25$

$P_0 = 1.9 \times 10^{-3}$ Wcm^{-2}

The RMS current at frequency $\omega = 2\pi f$ can now be evaluated, using equation 5.8 or 5.9. For the frequency range of figure 5.2, $2\pi f >> 2\kappa h^2 \cong 10^{-4}$ s^{-1} and equation 5.9 gives

$$I_{RMS}(f) \cong 192 \frac{E_a \sigma(T_0)}{\sqrt{f}} \qquad (10^{-9} A)$$

with E_a in eV, $\sigma(T_0)$ in $\Omega^{-1}cm^{-1}$, and f in Hz.

The thermally induced currents for the three highest conductivity zones of film 960229 are calculated for $T_0 = 293$ K using the σ and E_a data of figure 4.2 (f, g, h) and equation 5.8. (equation 5.9 could also be used in this frequency range). The calculated currents are

plotted in figure 5.2. The $\omega^{-1/2}$ frequency dependence of the calculated currents is in good agreement with the experimental results of figure 5.2 (a, b), which suggests that the currents observed for the two highest conductivity zones are thermally induced by laser heating. The calculated magnitudes of the currents in the two high conductivity zones are about 50% greater than the measured magnitudes. This may be due to systematic error introduced by neglecting the $CuInSe_2$ film thickness and thermal properties in the derivation of equation 5.8, and/or uncertainties in the values of the various parameters in equation 5.8. For the zones with intermediate dark conductivities (figure 5.2 c, d, e), a transition from $\omega^{-1/2}$ frequency dependence (thermal effects) to approximate frequency independence (photoconductivity) is observed as the laser chopping frequency is increased. The currents observed at the three zones with the lowest dark conductivities (figure 5.2 f, g, h) are nearly frequency independent, indicating that photoconductivity dominates over the entire chopping frequency range. Thermally induced currents are significant only for poor photoconductors with very low gain and high dark conductivity.

The temperature frequency response of a thin film on a substrate has been analyzed in a somewhat different way in [6]. At high frequencies, the effective conductance G_e and effective thermal capacitance C_e of the top layer of the substrate, of thickness equal to the thermal diffusion length $1/\Omega$ (see equation 5.6), determine the surface temperature. The effective values of conductance and capacitance are then used in the lumped mass model (equation 5.1). Since $G_e \propto \Omega$ and $C_e \propto 1/\Omega$ and $\Omega \propto \omega^{1/2}$, we obtain $\Delta T(\omega) \propto \omega^{-1/2}$.

5.2 Photoconductivity

5.2.1 Photoconductivity Model

In figure 5.2, the photo response of the $CuInSe_2$ films is measured in units of photoconductivity gain, as well as in amperes. The usual definition of photoconductivity gain [7] is the ratio of the excess carrier particle current through the sample to the total carrier generation rate in the sample. Since the reflectance and absorption spectra of $CuInSe_2$ are not known precisely, the generation rate cannot be accurately determined at all wavelengths. We therefore define a practical photoconductivity gain given by

$$\text{gain} = \frac{\text{excess carrier particle current (electrons + holes / s)}}{\text{incident photon particle current (photons / s)}}$$

At photon energies greater than the $CuInSe_2$ band-gap, the light is strongly absorbed, and if we neglect reflection, the generation rate can be assumed equal to the incident photon current. In this case, the above two definitions of photoconductivity gain are equivalent.

The gain is not an intrinsic property of the photoconductor material. It depends on the applied voltage and the electrode separation, and for any given sample dimensions, it is proportional to the change in conductivity $\Delta\sigma$ due to the incident light.

As discussed in chapter 4, the effect of energy barriers at grain boundaries on carrier transport is contained in an effective film mobility with exponential dependence on barrier height. Illumination increases the film conductivity by increasing the free carrier density and/or reducing the height of the energy barriers at grain boundaries. Following the method of [8] and assuming a p-type sample, we have

$$\sigma = qp\mu_f = qp\mu_b \exp\left(-\frac{q\phi}{kT}\right) \qquad (5.10)$$

The change in conductivity $\Delta\sigma$ due to illumination is given by

$$\Delta\sigma = q\mu_f \Delta p + qp\Delta\mu_f = q\mu_f p\left(\frac{\Delta p}{p} - \frac{q\Delta\phi}{kT}\right) \qquad (5.11)$$

The mobility barrier is due to trapped charge at the grain boundaries which cause band bending and depletion layers in the adjacent grains. Using Gauss's law, the width of the depletion layers W in two adjacent grains can be expressed as a function of the net surface charge density qN_s (assumed positive) and the net acceptor density N_A in the grains.

$$2N_A W = N_S \qquad (5.12)$$

The grains are said to be partially depleted or fully depleted, depending on whether the depletion layer width is less than or greater than the grain size. According to a recent study of 0.5 to 1 μm thick $CuInSe_2$ films deposited on glass [9], the depletion layer width varies from 6 nm to 22 nm, as the Cu/In ratio is reduced from 1.2 to 0.4. The depletion layer widths are much less than the 100 to 400 nm typical grain sizes reported in [9] , so the grains are only partially depleted.

For partially depleted grains, the potential barrier height ϕ is obtained by integrating Poisson's equation across the depletion region width, and then using equation 5.12 for W.

$$\phi = \frac{qN_A W^2}{2\varepsilon} = \frac{qN_S^2}{8\varepsilon N_A} \qquad (5.13)$$

In illuminated p-$CuInSe_2$ films, minority carriers (electrons) generated within a minority carrier diffusion length of the depletion region diffuse to the edge of the depletion region, then are drawn to the grain boundary by the depletion region electric field. The electrons recombine with trapped holes at the grain boundary. The hole traps are assumed positively charged when occupied, so the electrons reduce the net surface charge density

qN_s at the grain boundary. Using equation 5.13, the change in barrier height due to the change $q\Delta N_S$ in the net surface charge density is given by

$$\Delta\phi = \frac{qN_S\Delta N_S}{4\varepsilon N_A} \qquad (5.14)$$

Substitute $\Delta\phi$ in 5.11, and taking $p \cong N_A$, we obtain

$$\Delta\sigma = q\mu_f\left(\Delta p - \frac{q^2N_S\Delta N_S}{4\varepsilon kT}\right) \qquad (5.15)$$

This equation predicts that the photoconductivity gain is independent of the equilibrium carrier concentration, and proportional to the film mobility. Note that ΔN_S is negative, so that the second term in equation 5.15 makes a positive contribution to $\Delta\sigma$.

5.2.2 Measurement of Photoconductivity Spectra

The apparatus used for the measurement of photoconductivity spectra is shown in figure 5.3. The Cary 17 spectrophotometer includes a high intensity tungsten-halogen white light source, and a precision scanning monochromator. The output from the monochromator is chopped at 30Hz, and split into two identical beams. The probe beam is extracted from the spectrophotometer and focused by a spherical mirror onto the film zone to be tested. The reference beam is incident on a PbS photoconductive cell, with photocurrent proportional to the incident photon flux. A fixed bias potential (14 V) is applied to the film zone and the AC photocurrent through the film is amplified by a low noise AC current preamplifier. The output of the preamplifier is connected to the lock-in amplifier signal input. Low noise AC signal processing techniques are necessary because the typical photocurrent is very small ($I_p < 10^{-9}$ A rms). The lock-in phase reference input is derived from the beam chopper inside the spectrophotometer. The monochromator changes the output wavelength at a precise rate (1 nm/s, typically) while the data acquisition computer records the lock-in amplifier DC output signal and the PbS cell reference signal, at a fixed time interval (5 s, typically). The PbS cell is calibrated at 633 nm using a reference Si photo-diode of known quantum efficiency [10]. The photoconductive gain of the PbS cell is assumed to be constant over the wavelength range, and the reference signal from the PbS cell is used to normalize the film photocurrent by the incident light intensity. Normalization is essential because of the large and abrupt variations in monochromator output intensity, as shown in figure 5.4. The peaks in intensity at 980 and 1266 nm are diffraction grating anomalies (Wood's anomalies), which occur when a diffraction order, other than the one used, diffracts at 90° to the grating surface normal [11].

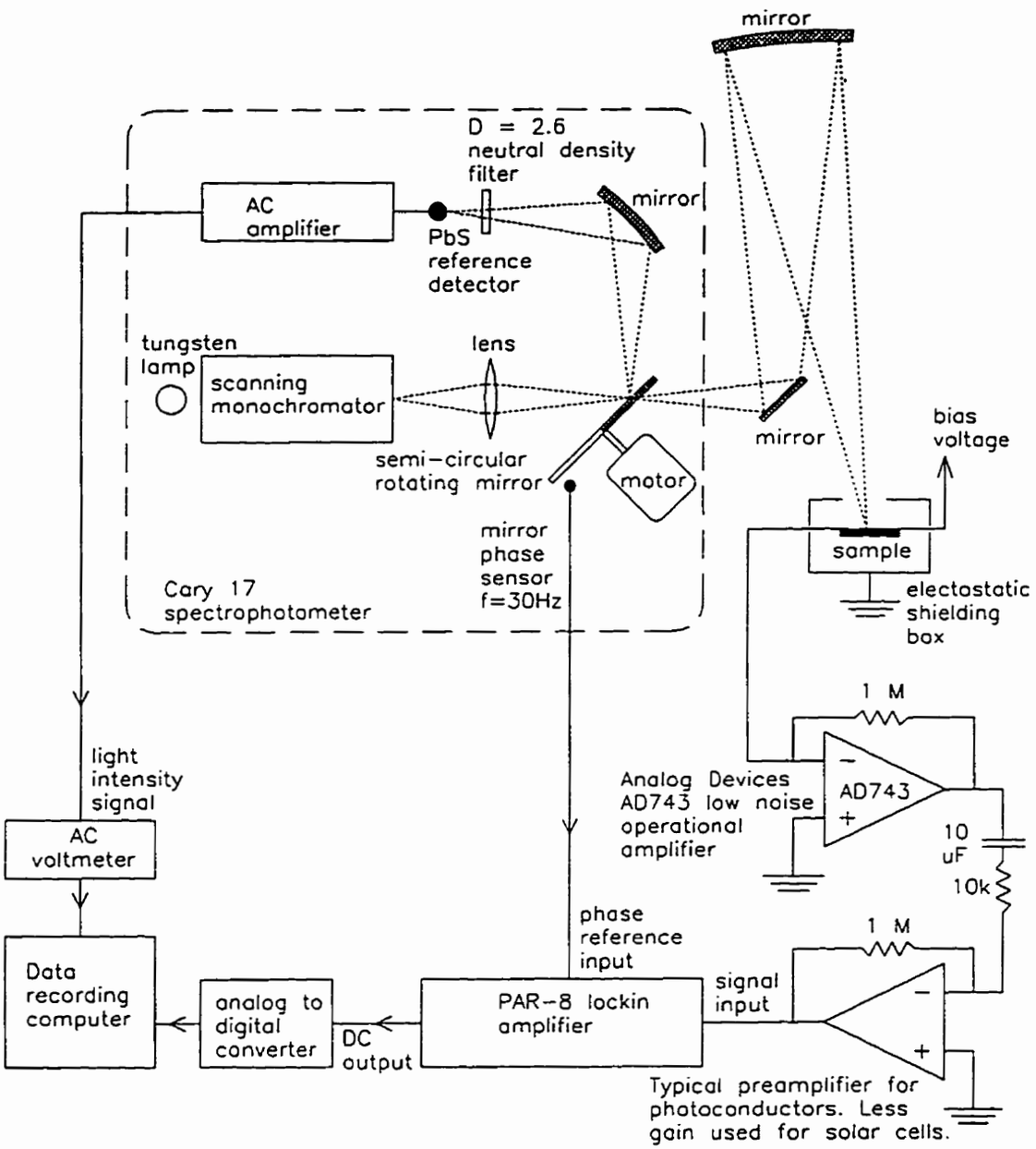

Figure 5.3

Schematic diagram of the system used for measurement of thin film photoconductivity spectra and solar cell spectral response. A simplified, but functionally equivalent diagram of the Cary 17 optical system is shown. Sample bias +15 volts for photoconductor test, typ. 0 volts for solar cell test. Neutral density filter added to reference beam to prevent saturation of PbS detector at highest beam intensities.

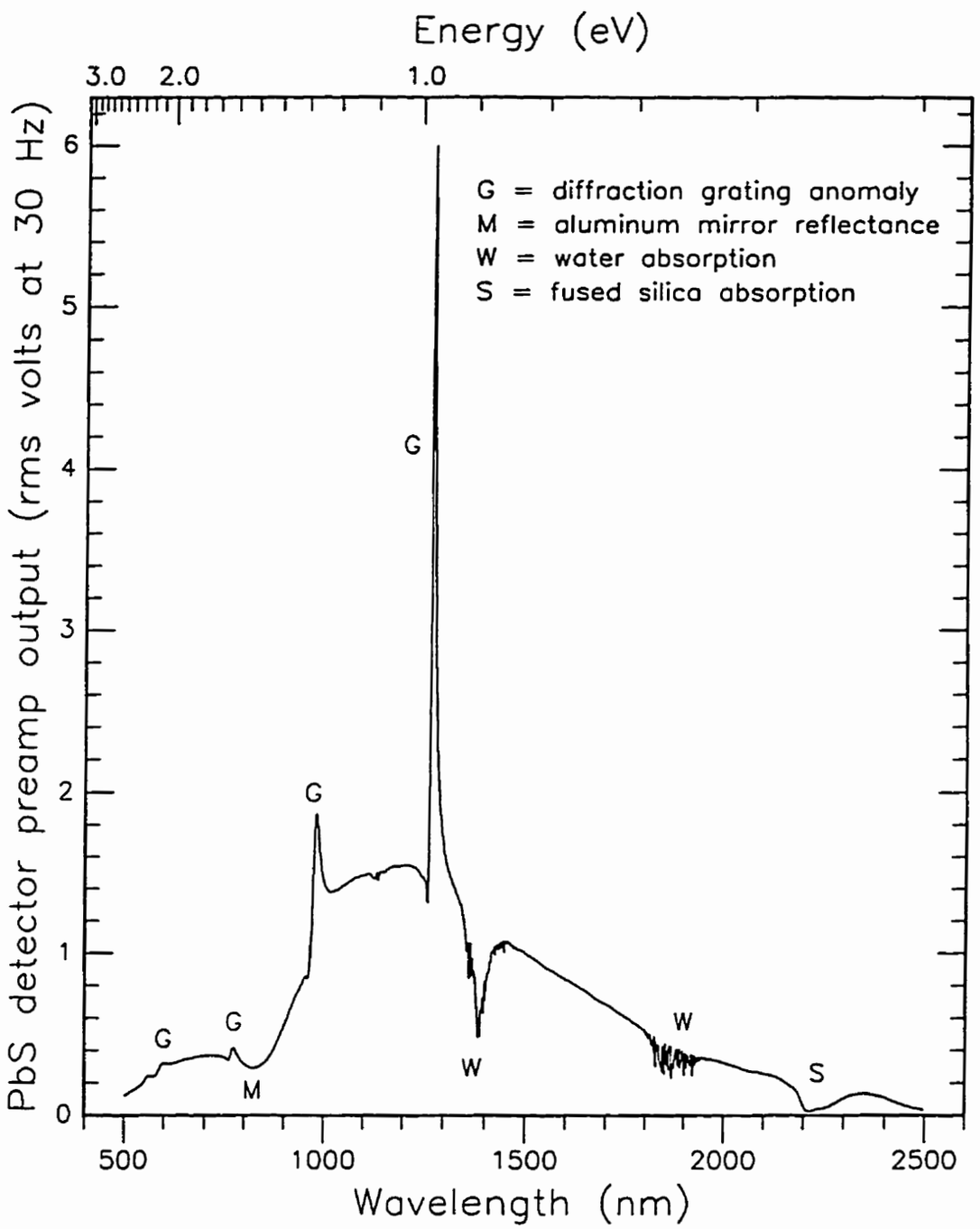

Figure 5.4

Cary 17 spectrophotometer reference beam intensity vs. wavelength as measured by PbS detector inside Cary 17 Monochromator passband 0.5 nm. Black body spectrum altered by grating anomalies, absorption, and mirrors.

5.2.3 The Photoconductivity Spectrum of a Single Layer Film

The photoconductivity spectra for 8 zones of film 960229 are shown in figure 5.5. The spectra for the two highest conductivity zones (figure 5.5 a, b) do not represent true photoconductivity because, as shown in figure 5.2, thermal effects dominate at the 30 Hz chopping frequency. The relative strength of the signals (a, b) is also consistent with this interpretation. The lower conductivity zones show the expected spectral response, with the signal decreasing rapidly for energy below about 1 eV (figure 5.5, c-h). The anomalous features in the photoconductivity spectra at 980 and 1266 nm are due to imperfect normalization of the spectrophotometer intensity peaks at those wavelengths.

5.2.4 The Photoconductivity Spectrum of a Two Layer Film

The photoconductivity spectra for 16 zones of two layer film 960308 are shown in figures 5.6 and 5.7. Film 960308 was deposited with one half ($y > -2.54$ cm), 1% sodium doped, and the other half, ($y < -2.54$ cm), not doped. This two layer film has about 100 times higher photoconductivity gain than the single layer film 960229. As a result, the thermal effects discussed in section 5.1 are negligible at the 30 Hz chopping frequency, with the possible exception of the two high conductivity Cu-rich zones at $x = -1.78$ cm (see figure 4.6). The spectra at zones in the sodium free half (figure 5.6), and the corresponding zones in the sodium doped half (figure 5.7), are quite different in form. The sodium doped zones have pronounced gain maxima at $\lambda \cong 1225$ nm (1.012 eV), whereas the gain increases steadily with increasing energy in the sodium free zones. Igalson [12], shows a p-$CuInSe_2$ thin film (substrate not specified) spectrum similar to figure 5.6 (c) and a p-$CuInSe_2$ single crystal spectrum similar to figure 5.7 (c). Kazmerski [13] reports a peak at 1.04 eV for an n-type film (substrate not specified) of thickness 2 μm with 1 μm grains. The wavelength at the peak is assumed to correspond to the $CuInSe_2$ energy gap, and the change in the peak wavelength with temperature is used to determine the temperature dependence of the energy gap. Isomura [14] reports a peak at 1.01 eV for some n-type films deposited on "slide" (soda-lime?) glass. According to Slifkin [15], the spectrum of an n-type $CuInSe_2$ single crystal has a weak, broad maximum at 1.25 eV. When the crystal is converted to p-type by annealing under maximum Se pressure, a very sharp maximum appears at 0.98 eV, having about ten times greater gain than the weak maximum at 1.25 eV. DeVore [16] developed an idealized model of the photoconductivity vs. absorption coefficient for a uniform (i.e. single crystal) slab of semiconductor with arbitrary thickness, surface recombination velocity, diffusion constant and bulk lifetime. When the surface recombination rate exceeds the volume recombination rate, the model predicts a photoconductivity peak at wavelengths for which the sample thickness is a few times greater than the absorption length, similar to the observed photoconductivity spectrum of

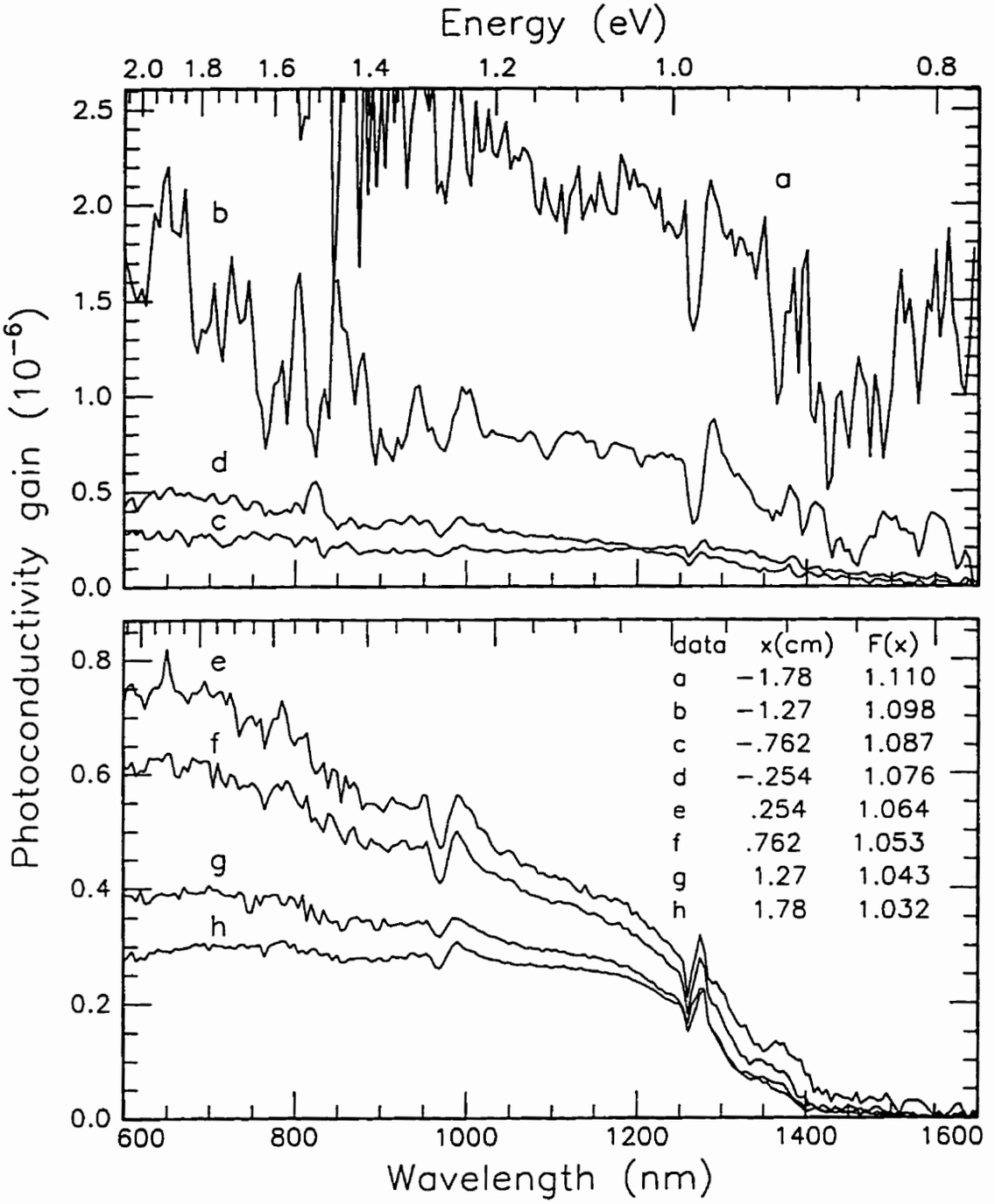

Figure 5.5

Photoconductivity spectra at different x positions for single layer $CuInSe_2$ film 960229 at y=−1.52 cm. Monochromator passband 10 nm; Chopping frequency 30 Hz; Film temperature 22°C.

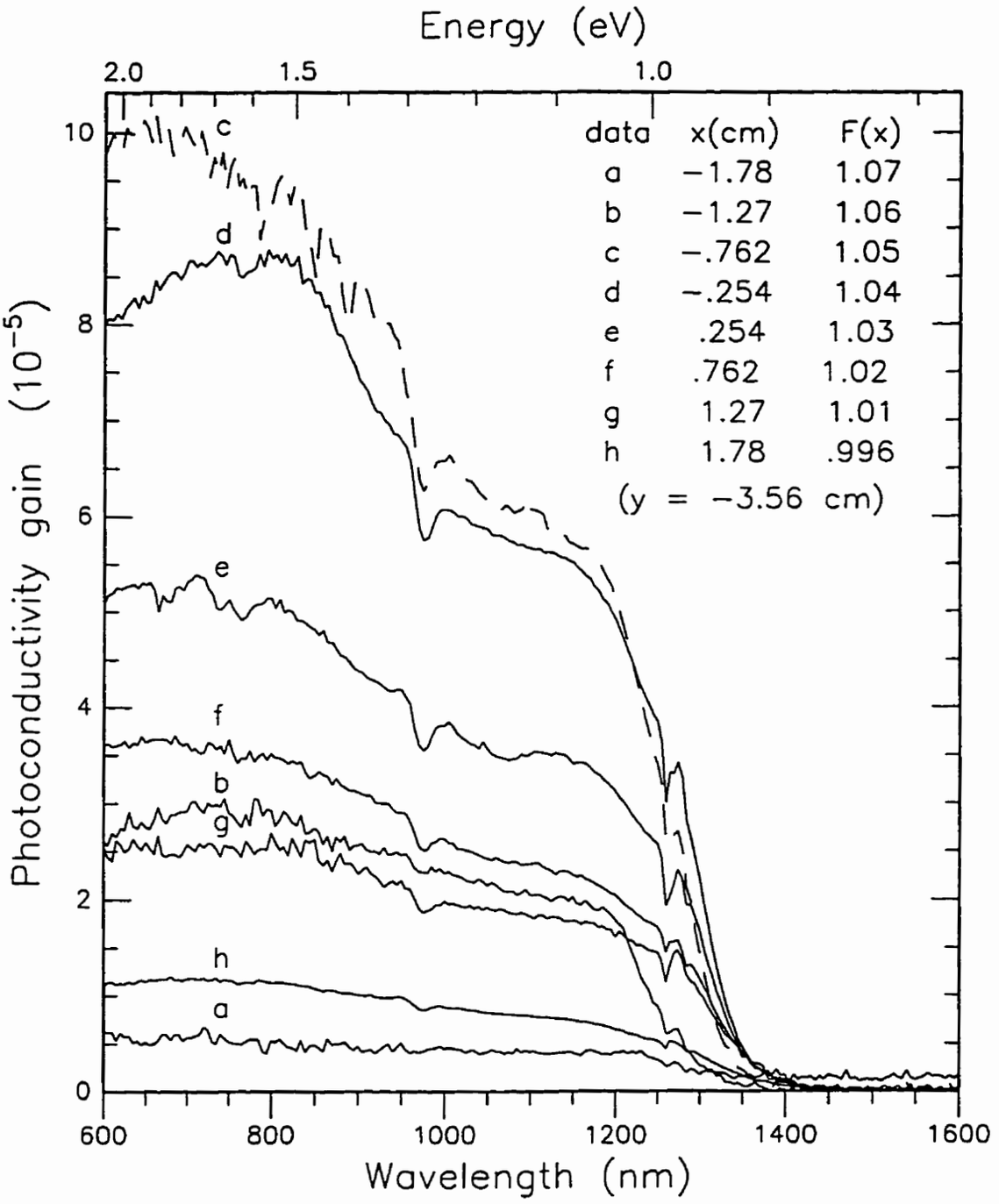

Figure 5.6

Photoconductivity spectra at different x for two layer $CuInSe_2$ film 960308 without Na doping. Monochromator passband 10 nm; Chopping frequency 30 Hz; Temperature 22°C; V_{bias}=14 V

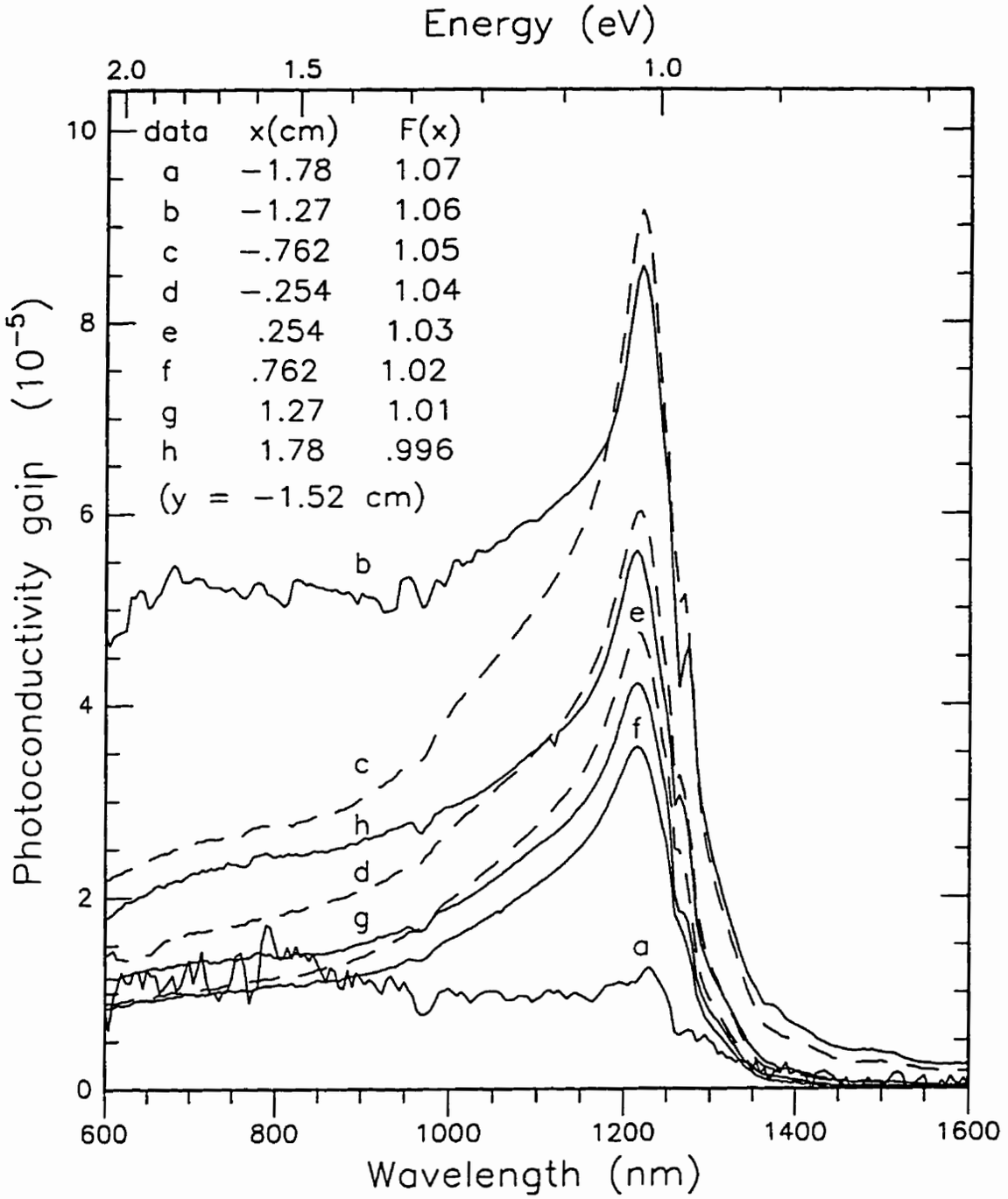

Figure 5.7

Photoconductivity spectra at different x for two layer $CuInSe_2$ film 960308 with 1% Na doping. Monochromator passband 10 nm; Chopping frequency 30 Hz; Temperature 22°C; V_{bias}=14 V

the sodium doped $CuInSe_2$ film. In other words, in equation 5.11, it seems that the excess carrier concentration term ($\propto \Delta p$), not the grain boundary potential barrier reduction term ($\propto \Delta\phi$), dominates the photoconductivity $\Delta\sigma$ of the sodium doped film at longer wavelengths. An attempt was made to try to estimate the bulk majority carrier lifetime using the DeVore model, but reasonable fits were obtained only at unrealistic values of the diffusion coefficient (too small) and lifetime (too long), probably because the DeVore model does not include the effects of minority carrier trapping and grain boundaries. Slifkin finds reasonable agreement with the DeVore model only for n-$CuInSe_2$ single crystals which have been sensitized by annealing in the presence of $CuInSe_2$ powder for 2 hours at 600 °C, whereas the photoconductivity of the as-grown crystals is controlled by a very thin (70 to 80 nm) surface layer [17].

The photoconductivity gain is reduced when a film is simultaneously illuminated with a bias light source at a strongly absorbed wavelength (633 nm). The spectra with and without bias illumination at x = –0.76 cm are shown in figure 5.8 (top), for the sodium doped and sodium free zones. The ratio of gain with bias to the gain without bias light is shown in figure 5.8 (bottom). We see that the gain of the sodium free film is much more sensitive to bias light. This suggests that, in the sodium free film, the bias light neutralizes many of the grain boundary hole traps which would otherwise contribute to the energy barrier photoconductivity term in equation 5.11. In the sodium free film, the gain ratio varies little with wavelength, so the energy barrier term probably dominates the photoconductivity at all wavelengths. In the case of the sodium doped film, the gain ratio approaches one at the weakly absorbed wavelengths, indicating that the excess carrier term may be dominant at longer wavelengths.

The low short wavelength response of the sodium doped film may be due to a very high recombination velocity at the film top surface. Segregation of sodium to the film surface has been observed [18, 19] and this may affect the surface recombination velocity.

The electron microscope images and the specular reflectance, transmittance, and x-ray diffraction data of chapter 3 indicate that the sodium doped films have more oriented, closely packed grains. The morphology of a film may influence the photoconductivity spectrum.

Zones x = –1.27 cm and –0.76 cm of the sodium doped film have significant gains at photon energies below the $CuInSe_2$ energy gap, as seen in figure 5.7 (b, c), whereas the corresponding sodium free zones do not. This is possibly due to electron transitions from the valence band to electron trap levels near the conduction band. A fraction of the trapped electrons is thermally released to the conduction band, and the remainder recombine with free holes. The free carrier lifetimes are determined by recombination via

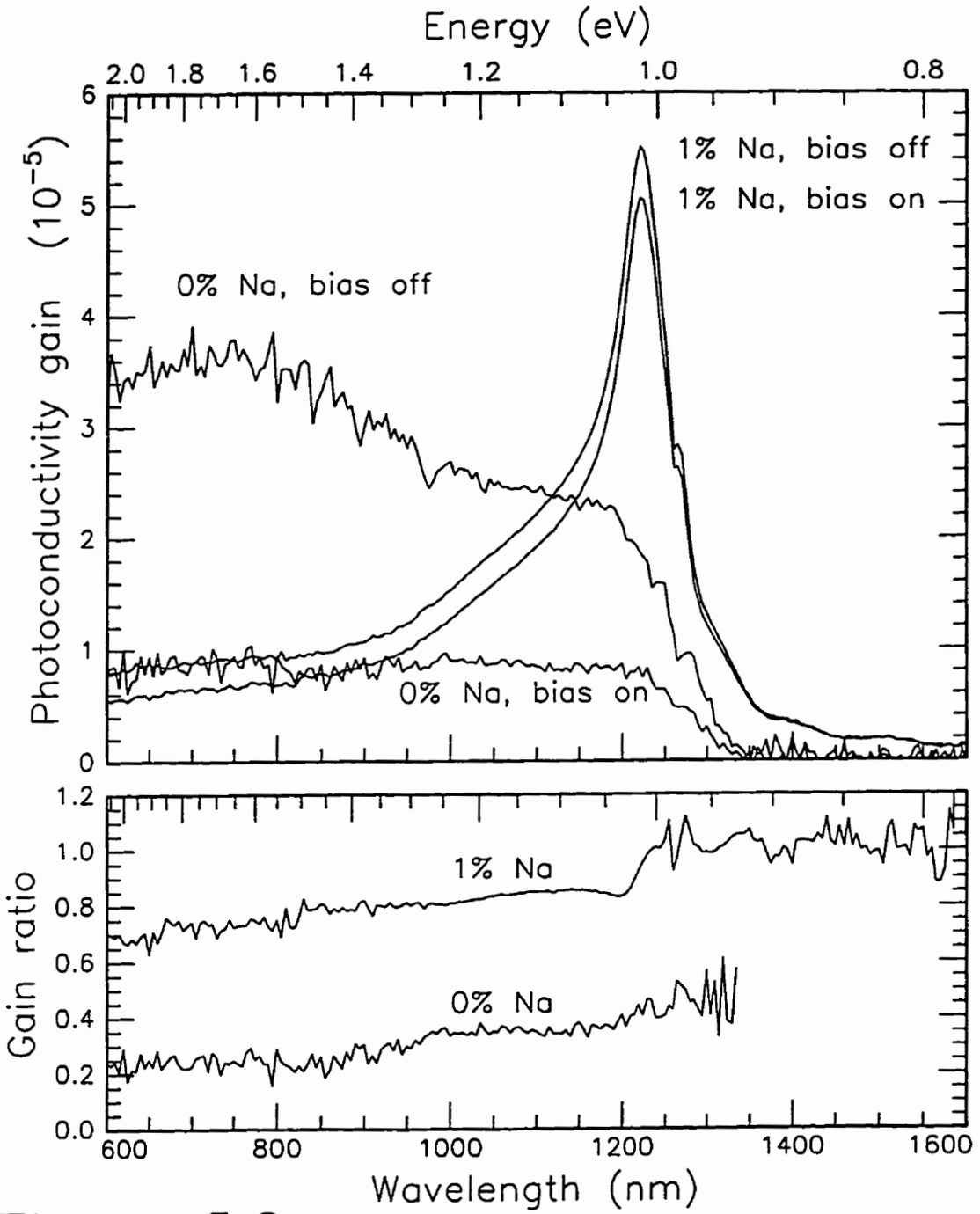

Figure 5.8

Top: photoconductivity spectra of $CuInSe_2$ film 960308 with or without DC bias light and 0% Na or 1% Na. Bottom: Ratio of gain with to gain without bias light Bias light intensity 2 $mWcm^{-2}$ at 633 nm x=−0.76 cm; y=−3.56 (0% Na) or y=−1.52 (1% Na)

other (deeper) gap states. We assume that holes are the majority carrier in the photoconductivity. The p-$CuInSe_2$ single crystal spectrum [12] also shows significant gain below the band gap energy. Note that a slight maximum is seen in figure 5.7 (b, c) at λ = 1500 nm (0.826 eV). This is probably due to thin film interference effects (see figure 3.11 (b)). However, a weak peak at 0.82 eV due to an unspecified impurity has been reported in the photoconductivity spectrum of n-$CuInSe_2$ single crystals [17].

The photoconductivity spectrum of zone x = –0.76 cm of the sodium doped film at various temperatures is shown in figure 5.9. The peak photoconductivity gain increases with temperature to a maximum at about 30 °C then decreases slowly. This is somewhat similar to the mobility temperature dependence of this film zone, as shown in figure 4.7 (c). The gains at photon energies well below the band gap (i.e. $\lambda > 1225$) approach zero at low temperatures. For short wavelengths (say 700 nm), the light is strongly absorbed and most generation takes place at the top surface of the film, so that the surface recombination rate limits the number of carriers available that can contribute to Δp and ΔN_s. Assume that at 700 nm, the surface recombination rate, Δp and ΔN_s are approximately temperature independent. Then, according to equation 5.15, the temperature dependence of $\Delta\sigma$ at 700 nm is controlled mainly by the film mobility μ_f. Thus the photoconductivity gain at 700 nm can be used to normalize the gain at long wavelengths, so as to approximately remove the mobility temperature dependence. The normalized gain at several long wavelengths vs. temperature is graphed in figure 5.10. For photon energies less than the energy gap, the thermal activation energy of the normalized gain vs. temperature should be roughly equal to the energy of the electron traps filled by the incident light. This trap energy should also be about equal to the difference between the band-gap energy and the incident photon energy. The calculated trap energies for $\lambda > 1225$ (see the table in figure 5.10) are in fair agreement with this reasoning. The thermal activation energy at λ = 1225 nm can be interpreted as being due to a shallow level which changes from a recombination center to a trap as the temperature is increased.

It should be noted that the photoconductivity gain in figures 5.8 and 5.9 is significantly lower ($\approx$2 ×) than the gain in figures 5.6 and 5.7. The data of figures 5.6 and 5.7 were measured before the flash photocurrent decay experiments described in section 5.2.5 below, whereas the data of figures 5.8 and 5.9 were recorded after the flash experiments. The decrease in dark conductivity after the flash experiments has been noted in section 4.3. The samples were illuminated with short white light pulses ($\cong$ 5 μs) from a Xe flash lamp, with peak intensities of about 250 Wcm^{-2} ($\cong$ 2500 suns). The room temperature decay measurements were conducted in air, and each film zone was exposed to hundreds of flashes. It is possible that the flash energy has an annealing effect, similar to a heat treatment in air, so that some electrically active defects are passivated by oxygen. In

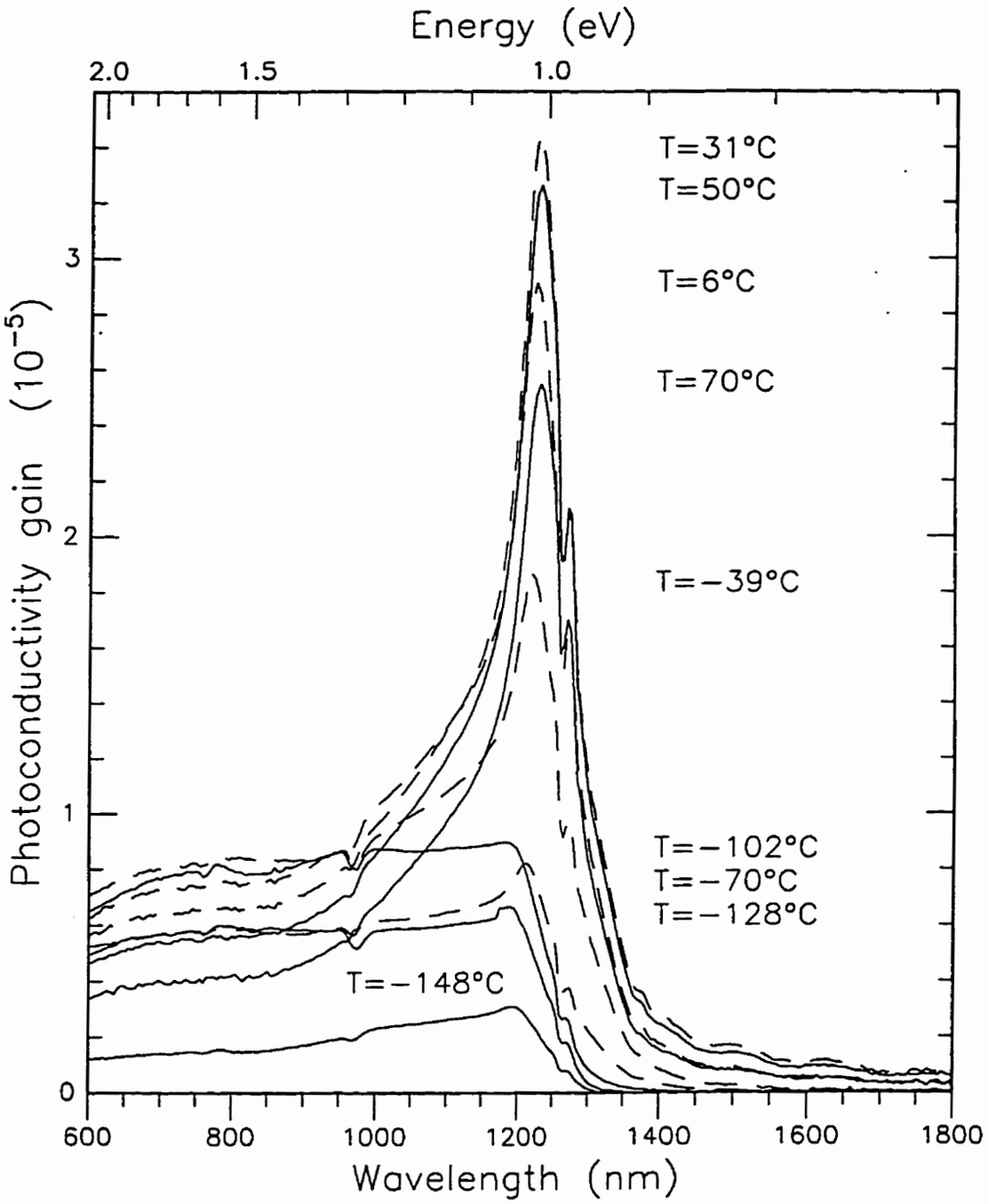

Figure 5.9

Photoconductivity spectra at different temperatures for two layer $CuInSe_2$ film 960308 with 1% Na. Monochromator passband 10 nm; Chopping frequency 30 Hz; x=−.76, y=−1.52 cm; V_{bias}=14 V.

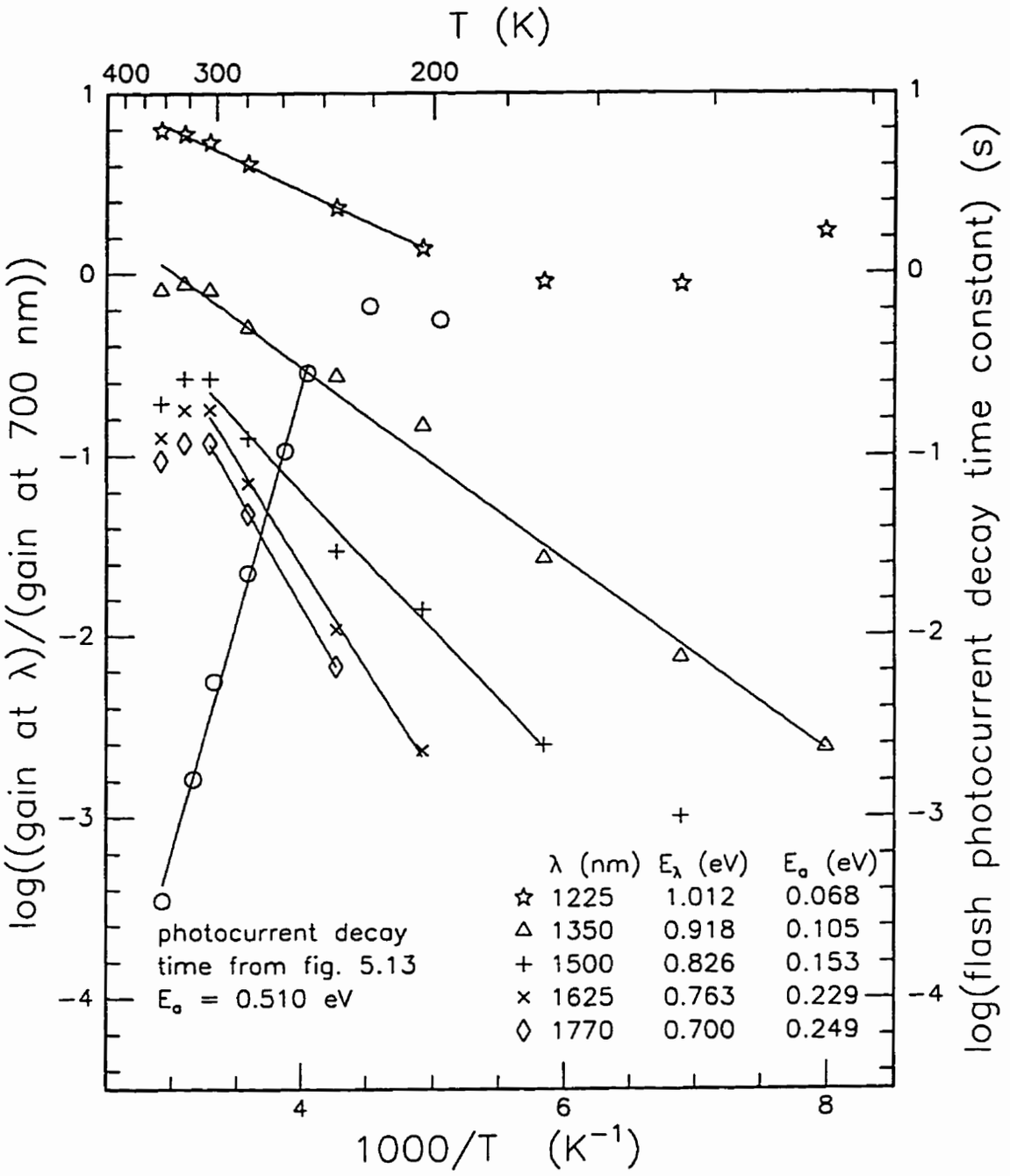

Figure 5.10

Non−circular symbols: Photoconductivity gain at λ nm divided by gain at 700 nm vs. temperature. Circles: Flash photocurrent decay time constant. Activation energy from slope of linear fits shown

figure 6.7, we see that the photoconductivity gain of CdS films is reduced by air annealing. The effect of air annealing on $CuInSe_2$ is described in section 7.3.3.

Comparison of figures 3.19 and 5.6 shows that, with the exception of the zone at x = −1.78 cm, the sodium free zones with high photoluminescence intensity have low photoconductivity gain, and vice versa. A possible explanation is as follows. Suppose that the grain boundary energy barrier term in equation 5.15 dominates the photoconductivity of the sodium free films. Assume that the surface state density is N_S, and in the dark all states are occupied by holes and positively charged. According to equation 5.15, the photoconductivity is then proportional to N_S. As described in section 5.2.1, optically generated free electrons recombine with holes trapped in surface states. The surface states may play a role similar to that of the non-radiative recombination centers postulated in the bulk photoluminescence model of section 3.6.5. Based on these assumptions, the photoluminescence emission intensity should decrease as N_S increases.

Comparison of figure 3.20 (e, f, g, h) with figure 5.7 (e, f, g, h) shows that these sodium doped zones have similar photoconductivity gain, whereas their photoluminescence intensity varies by about one hundred times. In this case, the photoluminescence intensity variation with position may be due to change in a parameter, such as the density of donor defects N_D, which has little effect on the photoconductivity, but a strong influence on the photoluminescence (see equation 3.24).

The zone x = −0.76 cm has the highest peak photoconductivity gain (figure 5.7 c) and the lowest photoluminescence intensity (figure 3.20 c) of the sodium doped zones. If we assume that the bulk term in equation 5.15 dominates the peak photoconductivity, a large Δp is consistent with low recombination rates, both radiative and non-radiative.

The above discussion of photoconductivity and photoluminescence is quite speculative, since photoconductivity spectra measured at 295 K are compared with photoluminescence spectra taken at 85 K. The comparisons would be more meaningful if the photoconductivity spectra were also measured at 85 K.

5.2.5 Time Decay of Photocurrent in the Two Layer Film

The photoconductivity flash response apparatus is shown in figure 5.1 (b). Each zone of 960308 is illuminated by a Xe flash lamp, and the time decay of the photocurrent is recorded with a digital storage oscilloscope. The decay transients for the sodium doped and sodium free zones are shown in figure 5.11. At positions x = -1.27, -0.76 and -0.25 cm, the transient current is 10 to 20 times greater in the sodium doped zones, than in the corresponding sodium free zones. The two zones at x = -1.78 cm each have a similar

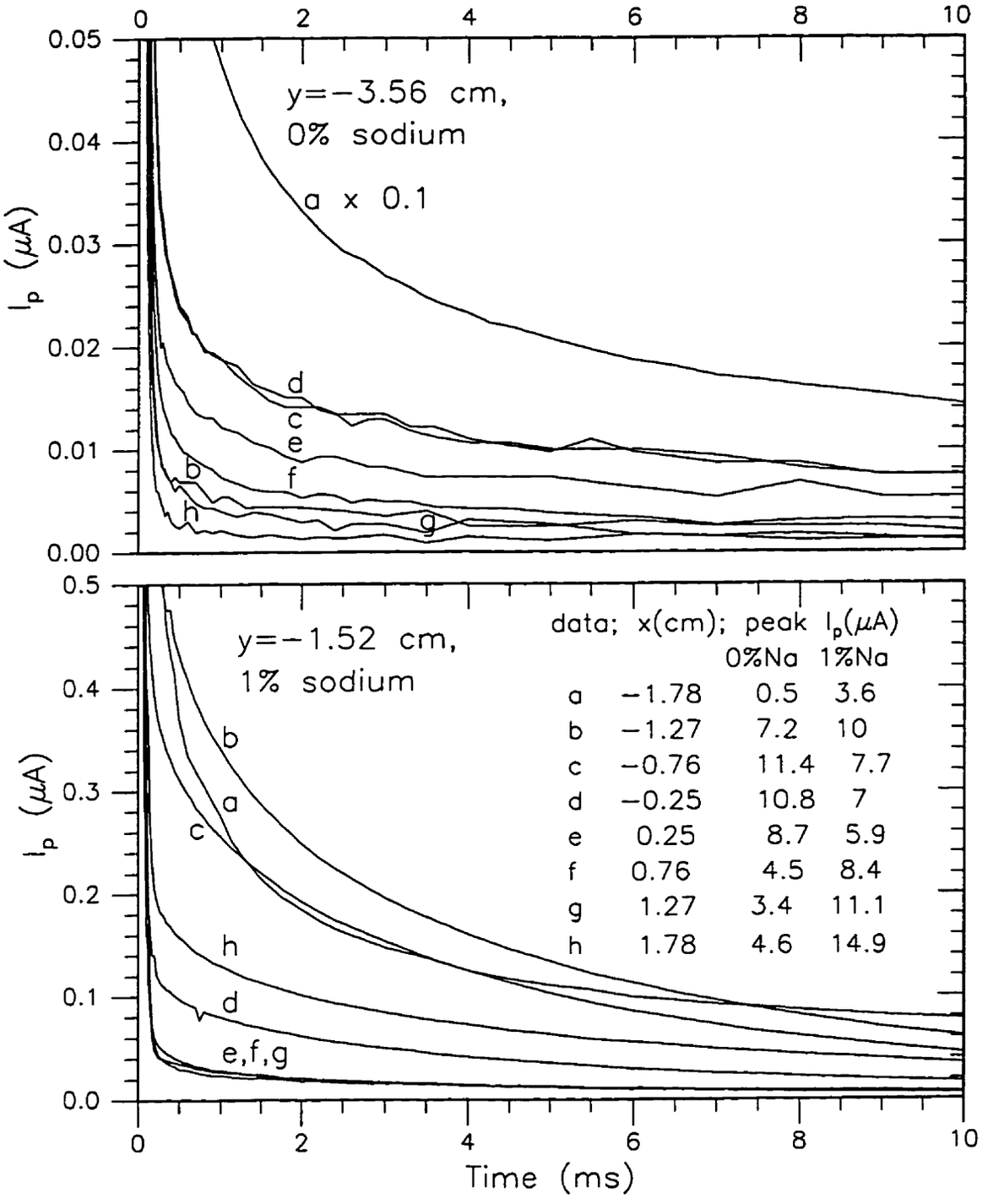

Figure 5.11

Photocurrent decay for two layer film 960308 with 0% Na (top) and 1% Na (bottom). Xe flash lamp triggered at t=0. Note different I_p scales.

transient response, independent of the sodium content. According to case 1 in section 5.1 above, the transient current I(t) due to the thermal effect of the flash energy impulse is

$$I(t) \propto \sigma t^{-\frac{1}{2}}$$

where σ is the dark conductivity. Since the conductivity at the two zones with x = −1.78 cm is over 200 times larger than at the other zones (see figure 4.6), the transient current caused by the thermal effect is largest for these two. The log(I) vs. log(t) plot (figure 5.12, a) of each x = −1.78 zone has a slope equal to −0.5, which indicates a thermal effect. The large transient currents of the remaining lower conductivity sodium doped zones do not obey a simple power law or exponential time dependence. It is assumed that the decays are due to thermal emptying of electron traps in the grain bulk [**12**], and/or at the grain boundaries, which were filled during the flash. Assuming bulk trap states dominate, the additional free holes in the valence band maintain overall charge neutrality, and their density Δp decreases as the traps empty. Assuming surface trap states dominate, the mobility barrier is temporarily lowered by a reduction ΔN_S in the effective positive surface charge due to trapped electrons. As the electron traps empty, the N_S increases and the barrier height increases. The photoconductivity decay at different temperatures for the sodium doped film at x = −0.76 cm is shown in figure 5.13. The decay transient is more rapid at higher temperatures, which is consistent with thermal emptying of the traps. Since a distribution of traps covering a range of energies is likely, then the decay current is a (continuous) sum of exponential decays with different temperature dependent time constants and amplitudes. In the data of figure 5.13, the nearly linear initial portions of the decay curves suggest the presence of a large concentration of traps at a particular energy level. The decay time constant at each temperature is determined from the slope and tabulated in figure 5.13. The time constants vs. temperature are plotted in figure 5.10, and the slope indicates an activation energy of 0.51 eV. A deep electron trap at 0.52 eV has been reported in [**12**].

The photocurrent vs. time for monochromatic light at x = −0.76 cm is shown in figure 5.14. The waveforms are arranged in four groups for comparison. The waveform at the top of figure 5.14 is the 30 Hz chopped output intensity from the Cary 17 monochromator, as measured with a fast Si photo-diode. Waveforms (a, b, c) are at 600 nm and three temperatures. Waveforms (d, e, f) are at 1220 nm and three temperatures. The temperature dependent rise and decay of the photocurrent is typical of the photoconductivity of materials with high trap densities [**20**]. All waveforms are for the sodium doped film, except (g) which is for the corresponding sodium-free film. The three T=295 K waveforms are grouped at the bottom of figure 5.13 for comparison. Note that the photoconductivity decay transient at 1220 nm for the sodium doped film (f) is larger

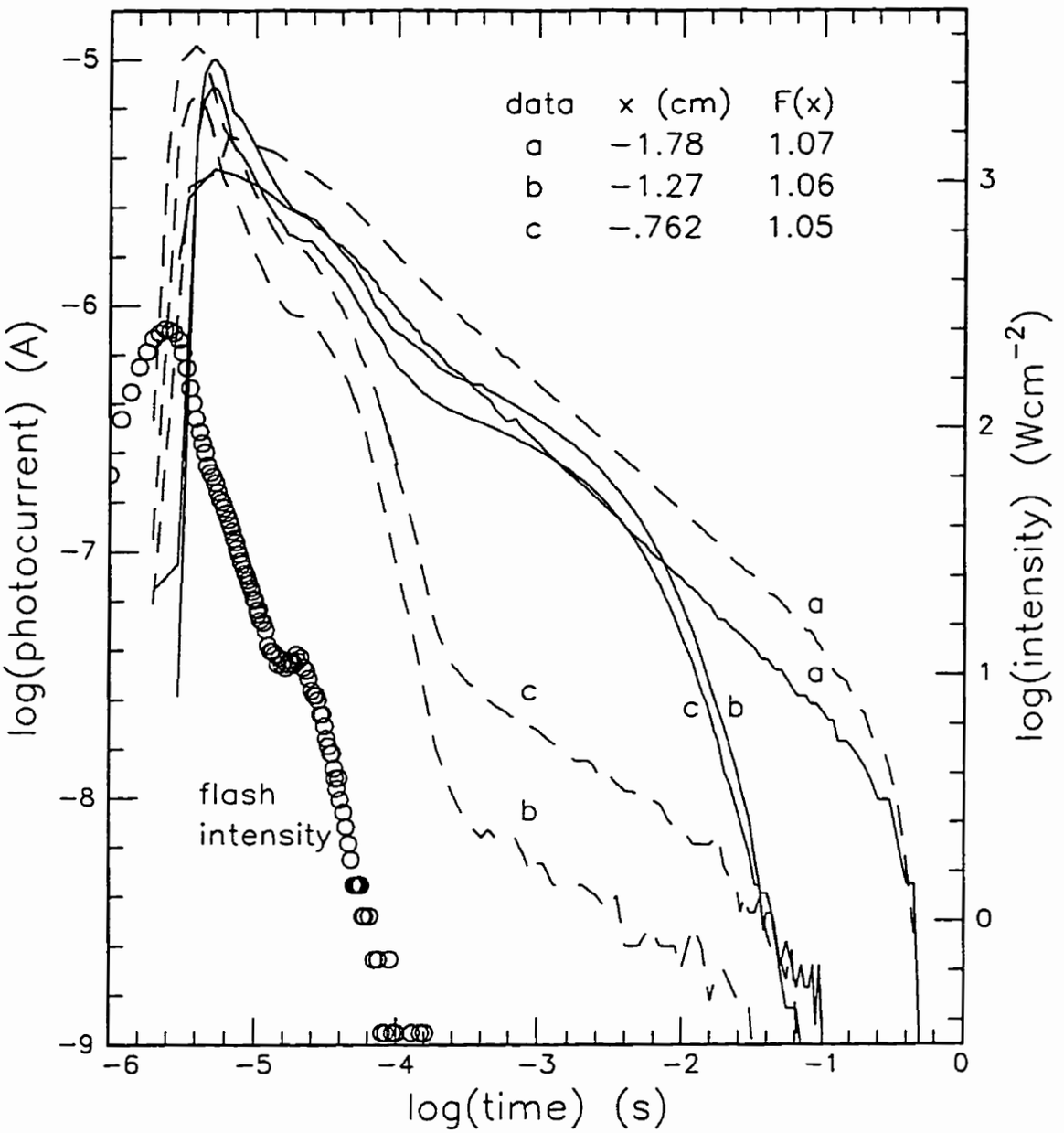

Figure 5.12

Photoconductivity transient response for $CuInSe_2$ film 960308 with 0% Na (dashed line) and 1% Na (solid line). Temperature 22°C; V_{bias}=15 V. Flash triggered at t = 0; circles show intensity.

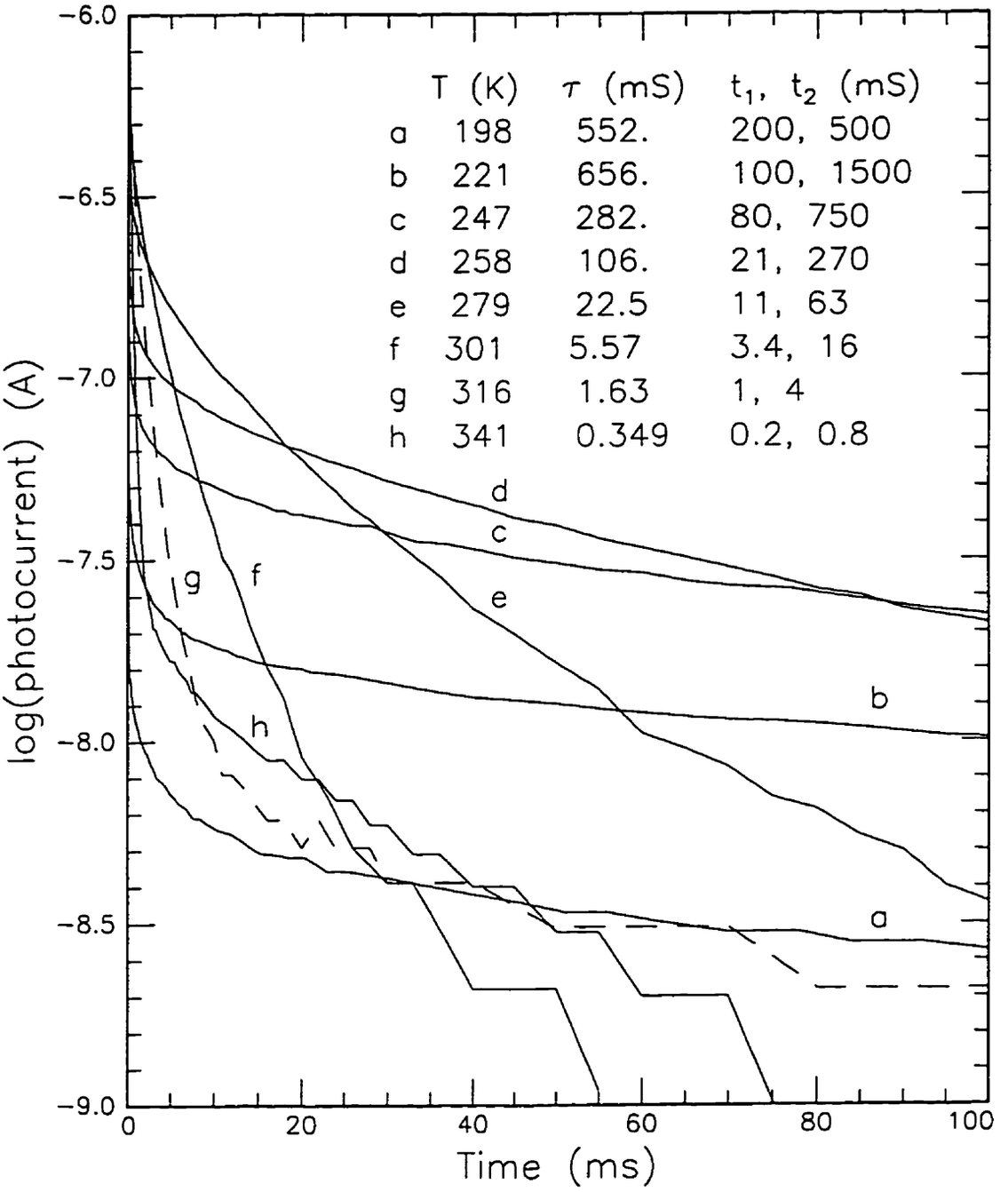

Figure 5.13

Flash response at various temperatures of sodium doped film 960308 at (x,y) = (−0.76,−1.52) cm Decay time τ evaluated from slope of least squares fit to data in interval t_1, t_2

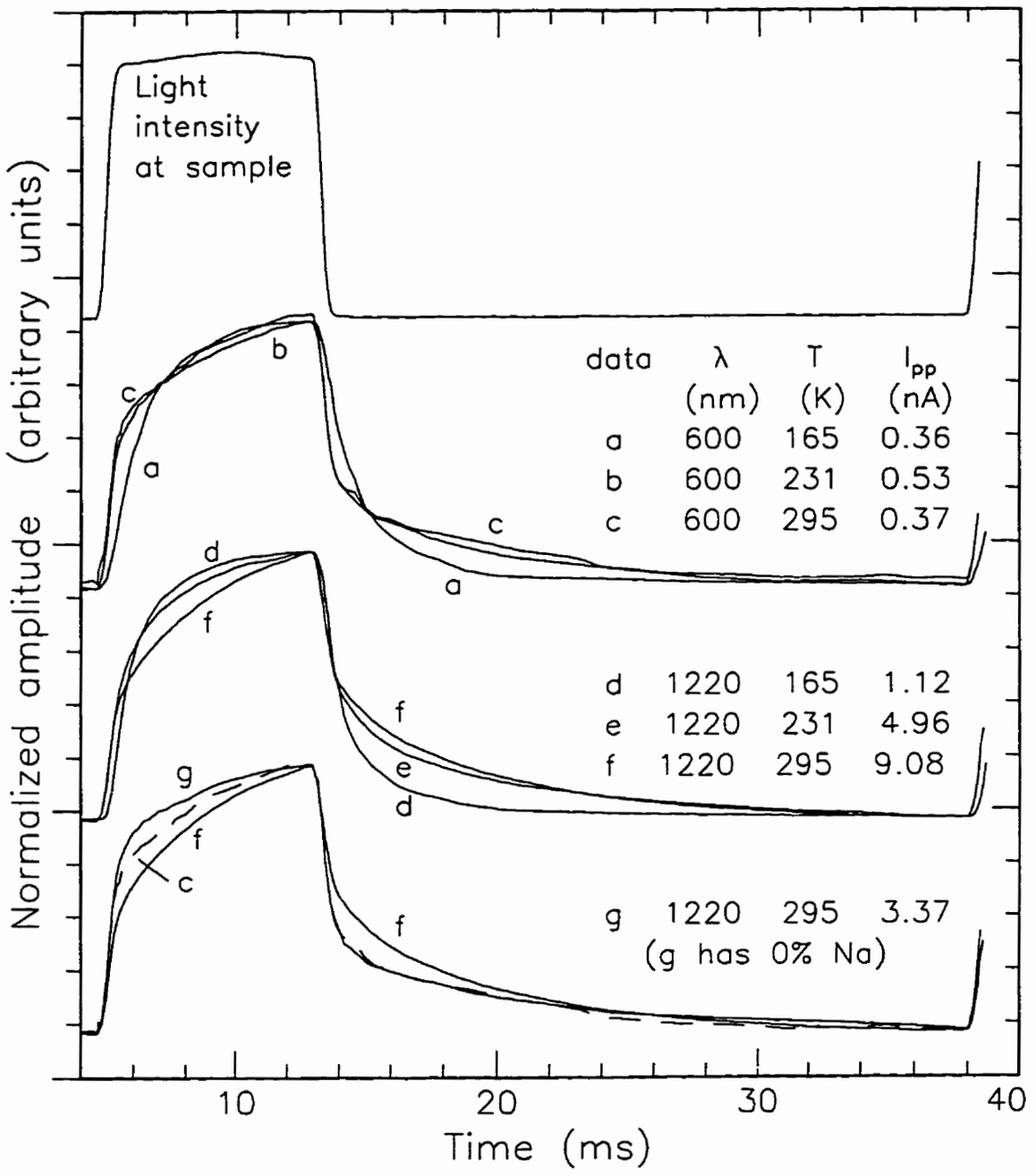

Figure 5.14

Photocurrent waveforms for $CuInSe_2$ film 960308 illuminated with monochromatic light. I_{pp} is peak to peak current. All at x = −.76 cm and y=−1.52 cm, 1% Na, except (g) at y=−3.56 cm, 0% Na (c,f) each plotted twice to facilitate comparisons.

than that of the sodium free film (g), consistent with the results of figure 5.11 and 5.12. Note also that the transient component is larger at 1220 nm (f) than at 600 nm (c) for the sodium doped film. This supports the conclusion that the photoconductivity processes in the sodium doped film differ depending on whether most generation takes place near the surface or in the bulk.

5.3 References

1 R.A. Smith, F.E. Jones, R.P. Chasmar, *The Detection and Measurement of Infrared Radiation*, (Oxford University Press, London, 1968)

2 H.S. Carslaw, J.C. Jaeger, *Conduction of Heat in Solids*, (Oxford, 2nd edition, 1959)

3 *7059 Material Information*, Corning Glass Works, Corning, New York (1977)

4 E.B. Shand, *Glass Engineering Handbook*, (McGraw Hill, New York, 1958)

5 J. H. Lienhard, *A Heat Transfer Textbook*, (Prentice-Hall, New Jersey, 1981)

6 M. Fardmanesh, A. Rothwarf, "Low and Midrange Modulation Frequency Response for YBCO Infrared Detectors", IEEE Trans. Appl. Supercond. vol. 5, no. 1, p. 7 (1995)

7 R.H. Bube, *Photoconductivity of Solids*, (Wiley, New York, 1960)

8 R.L. Petritz, "Theory of Photoconductivity in Semiconductor Films", Phys. Rev. **104**, 1508 (1956)

9 R. Pal, K.K. Chattopadhyay, S. Chaudhuri, A.K. Pal, "Photocondctivity in $CuInSe_2$ films", Sol. Energy Mater. Sol. Cells, **33**, 241 (1994)

10 A Hamamatsu S1226-8BQ silicon photodiode with quantum efficiency 0.647 @ 633 nm is used to calibrate the photoconductivity gain scale.

11 J. E. Stewart and W. S. Gallaway, "Diffraction Anomalies in Grating Spectrophotometers", Applied Optics **1**, 421 (1962)

12 M. Igalson, "Photoconductivity of p-type $CuInSe_2$", Phys. Stat. Sol. (a) **139**, 481 (1993)

13 L.L. Kazmerski and C.C. Shieh, "Photoconductivity Effects in $CuInS_2$, $CuInS_2$ and $CuInTe_2$ Thin Films", Thin Solid Films, **41**, 35 (1977).

14 S. Isomura, A. Nagamatsu, K. Shinohara, T. Aono, "Preperation and Some Semiconducting Properties of $CuInSe_2$ Films", Solar Cells, **16**, 143 (1986)

15 M.A. Slifkin, A. Al-Rahmani, M. Imanieh, R.D. Tomlinson and H. Neumann, "Annealing Effects on Photoconductivity Spectra of $CuInSe_2$ Single Crystals", Cryst. Res. Technol. **26**, 1011 (1991)

16 H.B. Devore, "Spectral Distribution of Photoconductivity", Phys. Rev. **102**, 86 (1956)

17 M.A. Slifkin, A. Al-Rahmani, M. Imanieh, R.D. Tomlinson, H. Neumann, "Photoconductivity Spectra of n-type $CuInSe_2$ Single Crystals", Cryst. Res. Technol. **26**, 109 (1991)

18 J.H. Scofield, S. Asher, D. Albin, J. Tuttle, M. Contreras, D. Niles, R. Reedy, A. Tennant and R. Noufi, "Sodium diffusion, selenization, and microstructural effects associated with various molybdenum back contact layers for CIS-based solar cells", *Proc. of the 24th IEEE Photovoltaic Spec. Conf.* (IEEE, New York, 1994), p. 164

19 A. Rockett, M. Bodegard, K. Granath and L. Stolt, "Na Incorporation and Diffusion in $CuIn_{1-x}Ga_xSe_2$", *Proc. of the 25th IEEE Photovoltaics Spec. Conference*, (IEEE, New York, 1996), p. 985

20 S.M. Ryvkin, *Photoelectric Effect in Semiconductors*, (Consultants bureau, New York, 1964)

Chapter 6

Molybdenum and Cadmium Sulfide Films

The solar cells will be described in detail in chapter 7. In the present chapter, the deposition and characterization of molybdenum (Mo) and cadmium sulfide (CdS) films are described. The $CuInSe_2$/CdS solar cell uses a Mo film as the ohmic contact to the p-$CuInSe_2$, and an n-type CdS film as the window layer.

6.1 Molybdenum Films

6.1.1 Description of the Radio Frequency Sputtering System

Molybdenum has a very low vapor pressure at the temperatures that can be reached with resistively heated sources, so that electron beam evaporation or sputtering are the only practical means for the physical vapor deposition of Mo films. The radio frequency (RF) sputtering process was used for this work and is described in the following.

In the most basic RF sputtering system, shown in figure 6.1, two flat disk electrodes are installed inside a vacuum chamber. The RF shields, and the walls of the vacuum system are at ground (zero) potential. Consider first the usual case where the sputter mode switch is set to normal sputter, so that the bias electrode is grounded. The combination of bias electrode and RF shields forms one large ground electrode. An RF power supply (13.56 MHz) is connected through an adjustable impedance matching network to the target electrode. Note that a series connected capacitor C1 guarantees zero time average (DC) current flow to the electrodes. The surface of the target electrode is composed of a thick layer of the source material (Mo) which is to be sputter deposited onto the substrate.

Argon is added to the vacuum chamber at a rate sufficient to maintain the steady state pressure at approximately 40 mTorr. A glow discharge is produced in the volume between the electrodes when the RF voltage is applied. The discharge is composed mostly of neutral argon, with some argon ions and energetic free electrons. The argon ions are too massive to directly gain significant kinetic energy from the rapidly varying RF electric field. To a good approximation, the argon ions "see" only the DC electric field.

The free displacement amplitude of the electrons is much larger than their mean free path in the argon gas. Thus the motion of the electrons can be characterized by a pressure dependent mobility. For electrons, the cold electrodes are essentially blocking contacts, since they can remove an unlimited number of electrons from the discharge but can contribute only the few secondary electrons generated during ion impacts. Therefore, as the RF field drives the high mobility electron cloud alternately toward either electrode,

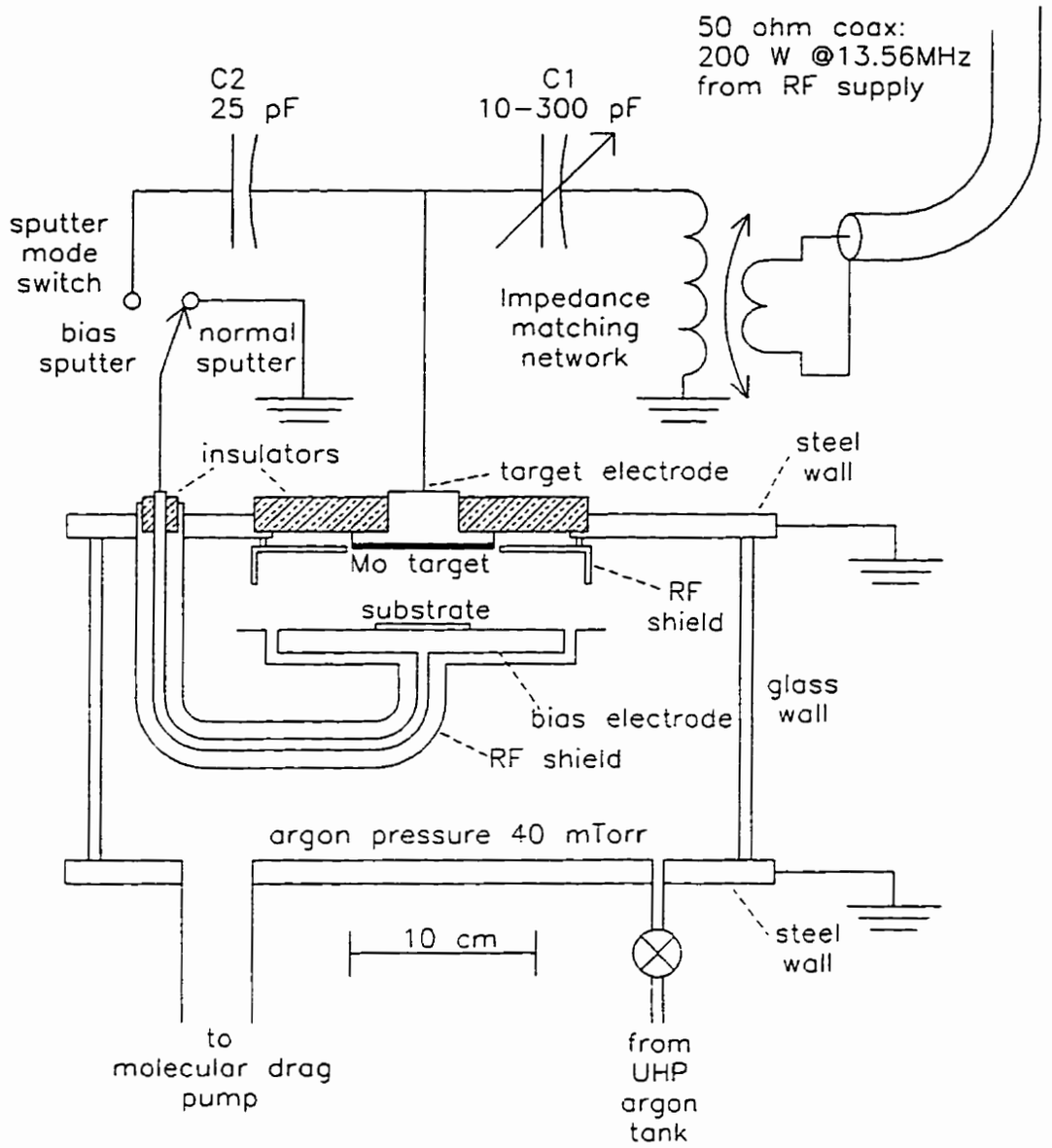

Figure 6.1

RF sputtering system used for deposition of Mo on glass substrates. Transformer and C1 adjusted for impedance matching to 50 ohm cable. Normal or bias sputtering modes selected with switch. Substrate bake–out heater not shown.

electrons are rapidly removed from the regions near the electrodes. The discharge reaches a steady state configuration, consisting of a high conductivity approximately neutral central plasma, bounded by high electric field, electron deficient, low conductivity, positive space charge sheath regions adjacent to the electrodes. Since the plasma is surrounded by positively charged sheaths, it is at a positive DC potential with respect to either electrode .

A simple equivalent circuit [1] can be used to arrive at approximate expressions for the DC target and plasma potentials. The target sheath and ground sheath are modeled by capacitors connected in series between the target and ground electrodes. The plasma potential is equal to that of the circuit node between the two capacitors. Each capacitor is shunted by a diode and a large resistor. The diode carries electron current flow into the plasma and the resistor carries DC ion current out of the plasma. The RF potential of the plasma is determined by the ratio of the sheath capacitors. At all times during the full RF cycle, the diodes force the plasma potential to be greater than or equal to both target and ground electrode potentials. The external capacitor C1 requires that the net (ion + electron) DC current flow to either electrode must be zero. Thus for each RF cycle, the maximum plasma potential must be just equal to the maximum target potential, to briefly allow electron flow to the target electrode. Similarly, the minimum plasma potential must be just equal to the ground electrode potential, to briefly allow electron flow into the ground electrode. Based on this simple model, the DC potentials are

$$V_p = \frac{C_t}{C_t + C_0} V_{RF} \qquad (6.1)$$

$$V_t = \frac{C_t - C_0}{C_t + C_0} V_{RF} \qquad (6.2)$$

$$\Delta V = V_p - V_t = \frac{C_0}{C_0 + C_t} V_{RF} \qquad (6.3)$$

V_{RF} is the RF voltage amplitude at the target electrode, C_t, C_0 are the target and ground sheath capacitances, respectively, and V_t, V_p are the target and plasma DC potentials. The potential difference ΔV accelerates ions to the target with sufficient kinetic energy to remove target atoms (sputter Mo) from the target surface. Some of the sputtered Mo forms a thin film on the substrate.

For a given RF amplitude V_{RF}, the sheath capacitance ratio determines the size of the DC potentials. According to [2], assuming that the ion current density is space charge limited and the same at each electrode, and that the sheath capacitance is proportional to the electrode area A divided by the sheath thickness, then the capacitance ratio is given by

$$\frac{C_t}{C_0} = \left(\frac{A_t}{A_0}\right)^4 \qquad (6.4)$$

More recent experimental data [1] suggest that

$$\frac{C_t}{C_0} \cong \left(\frac{A_t}{A_0}\right)^2 \qquad (6.5)$$

Thus for an electrode area ratio much less than unity, equations 6.1, 6.3, 6.4 and 6.5 show that the ion accelerating potential is near V_{RF} and the plasma potential approaches zero. Since the total area of the ground electrode includes the bias electrode as well as the RF shields, we estimate $A_0 \cong 10A_t$. Using equation 6.5 and 6.3, we obtain $\Delta V \cong 0.99V_{RF}$. From 6.1 and 6.5 we get $V_p \cong 0.01V_{RF}$. An important advantage of the low plasma potential is that ion impact energies at zero potential surfaces such as the bias electrode and the grounded shielding surfaces near the target electrode are minimized. Thus sputtering of these surfaces and contamination of the film by the surface materials are minimized.

For RF bias sputtering, the sputter mode switch connects the bias electrode through a small capacitor C2 to the RF signal at the target electrode. The discharge now has three electrodes. The RF amplitude at the bias electrode is set to a small fraction "b" of the amplitude at the target by the RF voltage divider consisting of C2 and the capacitance of the bias electrode to its grounded shield. Provided that the ground sheath capacitance at the RF shields is much larger than the target and bias sheath capacitances, one can show, using similar arguments as presented above, that a DC potential approaching $V_b \cong -bV_{RF}$ develops on the bias electrode. The substrate is placed on the bias electrode and is therefore bombarded by ions from the plasma with moderate energy $V_p - V_b$. This gentle sputtering of the growing film can remove weakly bonded impurities [3].

6.1.2 Sputter Deposition and Electrical Conductivity of Molybdenum Films

A Randex model 3140 RF sputtering system (figure 6.1) was used to deposit the Mo films. In figure 6.2 the conductivity of the sputtered Mo films, as measured by a four point surface probe, is plotted as a function of deposition date. Starting at the end of 1994, a deliberate effort was made to minimize contamination of the growing films by residual gas, particularly oxygen. Thereafter, ultra high purity argon (instead of high purity) is used as the sputtering gas, the argon feed lines are thoroughly purged and the chamber is baked out before starting a deposition. Bias sputtering was introduced on March 29, 1995 to further reduce impurity concentration. The increase in Mo film conductivity due to the systematic reduction of oxygen content can be clearly seen in figure 6.2.

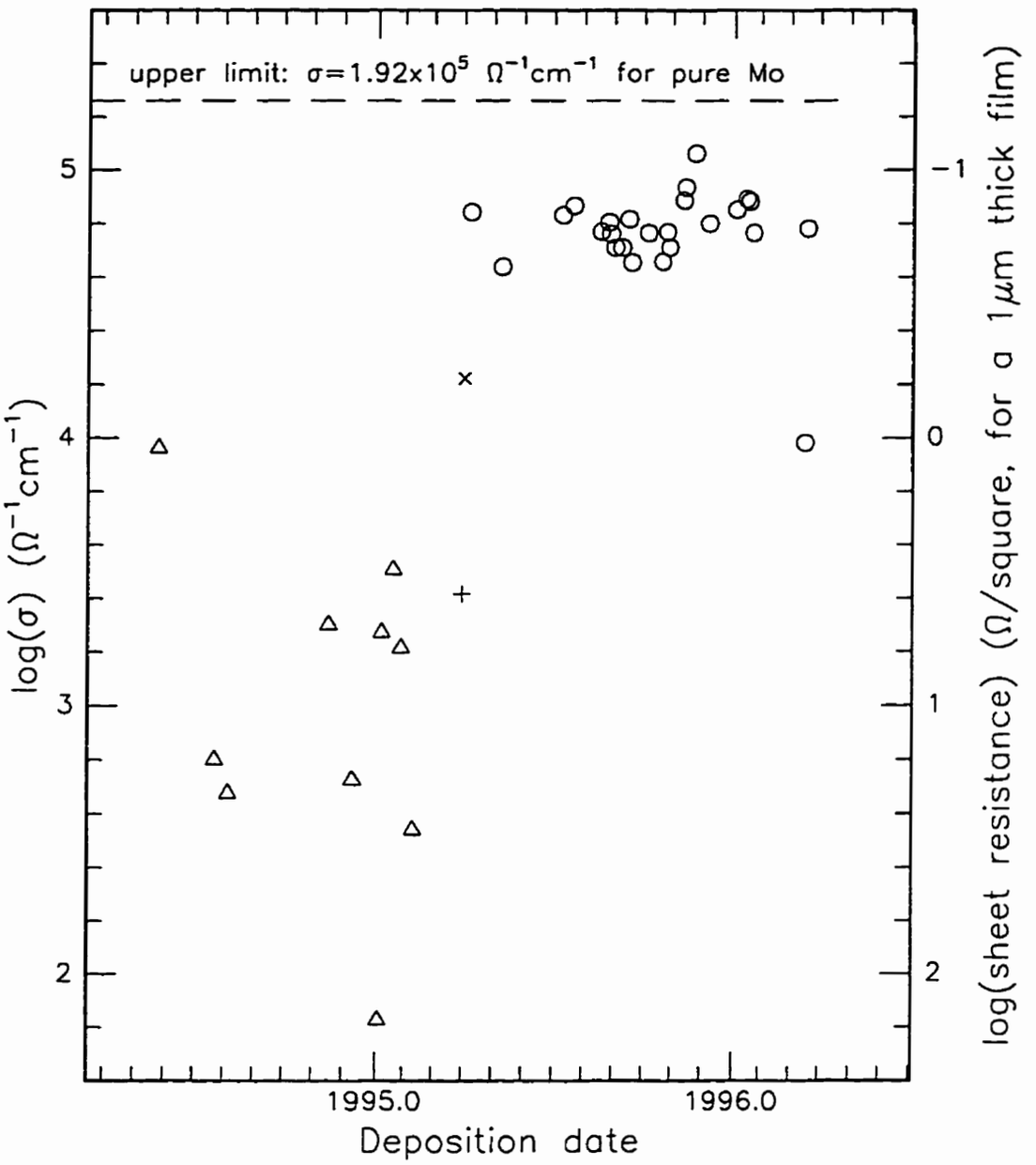

Figure 6.2

Effect of deposition conditions on Mo film conductivity σ:
(Δ) High purity argon, normal sputter.
(+) Ultra high purity (UHP) argon, normal sputter.
(x) UHP argon, bias sputter.
(o) UHP argon, bias sputter, chamber baked out.

In order to improve adhesion of the film to the substrate, prior to deposition the substrate is baked in vacuum for about 2 hours at 300 °C by a radiation heater mounted below the substrate. This bake-out is intended to remove adsorbed water from the substrate surface and dissolved water from the bulk. Mo films on 7059 glass generally adhere better than films on soda-lime glass. This may in part be due to the differences in thermal expansion coefficients (Mo: $5x10^{-6}$ K^{-1} , 7059 glass: $4.6x10^{-6}$ K^{-1} , soda-lime glass: $9.2x10^{-6}$ K^{-1}).

It was observed that bias sputtered films do not adhere to the glass as well as normal sputtered films. According to [3], bias sputtering purifies metal films for which the metal bonds more strongly to itself than to impurity atoms. One would expect a bias sputtered film to have a reduced interface density of chemical bonds with the substrate, leading to a corresponding reduction of adhesion. Therefore, in order to improve adhesion to the glass, the first 0.1 μm is deposited by normal sputtering, and the remainder of the film is deposited by bias sputtering. All films were sputtered with the argon pressure at 40 mTorr. The substrate temperature during sputtering is approximately 300 °C. Other sputtering parameters for a typical 1 μm thick film are shown in table 6.1 below.

Table 6.1: Typical Sputtering Parameters

sputter mode	time (minutes)	forward power (RF watts)	reflected power (RF watts)	V_t (volts)	V_b (volts)	deposited thickness (μm)
normal	0 to 5	200	< 5	−1950	0	0.1
bias	5 to 60	200	< 5	−1800	−150	0.9

6.2 CdS Films

6.2.1 Description of the CdS Deposition System

A hot wall deposition system is used to deposit the CdS window layer. CdS dissociates into Cd and S upon evaporation. These elements have relatively high vapor pressures, and condense to form stoichiometric CdS only under carefully controlled conditions. In a hot wall system a heated inner chamber (hot wall) is used to confine the vapour to a restricted volume in the vacuum chamber. This serves to minimize the loss of material, and produces a higher vapour pressure at the substrate for a given source temperature. Also, the vapour is approximately stoichiometric because there are no cold surfaces on which the lower vapour pressure component (Cd) can preferentially condense. Since film growth will occur only if the impingement rate exceeds the evaporation rate (or equivalently, if the hydrostatic pressure exceeds the equilibrium vapour pressure at the substrate temperature [4]), higher pressures inside the hot wall enclosure permit higher substrate temperatures to be used.

A diagram of the hot wall evaporation system is shown in figure 6.3. The hot wall, radiation heater, and heat shield are a separate assembly which rests in a locating hole in the aluminum support platform. This permits easy removal of the assembly for cleaning and heater wire repair. Also a separate electrode evaporation assembly can be substituted for the hot wall assembly when electrodes are deposited. Minimal thermal contact exists between the hot wall assembly and the support platform. This ensures maximum temperature uniformity of the hot wall assembly and further reduces heater power requirements. The hot wall assembly consists of a quartz glass inner wall, surrounded by a 6 turn heater coil wound from 0.01 inch tungsten wire. The heater coil is supported by 6 stainless steel rods with ceramic insulator feedthroughs for the tungsten wire. Surrounding the wire is a heat shield/reflector consisting of thin aluminum sheet with approximately 10% perforation with viewing holes. The In doping source and CdS source are located at the base of the hot wall enclosure. A stainless steel baffle plate is mounted at the bottom of the hot wall assembly. This plate closes off the bottom of the quartz tube except for two holes through which vapour from the sources pass. Small ceramic connecting tubes rest on top of the sources and pass through the baffle plate holes. This is intended to maximize the CdS pressure inside the hot wall enclosure, by minimizing the area of the escape passages. Thermocouples are mounted in the bases of the source crucibles to monitor source temperatures so that controlled evaporation rates can be obtained.

The following procedure is used to prepare the hot wall system for the deposition of a CdS film. First the hot wall assembly (figure 6.3) is removed from the vacuum chamber and the glass hot wall inside surface is cleaned in 25% HNO_3 in water, in order to remove the CdS deposited during the previous deposition. The hot wall assembly is re-installed in the vacuum chamber and baked-out in vacuum at full operating temperature, then cooled to room temperature. Liquid nitrogen is added to the vacuum system cold trap. The hot wall assembly is removed again, and the CdS source is filled with 1.1 g of CdS powder. The CdS source is heated in vacuum to 800 °C for about 5 minutes to out-gas volatile impurities, then cooled. Finally, the hot wall assembly and a substrate with a thermocouple bonded to its back surface are installed, and the chamber is again evacuated.

Figure 6.4 shows the temperatures during the deposition of a CdS/CdS:In film (#951002), and a pure CdS film (#951006b). The optimum temperatures of the CdS source, the hot wall and the substrate were determined in the experiments described in sections 6.2.2 and 6.2.3 below. The In source temperature was calibrated with a crystal microbalance, to provide In doping in the 0.1% to 1% range.

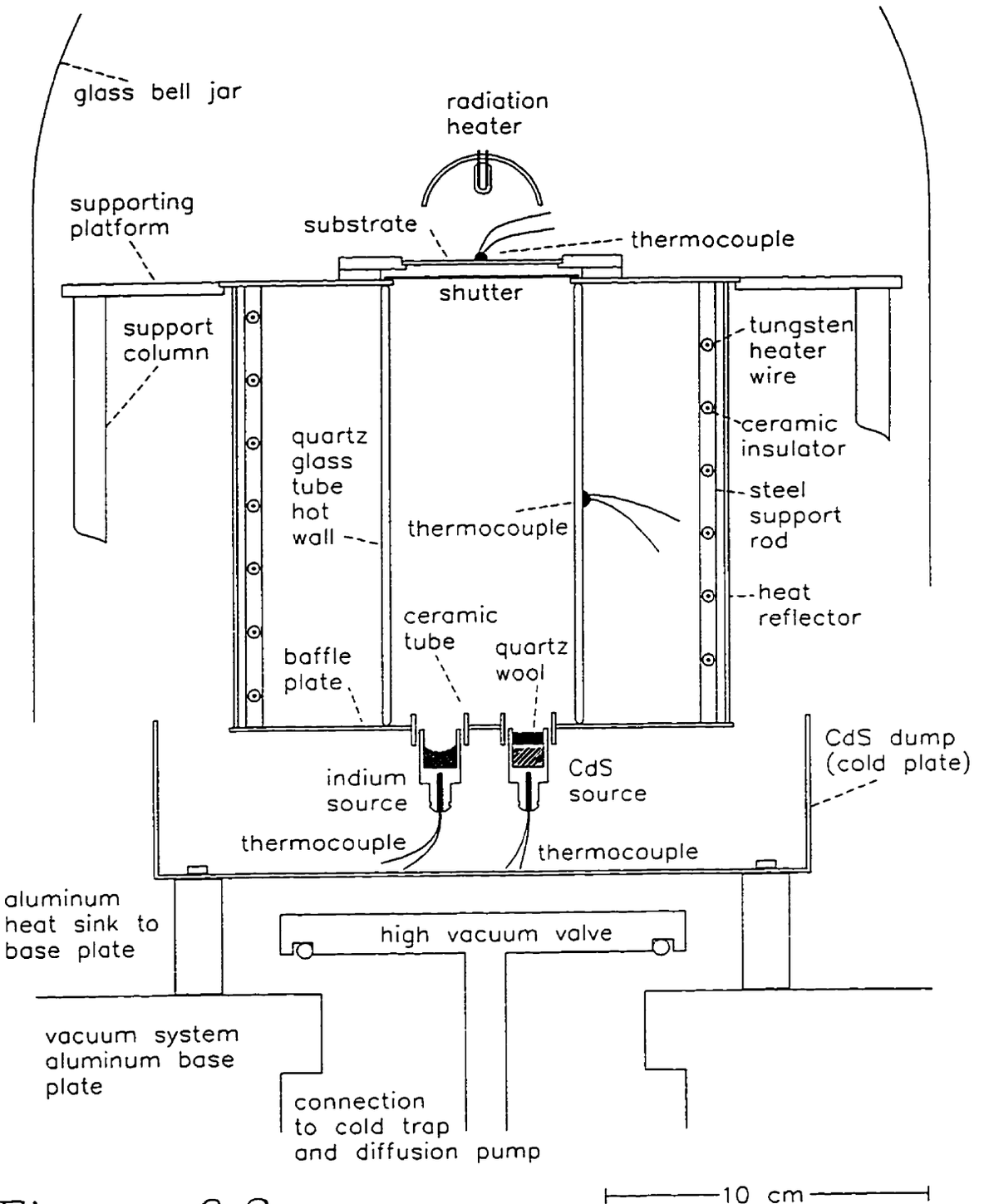

Figure 6.3

The CdS evaporation system includes a CdS source, an In doping source, and a hot wall enclosure. Radiation heaters are used to heat the substrate and wall. The view is a vertical cross section containing the axis of the quartz tube.

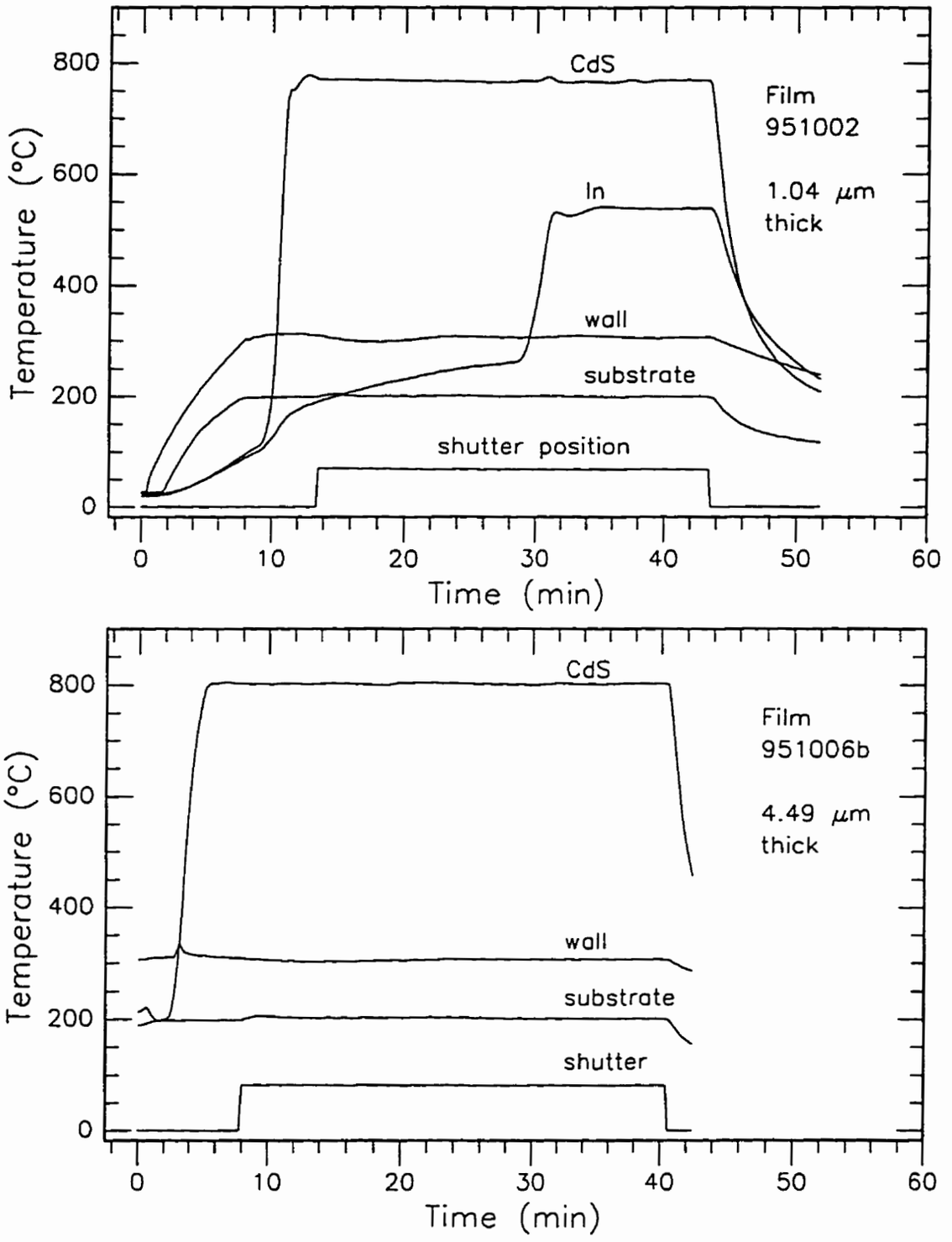

Figure 6.4

Deposition records for CdS films deposited on 7059 glass substrates. Shutter position = 0 means closed. Note small difference in CdS source temperatures.

6.2.2 CdS Evaporation Rate vs. Source Temperature

The type (f) source design of figure 2.5, originally developed for Cu and In evaporation, was also used in the CdS deposition system. After each deposition, the change in mass of the CdS in the source, and the evaporation time, were used to determine the mass evaporation rate of the CdS. Figure 6.5 is an Arrenhius plot of the evaporation rate. The temperature dependence of the CdS evaporation rate is expected to be [5] of the form

$$G = CT\exp\left(-\frac{\Delta H}{RT}\right) \qquad (gcm^{-2}s^{-1}) \qquad (6.6)$$

where ΔH is the heat of activation, and C is independent of temperature. The slope of lnG vs. 1/T is given by

$$\text{slope} = \frac{d(\ln G)}{d\left(\frac{1}{T}\right)} = -\frac{\Delta H}{R} - T \qquad (6.7)$$

From the data of figure 6.5, the slope obtained by least squares fit is

slope = -13956 K at $T \cong 1000$ K

From this we obtain

$\Delta H = 25.76$ kcal/mol

Due to systematic errors, described below, this estimate of ΔH is considerably less than a published value [5] obtained by careful measurements on CdS single crystals:

$(\Delta H)_{crystal} = 50.3$ kcal/mol

In figure 6.5, the evaporation rate is plotted with respect to the temperature of the thermocouple in the evaporation source crucible, not the temperature of the CdS powder. As the powder temperature and evaporation rate are increased, more heat must flow from the crucible to the powder, in order to supply the ΔH needed to vaporize the powder. Since there is a thermal resistance between the crucible and the powder, the temperature difference between the crucible and powder increases as the crucible temperature and the heat flow increase. Thus the actual powder temperature varies over a smaller range than the range of thermocouple temperatures of the data points shown in figure 6.5, and the slope of the linear fit is less than would be expected if the powder temperature were measured and used as abscissae in figure 6.5.

The surface area of the CdS powder decreases as the CdS mass decreases during evaporation. Therefore at a fixed temperature, the evaporation rate (in grams per minute) decreases as the CdS evaporates. There is some error in the data of figure 6.5 because of variations in the initial and final CdS masses used in each evaporation experiment.

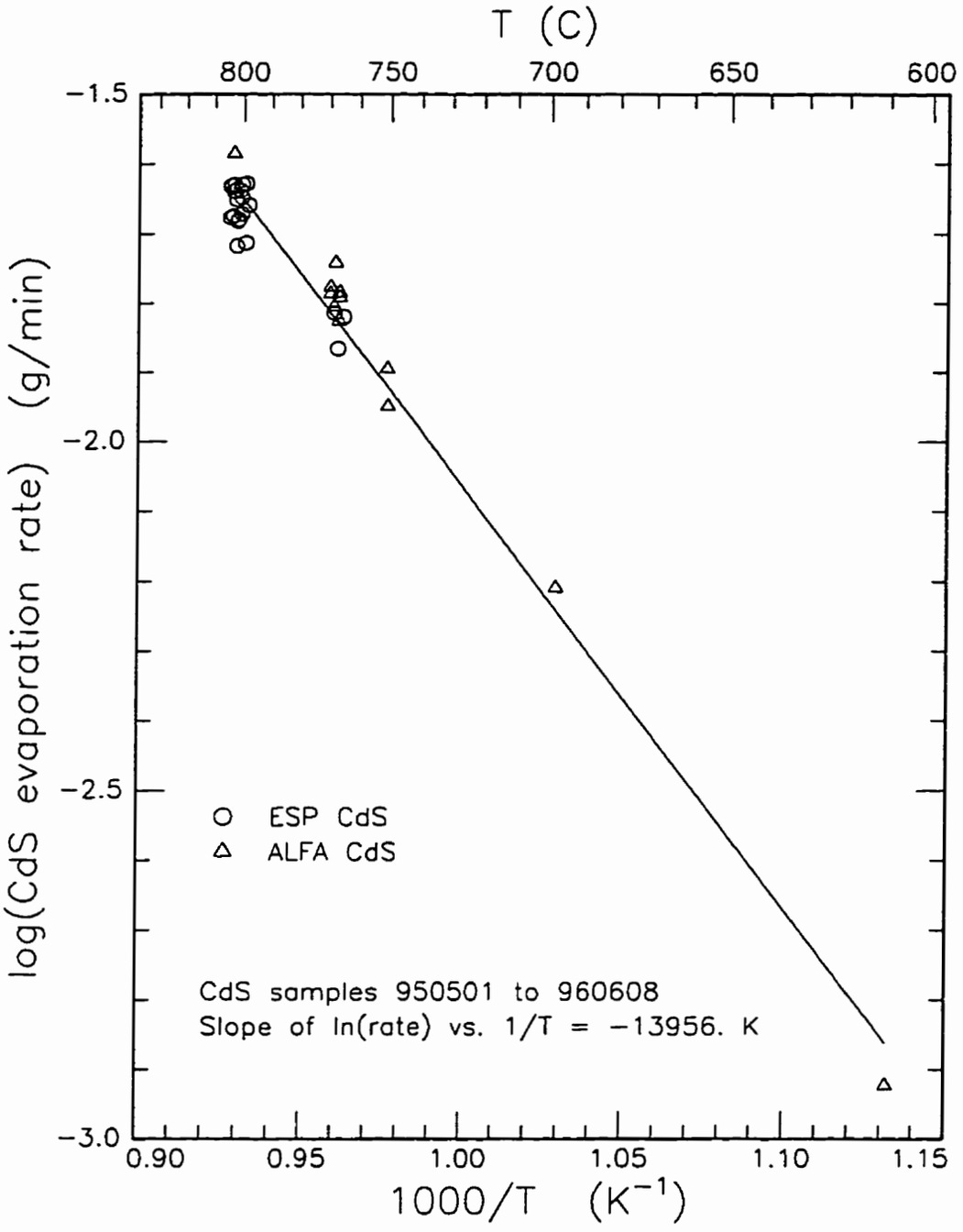

Figure 6.5

CdS evaporation rate as a function of source thermocouple temperature T. Each data point represents one film deposition experiment. The line is a least squares fit to the data.

6.2.3 The Effects of CdS Purity

More than 45 CdS films were evaporated during the course of the project. Many films were produced to evaluate the design of the CdS evaporation system, and to determine the appropriate combination of substrate temperature, hot wall temperature (T_{wall}), CdS source temperature (T_{CdS}), and indium doping source temperature (T_{In}) required to produce good quality films. An important observation is that the quality of the CdS powder used in the evaporation source can have a major influence on the film deposition process.

Containers of high purity CdS powder supplied by Alfa Inorganics (ALFA) and Electronic Space Products (ESP) were already in stock in the lab and both types were tried as evaporation source material. The film thickness of CdS deposited on the substrate per gram of CdS evaporated depends on the wall temperature. As shown in figure 6.6, the ALFA CdS yield has a much greater sensitivity to wall temperature than does the ESP CdS. Also the ESP CdS produced uniform films in a predictable way, whereas the ALFA CdS tended to produce non uniform, poor quality films. It is possible that the ALFA material was not sufficiently pure initially, or had been contaminated or chemically altered (formation of sulfate and/or chloride). The glass stopper on the ALFA CdS container did not provide an airtight seal, and the CdS was stored for many years in a closed cabinet with other containers of chemicals. Commercially available "pure" CdS can contain up to 10 ppm of heavy metals and 0.1 to 0.5% of chloride and sulfate [6]. Evaporation of such material does not lead to reproducible results. Considerable effort was wasted in initial experiments before it was recognized that poor quality films always resulted when the ALFA CdS was used.

6.2.4 Characterization of CdS Films

Several good quality (uniform, yellow-orange color) CdS films were selected for testing. The films were deposited on 7059 glass at 200 °C substrate temperature using ESP CdS powder as source material. The deposition conditions and dark conductivity at 20 °C for three films are shown in table 6.2 below. The dark conductivity of film 951006b was re-measured after a 15 minute anneal at 200 °C in air. A Hall measurement of film 951006b gave $n = 1.6 \times 10^{18}$ cm^{-3} and $\mu_n = 0.4$ $cm^2 V^{-1} s^{-1}$ before annealing.

Figure 6.7 shows the photoconductivity spectra of CdS film 951006b before and after annealing. The uniformly illuminated sample is 4.5 μm thick, of area 1.4×0.35 cm^2, and has indium contacts on the 0.35 cm sides. The air anneal reduces the photoconductivity gain and the dark conductivity, but increases the ratio of photoconductivity gain to dark conductivity. This effect has been described in [7] for both oxygen and copper impurities

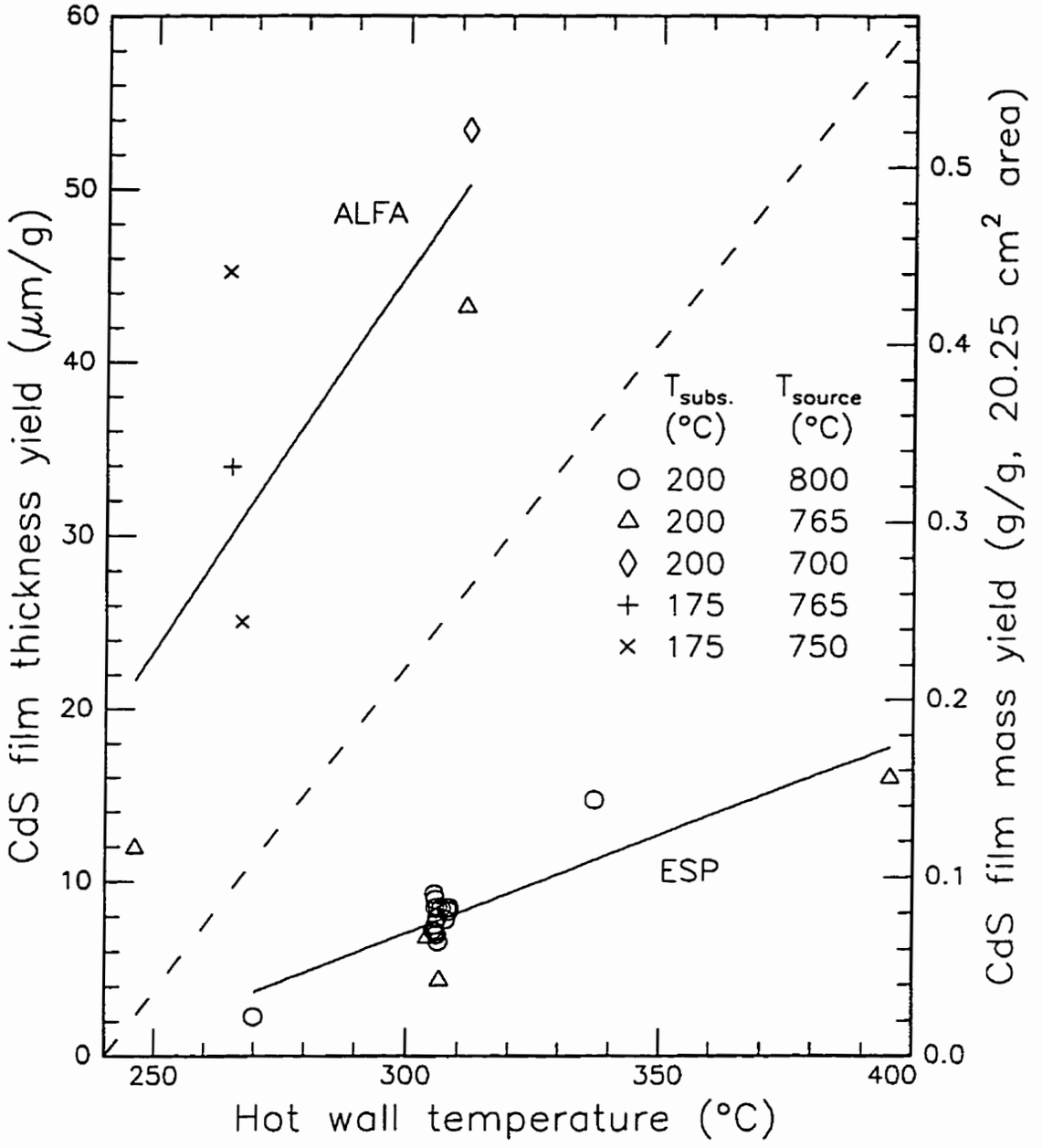

Figure 6.6

CdS film yield per gram CdS evaporated, as a function of the hot wall temperature. Data for CdS supplied by ALFA and ESP are seperated by the broken line. The solid lines are least squares fits. Substrate and source temperatures used during a deposition are indicated by the symbols.

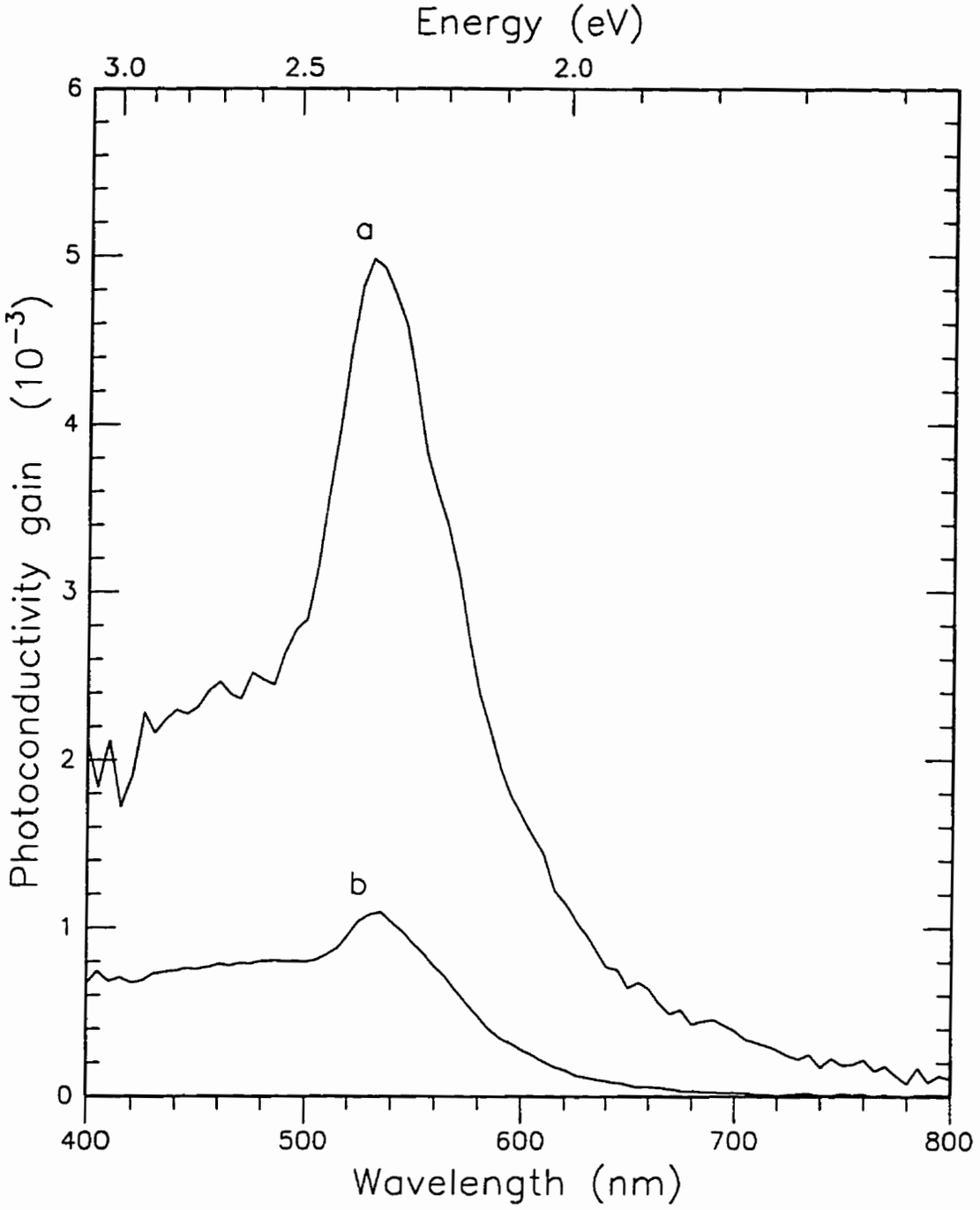

Figure 6.7

Photoconductivity spectrum of CdS film 951006b before (a) and after (b) 15 minute anneal in air at 200 °C. Monochromator passband 10 nm, chopped at 30 Hz; temperature 22°C; bias 14 V.

in CdS. According to [7], a typical CdS film produced by evaporation has excess Cd, either as S vacancies or Cd interstitials. These defects are donors. Oxygen, like copper, is a deep acceptor in CdS, with large ionization energy (≅1 eV). When oxygen acceptor defects are added to CdS, they compensate many of the donor defects, thereby substantially reducing dark conductivity. Any uncompensated acceptors act as recombination centers, which cause a reduction in free carrier lifetime and photoconductivity gain.

Optical transmission spectra for the three films are shown in figure 6.8. The main parameter affecting the measured transmittance for photon energies below the bandgap is the grain size. As is the case for large grain $CuInSe_2$ films without sodium doping (section 3.5.2), the large grain CdS films scatter most of the spectrophotometer light out of the beam path, resulting in very low measured transmittance.

Table 6.2: CdS Film Deposition Temperatures and Properties

film #	time (min)	T_{wall} (°C)	T_{CdS} (°C)	T_{In} (°C)	thickness (μm)	grain size (μm)	indium doping (%)	dark conductivity ($\Omega^{-1}cm^{-1}$)
951002	28	307	767	540	1.04	<0.3	0.2	160
951004	20	270	802	off	1	1	0	0.04
951006b	33	307	802	off	4.5	2 to 5	0	0.09
951006b (annealed in air)	33	307	802	off	4.5	2 to 5	0	0.005

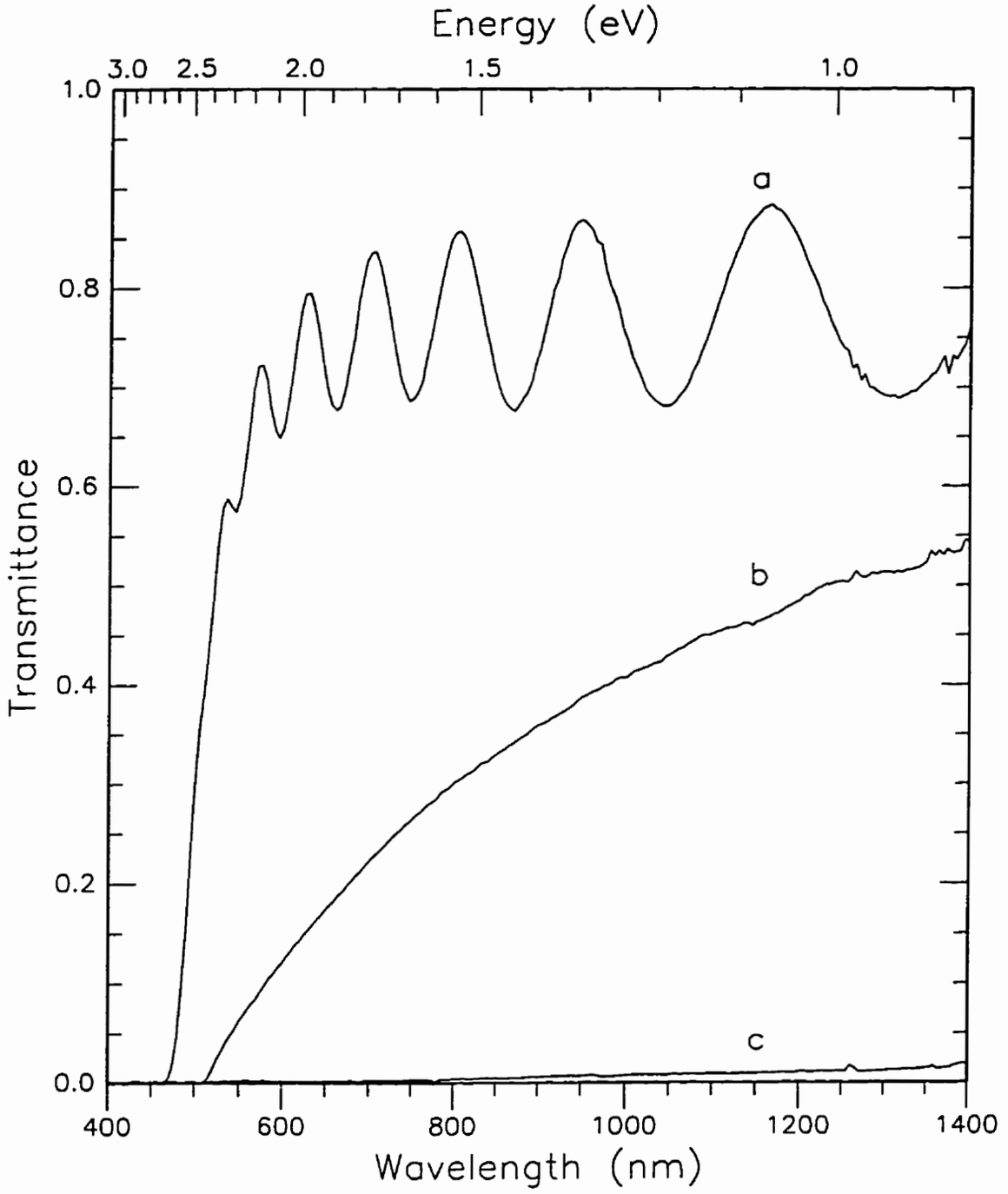

Figure 6.8

Transmittance of CdS films of thickness d (μm), grain size gs (μm), conductivity σ ($\Omega^{-1}cm^{-1}$) and indium doping In (%).
(a) film 951002: d=1.04, gs<0.3, σ=160, In=0.2
(b) film 951004: d=1, gs=1, σ=0.04, In=0
(c) film 951006b: d=4.5, gs=2 to 5, σ=.09, In=0

6.3 References

1 K. Kohler, J.W. Coburn, D.E. Horne and E. Kay, "Plasma potentials of 13.56 MHz RF argon glow discharges in a planar system", J. Appl. Phys. **57**, 59 (1985)

2 H.R. Koenig, L.I. Maissel, "Application of RF discharges to sputtering", IBM J. Res. Dev. **14**, 168 (1970)

3 *Handbook of Thin Film Technology*, edited by L. Maissel and R. Glang (McGraw Hill, New York, 1970)

4 A. Lopez-Otero, "Hot wall epitaxy", Thin Solid Films, **49**, 3 (1978)

5 G. A. Somorjai, "The Evaporation Rate and Mechanism of CdS and CdSe", *Proc. of International Symposium on Condensation and Evaporation of Solids*, (Gordon and Breach, New York, (1962))

6 A. Vecht, "Methods of Activating and Recrystallizing Thin Films of II–VI Compounds" *Physics of Thin Films*, **3**, edited by G. Hass and R. Thun (Academic Press, New York, 1966)

7 R.H. Bube, "Photoconductivity of Solids", (Wiley, New York, 1960)

Chapter 7

$CuInSe_2$/CdS Solar Cells

Most solar cells produced during this project were based on the simplest cell design which has demonstrated relatively high energy efficiency. The structure, shown in cross-section in figure 7.1, is similar to that of the 9.4% efficient cell developed at Boeing in 1981 [1], without the anti-reflection coating. Many improvements to the basic Boeing design have since been made, as described in section 1.2, but more sophisticated fabrication techniques are required. The typical device of figure 7.1 has a 1 μm thick molybdenum (Mo) back contact, a 3 μm thick p-$CuInSe_2$ absorber layer, a 4 μm thick n-type cadmium sulfide (CdS) window layer and a 2 μm thick Al/Ni front contact grid.

7.1 Solar Cell Fabrication Procedure

7.1.1 Mo Back Contact Deposition

The glass substrate is cleaned by the method of section 2.1. It is then placed in the RF sputtering system where a 1μm thick Mo film is deposited on one face of the substrate, using the method of section 6.1.

7.1.2 Deposition of the $CuInSe_2$ Absorber Layer

After the Mo contact is deposited on the glass substrate, the substrate is removed from the sputtering system. If required for experimental purposes, the Mo film is coated with a thin layer of NaOH by one of the methods described in 2.5. The substrate is then installed in the $CuInSe_2$ deposition chamber of figure 2.1, and the $CuInSe_2$ absorber layer is deposited through a mask of aperture 4 x 4 cm^2 by the method described in Chapter 2.

7.1.3 CdS Window Layer Deposition

After removal from the $CuInSe_2$ deposition chamber, the back surface of the substrate is slightly roughened with fine sand paper and a copper-constantan thermocouple is bonded to it using Torr Seal [2] epoxy. The thermocouple is required for substrate temperature control in the subsequent CdS deposition step. The indium wetted type K thermocouple used during the $CuInSe_2$ deposition is not used for the CdS deposition because the mechanical fixture used to press the thermocouple pad against the back surface of the substrate could not be easily installed in the CdS system. Epoxy bonding is not used during the $CuInSe_2$ deposition because the substrate temperature is too high. The CdS window layer is deposited using the hot wall evaporation system, as described previously in section 6.2.1

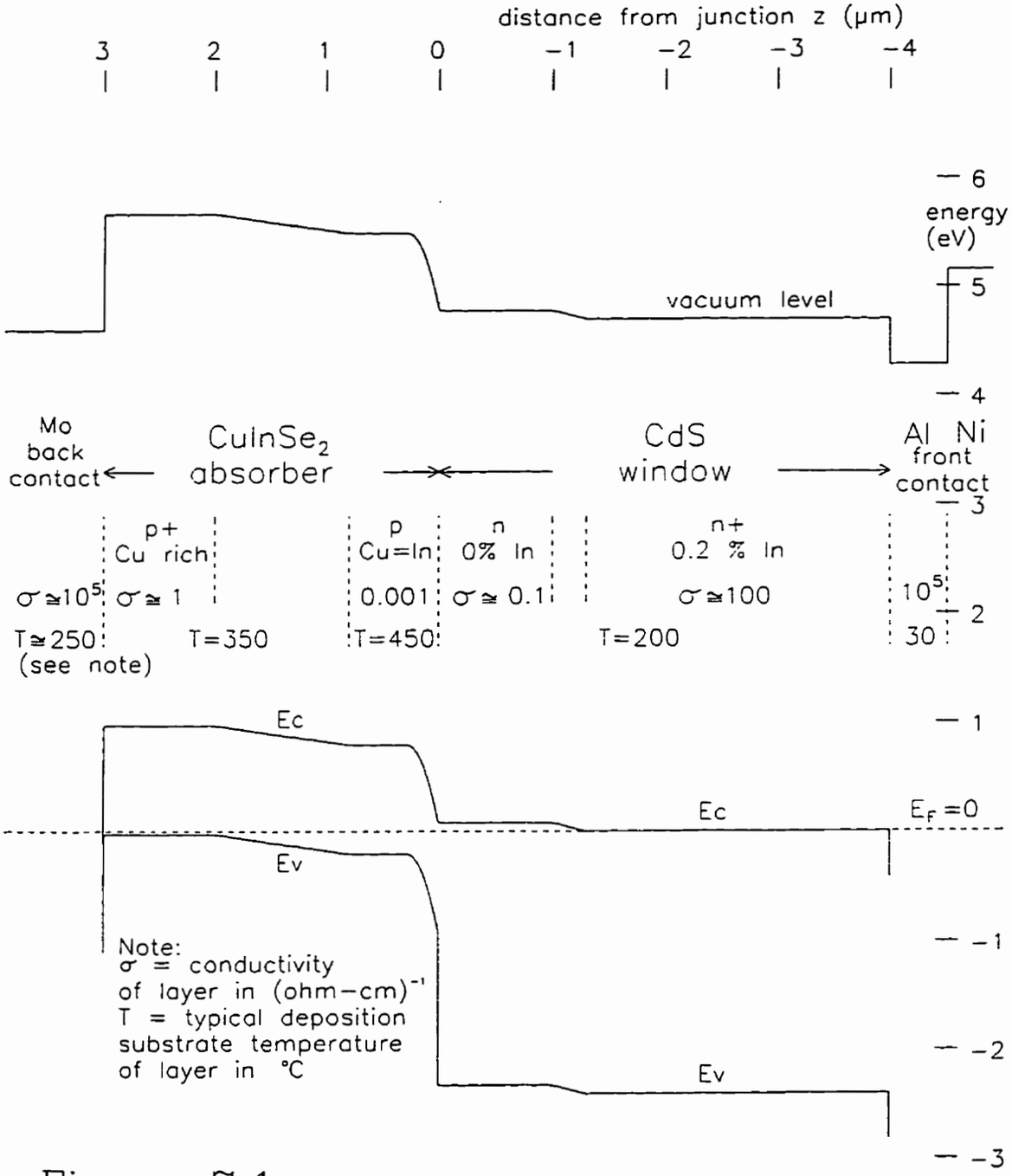

Figure 7.1

Energy diagram for Mo/$CuInSe_2$/CdS/Al/Ni solar cell.
Assumed parameters (energy eV, density cm^{-3}):
Mo: ϕ =4.6 ; Al: ϕ=4.28 ; Ni: ϕ=5.15
$CuInSe_2$: p+=10^{19}, p=10^{16}, E =1, X=4.7
CdS: n+>10^{20}, n=10^{18}, E =2.4, X=4.7
semiconductor dielectric constant =10ε_o

7.1.4 Front Contact Deposition

Before deposition of the top contacts, the epoxy bonded thermocouple is removed from the back surface of the substrate with a rotating wire brush.

The top electrode consists of a layer of aluminum followed by a nickel layer, both deposited by evaporation. Each layer is approximately 0.5 to 1 μm thick. A layer of aluminum is deposited first because it has high conductivity and forms a good ohmic contact with n-CdS. Nickel is used to coat the aluminum because of its resistance to oxidation and because it is harder than the platinum probe wires used for contacting.

For aluminum evaporation, an F2–3x.025W tungsten filament source was used and for nickel evaporation, an S9A–.010W tungsten boat source was used [3]. Typically, the sources must be replaced after two evaporation cycles, because Al and Ni alloy rapidly with tungsten at the high source temperatures used ($T_{Ni} \cong 1800$ °C, $T_{Al} \cong 1500$ °C).

The electrodes are defined by evaporating the metals through thin slits in stainless steel masks. To produce a grid, the mask is rotated 90° and a second evaporation is performed.

7.1.5 Edge Definition and Air Anneal of Solar Cells

After completion of the fabrication process, a stainless steel scribe is used to remove the semiconductor layers around the outer edge of the $CuInSe_2$ layer, down to the Mo layer, and thus define a square active area (typically 3.9 x 3.9 cm^2), slightly smaller than the mask through which the $CuInSe_2$ film is evaporated. The scribing technique is quite practical because the $CuInSe_2$ film does not adhere strongly to the Mo contact. After completion of the scribing process, the solar cell is annealed in air for 15 minutes at approximately 190 °C. The annealing step is required for optimum performance of the finished cell.

7.1.6 Solar cell Deposition Data Records

A data acquisition computer was used to record deposition data for all CdS and $CuInSe_2$ films with sample numbers equal to or greater than 950508. The absorber and window film deposition records for some solar cells of interest are shown in figures 7.2 to 7.7. The source and substrate temperatures, the deposition rates measured at the microbalance crystal, and the shutter position, are shown in each $CuInSe_2$ deposition record. The calibration of the Cu and In sources takes place before the shutter is opened. Prior to the start of deposition, the substrate temperature is raised to 450 °C to bake-out adsorbed water. The In source is at a reduced temperature during the first few minutes of deposition, so that the initial deposition is highly Cu-rich (i.e. $F >> 1$). For all two layer $CuInSe_2$ films (figures 7.2 to 7.6), the substrate temperature is at 450 °C during the first

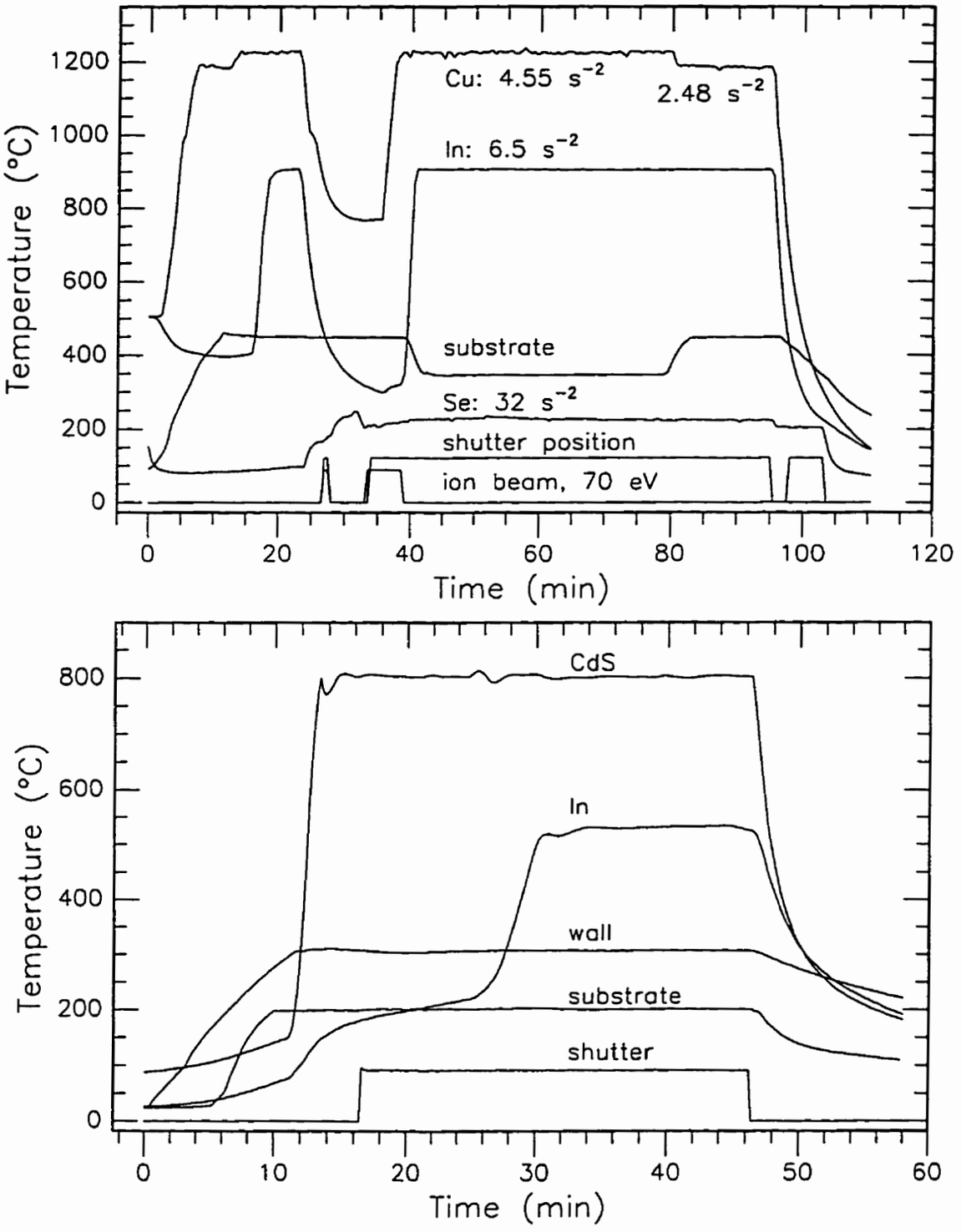

Figure 7.2

Film deposition records for solar cell 951003.
Top, $CuInSe_2$: temperatures, rates, shutter, ion beam.
Bottom, CdS: temperatures, shutter (closed = 0).

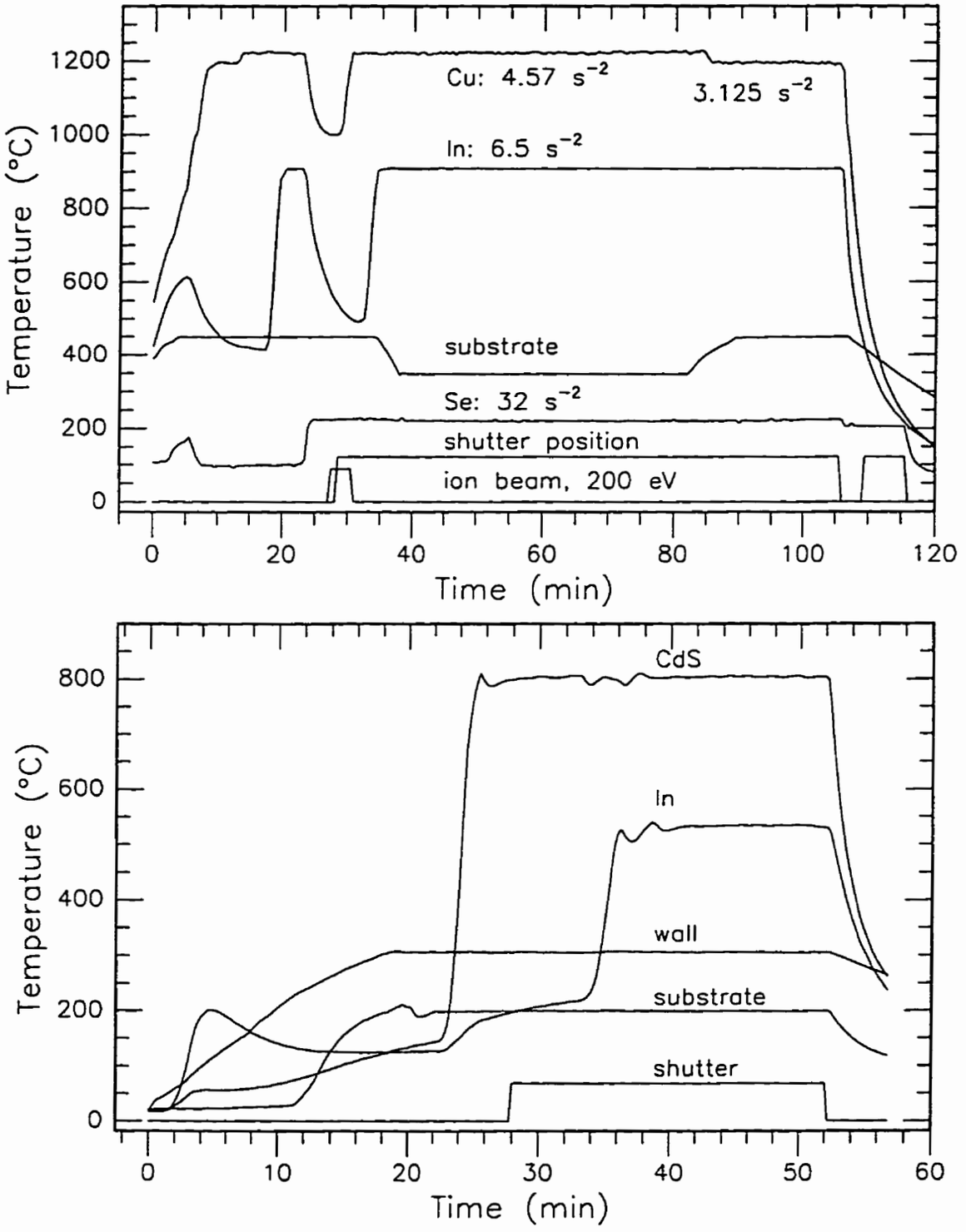

Figure 7.3

Film deposition records for solar cell 951124.
Top: $CuInSe_2$; temperatures, shutter, rates, ion beam.
Bottom: CdS; temperatures, shutter (closed = 0).

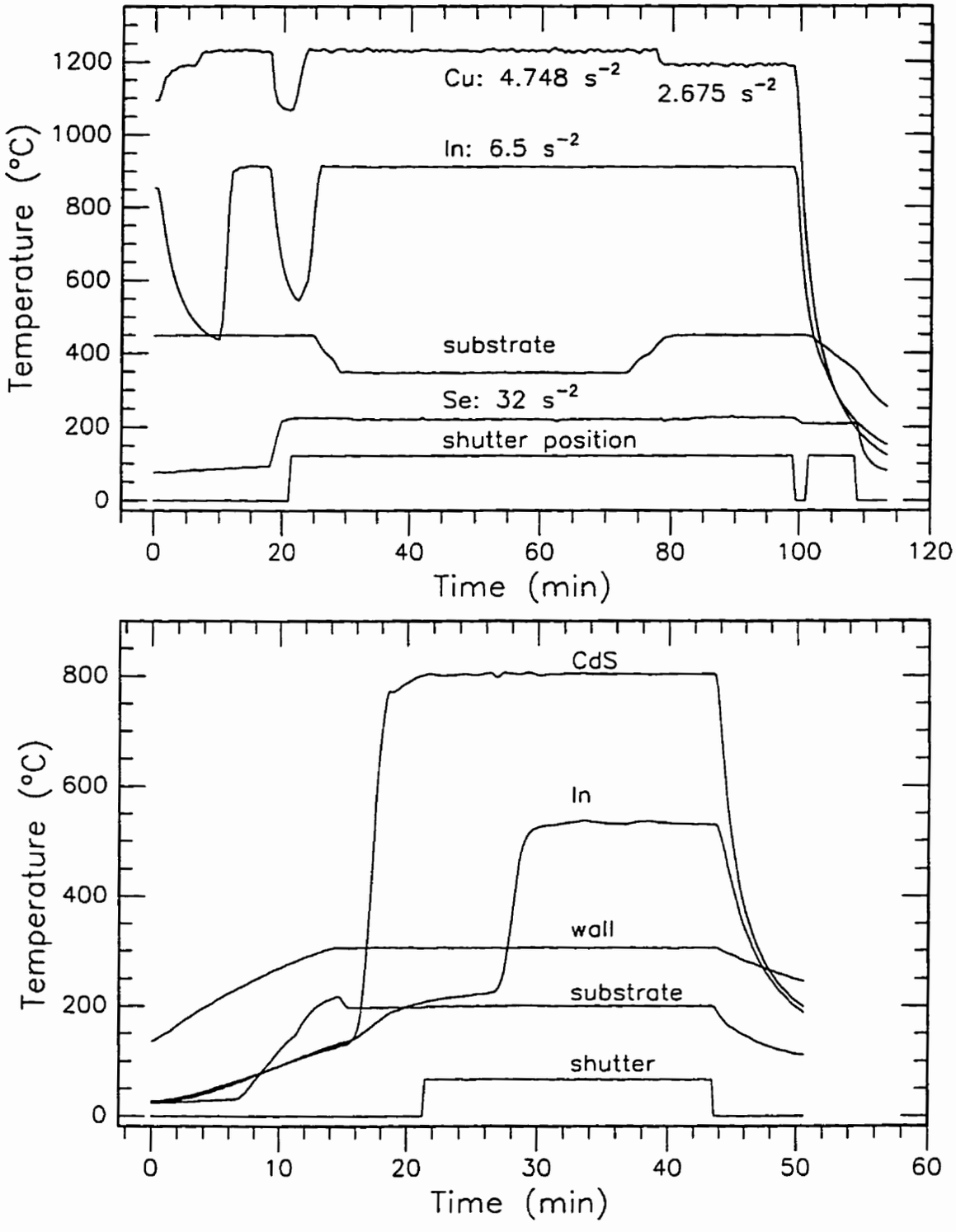

Figure 7.4

Film deposition records for solar cell 951207.
Top: $CuInSe_2$; temperatures, rates, shutter.
Bottom: CdS; temperatures, shutter (closed = 0).

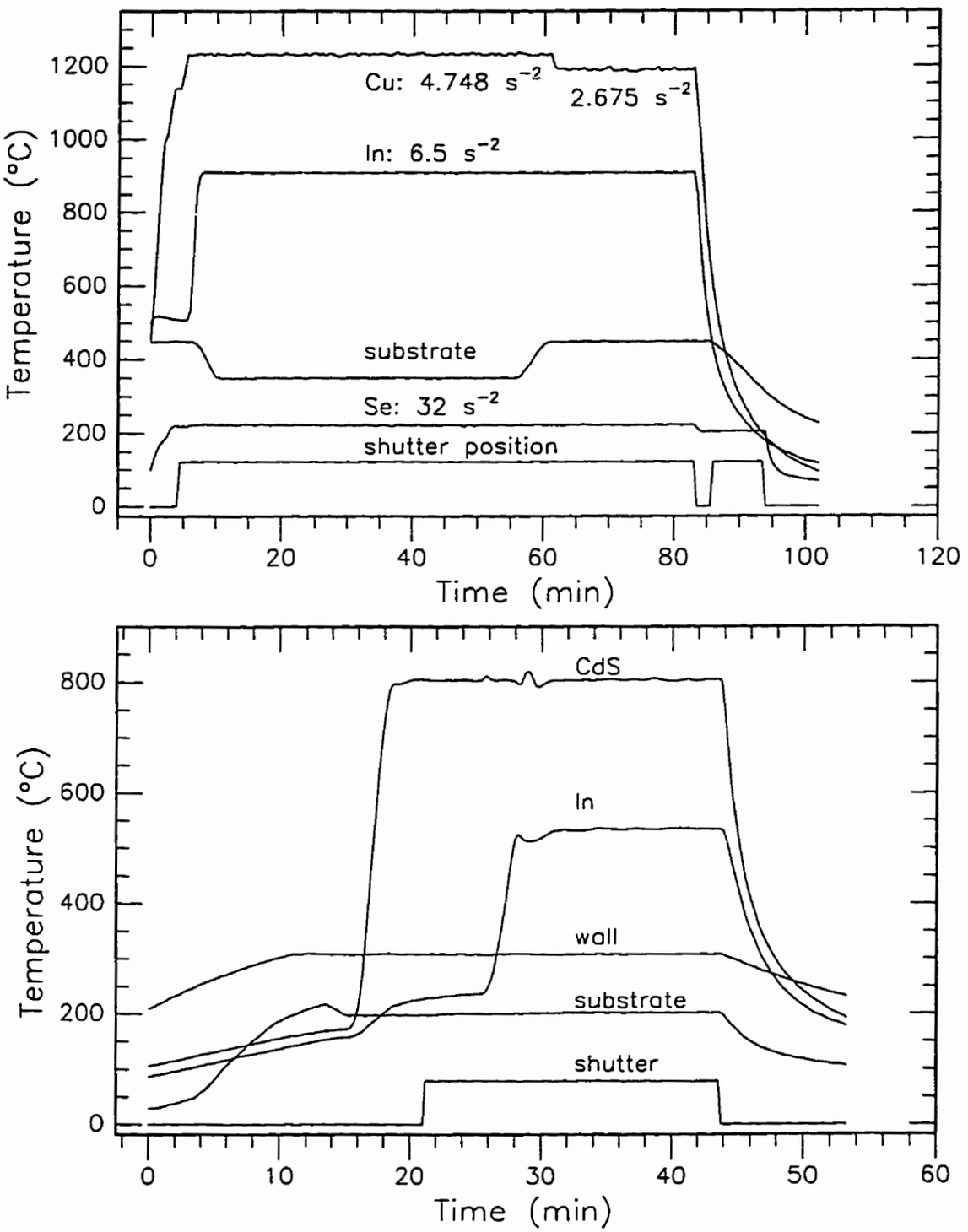

Figure 7.5

Film deposition records for solar cell 960120.
Top: $CuInSe_2$; temperatures, rates, shutter.
Bottom: CdS; temperatures, shutter (closed = 0).

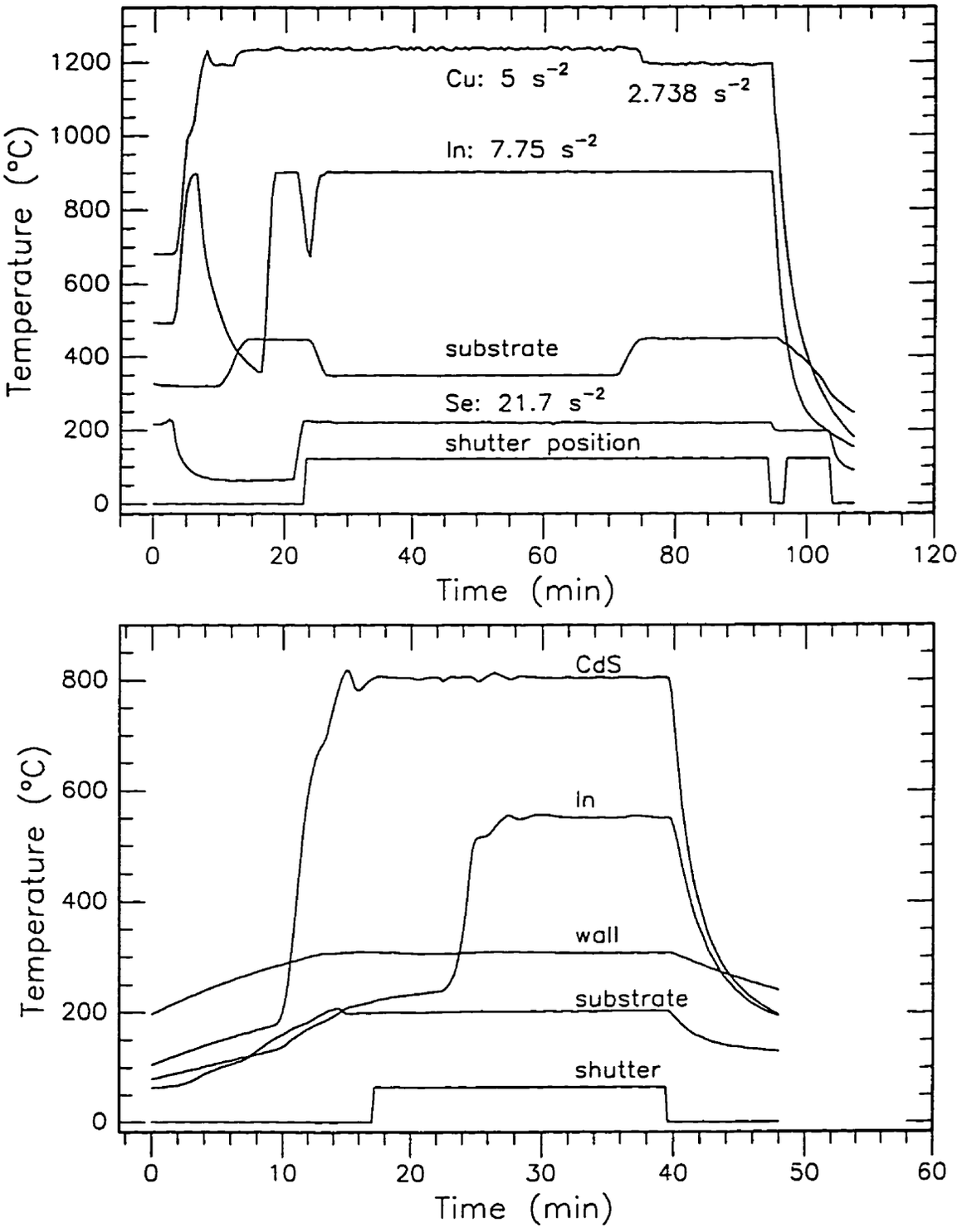

Figure 7.6

Film deposition records for solar cell 960314

Top: $CuInSe_2$; temperatures, rates, shutter

Bottom: CdS; temperatures, shutter (closed = 0)

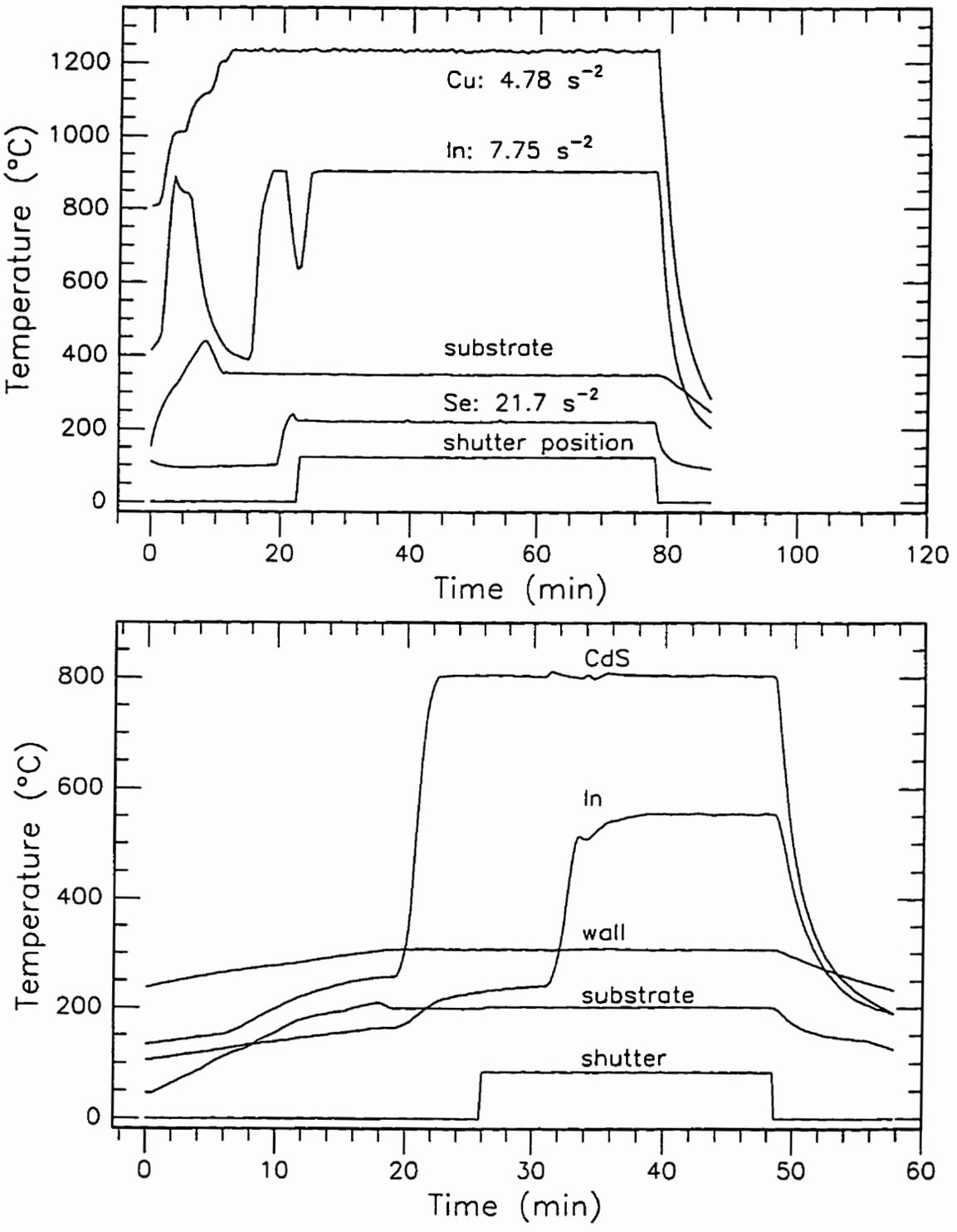

Figure 7.7

Film deposition records for solar cell 960316.
Top: $CuInSe_2$; temperatures, rates, shutter.
Bottom: CdS; temperatures, shutter (closed = 0).

few minutes of growth, to improve film adhesion. The substrate temperature is reduced to 350 °C for the remainder of the Cu-rich bottom layer, then the Cu source temperature is reduced and the substrate temperature increased to 450 °C for the In-rich top layer. At the end of a two layer deposition, the Cu and In sources are cooled, and the shutter is re-opened while the Se source is still on, in order to reduce Se loss from the film as the substrate cools to 300 °C. In figure 7.2, a 70 eV argon ion beam was used to pre-clean the Mo surface at t ≅ 27 min. In figures 7.2 and 7.3, ion beam assisted deposition is used during the first few minutes of film growth, to improve adhesion of the $CuInSe_2$ film. In figure 7.7, a single layer film is deposited, so the Cu source temperature and substrate temperature are held constant during the entire time the shutter is open.

The solar cell device number is the same as the sample number of the $CuInSe_2$ absorber film in the cell. Deposition data for some select solar cells are listed in table 7.1.

7.2 Solar Cell Optimization

The solar cell fabrication method outlined in section 7.1 and the film deposition techniques described in detail in chapters 2 and 6 were developed concurrently during a deliberate effort to produce energy efficient solar cells. The first solar cells had nearly ohmic current-voltage characteristics (fill factor ≅ 0.25) and energy efficiency less than 0.05%. The major causes of low cell performance were identified through experimentation, and study of the relevant literature. As the problems were corrected, typical device efficiency improved. The deposition conditions, substrate material, film thickness etc. for all of the $CuInSe_2$ films are listed in appendix A, and similar data for CdS is in appendix B. The measured solar cell parameters and calculated efficiencies are listed in appendix C. Brief descriptions of the major problems encountered and the necessary changes and improvements made are described below.

7.2.1 Improving the $CuInSe_2$ Films

The first $CuInSe_2$ films were deposited using commercial crucible sources and manual control of source temperatures. Manual control and crude thermocouple mounting schemes do not allow the precise control of evaporant temperatures needed for the growth of good quality $CuInSe_2$ films. The solution of the evaporation rate problem is the subject of chapter 2. Sample 950830 was the first film made after the source temperature control problems had been eliminated.

The first substrate heater was an electrically heated solid copper block in contact with the substrate. A thermocouple passes through a small access hole in the block and is bonded to the back surface of the substrate with epoxy. A feedback temperature controller was designed, with an error amplifier controlling a DC power supply. The error amplifier

Table 7.1: $CuInSe_2$/CdS Solar Cell Deposition Data

device # (y-m-d)	Cu rate (Hz/s)	Cu time (min)	Indium rate (Hz/s)	Indium time (min)	dep. ratio F	thick $CuInSe_2$ (micron)	thick CdS (micron)	total area (cm^2)	comments
951003b	4.55	42.5	6.5	39.5	1.247	1.62			70 eV ion beam bonding to Mo
951003t	2.48	15	6.5	15	0.632	0.51			first large junction area device
951003					1.078	2.13	5.58	15.1	first device > 1% efficient
951023b	4.749	41.5	6.5	41.5	1.210	1.69			top 0.1 micron of Mo contact
951023t	2.59	25	6.5	25	0.660	0.86			is partly oxidized for adhesion
951023					1.003	2.54	3.84	15.1	cell has high series resistance
951025b	4.749	35	6.5	35	1.210	1.42			top 0.1 micron of Mo contact
951025t	2.59	30	6.5	30	0.660	1.03			is partly oxidized for adhesion
951025					0.956	2.45	3.83	15.1	cell has high series resistance
951111b	4.57	58.5	6.5	58.5	1.165	2.35			top 0.1 um of Mo deposited
951111t	3.125	22	6.5	22	0.796	0.79			in normal sputter mode
951111					1.064	3.7(w)	4.00	15.1	to improve adhesion
951121b	4.57	55	6.5	50.5	1.268	2.09			200 eV ion beam bonding to Mo
951121t	3.125	19	6.5	19	0.796	0.68			
951121					1.139	2.77	4.19	15.1	
951124b	4.57	55.5	6.5	51	1.267	2.11			200 eV ion beam bonding to Mo
951124t	3.125	20.5	6.5	20.5	0.796	0.73			
951124					1.132	3.09 (w)	4.49	15.1	
951207b	4.748	55	6.5	52.5	1.267	2.17			sodalime glass substrate
951207t	2.675	21	6.5	21	0.682	0.72			highest efficiency
951207					1.100	3.41(w)	3.94	14.4	poor Mo adhesion to glass
951209b	4.748	55.5	6.5	52	1.291	2.16			sodalime glass substrate
951209t	2.675	21.5	6.5	21.5	0.682	0.74			poor Mo adhesion to glass
951209					1.113	3.27(w)	3.66	14.4	
960113b	4.748	56	6.5	54.5	1.243	2.24			for w<0 cm, Mo coated substrate
960113t	2.675	21.5	6.5	21.5	0.682	0.74			dipped in 0.1 M NaOH in ethanol
960113					1.084	2.98	3.95	10.0	for w>0, only 20% adhesion
960120b	4.748	56	6.5	54	1.255	2.23			NaOH evaporated for w>1 cm,
960120t	2.675	22	6.5	22	0.682	0.76			to obtain 3.5% sodium doping
960120					1.089	2.98	4.41	3.7	$CuInSe_2$ peeled off elsewhere
960314b	5	51.5	7.75	50.5	1.189	2.23			0.5% NaOH at y<-2.54 cm,
960314t	2.738	19.5	7.75	19.5	0.638	0.72			1% NaOH at y>-2.54 cm
960314					1.035	3.16(w)	3.96	11.1	30% $CuInSe_2$ adhesion, at y>-2.54
960316	4.78	55	7.75	54	1.135	2.49(w)	4.17	15.1	1% NaOH at y>-2.54 cm

Notes:

Suffixes "b" and "t" are bottom and top layer of CuInSe2 ; No suffix pertains to entire device.

Total area is after any peeling of $CuInSe_2$; bottom layer substrate T= 350 C, top layer T = 450 C.

All devices on Corning 7059 glass except 951207 and 951209 which are on sodalime glass.

All $CuInSe_2$ thicknesses calculated except where indicated by "(w)" which are by weight.

All CdS thicknesses are determined by weight; All Mo films are approximately 1 micron thick.

Rates are at crystal; multiply Cu/In rate ratio by .9167 to obtain F at substrate, prior to 960314

compares the substrate thermocouple voltage with a reference voltage. A thermal contacting grease is required for good heat transfer to the substrate. At higher temperatures (>250 °C), silicone grease and epoxy cannot be used, so instead, a higher block temperature was used, allowing radiation heat transfer. The thermocouple was attached to a small stainless steel cylinder and held against the substrate by a weight. The cooling time constant of the heater block in vacuum is of the order of hours. More rapid temperature control is needed for depositing the two layer $CuInSe_2$ films used in the best solar cells. Fast heating is required to raise the substrate temperature from 350 °C to the 450 °C necessary for the deposition of the second layer. If the heating rate is too slow, the evaporation sources would have to be temporarily switched off to conserve source material. Fast substrate cool-down at the end of the deposition is required to minimize Se loss, which could convert the film from p to n-type.

A radiation heater was therefore designed, consisting of 0.01 inch tungsten wire wound on two ceramic rods placed inside a radiation reflector about 2 cm apart and about 1.5 cm from the back of the substrate. The thermocouple is placed inside a radiation shield tube and indium metal is used for thermal contact between the thermocouple and the substrate. The tungsten wire is heated to incandescence by the DC power supply of the temperature controller described above. Sample 950126 is the first film made using the radiation heater and indium contacted thermocouple. Sample 950901 is the first film for which evaporation from the Se source was maintained for $T_s > 300$ °C during substrate cool-down, in order to reduce Se loss from the finished film.

As the deposition process became more sophisticated, it became very difficult to manually record data. A simple program was written, based on existing subroutines and hardware, which commands a data acquisition computer to record up to eight analog, differential input channels with independently selected gains and a specified sampling interval. This was used to record all temperatures, the shutter position and, if required, the ion-beam status for all $CuInSe_2$ samples after 950407.

After sample 950508, the vacuum chamber was completely disassembled and all internal surfaces cleaned, including the diffusion pump and cold trap. At this time, it was discovered that the output port from the pumping stack in the diffusion pump was not aligned with the foreline pipe. This may have caused increased base pressure and back-streaming. The original motivation for the cleaning was to remove possible contaminants such as Zn and Cd (donors in $CuInSe_2$ [4]) which were used in the same chamber by previous students.

The mechanically complex combination of shutter and mask changing carousel initially installed in the chamber was unnecessary and very difficult to clean and to use, so it was

removed. A much simpler system was constructed in which a single shutter covers the microbalance crystal, or the substrate, or neither, with no in-situ mask changing capability. The crystal was moved into the plane of the substrate and much closer to the substrate. The Cu and In sources were moved as close together as possible. This configuration, shown in figure 2.16 (a), was used for samples 950708 to 960123. An intermediate configuration (not shown) was used for samples 960218 and 960221. After 960221, the sources were moved to the final configuration of figure 2.16 (b).

After sample 950906, the fused silica (quartz glass) chimney used around the Cu source was replaced with a tantalum tube, because of concerns about possible doping of the $CuInSe_2$ film with SiO_x.

7.2.2 $CuInSe_2$ Adhesion to the Mo Contact

The problem of Mo adhesion to the glass substrate and its solution have been briefly discussed in section 6.1.2. Mo to glass adhesion failures became a problem only after the means for producing high purity Mo films were developed. As the purity of the Mo was increased, $CuInSe_2$ to Mo adhesion failures began to occur frequently, particularly for two layer, thick films on Mo coated 7059 glass substrates. In some cases more than 95% (listed as 5% adhesion in appendix A) of the $CuInSe_2$ film area peeled from the Mo while the film was still in the vacuum chamber. The problem of adhesion of $CuInSe_2$ to Mo has been reported elsewhere [5, 6]. Some proposed solutions include using a mixed 70% Mo, 30% Cu contact electrode formed by co-sputtering of Mo and Cu [7], or the addition of a thin layer of Ga at the interface [8].

The Ga bonding technique was attempted here several times. The indium source is removed and an alumina (Al_2O_3) crucible containing Ga is installed in its place. Typically the Mo surface of the substrate is sputter cleaned with a 200 eV argon ion beam to remove oxides before deposition of a 15 nm Ga film. Then the chamber is opened, the Ga source is removed and the In source re-installed, and a $CuInSe_2$ film is deposited. The Ga layer did not improve adhesion, as indicated in appendix A (samples 950826, 950830, 950901, 950905, 950913, 950915).

In a different approach to solving the adhesion problem, a thin layer of partly oxidized Mo was used to bond the $CuInSe_2$ to the high purity Mo. The oxygenated layer is produced by switching from bias sputter mode to normal sputter and introducing a controlled air leak for the top 0.1 μm of the Mo film. If the additional specific contact resistance is due only to the bulk resistance of a 0.1 μm layer of oxygenated Mo of conductivity $\cong 10^4\ \Omega^{-1}cm^{-1}$, there should be a negligible ($10^{-9}\ \Omega cm^2$) increase in solar cell specific series resistance. (specific resistance is defined by V=JR). However when solar cells (951023, 951025) are

made with the oxygenated Mo bonding layer, excellent adhesion is obtained, but the series resistance increase is of the order of 10 Ωcm^2. (see figures 7.11 and 7.17 below). The dramatic increase in contact resistance occurs because the size of the energy barrier for hole transport from the metal contact to the p-$CuInSe_2$ depends on the work function of the contact metal. Oxidizing the Mo reduces the work function from the maximum ϕ=4.6 eV of pure Mo. For pure Mo on p-$CuInSe_2$ single crystals with $N_A=2x10^{16}$ cm^{-3} , a 0.8 eV barrier is observed [9]. For the heavily doped ($N_A \cong 10^{19}$ cm^{-3}) Cu rich $CuInSe_2$ used at the Mo contact in solar cells, the barrier height and width are reduced so that a nearly ohmic contact is obtained [10]. The barrier height at the $CuInSe_2$/Mo interface in a solar cell is about 0.5 eV [11], and the specific contact resistance has been determined to contribute a negligible 0.021 Ωcm^2 to the total specific series resistance R_s=0.9 Ωcm^2 of a 10.7% efficient device [12].

It was found that $CuInSe_2$ to Mo adhesion is improved if the Mo/7059 substrate is argon ion bombarded [13] and the deposition is Cu-rich (F>>1) during the initial phase of film nucleation and growth. Copper rich films generally adhere better, and provided that the sputter rate is less than the deposition rate, the extra energy provided by the ion beam should promote the formation of Mo-Se chemical bonds. This method was successfully applied to device 951003, at a beam energy of 70 eV, and to devices 951121 and 951124 at 200 eV (see figures 7.2, 7.3). The approximate sputter rate as a function of beam voltage is shown in figure 7.8. This was determined experimentally by monitoring the microbalance crystal frequency while sputter etching the accumulated Cu+In+Se mixture from the surface of the crystal. The order of magnitude of the ion beam current density J_{ion} at the crystal can be estimated using

$$J_{ion} = \frac{q}{YM} \times (\text{mass etch rate per unit area})$$

where Y is the sputtering yield (sputtered atoms/ion), M is the mass of the sputtered atoms and q is the electron charge. Assuming Y $\cong$ 1 at 600 eV ion energy [14], M = atomic mass of Se and using a mass etch rate of $7x10^{-8}$ $gcm^{-2}s^{-1}$ from figure 7.8, we obtain $J_{ion} \cong 85$ μAcm^{-2}. This can be compared with $J_{ion} \cong 250$ μAcm^{-2} calculated for a 20 mA ion current, assuming that the beam cross-section diverges to 10 cm diameter at the plane of the crystal. From the data in Appendix A, for 951003, 951111, and 951124, the typical film deposition rate is 3.6 $x10^{-7}$ $gcm^{-2}s^{-1}$, which is much greater than the maximum sputter rate measured.

All $CuInSe_2$ films deposited on Mo/soda-lime adhere well, without any special bonding techniques. This may be due to better matching of the thermal expansion coefficient of $CuInSe_2$ ($8.32x10^{-6}$ and $7.89x10^{-6}$ K^{-1} for a and c axis, respectively [15]) to soda-lime glass ($9.2x10^{-6}$ K^{-1}) than to 7059 glass ($4.6x10^{-6}$ K^{-1}). Another possibility is that the

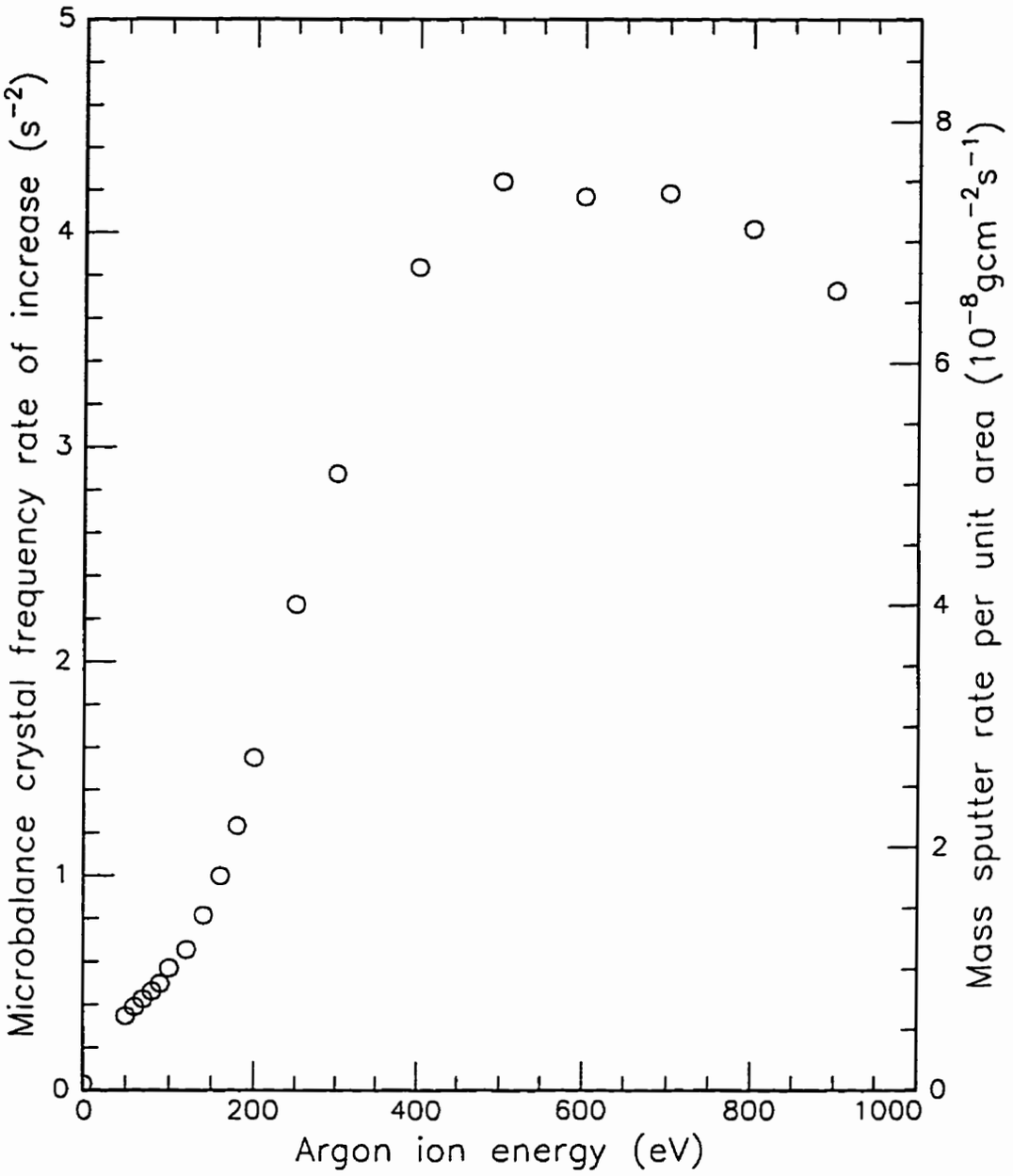

Figure 7.8

Ion sputter etch rate vs. argon ion energy for sputter etching Cu/In/Se mixture from crystal microbalance. Ion current 20 mA, estimated ion current density is about 100–300 μAcm^{-2}.

sodium which diffuses through the Mo from the substrate chemically assists adhesion [5]. This is in agreement with the fact that all $CuInSe_2$ films deposited on NaOH/Mo/7059 adhere well, with the exception of 960314 where only 30% of the film area adhered on the half of the substrate coated with 1% NaOH. In the case of cell 960120, the $CuInSe_2$ peeled everywhere, except for the 1/4 of the total film area where 3.5% NaOH was deposited. For 960113, 100% adhesion was obtained on the half of the substrate area that had been dipped in NaOH/ethanol solution, whereas the indium rich portion of the sodium free half peeled off.

The rate at which sodium diffuses through Mo depends on the crystallite packing density of the Mo film. Mo films sputter deposited at 10 mTorr argon pressure are more porous than those deposited at 0.5 mTorr. SIMS profiles have shown that during $CuInSe_2$ deposition at 450 °C on the Mo film, Na accumulates at both $CuInSe_2$ surfaces, with up to 10% Na in the 20nm thick region near the $CuInSe_2$ top surface [16]. The final Na impurity level in the $CuInSe_2$ does not depend on the porosity of the underlying Mo film, which suggests that the limits to Na transport are thermodynamic, rather than kinetic .

As shown in figure 7.17 below, the sodium containing devices (951207, 960120, 960314) have somewhat lower specific series resistance than those deposited on Mo/7059 substrates without sodium doping. This could be because Na increases the net acceptor density in the $CuInSe_2$ [17]. This would lower the bulk $CuInSe_2$ resistance, as well as the contact resistance at the Mo.

7.2.3 Improving the CdS Films

Many solar cells were ruined by the deposition of a low quality CdS window layer. The first CdS films were deposited without a shutter between the substrate and the CdS source, so that the surface was exposed to out-gassed impurities during the initial CdS source warm-up. The solar cell J-V curves were basically straight lines (ohmic), probably because of large interface recombination current. After the installation of a preliminary crude shutter in the CdS system, diode type J vs.V curves and a 5 to 10 fold increase in energy efficiency were obtained (see appendix C).

Next, the CdS vacuum system was dis-assembled, in order to clean the system, repair leaks, install additional thermocouple feed-throughs, install type (f) sources for both the CdS and indium doping sources, install a rotary mechanical feed-through for the shutter and a properly designed hot wall enclosure. Even after these improvements, uniform CdS films of a specified thickness and conductivity could not be deposited reproducibly. The problem was solved after the aluminum contact heater block was removed and replaced with a tungsten lamp radiation heater. The radiation heater allows direct viewing of the

film nucleation and growth process when a plain glass substrate is used. A series of experiments (950928 to 951006b, see section 6.2.3 and appendix B) revealed that uniform films cannot be obtained with ALFA CdS, but when ESP CdS is used, uniform high quality films are consistently obtained.

Previously, the solar cell CdS window layers had been deposited through a mask with holes to produce a 4 x 4 array of small (8 mm diameter) cells. With the introduction of ESP CdS, the mask was eliminated in favor of depositing one large (3.9x3.9 cm^2) solar cell, with the option of selecting a smaller area device by scribing through the semiconductor to the Mo contact. Device 951003 was the first large area device made with ESP CdS and the first device with energy conversion efficiency greater than 1%.

The thickness of CdS films could not be measured with a stylus type surface profiler, since the large pressure at the stylus tip damages the film. Therefore, after CdS film 951004, the substrates were weighed before and after deposition and the film thickness was calculated from the measured film mass, the area, and the bulk density of CdS. The same technique was adopted for $CuInSe_2$ (after 951025) and Mo films (after 951109).

7.3 Solar cell characterization

7.3.1 Heterojunction Energy Diagram and Circuit Model

An idealized energy diagram of a $CuInSe_2$/CdS heterojunction solar cell is shown in figure 7.1. The difference in the energy gaps of the two compounds requires that there be a discontinuity at the metallurgical interface in either or both of the bands. Estimates of the conduction band discontinuity ΔE_c (in eV) taken from the literature are given in table 7.2, where $\Delta E_c > 0$ indicates that the conduction band minimum at the interface is higher in the CdS than in the $CuInSe_2$ (i.e. a "spike" occurs in the conduction band).

As seen in table 7.2 , there is considerable uncertainty in the value of ΔE_c. In figure 7.1, $\Delta E_c = 0$ is assumed. The presence of a "spike" in the conduction band ($\Delta E_c > 0$), does not necessarily result in poor solar cells. Numerical solutions of Poisson's equation and the continuity equations for the heterojunction **[18, 19]** show that, for the assumption of transport dominated by recombination either at the interface or in the $CuInSe_2$ depletion region, solar cell efficiency is not significantly affected for $0 < \Delta E_c < 0.4$ eV.

For photon energies less than the band gap of the CdS window (2.4 eV) and greater than the bandgap of the $CuInSe_2$ absorber (1 eV), carrier generation takes place in the absorber. Since $CuInSe_2$ has a very high absorption coefficient, most of the generation takes place in the absorber depletion region. This is contrary to the case of indirect gap Si solar cells, where most generation takes place outside the depletion region, so that large

minority carrier diffusion lengths are needed for good quantum efficiency. For photon energies greater than the CdS bandgap, most holes generated in the n-CdS window layer do not reach the junction because the optical absorption length and hole diffusion length are much less than the window layer thickness. The large energy barrier in the valence band prevents significant hole transport from the p to n side of the junction, even if the device is forward biased. Thus electrons dominate transport across the junction.

Table 7.2: Measurements of Conduction Band Discontinuity ΔE_c

ΔE_c (eV)	Method used to determine ΔE_c	Ref.
–0.08	extrapolate V_{oc} vs. T to T=0, to determine diffusion potential.	[20]
–0.28	difference between electron affinities of $CuInSe_2$ and CdS	[23]
–0.03	determine valence band discontinuity ΔE_v by measuring valence band maxima relative to Ge by synchrotron-radiation photoemission as Ge is deposited on single crystals of the compounds, then calculate ΔE_c from ΔE_v and the energy gaps.	[21]
1.08	determine ΔE_v by monitoring synchrotron-radiation photoemission spectrum as CdS is deposited on single crystals of $CuInSe_2$	[22]
0.31	calculated by linear augmented plane wave method	[23]
0.28	ultraviolet light photoelectron spectroscopy to determine valence band maxima relative to Ge, as in [21]	[24]
0.7	synchrotron-radiation photoemission as CdS is deposited on $CuInSe_2$ single crystals cleaved in vacuum	[25]
0.32	x-ray photoemission spectroscopy while sputtering through CdS/$CuInSe_2$ heterojunction	[26]

For a given carrier generation function and boundary conditions, the transport equations for electrons and holes are solved to obtain the carrier concentrations n and p. The total current density J(V) can then be calculated as the sum of the diffusion and drift components of electron and hole current at any convenient plane parallel to the junction. If the diffusion constant, electric field and minority carrier lifetime are independent of carrier density, then the transport equations are linear in carrier density. In this case the carrier densities at any point can be written as the sum of the densities due to processes which occur in the dark and processes which occur in the light, and the current density J(V) can be considered as the superposition of dark and light current densities [27]. In general the light current is bias voltage dependent, but in the case of an ideal solar cell, it is assumed to be independent of bias. An illuminated ideal solar cell is modeled as a diode, forward

biased by a parallel-connected, constant current source which represents the light-generated current. The current density vs. voltage relation for the ideal solar cell is

$$J(V) = J_D(V) - J_L \qquad (7.1)$$

The diode current density J_D is independent of light intensity, and the light current density J_L is proportional to light intensity (for a given spectral distribution) and independent of bias voltage. A good quality single crystal Si solar cell is represented well by the ideal model. For the Si cell, the diode current transport is dominated by minority carrier injection into the quasi-neutral regions (QNR), and subsequent diffusion and recombination in the QNR. (Shockley diode model [28]).

In many non-lattice-matched heterojunctions such as CdS/$CuInSe_2$, the quantum efficiency and therefore the light current density, depend on bias voltage, so that

$$J(V) = J_D(V) - J_L(V) \qquad (7.2)$$

A realistic solar cell model must also include shunt R_p and series R_s specific resistances. With shunt and series resistance included the solar cell current is given by:

$$J(V) = J_D(V - JR_s) + \frac{V - JR_s}{R_p} - J_L(V - JR_s) \qquad (7.3)$$

For cases where the shunt current dominates the current flow at small V, the shunt resistance R_p can be obtained from the slope of the dark J vs. V at V= 0:

$$\left.\frac{dJ}{dV}\right|_{V=0} \cong \frac{1}{R_p}$$

For good quality $CuInSe_2$/CdS cells, the dominant diode current transport mechanism is believed to be carrier recombination in the $CuInSe_2$ space charge region [19, 29, 30], not interface recombination or minority carrier injection into the QNR. As seen in figure 7.1, the $CuInSe_2$ absorber is inverted at the interface (from p to n type) so that most interface states are below the Fermi level and therefore occupied by electrons. The interface recombination rate is thus controlled by the hole concentration at the interface. The hole concentration at the interface is small because of the absorber inversion, and because holes generated in the absorber are drawn away from the interface by the space charge electric field. For transport dominated by electron recombination via gap states in the absorber space charge region, the diode current density is given by

$$J_D(V) = J_0\left(\exp\left(\frac{qV}{AkT}\right) - 1\right) = J_{00}\exp\left(-\frac{E_g}{2kT}\right)\left(\exp\left(\frac{qV}{AkT}\right) - 1\right) \qquad (7.4)$$

where E_g is the $CuInSe_2$ energy gap, A is the diode ideality factor with A=2 for recombination states at mid-gap and $1 < A < 2$ for an exponential distribution of states

[29]. For the case of mid-gap recombination states, J_{00} is proportional to the density of gap states, and varies slowly with temperature [11].

7.3.2 Measurement of Current vs. Voltage characteristics:

The current vs. voltage data were obtained using the apparatus shown in figure 7.9. The current flows through four parallel connected platinum wires at the top Ni grid, and three alligator clips at the Mo back contact. Separate voltage measurement probes were used, so that the voltage drops across the resistances of the current sourcing wires and contacts to the cell are not included in the measured voltage. A rudimentary solar simulator, consisting of a 75 watt tungsten-halogen flood lamp and a water infra-red filter was used. The height of the lamp above a small (0.5 cm^2) $CuInSe_2$/CdS reference solar cell was adjusted so that the short circuit current at the maximum intensity position in the horizontal plane containing the cell, is equal to the short circuit current measured in bright sunlight with the same cell. This intensity is then referred to a commercial Si photodiode (Hamamatsu S1226-8BQ, 0.34 cm^2) for subsequent calibrations. Since the intensity decreases as one moves away from the lamp optical axis, for larger cells the simulator tends to produce a somewhat lower integrated intensity, and hence a lower light current than would actually be obtained in sunlight. The simulator is equivalent to AM1.5 (83.18 $mWcm^{-2}$ [10]) sunlight , with uncertainty +0%, –30%.

Figures 7.10-7.15 show the external current density J vs. applied external voltage V for $CuInSe_2$/CdS solar cells at room temperature, both in the dark and under illumination with the solar simulator. J is determined by dividing the total current measured at the cell terminals by the total junction area. J–V plots immediately before and after annealing in air for 15 minutes at 190 °C are shown.

7.3.3 The Effect of Air Annealing

The improvement in cell performance after air annealing is attributed to passivation of Se vacancy donor defect states V_{Se} at the $CuInSe_2$ grain surfaces by oxygen [31,32]. Selenium vacancies at the $CuInSe_2$ surface donate two electrons which are delocalized by recombination with valence band holes in the case of p-type material, or by direct admission to the conduction band in n-type material. The release of the two electrons into the band results in a localized positive surface charge at the In atom associated with the V_{Se}. The oxygen atoms of a physisorbed O_2 molecule can each acquire two electrons from the band, and with thermal activation, become chemisorbed by two In-O chemical bonds at the In atoms of a pair of adjacent V_{Se} sites. Thus the originally donated electrons are removed from the band and incorporated into the In-O bonds. The two donor defects are effectively eliminated.

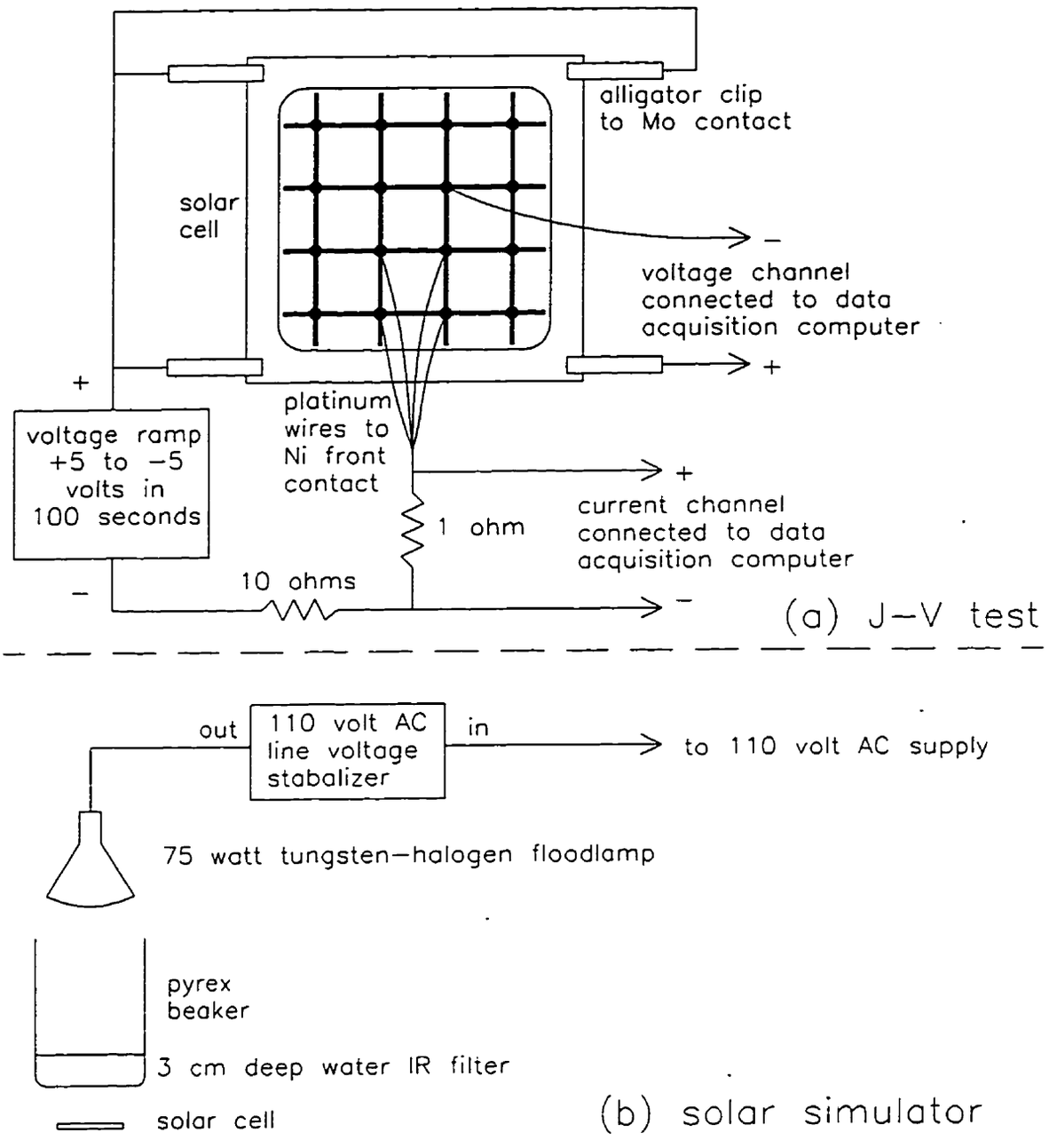

Figure 7.9

(a) J−V test connections. Voltage polarities are shown for forward bias in the dark. The platinum probe wires are positioned with micro−manipulators (not shown). (b) The solar simulator used for indoor tests. The height of the lamp is adjusted to give intensity such that the short circuit current of a $CuInSe_2$/CdS standard cell is the same as in bright sunlight.

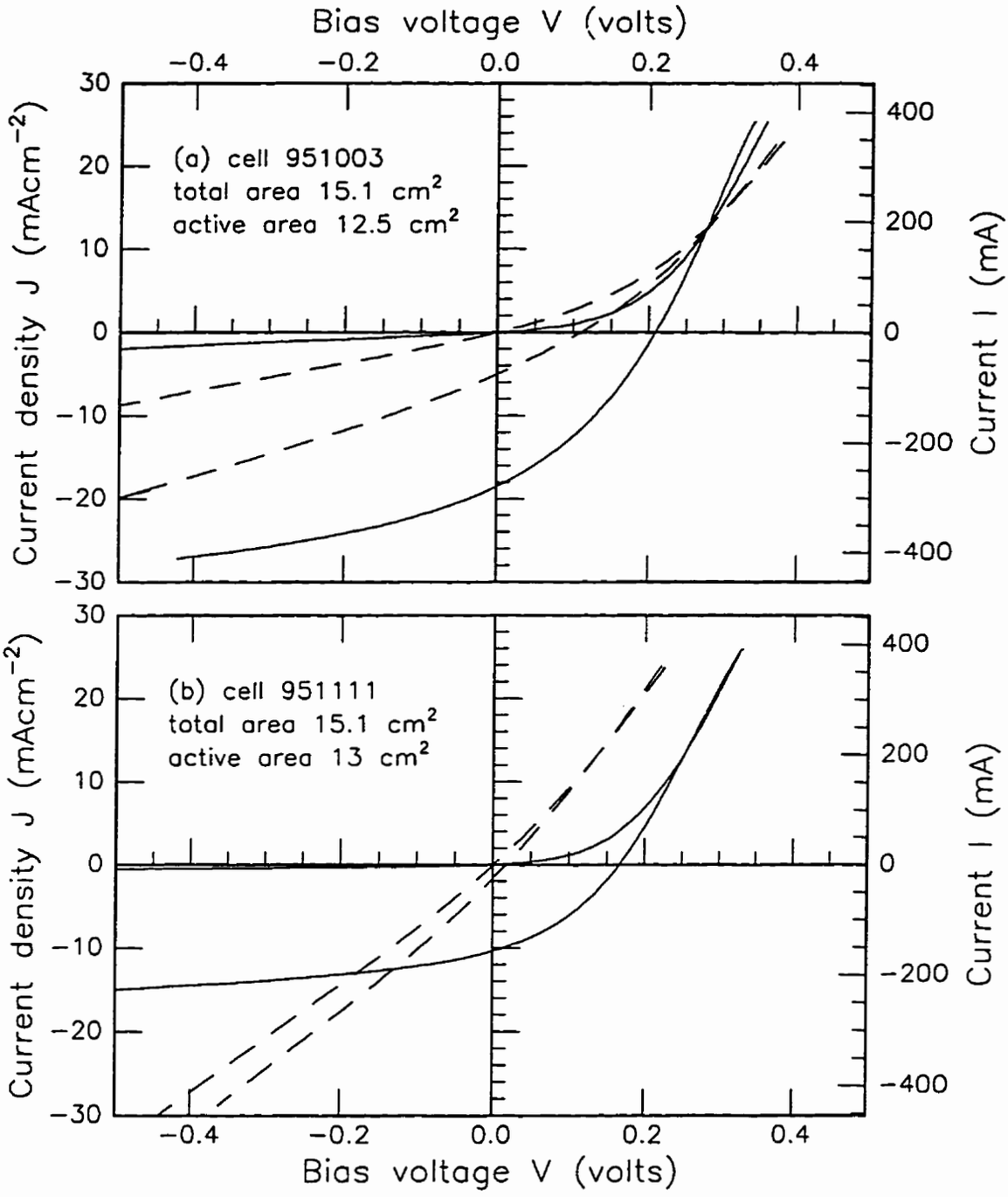

Figure 7.10

Dark and light J vs. V of $CuInSe_2/CdS$ solar cells, before (broken curves) and after (solid curves) air anneal. Simulated AM1.5 sunlight, T_{sub}=22°C, Corning 7059 glass substrate, 0% Na

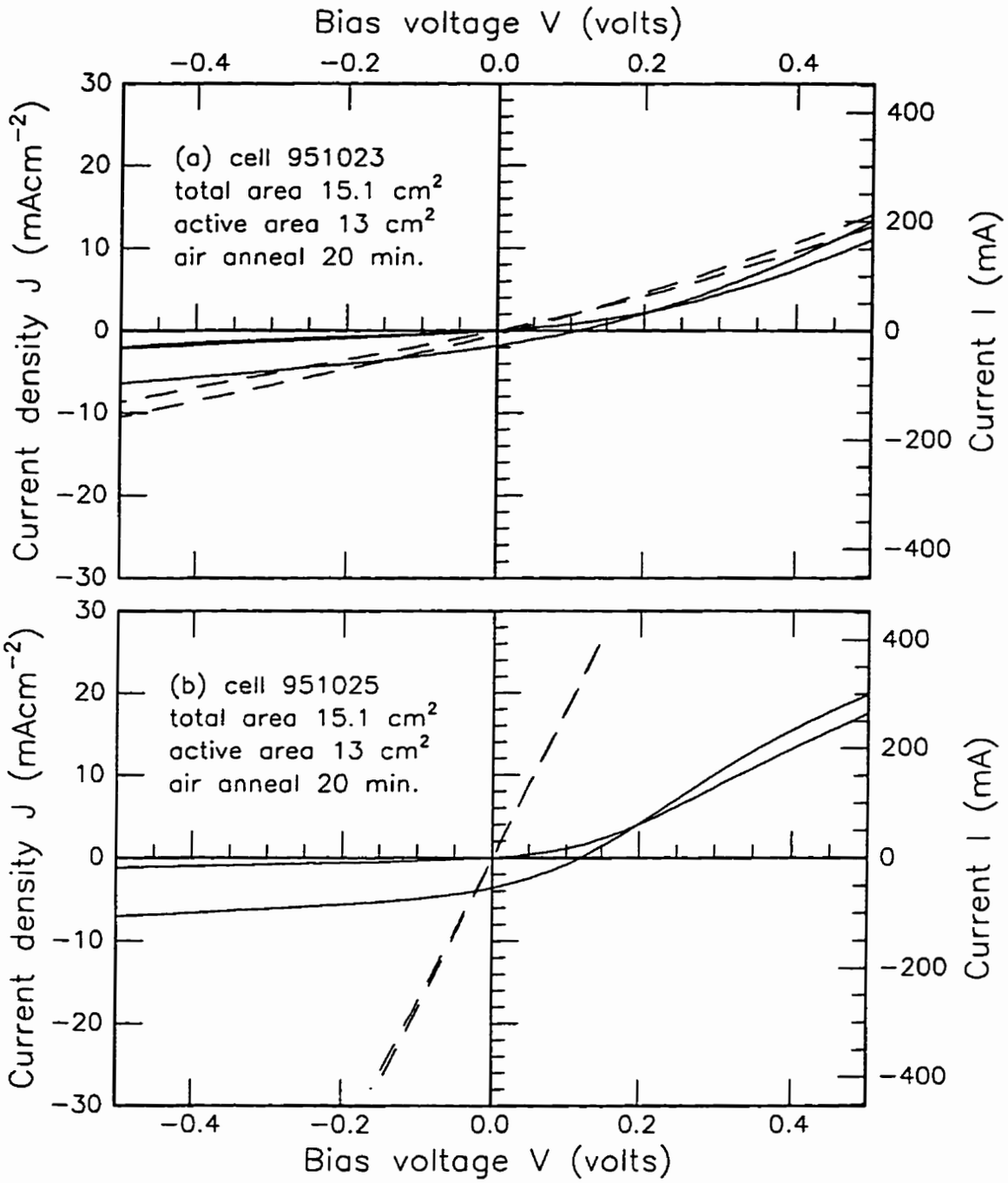

Figure 7.11

Dark and light J vs. V of $CuInSe_2/CdS$ solar cells, before (broken curves) and after (solid curves) air anneal. Simulated AM1.5 sunlight, T_{sub}=22°C. 7059 glass, 0% Na, Mo contact partially oxidized

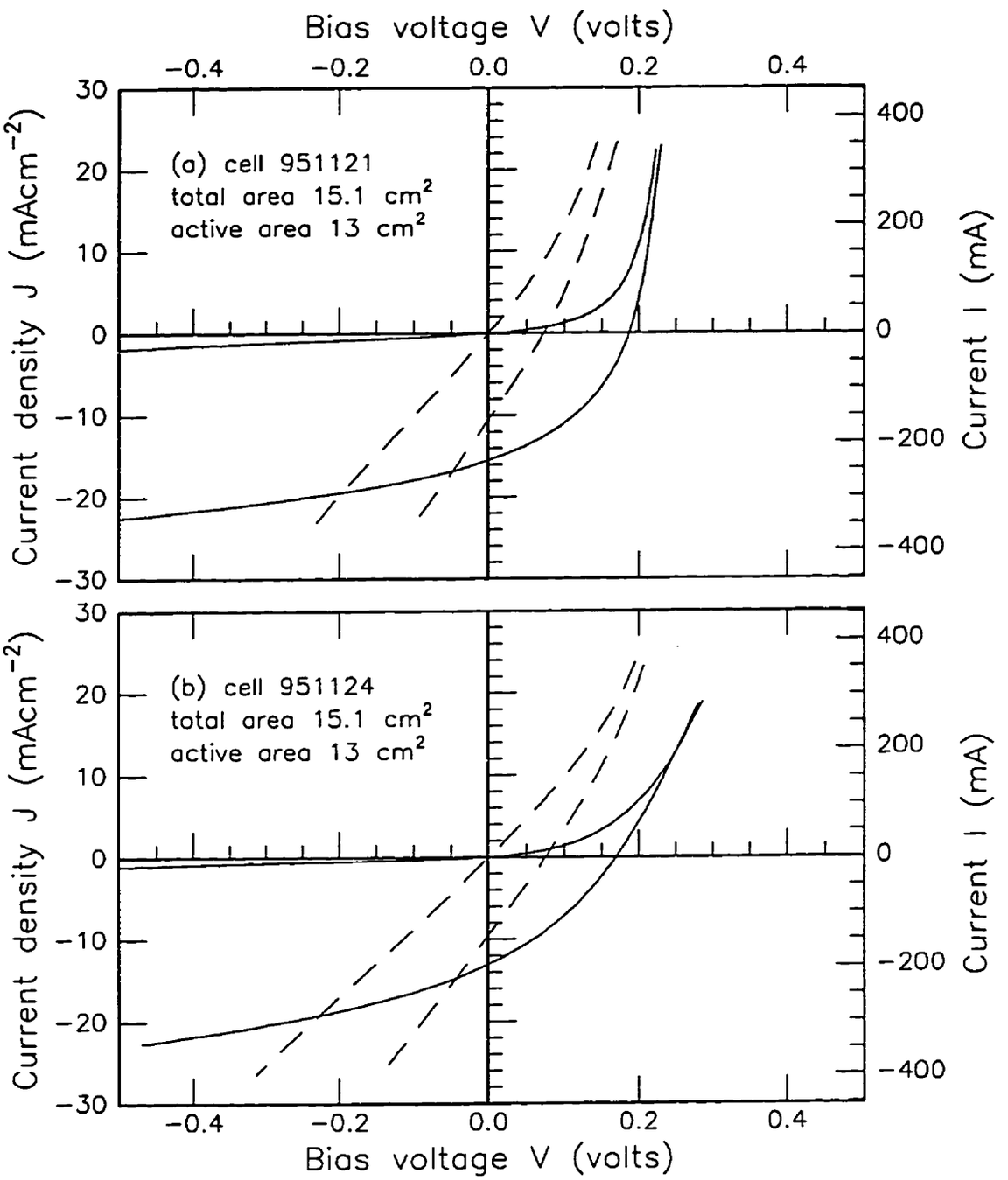

Figure 7.12

Dark and light J vs. V of $CuInSe_2$/CdS solar cells, before (broken lines) and after (solid lines) air anneal. Simulated AM1.5 sunlight, T_{sub}=22°C, Corning 7059 glass substrate, 0% Na

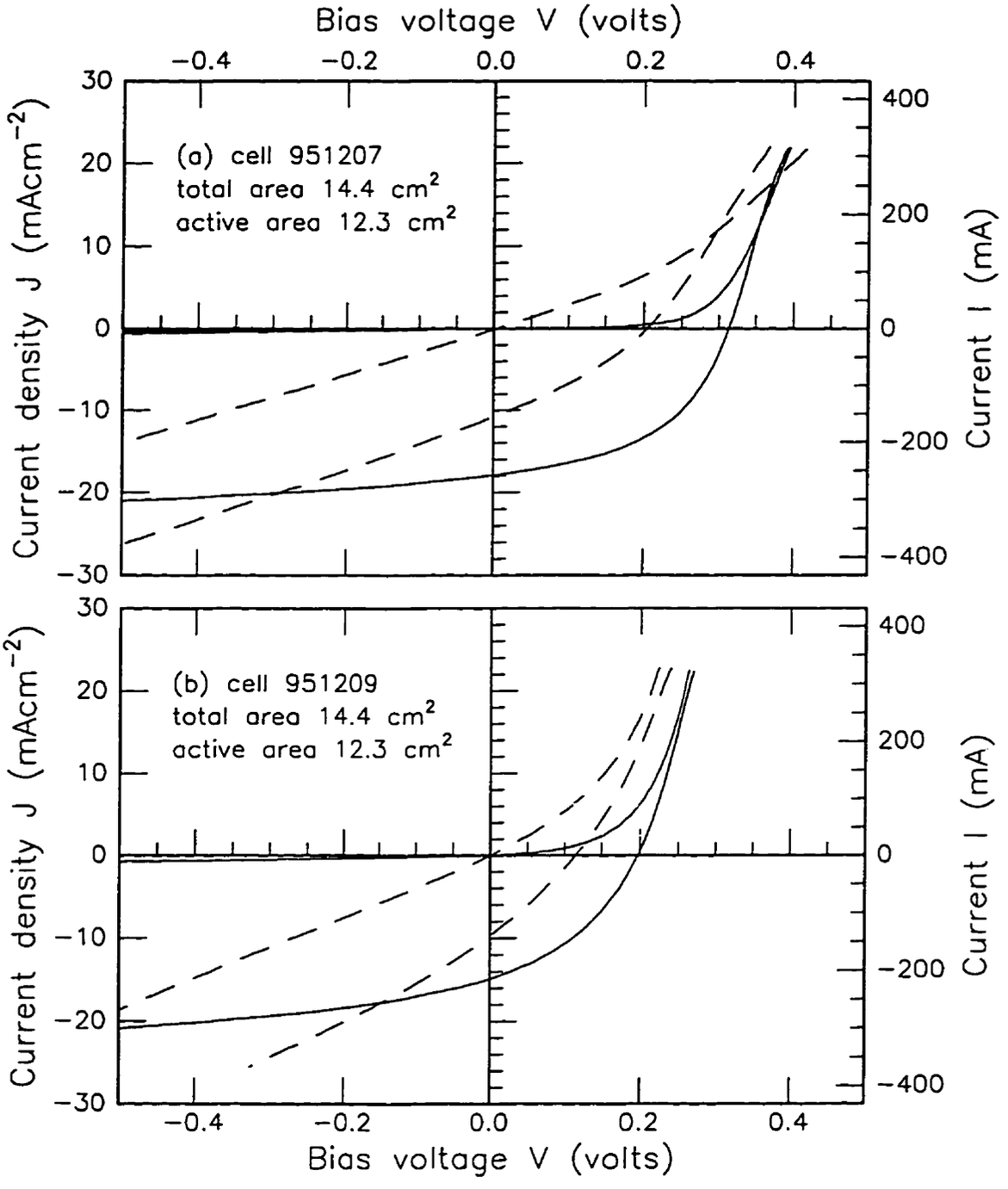

Figure 7.13

Dark and light J vs. V of $CuInSe_2/CdS$ solar cells, before (broken lines) and after (solid lines) air anneal. Simulated AM1.5 sunlight, T_{sub}=22°C Kodak CAT 141 3020 slide cover glass substrate.

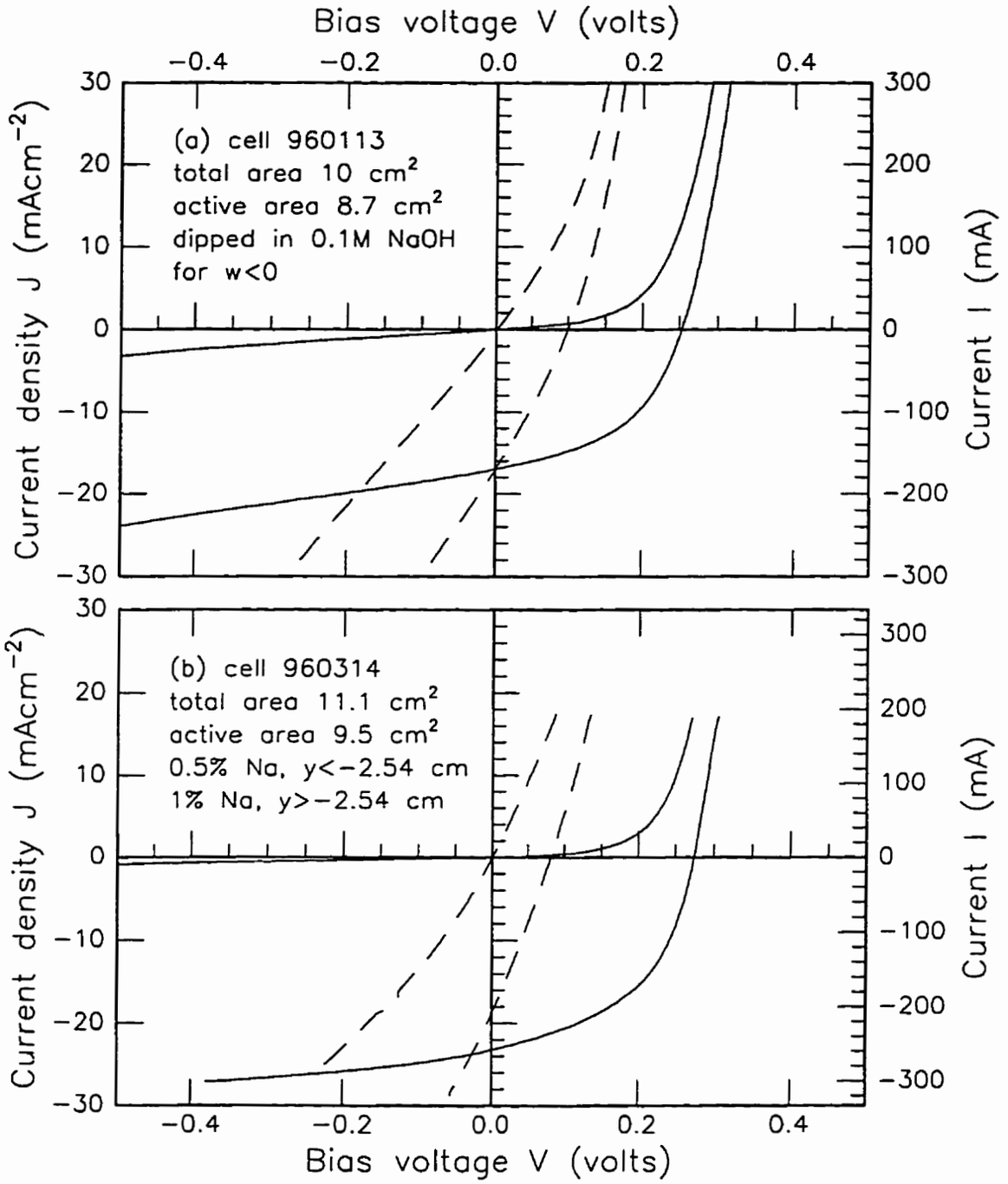

Figure 7.14

Dark and light J vs. V of $CuInSe_2/CdS$ solar cells, before (broken lines) and after (solid lines) air anneal. Simulated AM1.5 sunlight, T_{sub}=22°C, Corning 7059 glass substrate, %Na as indicated.

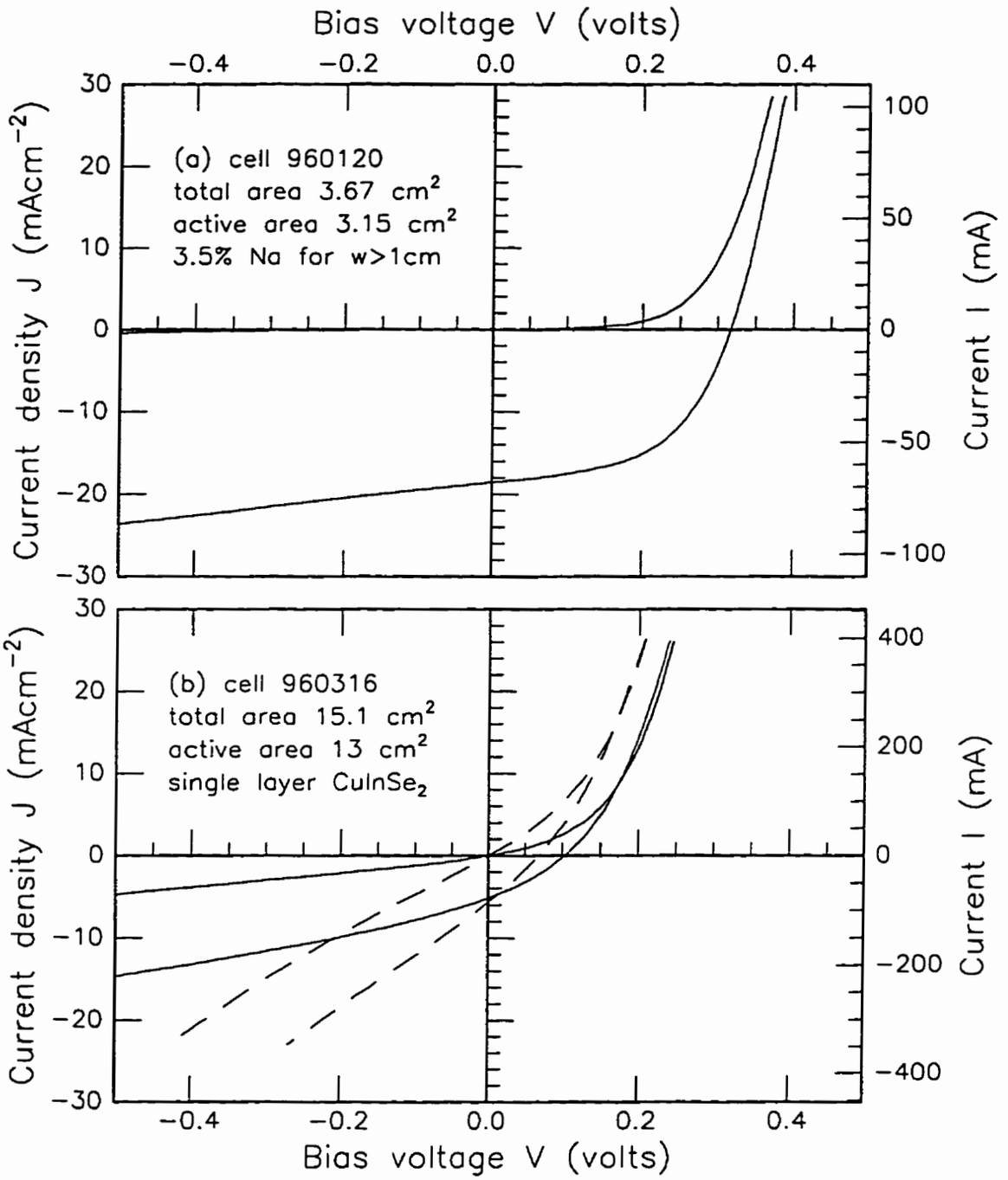

Figure 7.15

Dark and light J vs. V of $CuInSe_2$/CdS solar cells, before (broken lines) and after (solid lines) air anneal. Simulated AM1.5 sunlight, T_{sub}=22°C. Corning 7059 glass substrate.

The passivation of the V_{Se} defects improves the overall photovoltaic properties of the film [**33**]. Since p-$CuInSe_2$ films are highly compensated, the reduction in donor defect density results in an effective increase in acceptor density. The removal of some of the positive surface charge lowers the energy barriers to hole transport across grain boundaries, and the minority carrier recombination rate at the grain boundary surfaces is reduced.

Solar cells made with $CuInSe_2$ formed by selenization of the metals in 1 atm H_2Se at 400 °C do not require air annealing for optimization, since the Se over-pressure ensures that the V_{Se} density is much lower than in the case of three source evaporated films [**34**].

As seen in figures 7.10-7.15, the J-V curves change from a nearly ohmic J-V before heat treatment to a rectifying characteristic after heat treatment. According to [**35, 36**], immersion of solar cells in hydrazine (N_2H_4, an oxygen scavenging liquid) for about 3 minutes reverses the effect of the air anneal and returns the J-V curves to the original pre-annealed state. The cycle of reduction in hydrazine and oxidation in air can be repeated several times, with J-V alternating between ohmic and rectifying states.

On May 29, 1996 after approximately 6 months storage, cell 951207 was tested in sunlight. The J-V curve (figure 7.19 e) had not significantly changed from the original J-V data taken immediately after the first air anneal at 190 °C in December 1995 (figure 7.13 (a)). Device 951209 was also tested outdoors, but showed a substantial increase in reverse saturation current relative to figure 7.13 (b).

On June 26, 1996, after a failed attempt at measuring the junction capacitance, a repeat J-V test revealed that device 951207 had become nearly ohmic. At the time this was attributed to a new shunt path at the cell edges, but careful examination failed to reveal its location.

On February 13, 1997, about one year after the first air annealed J-V data of figures 7.10-7.15 were taken, the dark J-V curves were measured again. The J-V for 951207 was still ohmic, and device 951209, also on soda-lime glass, had also changed to an ohmic state. The devices (960314, 960113, 960120) deposited on sodium-free 7059 glass, with added NaOH, had also approached an ohmic state. A second, 20 minute air anneal at 190 °C returned the J-V data for all devices to the rectifying state. The dark J-V data immediately before, and after, the second air anneal are shown in figure 7.16. Device 960120 showed only a slight change over the 1 year period, and was therefore not annealed a second time. Sodium free devices on 7059 glass showed no discernible change over the one year period, and were therefore not annealed a second time.

It seems that a spontaneous reversal of the effects of the first air annealing takes place in the sodium doped devices over a period of months. This is perhaps analogous to the

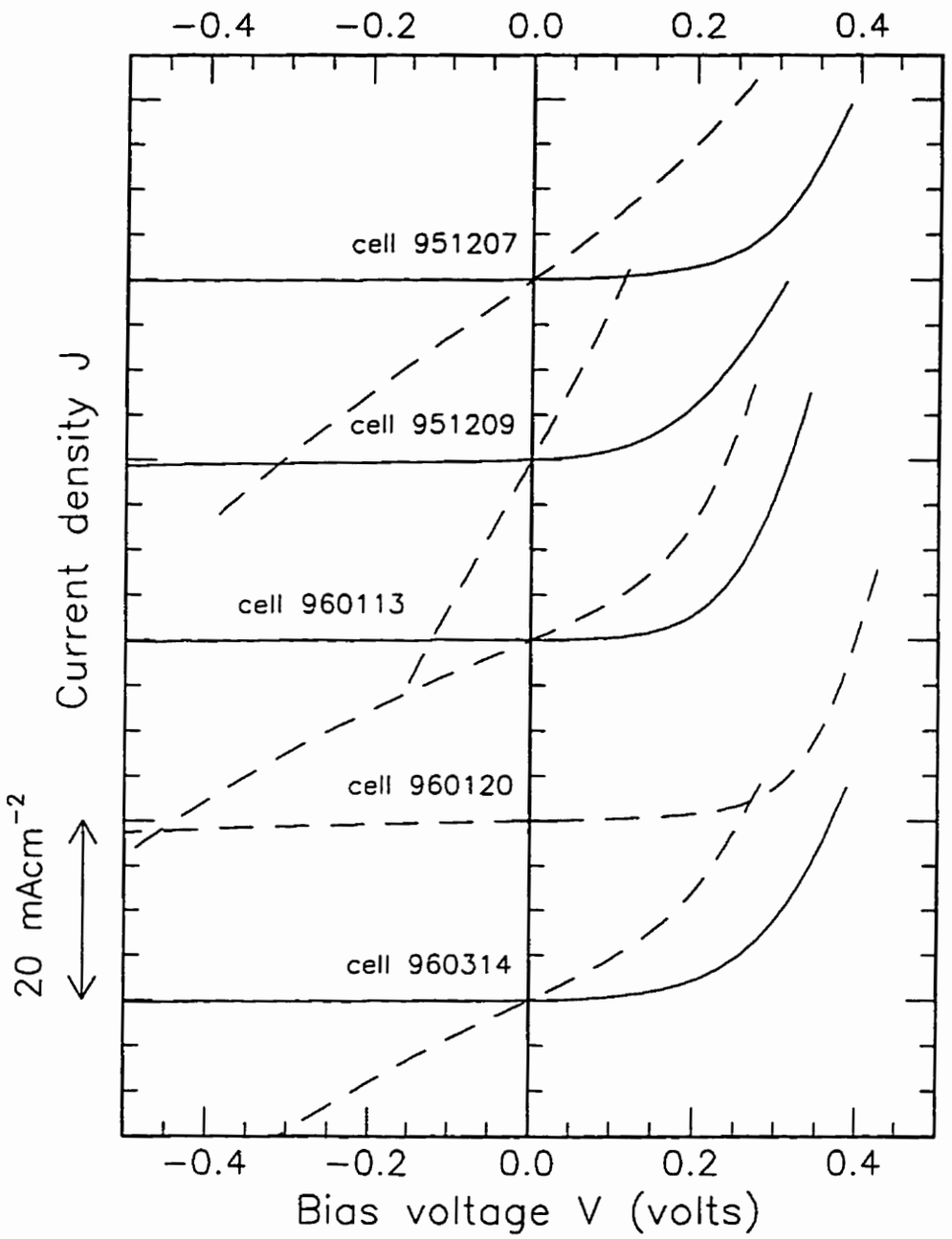

Figure 7.16

Dark J vs. V of sodium doped $CuInSe_2/CdS$ solar cells approximately one year after first air anneal (broken lines) and immediately after repeating air anneal (solid lines). Cells without sodium did not degrade during the year after the first anneal.

oxidation/reduction cycle described in [35, 36]. Recent experiments with $Cu(In,Ga)Se_2$ films suggests that chemical reactions involving water adsorbed from humid ambient air and Na may affect the long term stability of solar cells [37]. This is consistent with the fact that the local weather was hot and humid in the interval May 29 to June 26 1996, during which time the J-V curve for 951207 became ohmic.

The optimum air annealing temperature is about 200-225 °C, as determined by a series of 1 hour anneals at progressively higher temperatures, from 125 to 350 °C, at 25 °C intervals, and above about 275 °C, there is a rapid reduction of the short circuit current and open circuit voltage [38]. Auger electron spectroscopy depth profiling shows that at 220 °C, significant interdiffusion of S and Se takes place, and above about 350 °C, rapid Cd diffusion occurs [39]. The nominal annealing temperature used here is 190 ± 5 °C. The substrates were placed inside an oven on a thick aluminum plate, held at the nominal temperature, as measured by a thermocouple fastened to the plate.

7.3.4 Evaluation of Diode Parameters From Measured J-V Data

The values for A, J_0 and R_s can be determined from the post-anneal dark J-V curves of figures 7.10-7.15, by using the procedure described in [29]. In the dark and assuming a large shunt resistance (i.e. $J_L = 0$ and $R_p \rightarrow \infty$), equations 7.3 and 7.4 show that

$$J = J_0\left(\exp\left(\frac{q(V - JR_s)}{AkT}\right) - 1\right) \qquad (7.5)$$

Solve for V and differentiate to obtain

$$\frac{dV}{dJ} = R_s + \frac{AkT}{q(J + J_0)} \qquad (7.6)$$

For forward bias, $J >> J_0$, so that according to equation 7.6, the slope and dV/dJ intercept of a plot of dV/dJ vs. 1/J can be used to estimate A and R_s, respectively. These plots are shown in figure 7.17 for eight solar cells, at room temperature in the dark, with A and R_s values tabulated.

Equation (7.5) can be used to show that

$$\ln(J + J_0) = \ln(J_0) + \frac{q}{AkT}(V - JR_s) \qquad (7.7)$$

Again, since $J >> J_0$ in forward bias, the slope and log(J) intercept of a plot of log(J) vs. $V-JR_s$ can be used to estimate A and J_0, respectively. The plots are shown in figure 7.18, for the R_s values of figure 7.17. Estimates of A and J_0 (in μAcm^{-2}) are tabulated.

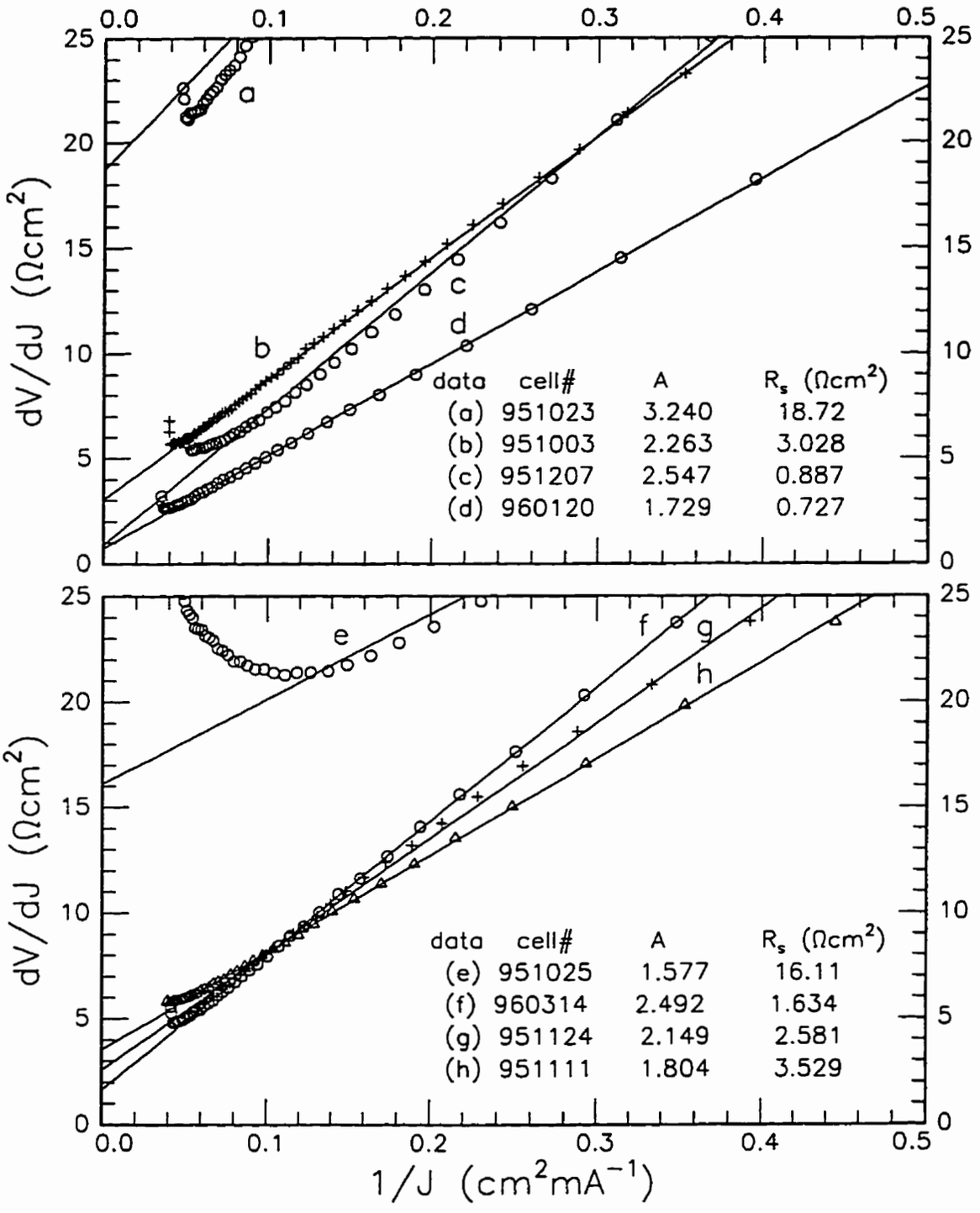

Figure 7.17

dV/dJ vs. 1/J for several $CuInSe_2$/CdS solar cells in the dark at T=295 K. The dV/dJ intercept is equal to R_s. The slope is equal to AkT/q.

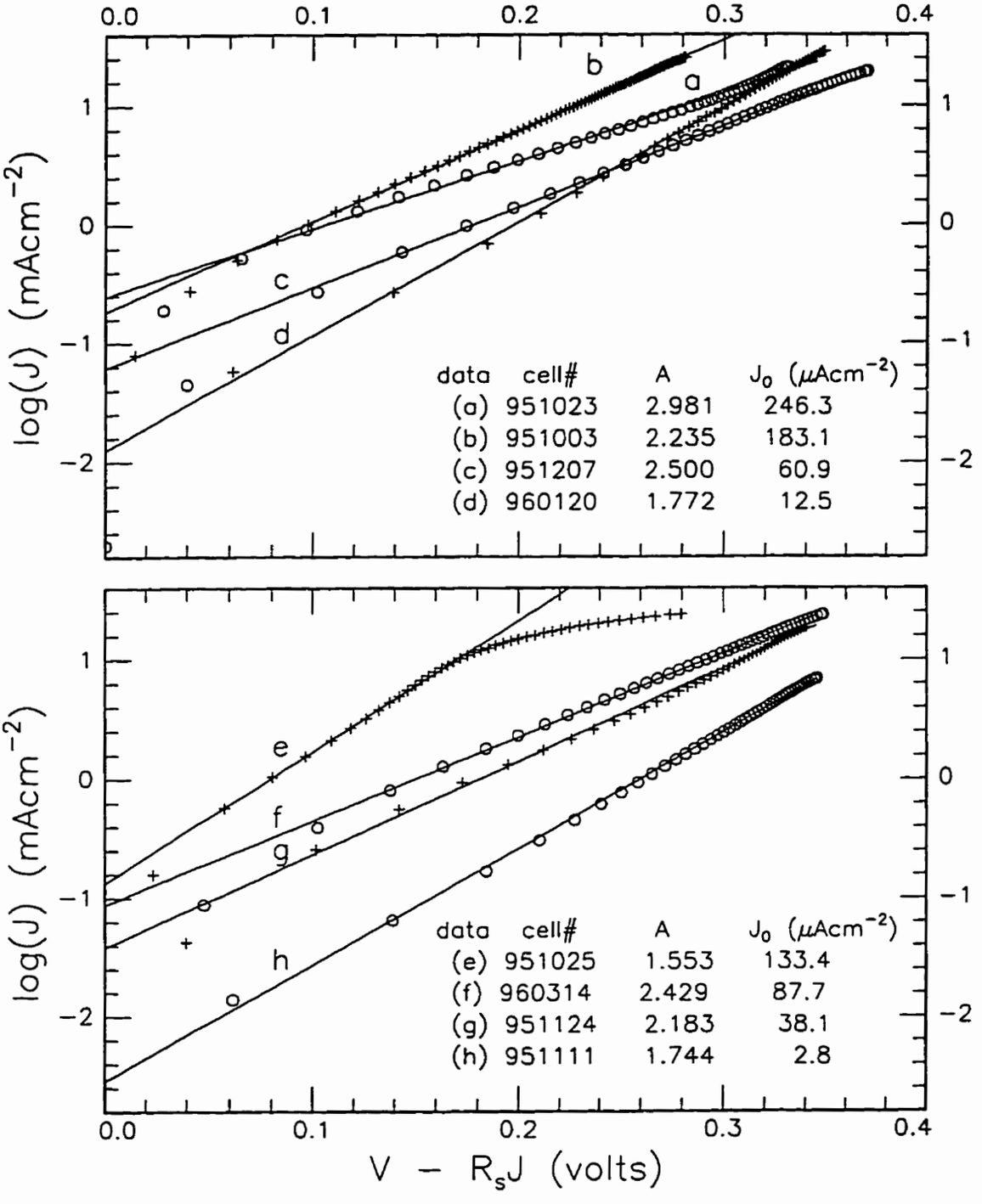

Figure 7.18

log(J) vs. voltage for $CuInSe_2$/CdS solar cells in the dark at T=295 K. The J intercept is at J_0. The slope is proportional to q/AkT.

Comparison of the tabulated data of figures 7.17 and 7.18 confirms that similar A values are obtained by both graphical methods.

7.3.5 Solar Energy Conversion Efficiency

The solar energy conversion efficiency $\eta(V)$ is defined as the ratio of the electrical output power from the cell, divided by the total solar input power. This can be written in terms of J, V and the total solar irradiance P_s ($mWcm^{-2}$) as

$$\eta(V) = \frac{-JV}{P_s} \qquad \text{and} \qquad \eta_{max} = \frac{(-JV)_{max}}{P_s}$$

For the J vs. V sign convention used here, –JV is the power density output ($mWcm^{-2}$) from the cell to the external circuit. Since an accurate solar simulator was not available, J vs. V curves for a few of the best $CuInSe_2$/CdS cells, and a commercial silicon cell, were measured outdoors in direct sunlight, with estimated cell temperatures in the range 20 to 30 °C. Because it was necessary to move the J vs. V apparatus outdoors, a portable analog x-y plotter was used to record the data, which was later converted to digital format. The current density J, calculated electrical output power –JV, and conversion efficiency η as functions of cell bias voltage are shown in figure 7.19. The maximum total area efficiency for each cell is calculated assuming that the solar irradiance is equal to the standard AM1 spectrum (air mass 1, 95.62 $mWcm^{-2}$ [40]). The best $CuInSe_2$/CdS cell is 951207 with total area 14.36 cm^2 and total area efficiency of 4.8%. The active area efficiency is 5.62%. This can be compared to published data for $CuInSe_2$/CdS cells with thick CdS window layers and no anti-reflection coating: η_{max} = 6.6%, area = 1.2 cm^2 [20] and η_{max} = 8.67 %, area = 1 cm^2 [41] (whether active or total area was not specified). As shown in section 7.3.8 below, the quantum efficiency of each cell varies with substrate position, so that in principle, higher energy conversion efficiency can be obtained by selecting a small test cell from the region with the highest quantum efficiency.

7.3.6 Junction Capacitance Measurements

The Anderson heterojunction theory [42] is an extension of the standard homojunction theory. Define a coordinate axis z, perpendicular to the plane of the junction, such that z = 0 is at the boundary between the $CuInSe_2$ and CdS, and positions z > 0 are in the $CuInSe_2$. Define the following quantities, where the index "1" refers to $CuInSe_2$ and "2" to CdS:

z_1, z_2 are widths of space charge region in each semiconductor.
N_1 is acceptor density, N_2 is donor density.
$\psi(x)$ is the electrostatic potential in the semiconductor.

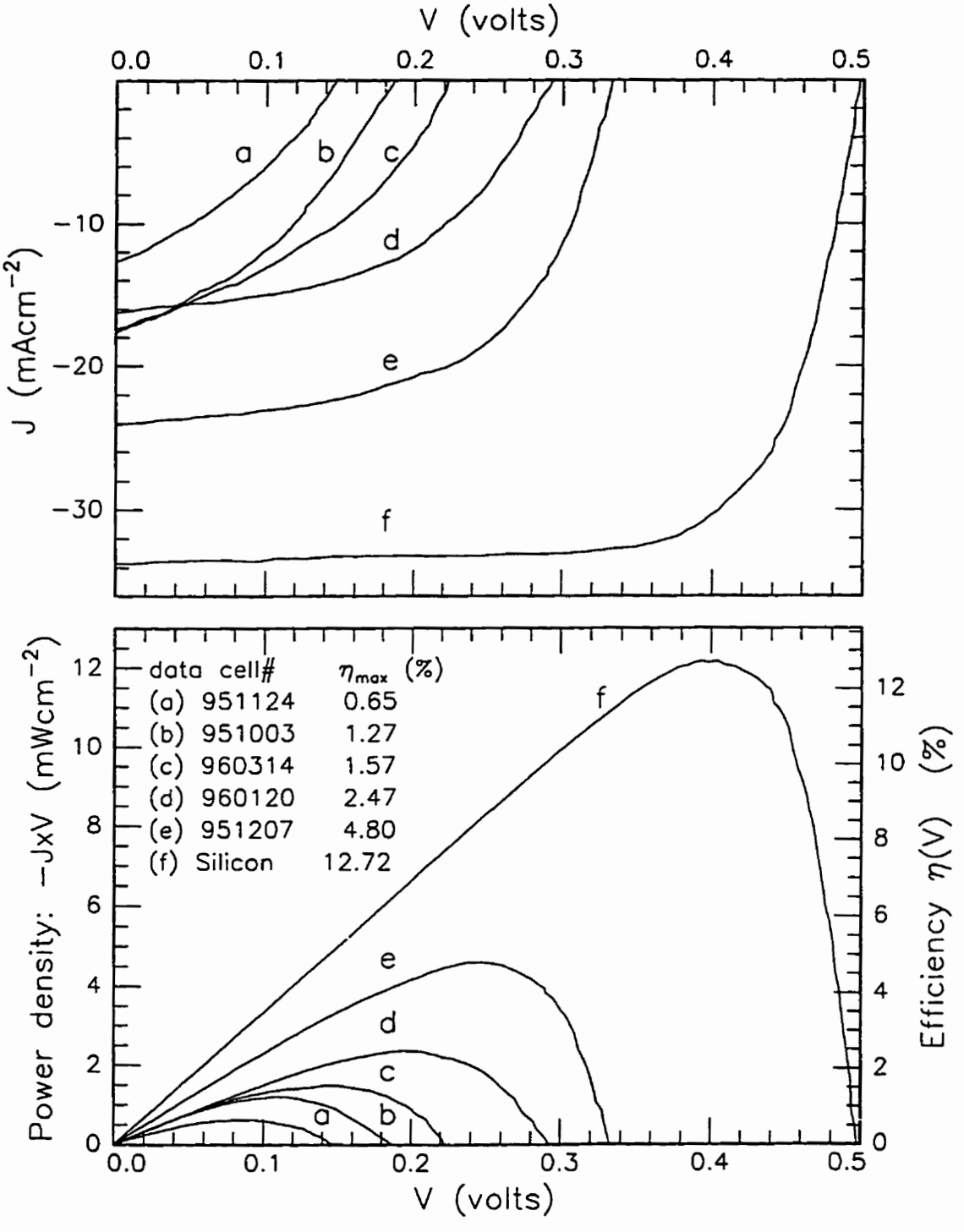

Figure 7.19

Top: J vs. V for $CuInSe_2/CdS$ cells and a crystal Si cell in sunlight. Bottom: output power density vs. V, total area efficiency vs. V assuming AM1 sunlight.

ρ is the space charge density.

ε_1, ε_2 are the semiconductor permittivities.

V_d is the diffusion potential, V is the applied bias voltage.

The electric field outside the space charge region is zero, so that from Gauss's law

$$-qN_1z_1+qN_2z_2 = 0 \qquad (7.8)$$

Integrate Poisson's equation $\frac{\partial^2\psi}{\partial z^2} = -\frac{\rho}{\varepsilon}$ from $z = z_1$ to $z = -z_2$, with the boundary conditions $\frac{\partial\psi}{\partial z} = 0$ at $z = z_1$ and $z = -z_2$; $\psi(z_1) = 0$, $\psi(-z_2)=V_d-V$ and ψ continuous at $z = 0$. We obtain

$$V_d - V = \frac{q}{2}\left(\frac{N_1z_1^2}{\varepsilon_1} + \frac{N_2z_2^2}{\varepsilon_2}\right) \qquad (7.9)$$

Substitute for z_1 or z_2 in equation (7.9) using equation (7.8) to obtain

$$z_1 = \sqrt{\frac{2(V_d - V)}{qN_1^2\left(\frac{1}{\varepsilon_1N_1} + \frac{1}{\varepsilon_2N_2}\right)}} \quad \text{and} \quad z_2 = \sqrt{\frac{2(V_d - V)}{qN_2^2\left(\frac{1}{\varepsilon_1N_1} + \frac{1}{\varepsilon_2N_2}\right)}} \qquad (7.10)$$

The junction capacitance per unit area is given by

$$C = \frac{d}{dV}(qN_1z_1) = \sqrt{\frac{q}{2\left(\frac{1}{\varepsilon_1N_1} + \frac{1}{\varepsilon_2N_2}\right)(V_d - V)}} \qquad (7.11)$$

A plot of C^{-2} vs. V has slope = $\frac{2}{q}\left(\frac{1}{\varepsilon_1N_1} + \frac{1}{\varepsilon_2N_2}\right)$ and intercept V_d. If the CdS donor density N_2 is known, or if $N_2 >> N_1$, the slope can be used to determine N_1.

The electric fields E_1 in the $CuInSe_2$ and E_2 in the CdS at $z = 0$ are obtained by integrating Poisson's equation with the boundary condition $\frac{\partial\psi}{\partial z} = 0$ at z = z1 and z = -z2

$$(E_1)_{z=0} = \frac{qN_1z_1}{\varepsilon_1} = \sqrt{\frac{2q(V_d - V)}{\varepsilon_1^2\left(\frac{1}{\varepsilon_1N_1} + \frac{1}{\varepsilon_2N_2}\right)}} \quad \text{and} \quad (E_2)_{z=0} = \sqrt{\frac{2q(V_d - V)}{\varepsilon_2^2\left(\frac{1}{\varepsilon_1N_1} + \frac{1}{\varepsilon_2N_2}\right)}} \qquad (7.12)$$

Plots of C^{-2} vs. V are shown in figure 7.20, with the slopes and intercepts tabulated. The $CuInSe_2$ acceptor density N_1 and space charge region thickness z_1 can be estimated.

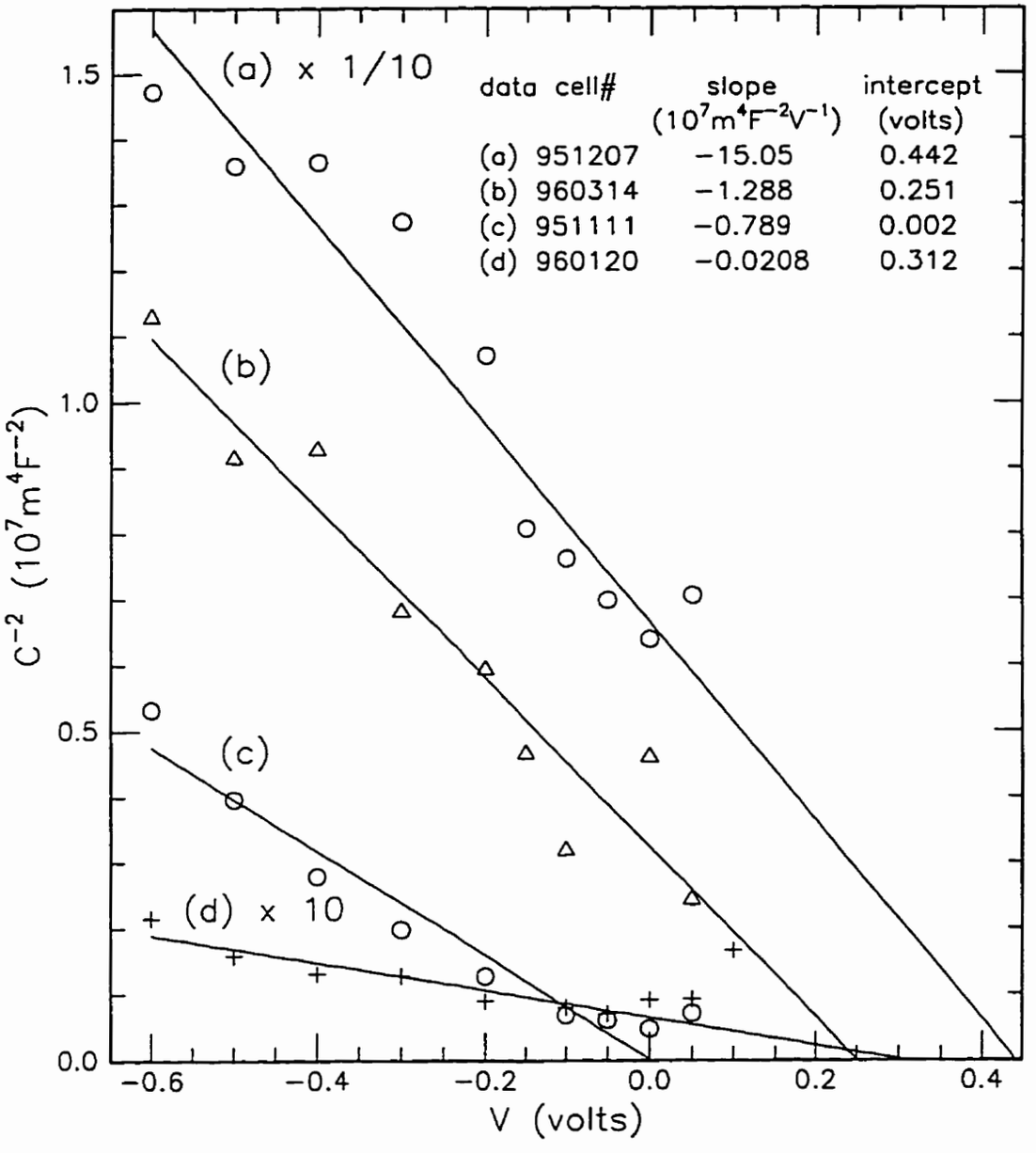

Figure 7.20

Inverse square capacitance $1/C^2$ vs. bias voltage for $CuInSe_2/CdS$ solar cells. Least squares fits to points $V \leqq 0$ only. Note multiplication by 1/10 and 10 of data sets (a) and (d), respectively.

The results are tabulated in table 7.3 below, for a CdS donor density $N_2=1.6\times10^{18}$ cm^{-3} (see section 6.2.4), $\varepsilon_1 = 15.6\varepsilon_0$ and $\varepsilon_2 = 8.78\varepsilon_0$ [43].

Table 7.3: Acceptor Density N_1 and Depletion Width z_1 in $CuInSe_2$ Absorber Layer

sample #	slope ($m^4F^2V^{-1}$)	intercept (volts)	N_1 (cm^{-3})	z_1 at V=0 (μm)
951207	-1.5×10^8	0.44	6.0×10^{14}	1.13
960314	-1.3×10^7	0.25	7.1×10^{15}	0.25
951111	-7.9×10^6	0.002	1.2×10^{16}	—
960120	-2.1×10^5	0.31	8.4×10^{17}	0.018

7.3.7 Solar Cell Spectral Response

According to the collection probability method [44], the total light current of the solar cell can be determined by the integral

$$J_L(V)=\int_\lambda\int_z g(z,\lambda)f(z,V)dzd\lambda \qquad (7.13)$$

Here $g(z,\lambda)$ is the spectral generation rate at position z and $f(z,V)$ is the minority carrier spatial collection probability at z. It can be determined by solution of the minority carrier transport equations for a very localized δ-function type generation rate. An exact expression for the spatial collection probability has been determined for an ideal p-n homojunction [45].

For the specific case of a $CdS/CuInSe_2$ solar cell with a thick window, the product of collection and generation in the CdS window layer ($z < 0$) is negligible. For incident spectral photon flux density $\Phi(\lambda)$, transmittance through the window $T(\lambda)$, a homogeneous absorber of thickness d and absorption coefficient $\alpha(\lambda)$, we have $g(z,\lambda)=\alpha(\lambda)T(\lambda)\Phi(\lambda)\exp(-\alpha(\lambda)z)$, so that the total light current density $J_L(V)$ is given by

$$J_L(V)=q\int_0^\infty\int_0^d T(\lambda)\alpha(\lambda)\Phi(\lambda)\exp(-\alpha(\lambda)z)f(z,V)dzd\lambda \qquad (7.14)$$

The quantum efficiency $Q(\lambda,V)$ is the ratio of the electric current density element dJ_L to "photon current" density element $q\Phi(\lambda)d\lambda$ due to incident light in the wavelength range λ to $\lambda+d\lambda$.

$$Q(\lambda,V)=\frac{dJ_L(V)}{q\Phi(\lambda)d\lambda}=T(\lambda)\alpha(\lambda)\int_0^d\exp(-\alpha(\lambda)z)f(z,V)dz \qquad (7.15)$$

The system based on the Cary 17 spectrophotometer, shown in figure 5.3, was used to measure solar cell quantum efficiency spectra. The spectra for solar cell 951207 illuminated at three different points, at zero bias, and at one position and four different bias voltages are shown in figure 7.21. The spectra of cells 960120 and 960314 at different applied bias voltages are shown in figure 7.22. The spectrophotometer illumination "footprint" is approximately 0.5 x 1 cm^2.

As seen in figures 7.21, 7.22, the quantum efficiency decreases with increasing bias voltage, and the sensitivity of the quantum efficiency to bias is approximately independent of wavelength. Bias voltage dependence has been observed elsewhere for CdS/Cu_2S, CdS/CdTe [46] and CdS/$CuInSe_2$ [47] solar cells. Rothwarf [27,48] proposed a model in which junction field controlled interface recombination explains the observed voltage dependence in CdS/Cu_2S. According to this model, $f(z,V) = h(V)c(z)$, where $c(z)$ is the probability that an optically generated electron reaches the interface, and $h(V)$ is the probability that the electron crosses the interface into the CdS without recombining via interface states. The probability that an electron crosses the interface is given by

$$h(V) = \frac{\mu_2 E_2}{\mu_2 E_2 + S_{in}} \qquad (7.16)$$

Here E_2 is the electric field at the CdS side of the interface, μ_2 is the electron mobility in the CdS and S_{in} is the interface recombination velocity. In the case of the CdS/Cu_2S solar cell, the p-type Cu_2S absorber is heavily doped and most of the diffusion potential occurs in the lightly doped CdS. Thus the number of interface states occupied by holes, and therefore S_{in}, are practically independent of bias voltage. In the case of CdS/$CuInSe_2$ solar cells, as mentioned in section 7.3.1, bulk recombination in the absorber depletion region may dominate. If the bulk recombination region occurs very near the interface, then most of the light current must traverse the high recombination region and therefore the collection probability can still be separated into the form $f(z,V) = h(V)c(z)$.

If we assume that all electrons generated in the depletion region drift to the interface, then $c(z) = 1$ for $0 < z < z_1$. For $d\text{-}z_1 >> L_n$, where L_n is the electron diffusion length, the probability that an electron generated in the absorber QNR will diffuse to the depletion region is $c(z) = \exp((z_1\text{-}z)/L_n)$ for $z > z_1$. With this $c(z)$, we obtain

$$Q(\lambda,V) \equiv h(V)T(\lambda)\alpha(\lambda)\int_0^{\infty}\exp(-\alpha(\lambda)z)c(z)dz = h(V)T(\lambda)\left(1-\frac{\exp(-\alpha(\lambda)z_1}{1+\alpha(\lambda)L_n}\right) \qquad (7.17)$$

Assuming that the bias voltage dependence is due to interface recombination, we can use equation 7.16 to estimate S_{in}. For strongly absorbed light, the last term in equation 7.17 can be ignored, so that $Q(\lambda,V) \equiv h(V)T(\lambda)$. For device 951207 at $\lambda = 700$ nm and $V = 0$, we have $Q = 0.67$ from figure 7.21. Assuming $T \cong 0.76$ (see figure 6.8) we obtain

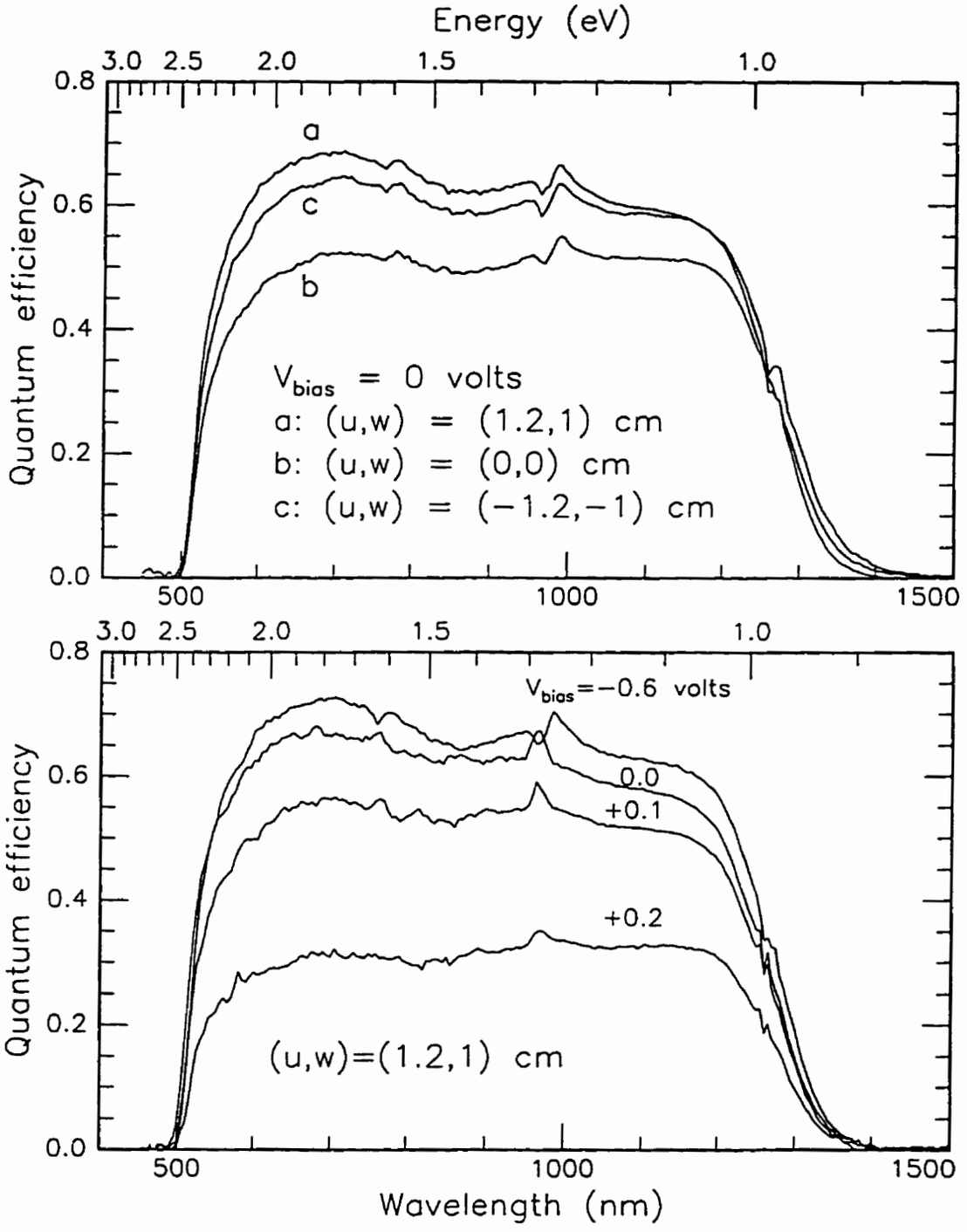

Figure 7.21

Quantum efficiency spectra for solar cell 951207.
Top: V_{bias} = 0, probe position (u,w) as specified.
Bottom: Position (u,w)=(1.2,1) cm, V_{bias} as specified.
Monochromator bandwidth 10 nm, chopped at 30 Hz.

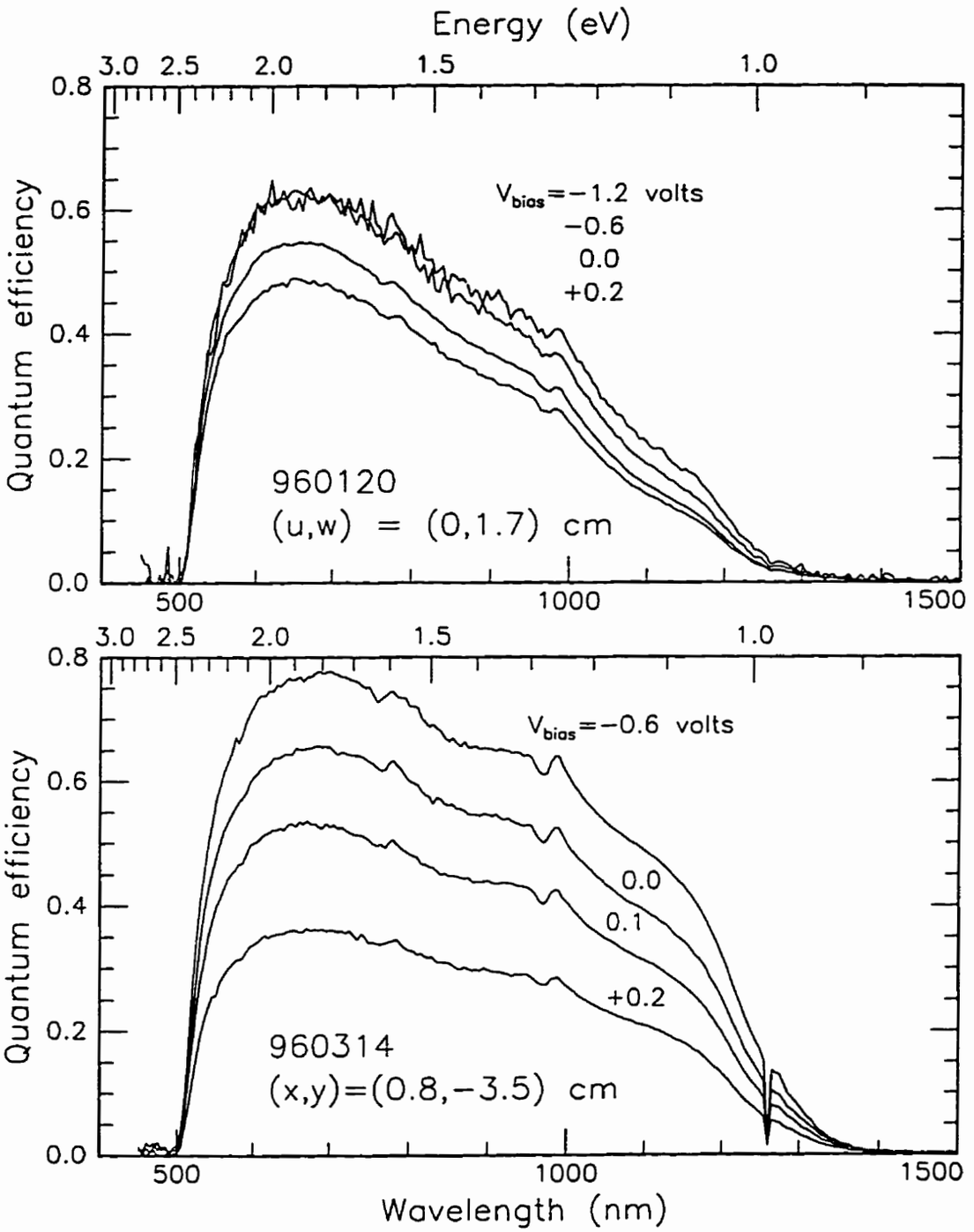

Figure 7.22

Quantum efficiency at different bias voltages.
Top: solar cell 960120; Bottom: solar cell 960314.
Monochromator bandwidth 10 nm, chopped at 30 Hz.

h = Q/T = 0.67/0.76 = 0.882. The electric field in the CdS at V=0 is E_2=14,000 V/cm by equation 7.12 and $\mu_2 = 300$ $cm^2V^{-1}s^{-1}$ for single crystal CdS [43]. Solving equation 7.16 gives the interface recombination velocity $S_{in} = 5.5x10^5$ cm/s at V = 0. At V = 0.2 volts, S_{in} increases to $4x10^6$ cm/s. Higher values of S_{in} are expected for forward bias, since S_{in} is proportional to the number of interface states occupied by holes, and forward bias should increase the absorber hole density near the interface.

7.3.8 Solar Cell OBIC Images

The scanning laser system, as described in section 3.4.1, was used to obtain optical beam induced current (OBIC) images of solar cells. The laser beam is raster scanned over the surface of the solar cell, and the output photocurrent is amplified by a current-to-voltage preamplifier with discrete gain settings (1,2 or 5 x 10^n V/A, n = 3 to 12). The amplifier output is digitized by an 8 bit analog to digital converter (ADC) and an 8 bit 512 x 512 pixel image is stored by a frame grabber and recorded by a data acquisition computer. Since the ADC operates over a fixed 0 to 1 volt range, and only discrete gains are used, the total number of distinct voltage levels in a particular OBIC image ranges from 102 to 256. The voltage scale is converted to a quantum efficiency scale by referencing to a commercial silicon or germanium photodiode, with quantum efficiency as specified by the manufacturer [49].

The size of the laser spot is adjusted by moving the solar cell away from the focal plane of the objective lens. For a large laser spot diameter equal to approximately 0.037 cm and beam power 117 μW, the intensity is 109 mW/cm^2, which is comparable to solar intensity. The images of figures 7.23 to 7.29 were obtained using a low intensity, large laser spot, with the intensity specified in each figure. All images are at 633 nm with a 0.037 cm spot, except figure 7.26 which was obtained at 1150 nm with an undetermined spot size. To obtain a clear image while minimizing light intensity, the laser spot and image pixel should be of similar size. Since the image pixel size of the OBIC images is 0.015 x 0.015 cm, the large 0.037 cm diameter spot causes some loss of resolution.

Since the electrical and optical properties of $CuInSe_2$ are sensitive to deposition ratio F, the quantum efficiency varies with substrate position for all of the solar cells tested. Refer to figure 2.16 for the relevant source configurations and the corresponding constant F contours.

Line graphs extracted from the OBIC images show quantum efficiency as a function of position x or u at a particular y or w value. Images (not shown) were also taken at 234 μW beam power, using a focused, diffraction limited spot about 0.001 cm in diameter and of high intensity (300 Wcm^{-2}). Line graphs taken from the low intensity OBIC images

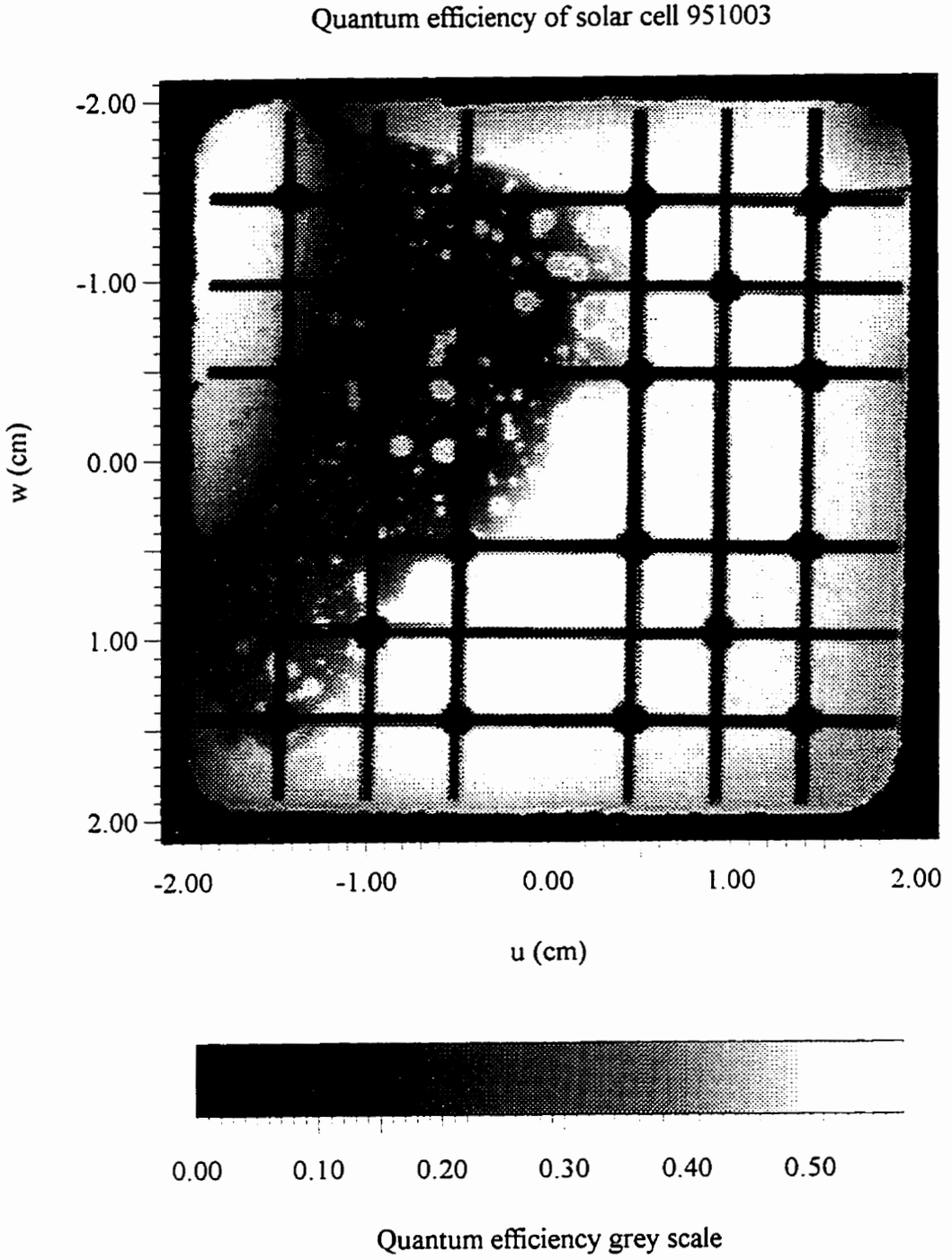

Figure 7.23

An OBIC image of solar cell 951003. The beam power is 117 μW, the intensity is 109 mW/cm^2, and the wavelength is 633 nm. Figure 2.16 (a) shows the (u,w,z) coordinates of the Cu, In and Se evaporation sources used for the $CuInSe_2$ deposition.

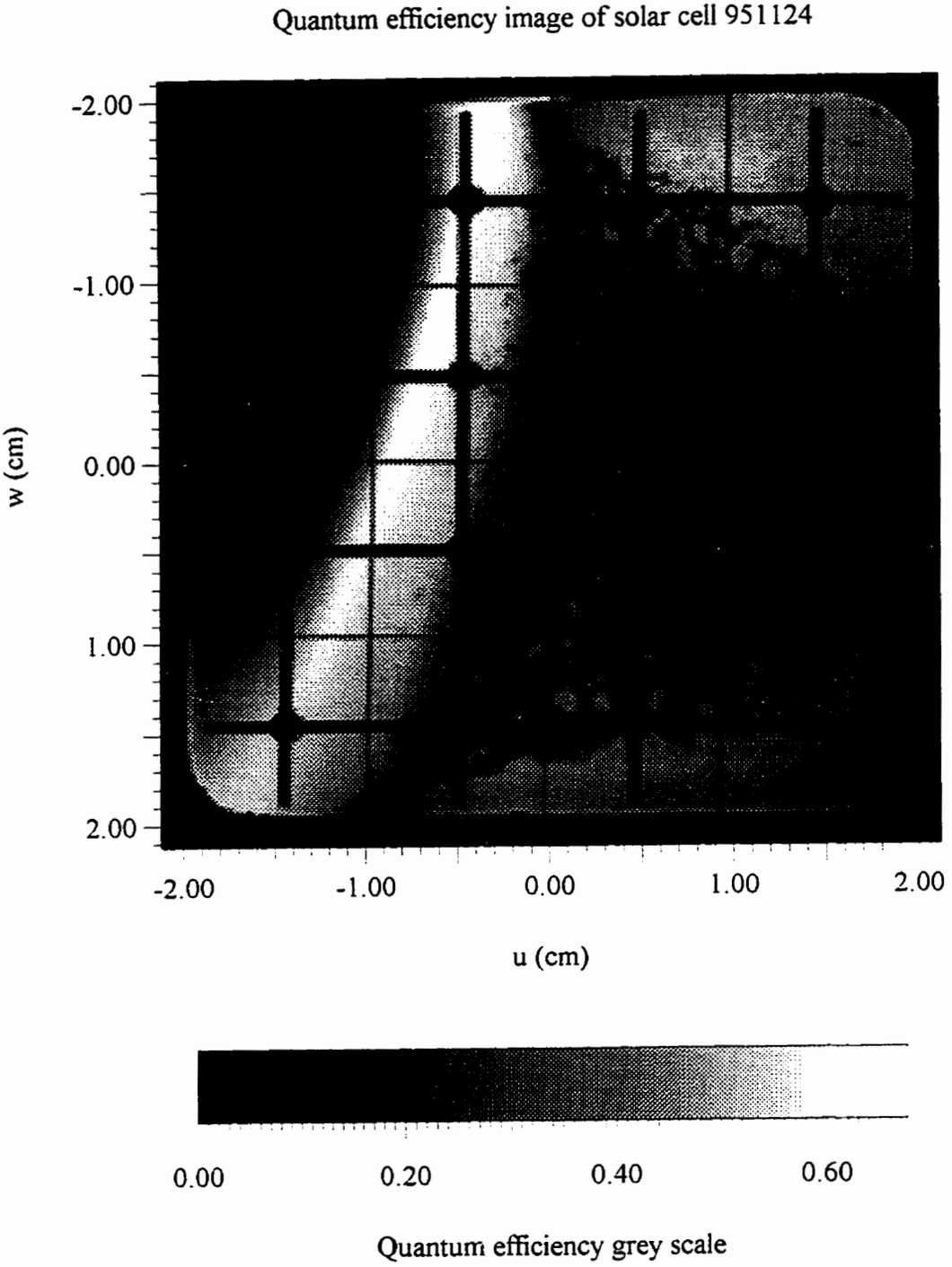

Figure 7.24

An OBIC image of solar cell 951124. The beam power is 117 μW, the intensity is 109 mW/cm^2, and the wavelength is 633 nm. Figure 2.16 (a) shows the (u,w,z) coordinates of the Cu, In and Se evaporation sources used for the $CuInSe_2$ deposition.

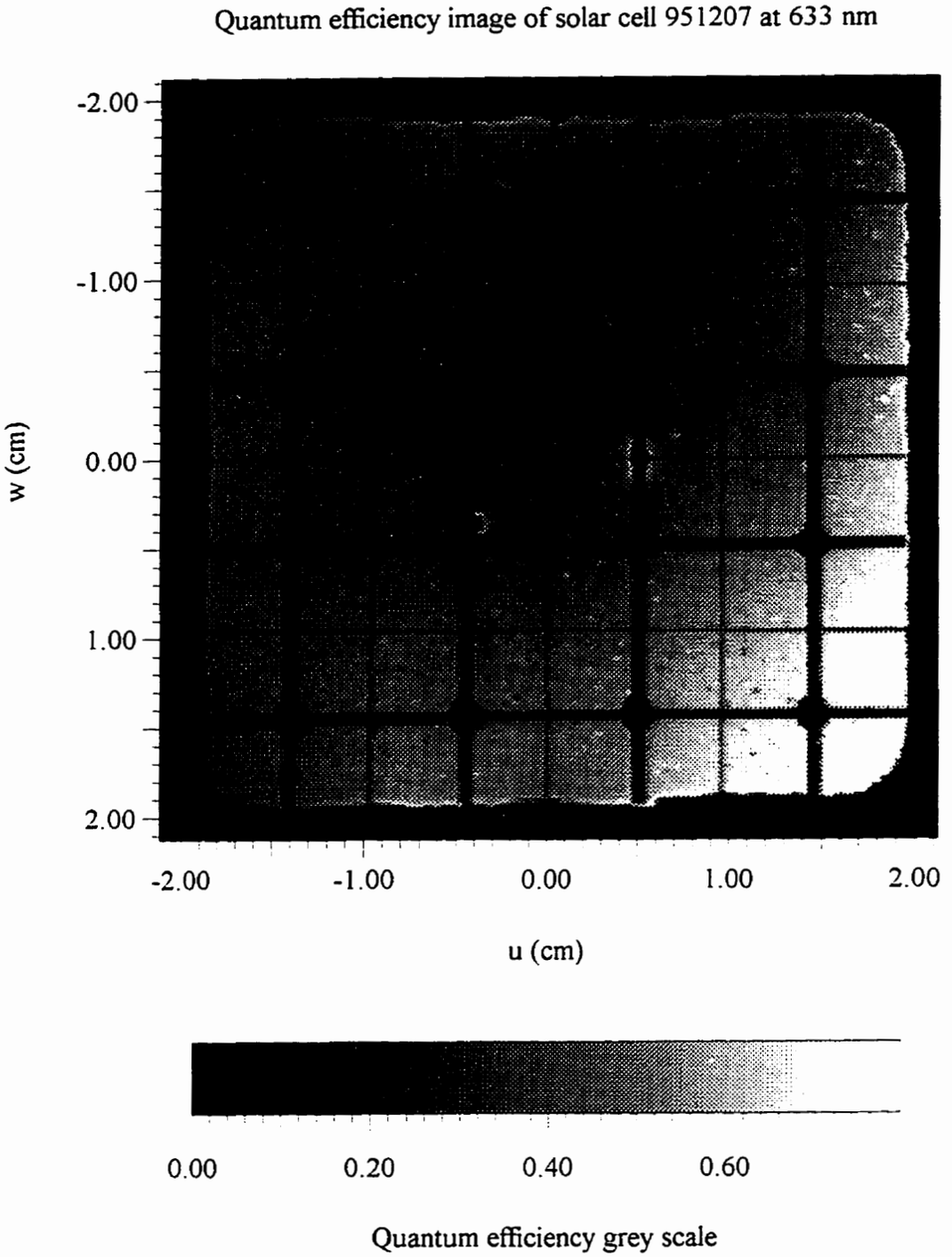

Figure 7.25

An OBIC image of solar cell 951207. The beam power is 123 μW, the intensity is 114 mW/cm^2, and the wavelength is 633 nm. Figure 2.16 (a) shows the (u,w,z) coordinates of the Cu, In and Se evaporation sources used for the $CuInSe_2$ deposition.

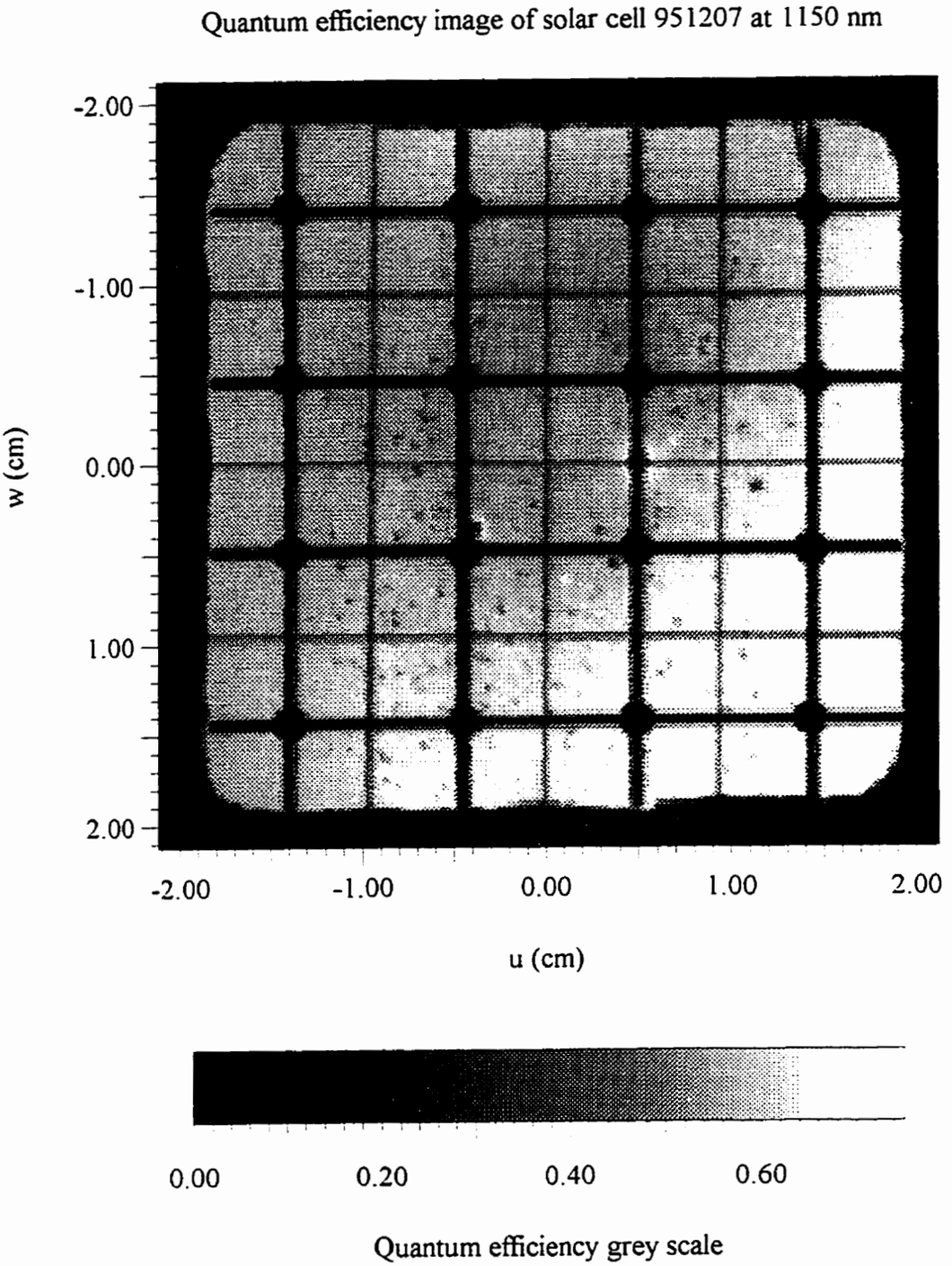

Figure 7.26

An OBIC image of solar cell 951207. The beam power is 44 μW, the beam intensity is low, and the wavelength is 1150 nm. Figure 2.16 (a) shows the (u,w,z) coordinates of the Cu, In and Se evaporation sources used for the $CuInSe_2$ deposition.

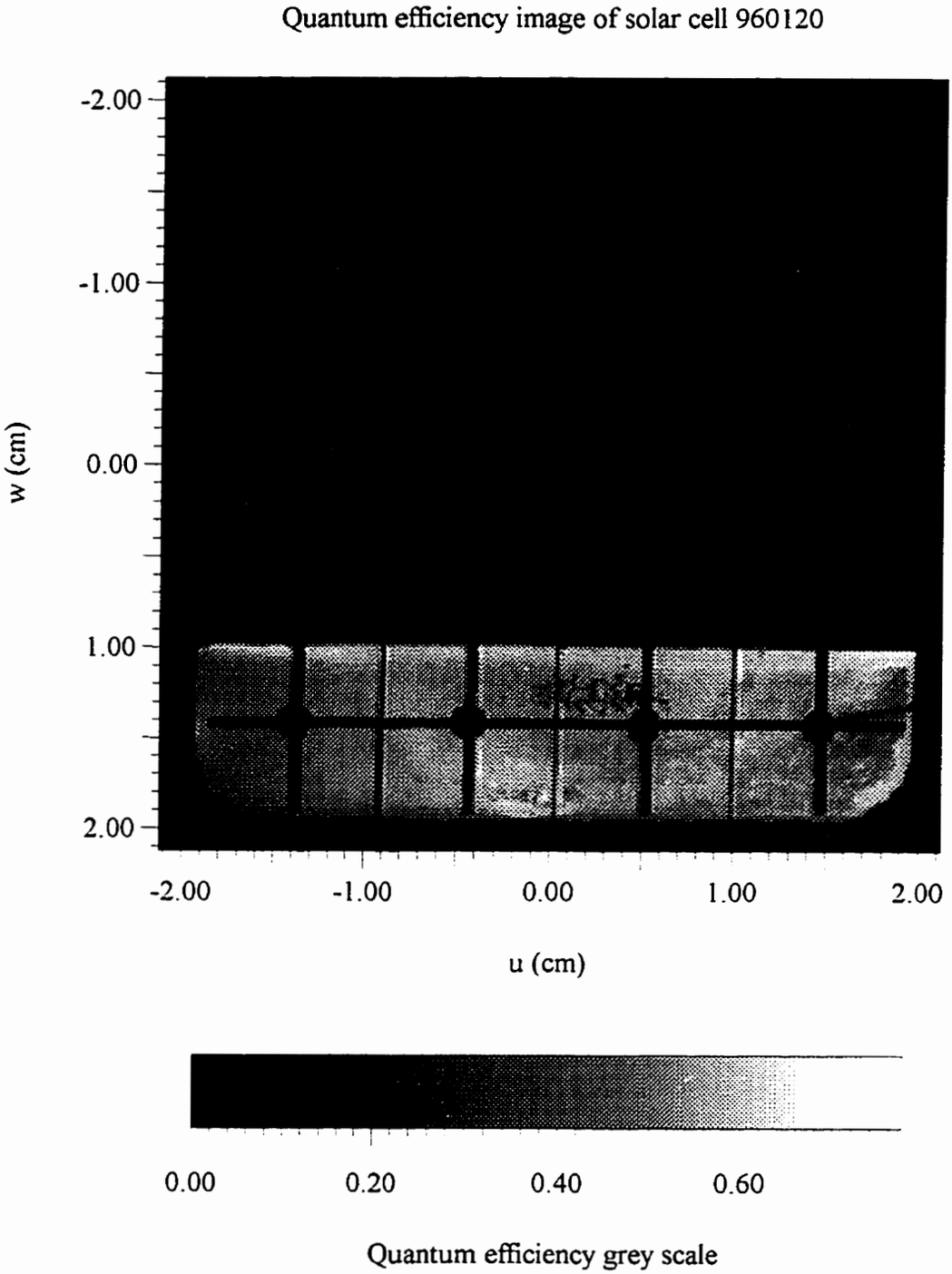

Figure 7.27

An OBIC image of solar cell 960120. The beam power is 117 μW, the intensity is 109 mW/cm^2, and the wavelength is 633 nm. Figure 2.16 (a) shows the (u,w,z) coordinates of the Cu, In and Se evaporation sources used for the $CuInSe_2$ deposition. The $CuInSe_2$ film peeled off everywhere except in the 3.5% sodium doped region, for w > 1 cm.

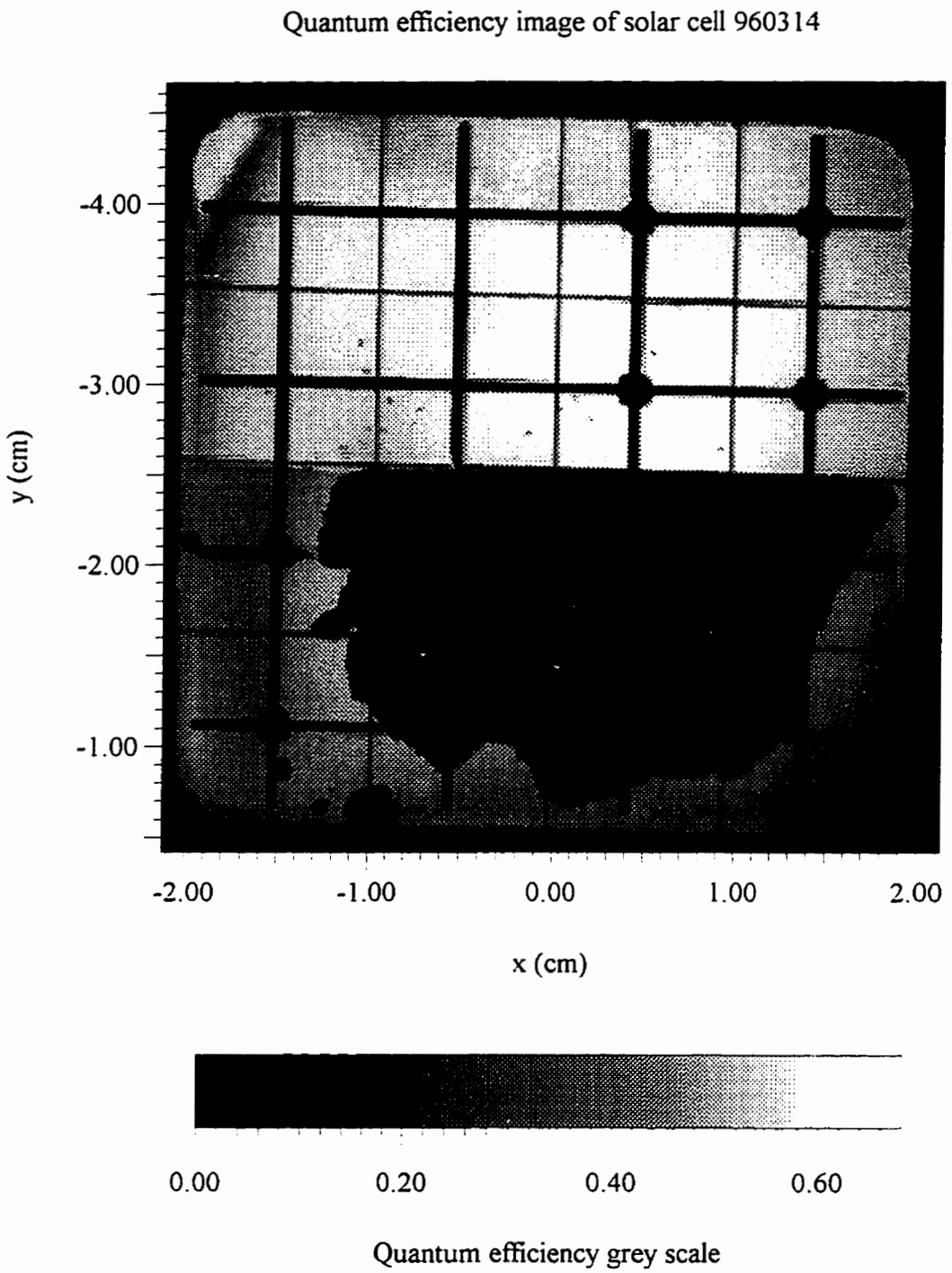

Figure 7.28

An OBIC image of solar cell 960314. The beam power is 117 μW, the intensity is 109 mW/cm^2, and the wavelength is 633 nm. Figures 2.10 and 2.16 (b) show the (x,y,z) coordinates of the Cu, In and Se evaporation sources used for the $CuInSe_2$ deposition.

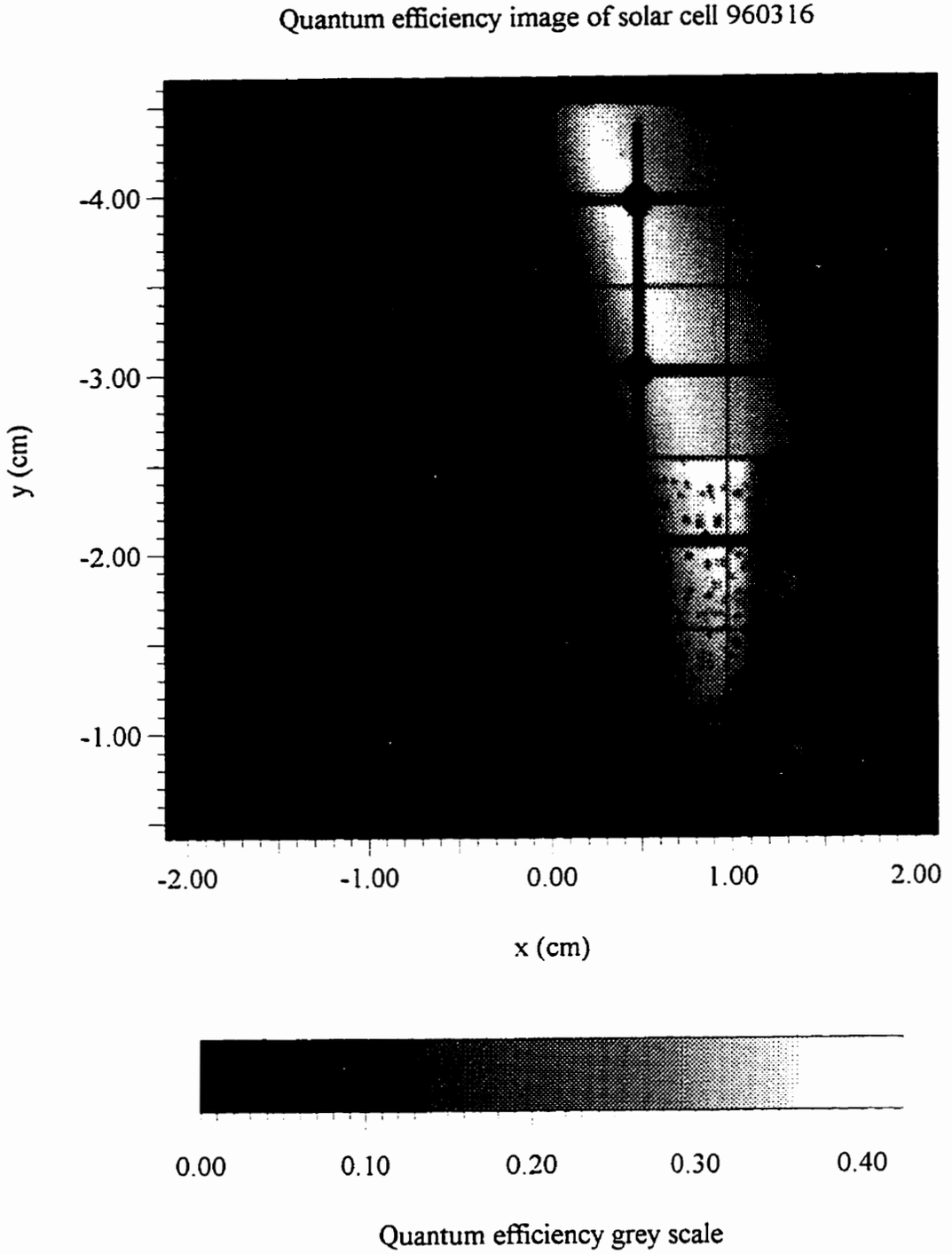

Figure 7.29

An OBIC image of solar cell 960316. The beam power is 117 μW, the intensity is 109 mW/cm^2, and the wavelength is 633 nm. Figures 2.10 and 2.16 (b) show the (x,y,z) coordinates of the Cu, In and Se evaporation sources used for the $CuInSe_2$ deposition. The cell has a single layer $CuInSe_2$ film. The film is 1% sodium doped for $y > -2.54$ cm.

of figures 7.23, 7.24, 7.28, and 7.29, as well as line graphs taken from the corresponding high intensity images, are shown in figures 7.30 and 7.31. Equation 7.15 shows that if the measured quantum efficiency depends on intensity, as is true here, then the absorption coefficient and/or the collection probability must also depend on the light intensity.

Quantum efficiency line graphs taken from figures 7.25 and 7.26 for solar cell 951207 are shown in figure 7.32. The line scans show that the 1150 nm response is more uniform than the 633 nm response. Note that the spectral response data of figure 7.21 (a,c) indicates nearly the same quantum efficiency at 633 and 1150 nm, whereas the OBIC data generally shows a higher response at 1150 than at 633 nm, for roughly the same positions. This discrepancy can be attributed to the uncertainty in the published typical quantum efficiencies of the detectors used for calibration [49], as well as the undetermined spectral variation of the external mirror reflectances and PbS detector gain, in the apparatus of figure 5.3. The generally uniform and high quantum efficiency of 951207 is consistent with the relatively high energy efficiency of this device.

Solar cell 960316 was made with a single layer of $CuInSe_2$, for the specific purpose of using OBIC to determine the sensitivity of the quantum efficiency to F. In figure 7.31, one can see that the quantum efficiency at low intensity exceeds 50% of its maximum value only for $1.085 < F < 1.105$. This suggests that, based on photocurrent considerations alone, in order to obtain reasonably efficient solar cells, the control of the Cu/In ratio for a single layer deposition process must be accurate to considerably better than ±1% over the solar cell area. This is extremely difficult to achieve by co-evaporation from independent Cu and In sources. With the particular geometry of figure 2.10, and film area 3.9 x3.9 cm^2, it is not possible.

The interpretation of the OBIC images for two layer films is less obvious. As described in section 2.4.3, intermixing occurs between the bottom copper rich layer and the top indium rich layer. As shown in figure 4.6, the conductivity of a two layer $CuInSe_2$ film (960308) is much less sensitive to F than is the conductivity of a single layer film (960229), at the same conductivity. The quantum efficiency of solar cells made with a two layer $CuInSe_2$ absorber also shows a similar reduction in sensitivity to F. The difference in sensitivity can be seen by comparing figure 7.30 (a), 7.31 (a) and 7.32 for two layer films, with figure 7.31 (b) for a single layer film. Comparison of the sodium-doped and sodium-free portions of figure 7.29 shows little change in F sensitivity due to sodium.

As shown by equations 7.14 and 7.15, a high quantum efficiency over the spectral response range of the solar cell is necessary in order to obtain a large light current density J_L when the solar cell is illuminated with sunlight. Since the maximum solar cell output power density is given by $(-JV)_{max}$, where J is given by equation 7.3, the maximum energy

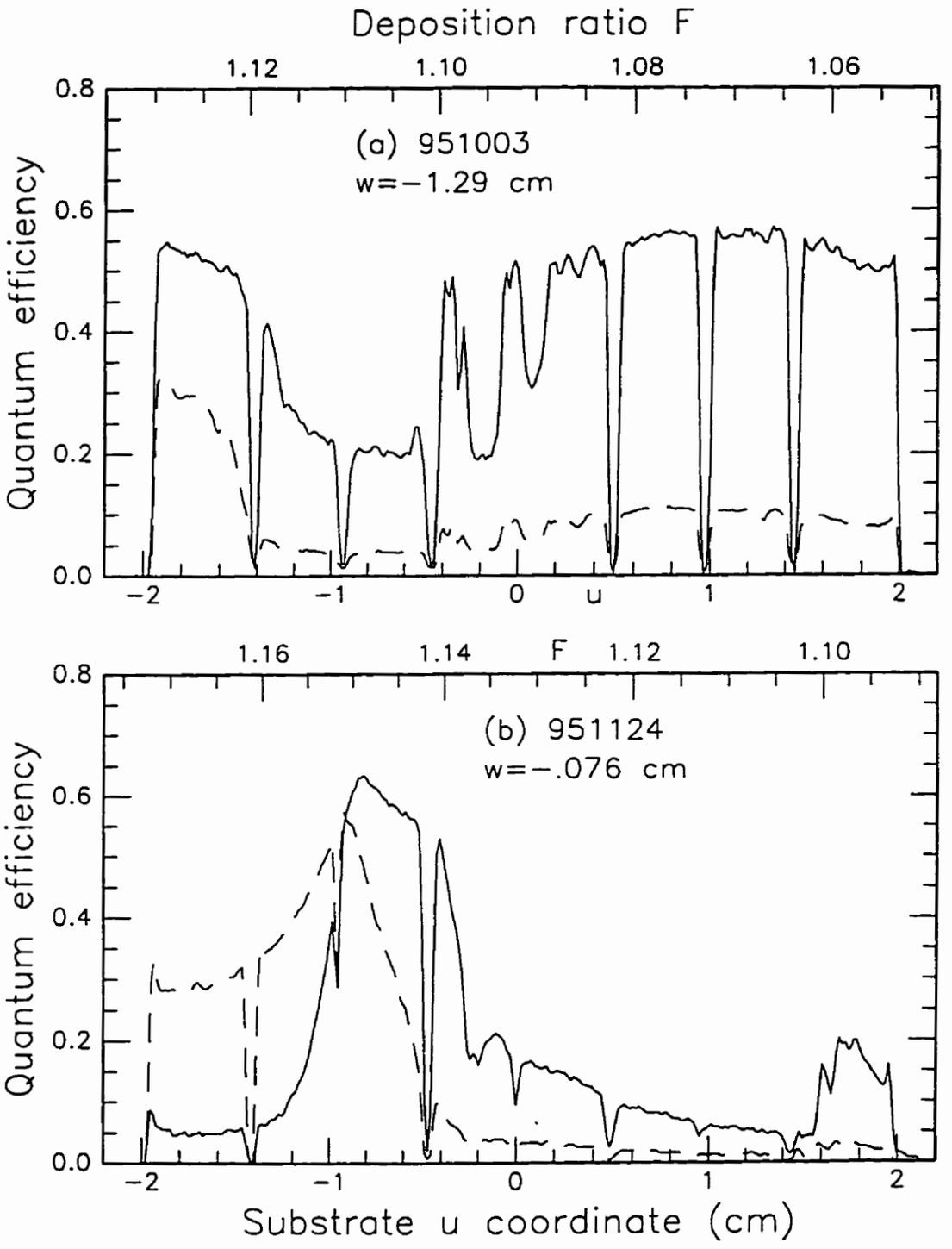

Figure 7.30

Quantum efficiency vs. substrate position u for solar cells at laser intensity 109 $mWcm^{-2}$ (solid lines) or 300 Wcm^{-2} (broken lines). Wavelength is 633 nm.

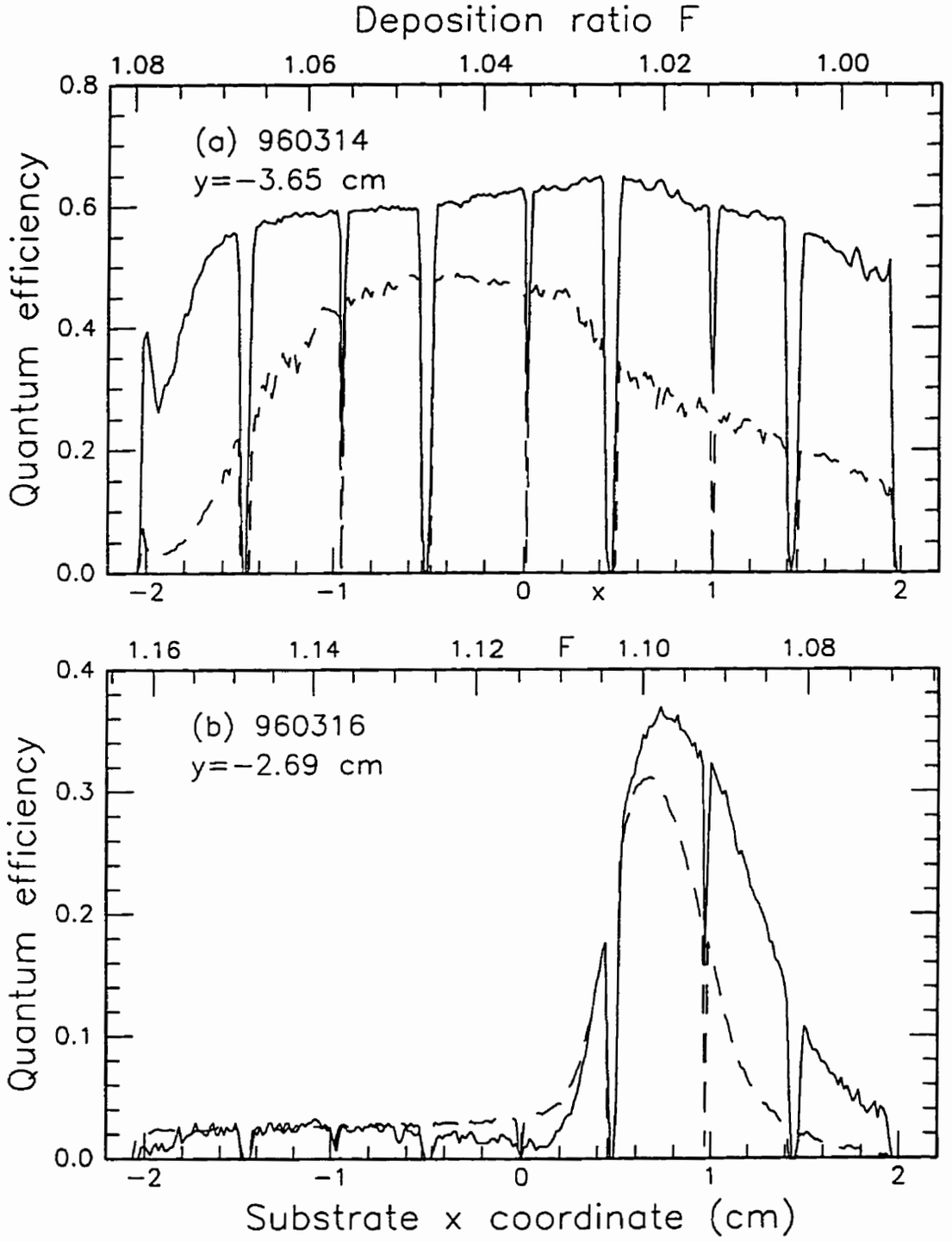

Figure 7.31

Quantum efficiency vs. substrate position x for solar cells at laser intensity 109 $mWcm^{-2}$ (solid lines) or 300 Wcm^{-2} (broken lines). Wavelength is 633 nm.

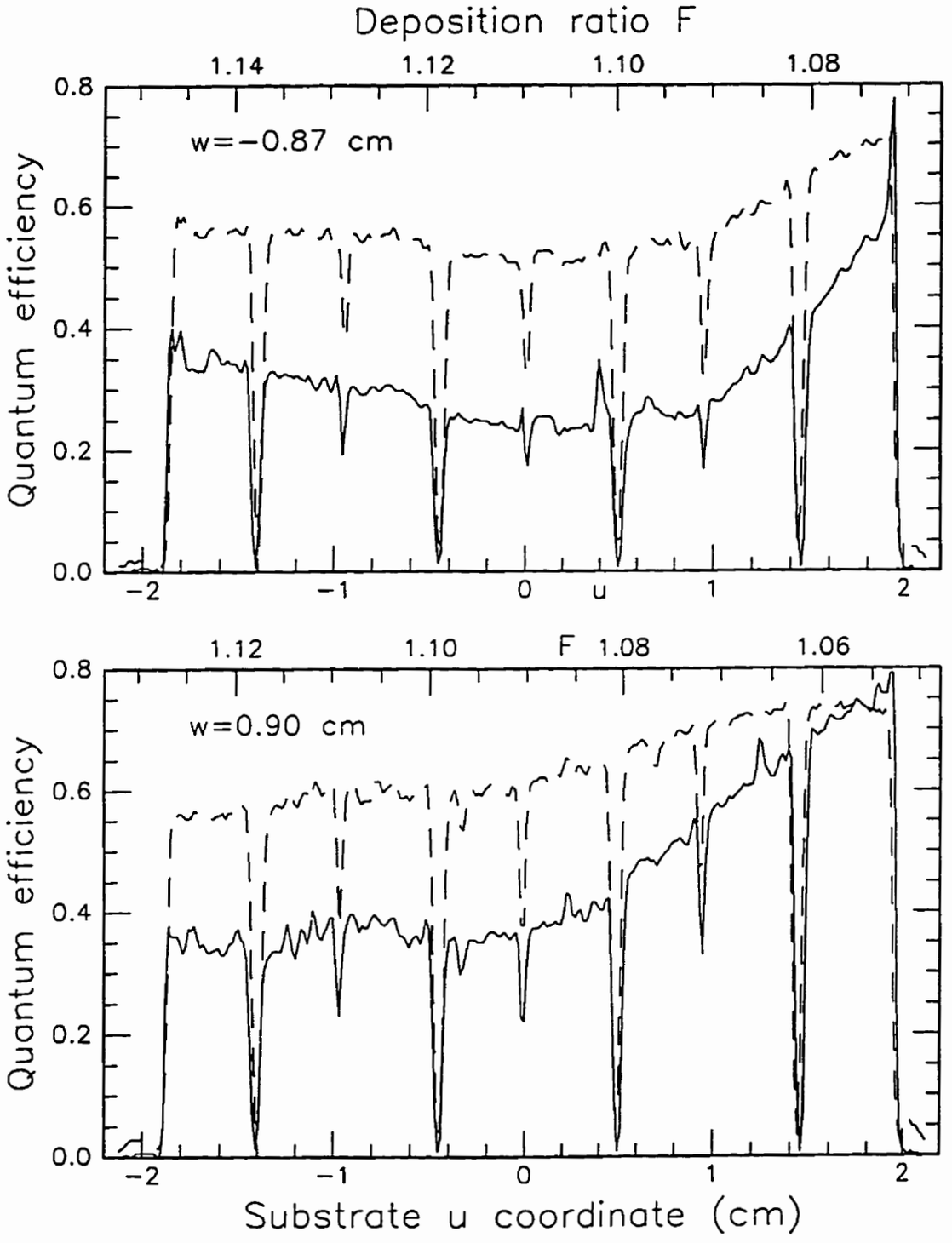

Figure 7.32

Quantum efficiency vs. position u for cell 951207 at 633 nm (solid lines) and 1150 nm (broken lines). Intensity is 114 $mWcm^{-2}$ at 633nm. Intensity is low, but not accurately determined, at 1150 nm.

conversion efficiency η_{max} (see section 7.3.5) depends on J_D, R_s and R_p as well as J_L. Thus a high quantum efficiency is not a sufficient condition for high energy conversion efficiency, and therefore the OBIC images at 633 or 1150 nm cannot be interpreted as solar cell energy efficiency maps.

The small round spots visible in figures 7.23 and 7.24 might be explained as follows. During the growth of $CuInSe_2$ films, a flake of condensed Cu+In+Se mixture may occasionally fall from an overhead surface into the hot Cu or In source and flash evaporate. This could cause ejection of droplets of source material up to the substrate. A spot seen in the OBIC image would correspond to a different Cu/In ratio at that location, and a corresponding shift in quantum efficiency.

The practical lower limit on laser power during an OBIC image measurement is determined by external noise sources. Nearby electronic equipment induces a noise current in the unshielded wires connecting the solar cell, and there is some stray light. The beam power used here is the minimum required for a satisfactory signal to noise ratio.

7.3.9 Photoluminescence Spectra of Solar Cells

Photoluminescence spectra were measured for the sodium-free solar cell 951124 at T = 85 K, using the same apparatus as described in section 3.6. Measurements were taken at points along the line w ≅ -0.05 cm, which is approximately the same line as in figure 7.30 (b). The spectra vs. position at zero bias are shown in figure 7.33. The positions of greatest photoluminescence emission, at u = -0.97 cm and u = -0.73 cm, also have the highest quantum efficiency. The $CuInSe_2$ emission band at about 1460 nm is observed at all positions, with varying intensity. A shorter wavelength emission at $\lambda < 1200$ nm is seen at u = -1.45, -0.97 and -0.73 cm. The emission vanishes as u increases and the F value decreases. As indicated in 7.34 (b), it is also present at room temperature (T ≅ 300 K). The observed emission may be the long wavelength tail of the 1.30 eV radiative transition between the CdS conduction band and Cd vacancies (electron acceptor; V_{Cd}^- before, and V_{Cd}^0 after hole capture) in the CdS, which is known to occur at room temperature [50, 51]. The 633 nm excitation is well below the CdS band-gap, so there can be no band-to-band absorption process in the CdS. Since the 633 nm light is strongly absorbed in the $CuInSe_2$, most free electrons are generated within the space charge region. The junction electric field draws these electrons toward the CdS/$CuInSe_2$ interface. A fraction of the electrons recombine with holes in the $CuInSe_2$ via gap states in the bulk, or via interface states. Most electrons cross the interface into the CdS conduction band. Some excess electrons in the CdS conduction band make the radiative transition to the V_{Cd}^0. There may also be direct transitions from the $CuInSe_2$ conduction

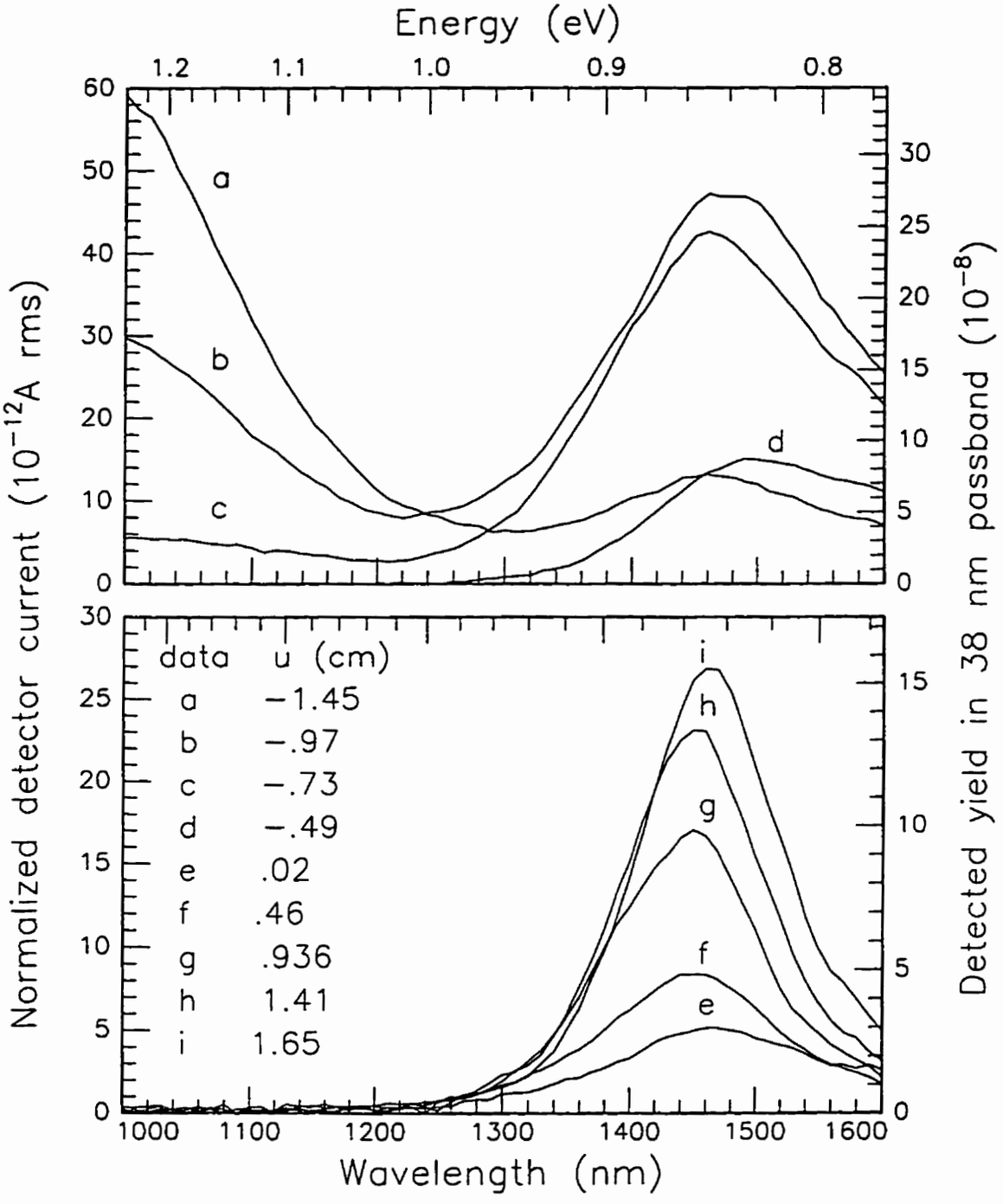

Figure 7.33

Photoluminescence spectra at different positions u at w=−0.05 cm of solar cell 951124. T_{sub}=85 K Excitation 1.33 mW at 633 nm, chopped at 330 Hz. Note different vertical scales.

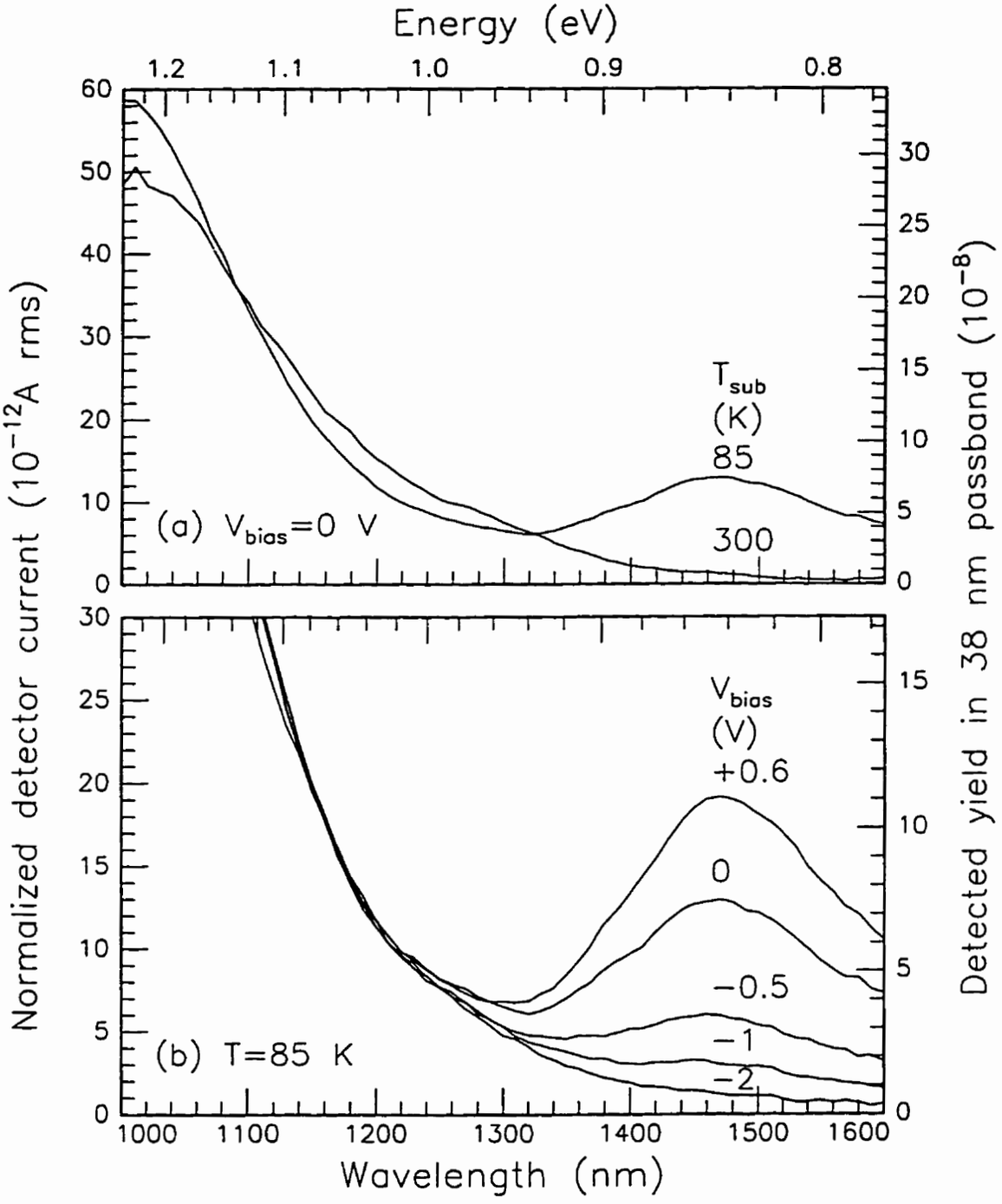

Figure 7.34

Photoluminescence spectra of solar cell 951124, at position u=−1.45 cm, w=−.05 cm.
(a) Zero bias, different temperatures.
(b) Different bias voltages, fixed temperature.

band to the V_{Cd}^0. The fact that the CdS emission intensity increases as the underlying $CuInSe_2$ becomes more Cu-rich (figure 7.33 a, b, c) suggests that Cu atoms that have diffused into the CdS from the $CuInSe_2$ could also cause the luminescence. A Cu atom on a Cd site in CdS acts as an acceptor level at about 1 eV above the valence band. Photoluminescence at about 1.2 eV due to electron transitions from the conduction band to Cu_{Cd}^0 has been observed in CdS:Cu [52]. Thus the observed emission could be due to Cu_{Cd} or V_{Cd}. The interpretation of the data is similar in either case.

The spectra at various bias voltages are shown in figures 7.34 (b) and 7.35, at three different positions. The $CuInSe_2$ photoluminescence signal increases as the bias voltage increases. Forward bias reduces the space charge electric field and should increase the steady state free carrier densities n, p in the $CuInSe_2$ space charge region near the interface. Following the model of section 3.6.5, this would also increase the neutral defect densities n_1, p_1 and the radiative recombination rate.

The quantum efficiency measurements described in section 7.3.7 show that, in forward bias, a large fraction of the photocurrent is lost to recombination. Since the photoluminescence yield is very small, radiative recombination alone cannot account for the reduction of photocurrent under forward bias. Although the quantum efficiency and photoluminescence yield are both affected by bias voltage, they must each be controlled by different recombination processes.

As seen in figure 7.34 (b) and 7.35 (a), the radiation from the CdS is not significantly affected by bias voltage. This could be because at the excitation intensity used, the CdS radiative recombination rate is saturated and controlled by the density of holes in the CdS, not the density of electrons. Since the CdS is more heavily doped than the $CuInSe_2$, most of the electrostatic potential drop and band bending occur in the $CuInSe_2$, so that a change in bias voltage does not cause much change in the CdS hole density near the interface.

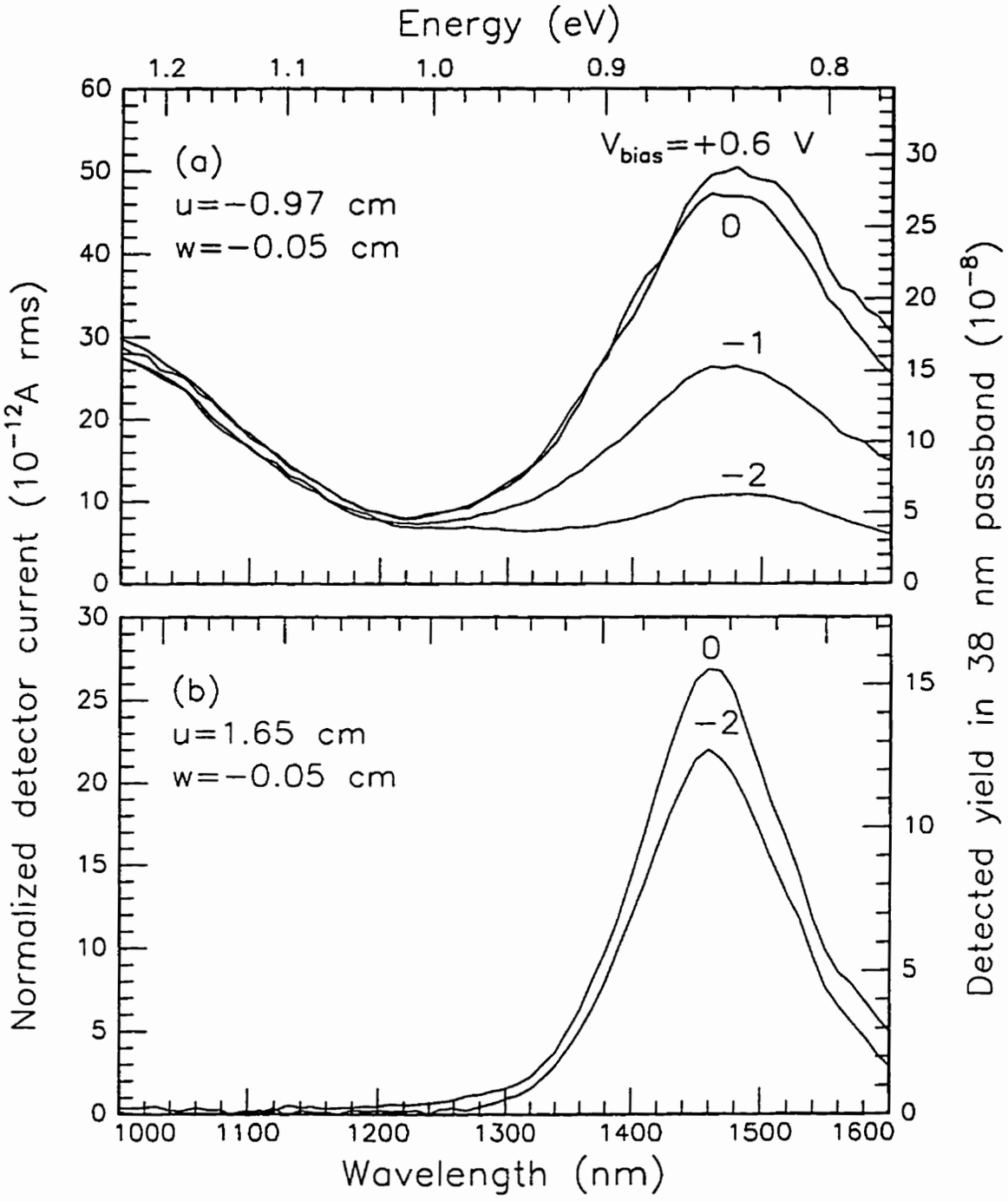

Figure 7.35

Photoluminescence spectra of solar cell 951124, at different bias voltages and measurement points (u,w). Excitation is 1.33 mW at 633 nm, chopped at 330 Hz. T_{sub}=85 K.

7.4 References

1 R.A. Mickelsen and W.S. Chen, "Development of a 9.4% efficient thin-film $CuInSe_2$/CdS solar cell", *Proc. 15th IEEE Photovoltaics Specialists Conf.* (IEEE, New York, 1981), p. 800

2 Torr Seal epoxy resin is a product of Varian Associates, Vacuum Products Division, Lexington, MA

3 *Vacuum evaporation sources catalog*, R.D. Mathis Company, P.O. Box 92916, Long Beach, CA 90809-2916, Tel. (310) 426-7049

4 J.L. Shay and J.H. Wernick, *Ternary Chalcopyrite Semiconductors: Growth, Electronic Properties and Applications*, (Pergamon, New York, 1975)

5 A. Rockett, F. Abou-Elfotouh, D. Albin, M. Bode, J. Ermer, R. Klenk, T. Lommasson, T.W.F. Russell, R.D. Tomlinson, J. Tuttle, L. Stolt, T. Walter and T.M. Peterson, "Structure and chemistry of $CuInSe_2$ for solar cell technology: current understanding and recommendations", Thin Solid Films, **237**, 1 (1994)

6 J. Ermer, R. Gay, D. Pier and D. Tarrant,"Challenges and progress in the scale up of $CuInSe_2$ thin film photovoltaic technology", J. Vac. Sci. Technol. A **11**, 1888 (1993)

7 L. Chung Yang, G. Berry, L.J. Chou, G Kenshole, A. Rockett, C.A. Mullan and C.J. Kiely, "Sputtered $CuInSe_2$ polycrystalline and epitaxial films and devices", *Proc. of 23th IEEE Photovoltaics Specialists Conf.*, p. 505 (IEEE, New York, 1993)

8 G. Pollock, and K. Mitchell, U.S. Patent No. 4,915,745 (1992)

9 T. Loher, C. Pettenkofer and W. Jaegermann, "Electronic properties of intimate Mo and CdS junctions in-situ formed on $CuInSe_2$ (011) cleavage planes", *Proc. of 24th IEEE Photovoltaics Specialists Conf.* p. 295 (IEEE, 1994)

10 A. L. Fahrenbruch, R.H. Bube, "*Fundamentals of Solar Cells*", (Academic Press, New York, 1983)

11 M. Roy, S. Damaskinos and J.E. Phillips, "The diode current mechanism in $CuInSe_2$/(CdZn)S heterojunctions", *Proc. of 20th IEEE Photovoltaics Specialists Conf.*, p. 1618 (IEEE, 1988)

12 W.N. Shafarman and J.E. Philips, "Direct current-voltage measurements of the Mo/$CuInSe_2$ contact on operating solar cells", *Proc. of 25th IEEE Photovoltaics Specialists Conf.*, p. 917 (IEEE, 1996)

13 3 cm ion beam source (model 3-1500-100) and power supply (model MPS-3000FC), Ion Tech Inc, 2330 E. Prospect, Fort Collins, Colorado 80525 (303) 221-1807

14 M.A. Lieberman and A.J. Lichtenberg, *Principles of Plasma Discharge and Materials Processing*, (Wiley-Interscience, New York, 1994)

15 A. Rockett and R.W. Birkmire, "$CuInSe_2$ for photovoltaic applications", J. Appl. Phys. 70, R81, (1991)

16 J.H. Scofield, S. Asher, D. Albin, J. Tuttle, M. Contreras, D. Niles, R. Reedy, A. Tennant and R. Noufi, "Sodium diffusion, selenization, and microstructural effects associated with various molybdenum back contact layers for CIS-based solar cells", *Proc. of 24th IEEE Photovoltaics Specialists Conference*, p.164, (1994)

17 M. Ruckh, D. Schmid, M. Kaiser, R. Schaffler, T. Walter and H.W. Schock, "Influence of substrates on the electrical properties of Cu(In,Ga)Se_2 thin films", *Proc. of 24th Photovoltaics Specialists Conf.*, p. 156 (IEEE, 1994)

18 G.B. Turner, R.J. Schwartz, and J.L. Gray, "Band discontinuity and bulk vs. interface recombination in CdS/$CuInSe_2$ solar cells", *Proceedings of the 20th IEEE Photovoltaic Specialists Conference*, (IEEE, New York, 1988), p. 1457.

19 A. Niemegeers, M. Burgelman, and A. De Vos, "On the CdS/$CuInSe_2$ conduction band discontinuity", Appl. Phys. Lett. 67, 843 (1995)

20 L. L. Kazmerski, P.J. Ireland, F.R. White, and R.B. Cooper, "The performance of copper-ternary based thin-film solar cells", *Proceedings of the 13th IEEE Photovoltaic Specialists Conference*, (IEEE, New York, 1978), p. 184.

21 M. Turowski, G. Margaritondo, M.K. Kelly, and R.D. Tomlinson, "Photoemission studies of $CuInSe_2$ and $CuGaSe_2$ and of their interfaces with Si and Ge", Phys. Rev. B **31**, 1022 (1985).

22 A. J. Nelson, S. Gebhard, A. Rockett, E. Colavita, M. Engelhardt, and H. Hochst, "Synchrotron-radiation photoemission study of CdS/$CuInSe_2$ heterojunction formation", Phys. Rev. B 42, 7518 (1990)

23 S. Wei and A. Zunger, "Band offsets at the CdS/$CuInSe_2$ heterojunction", Appl. Phys. Lett. **63**, 2549 (1993)

24 D. Schmid, M. Ruckh, H. W. Schock, "A comprehensive characterization of the interfaces in Mo/CIS/CdS/ZnO solar cell structures", *Proc. Ist World Conf. Photovoltaic Energy Conversion*, (IEEE, New York, 1994), p198.

25 T. Loher, W. Jaegermann, and C. Pettenkofer, "Formation and electronic properties of the CdS/CuInSe2 (011) heterointerface studied by synchrotron-induced photoemission", J. Appl. Phys. 77, 731 (1995)

26 D.W. Niles, M. Contreras, K. Ramanathan, and R. Noufi, "Determination of the valence-band offset of CdS/CIS solar cell devices by target factor analysis", *Proc. of 25th IEEE Photovoltaics Specialists Conf.*", (IEEE, N.J.,1996)

27 A. Rothwarf, "The superposition principle for current in solar cells", *Proceedings of 13th IEEE Photovoltaics Specialists Conference*, (IEEE, New York, 1978) p. 1312.

28 W. Shockley, *Electrons and Holes in Semiconductors*, (D. Van Nostrand, Princeton, N.J.,1950)

29 J.E. Phillips, R.W. Birkmire, B.E. McCandless, P.V. Meyers and W.N. Shafarman, "Polycrystalline heterojunction solar cells: A device perspective", Phys. Stat. Sol. **194**, 31 (1996)

30 A.J. Dhingra and A. Rothwarf, "Computer Simulation and Modeling of Graded Bandgap $CuInSe_2$/CdS Based Solar Cells", IEEE Trans. Electron Devices, 43, 613 (1996)

31 D. Cahen, R. Noufi, "Defect chemical explanation for the effect of air anneal on CdS/$CuInSe_2$ solar cell performance", Appl. Phys. Lett. **54**, 558 (1989)

32 D. Cahen, R. Noufi, "Surface passivation of polycrystalline, chalcogenide based photovoltaic cells", Solar Cells, **30**, 53 (1991).

33 E. Moons, D. Gal, J. Beier, G. Hodes, D. Cahen, L. Kronik, L. Burstein, B. Mishori, Y Shapira, D. Hariskos and H.W. Schock, "Effect of air annealing on the electronic properties of CdS/Cu(In,Ga)Se_2 solar cells", Sol. Energy Mater. Sol. Cells **43**, 73 (1996)

34 B. M. Basol and V.K. Kapur, "Deposition of $CuInSe_2$ films by a two stage process utilizing e-beam evaporation", IEEE Trans. Electron Devices, **37**, 418 (1990)

35 R. Noufi, R.J. Matson, R.C. Powell and C. Herrington, "The role of oxygen in $CuInSe_2$ thin films and $CdS/CuInSe_2$ devices", Solar Cells, **16**, 479 (1986)

36 R. Noufi, R.C. Powell and R.J. Matson," On the effect of stoichiometry and oxygen on the properties of $CuInSe_2$ thin films and devices", Solar Cells, **21**, 55 (1987).

37 C. Heske, G. Richter, Z. Chen, R. Fink, E. Umbach, W. Reidl, and F. Karg, "Influence of humidity on polycrystalline $Cu(InGa)Se_2$ thin films for solar cells: a study of Na and H_2O coadsorption", *Proc. of 25th IEEE Photovoltaics Specialists Conf.* p 861, (IEEE, 1996)

38 R. A. Sasala and J.R. Sites, "Annealing effects on individual loss mechanisms in CuInSe2 solar cells", Solar Cells, **30**, 101, (1991)

39 L.L. Kazmerski, O. Jamjoum and P.J. Ireland, "Formation, growth and stability of the $CdS/CuInSe_2$ interface", J. Vac. Sci. Technol., **21**, 486, (1982)

40 *Solar Energy Conversion*, edited by A.E. Dixon and J.D. Leslie, (Pergamom Press, Toronto, 1979)

41 R.A. Mickelsen, W.S. Chen, Y.R. Hsiao, and V.E. Lowe, "Polycrystalline Thin-Film $CuInSe_2$/CdZnS Solar Cells", IEEE Trans. Electron Devices, **ED-31**, 542 (1984).

42 R.L. Anderson, "Germanium-gallium arsenide heterojunctions", IBM J. Res. Dev., 4, 283 (1960)

43 *Semiconductors: Other Than Group IV Elements and III-V Compounds*, edited by O. Madelung (Springer-Verlag, Berlin, 1992).

44 M. A. Green, *Solar Cells: Operating Principles, Technology and System Applications* , (Prentice-Hall, N.J., 1982)

45 J. Sinkonen, J. Ruokolainen, P. Uotila, and A. Hovinen, "Spatial collection efficiency of a solar cell", Appl. Phys. Lett. **66**, 206 (1995)

46 K. W. Mitchell, A. L. Fahrenbuch, and R. H. Bube, "Evaluation of the CdS/CdTe heterojunction solar cell", J. Appl. Phys. **10**, 4365 (1977)

47 N. Murat Eron and A. Rothwarf, "Complete characterization of the heterojunction $CuInSe_2$/CdS(Zn) solar cell", *Proceedings 17th IEEE Photovoltaics Specialists Conference* , p.876 (IEEE New York 1984)

48 A. Rothwarf, J. Phillips, and N. Convers Wyeth, "Junction field and recombination phenomena in the CdS/Cu_2S solar cell: Theory and experiment ", *Proceedings of 13th Photovoltaics Specialists Conference*, p. 399 (IEEE, New York, 1978)

49 A silicon photodiode (Hamamatsu: S1226-8BQ, Q=0.647 @ 633 nm) is used for calibration at 633 nm, and a germanium photodiode (Germanium Power Devices: GM7VHR, Q≅0.62 @ 1150 nm) is used at 1150 nm

50 I.B. Ermolovich, V.V. Gorbunov, and G.I. Matvievskaya, "Properties of the Rn and IR-1 Luminescence Bands in Cadmium Sulfide Irradiated with Thermal Neutrons", Phys. Stat. Sol. (b) **106**, 45 (1981)

51 R.E. Hollingsworth and J.R. Sites, "Annealing Temperature Effects on $CuInSe_2$/CdS Solar Cells", Solar Cells, **16**, 457 (1986)

52 R. H. Bube, *Photoconductivity of Solids*, (Wiley, New York, 1960)

Chapter 8
Summary and Conclusions

8.1 $CuInSe_2$ Films

8.1.1 Film Deposition

A three source co-evaporation system was developed to deposit $CuInSe_2$ thin films for solar cells. The system uses temperature controlled sources, each calibrated with the same quartz oscillator microbalance. In order to obtain reproducible film compositions, the source crucible temperatures should not deviate from the calibration temperature by more than about ±1 °C during a deposition. The symmetrical placement of the Cu and In sources and the microbalance relative to the substrate (see figure 2.16 b) simplifies the calibration of the sources for a required deposition ratio F at the substrate, and provides a controlled stoichiometry gradient in the finished films.

The expected Cu and In atomic deposition rate ratio F was calculated for an assumed $\cos\theta$ flux distribution from the sources. This is compared with the Cu/In ratio measured by EDX in some representative films. The measured Cu/In is lower, and has a larger variation across the substrate, than is predicted by F. Because of concerns about a possible In-rich segregated surface layer affecting the EDX measurements, and since it was not convenient to perform EDX measurements on each $CuInSe_2$ absorber before deposition of the CdS window layer, the deposition ratio F is usually reported. The measured Cu/In ratio is less than F, and varies over a larger relative range than does F, as shown in figure 2.14. A least squares linear fit is used to predict the expected EDX measurement of the Cu/In ratio, at any given F.

8.2.1 Film Characterization

In all of the thin film x-ray diffraction patterns, the relative intensity of the (112) reflection is much greater than in a powder diffraction pattern [1]. Therefore, there is a preferred grain orientation with the (112) plane parallel to the substrate. Single layer Cu-rich films have sharper, more intense diffraction lines than do the single layer In-rich films, which is consistent with the fact that larger grains are observed in the SEM images of the Cu-rich films. The diffraction lines indicating the chalcopyrite ordering of the Cu and In atoms are most easily observed with films deposited by the two layer, two temperature method (see figure 3.3).

In-rich single layer films have small grains and high specular reflectance, whereas Cu-rich films have large grains and lower specular reflectance. This change in morphology with F is easily seen by eye or in a specular reflectance image such as figure 3.6.

The presence of a small amount of NaOH on the 7059 glass substrate used in a Cu-rich deposition results in a film with large grains and a relatively smooth surface. The smoothing effect of the NaOH on film 960308 is seen in the specular reflectance image of figure 3.7. The sodium doped smooth region of the film is ideal for optical transmission measurements using a standard dual beam spectrophotometer. The resulting transmission spectrum (figure 3.11) clearly shows the expected transmission cut-off at the band-gap energy. The absorption coefficient is calculated from the transmission data and the energy gap is found to be 1.014 eV for a two layer film (960308), and 1.008 eV for a single layer Cu-rich film (960309), both sodium doped. These values are in good agreement with the photoconductivity maximum at 1.012 eV for film 960308 (figure 5.7). Some values of energy gap reported in the literature are 1.04 eV [2] and 1.01 eV [3] for single crystals, and 0.95-1.01 eV for polycrystalline thin films with $0.58 < Cu/In < 1.08$ [4].

The photoluminescence spectrum and the emission intensity of the two layer film 960308 are very sensitive to small variations in stoichiometry. The highest emission intensities and the highest emission energies were observed at the most In-rich zones of this film (figures 3.19, 3.20). The photoluminescence emission intensity at the In-rich sodium doped zone is roughly five times greater than at the corresponding sodium free zone. For both zones, a rapid decrease in emission intensity is observed as the temperature is increased. This suggests that at higher temperatures, more optically excited excess carriers recombine via a competing thermally activated non-radiative process.

The conductivity of a single layer film (figures 4.2, 4.5) is very sensitive to F. Hall effect measurements show that this is due mostly to the large variation in carrier density (figure 4.3), while the mobility (figure 4.4) is less affected by F. For a single layer film, a transition from n to p-type transport is observed as F is increased. The electron mobility is higher than the hole mobility, and both are thermally activated, as expected for a polycrystalline film. The effective doping densities depend on the concentration and type of intrinsic defects present. Because there are three elements, the defect chemistry is complex [5], and the density and energy of the defects are difficult to determine accurately.

The two layer films have a relatively constant conductivity over a range of F (see figure 4.6). This is probably due to the presence of segregated stoichiometric and indium rich layers. Since little current flows in the high resistivity In-rich layer, the conductivity of the stoichiometric layer is what is actually measured.

A single layer film (960229) deposited at 350 °C is a poor photoconductor with very low gain, and at the higher conductivity film zones, any photoconductivity signal is hidden by the signal caused by the conductivity changes due to laser heating. The two layer film (960308) deposited at maximum substrate temperature 450 °C has a photoconductivity gain approximately 100 times greater than that of the low conductivity zones of the single layer film. Because of the higher photoconductivity gain of the two layer film, a variety of photoconductivity measurements are practical. These include the variation of the photoconductivity spectrum with temperature and bias light, and the transient response. The sodium doped zones have a large transient photo-current, and each has a spectral response maximum at a photon energy approximately equal to the energy gap (figure 5.7). In the sodium doped films, a deep electron trapping level may explain the large transient photo-current.

In general, the $CuInSe_2$ films deposited by the two layer, two temperature process demonstrate many of the properties expected for a 1 eV direct band-gap semiconductor. The initial Cu-rich deposition and the high final substrate temperature (450 °C) promote the growth of larger, higher quality chalcopyrite crystallites than are obtained by the lower temperature (350 °C) single layer deposition method.

8.2 $CuInSe_2$/CdS Solar Cells

8.2.1 Solar Cell Fabrication

A radio frequency sputtering system is used for the deposition of the Mo ohmic contact to the p-$CuInSe_2$. In order to obtain the highest conductivity Mo films, bias sputtering is used to minimize the impurity concentration and the density of voids. Stronger adhesion to the glass substrate is obtained if the first fraction of the film is deposited with zero substrate bias voltage.

Since CdS decomposes to Cd vapor and S vapor upon evaporation, a hot wall deposition system is required for the growth of the CdS solar cell window layer. The hot wall enclosure ensures that the Cd partial pressure is sufficiently high for the nucleation and growth of CdS on the substrate. Careful control of the temperatures of the hot wall, the substrate and CdS source is essential. There is evidence that the film nucleation process is very sensitive to the purity of the CdS source material.

In order to produce energy efficient devices, the Mo, $CuInSe_2$ and CdS films must each be of good quality. The Mo contact layer must be of high purity, so that the valence band energy barrier and the contact resistance at the p-$CuInSe_2$ are minimized. The $CuInSe_2$ absorber should have large, columnar chalcopyrite grains, in order to minimize minority carrier recombination at grain boundaries, and it must adhere well to the Mo contact. The

In doped CdS window should have sufficient thickness and conductivity to ensure low solar cell series resistance, and it must have high transmittance. The Al/Ni top contact grid should contribute little to the total series resistance, while shadowing only a small fraction of the total cell area.

The two layer $CuInSe_2$ films frequently fail to adhere to the Mo when 7059 glass substrates are used, whereas the $CuInSe_2$ adheres well to Mo deposited on soda-lime glass. Ion beam bombardment during an initial Cu-rich deposition enhances the $CuInSe_2$ adhesion to Mo on 7059 glass. A small amount of NaOH on the Mo also improves $CuInSe_2$ adhesion to Mo on 7059 glass.

8.2.2 Solar Cell Characterization

The interpretation of electrical measurements on large solar cells is complicated by the fact that the Cu/In ratio in the $CuInSe_2$ layer varies continuously across the substrate. A large cell is equivalent to a number of smaller cells connected in parallel, each deposited at a particular F. For example, the measured junction capacitance per unit area represents the average over the cell area of a continuously varying capacitance per unit area. In the case of the current vs. voltage measurements, the reverse saturation current density J_0 can be expected to depend on F, so that the diode current density J is non-uniform over the cell area, and the overall cell J-V characteristic is dominated by the regions with the highest J_0. To obtain measurements at particular F values, a number of small cells could have been isolated from the larger cell, so that within the area of each small cell, the value of F can be assumed fixed. This was not done because there was not enough time. There is no doubt that a higher "champion cell" efficiency could have been obtained if the best large cell were subdivided into many smaller cells and each small cell tested.

OBIC images of solar cells show that a solar cell with a two layer $CuInSe_2$ absorber is less sensitive to variations in F than is a cell based on a single layer absorber (figure 7.31). It is possible that solar cells based on two layer $CuInSe_2$ films function either as p-n or p-i-n type structures, depending on whether the overall film composition is stoichiometric or In-rich. If the overall composition is stoichiometric then the device is p-n and the top layer of $CuInSe_2$ has relatively high conductivity, and therefore, a narrow depletion region. If the overall composition is In-rich, then the top In-rich layer acts as a low conductivity intrinsic region, so the depletion region is wider. This conjecture is supported by the fact that the three best solar cells have net acceptor densities N_1 spanning three orders of magnitude, as determined by junction capacitance measurements (see table 7.3). Thus, provided that the overall film composition is not so Cu-rich that the Cu_2Se phase is present, the solar cell with two layer $CuInSe_2$ tolerates a range of absorber compositions.

This is consistent with published data [6] showing that cells with efficiencies exceeding 10% can be obtained in the composition range $0.85 < Cu/(In+Ga) < 1.03$.

The photoluminescence measurements on solar cell 951124 show that the position of maximum luminescence emission also has the highest quantum efficiency in the corresponding OBIC measurement. The photoluminescence emission intensity is reduced when a reverse bias is applied to the solar cell.

8.3 Problems and Possible Future Research

A solar cell fabricated in this project requires about 1 hour at 1 kilowatt for the RF sputtering system, about 2 hours at 4 kilowatts for the $CuInSe_2$ deposition system and about 1 hour at 1 kilowatt for the CdS evaporation system. This is a total of 10 kilowatt-hours, and does not include the energy used in baking-out the vacuum systems. At a year round average irradiance of 17 $mWcm^{-2}$, solar cell 951207 (4.8% efficient, 14 cm^2) would need to operate continuously for about 100 years just to recover the energy used during the film depositions. Clearly, any large scale manufacturing process would have to be much more energy efficient than the method used here.

It should also be noted that the very best cells, like the 17.7% efficient cell described in chapter 1, use wider band-gap alloys such as $Cu(In,Ga)Se_2$ or $Cu(In,Ga)(S,Se)_2$, in order to obtain a larger open circuit voltage and higher efficiency. The use of these more complex absorber materials would result in increased manufacturing costs.

The very high absorption coefficient of $CuInSe_2$ means that, in principle, a film only a few tenths of a micron thick is needed to absorb most of the incident power at energies above the band-gap. However, in practice, films at least about two microns thick are needed to obtain sufficiently large grain sizes for high efficiency devices. Since In and Ga are expensive, it is important to minimize the absorber layer thickness, in order to reduce the use of these metals.

Although the work function of Mo (4.6 eV) is too low to form a true ohmic contact to p-$CuInSe_2$, Mo has been used almost exclusively as the contact to p-$CuInSe_2$ films, because it resists chemical attack by Se at the high substrate temperatures necessary for the growth of good quality $CuInSe_2$ films. Indeed, the poor adhesion of $CuInSe_2$ films to Mo is probably due to the chemical resistance of Mo. An alternative contact material such as Ni has a larger work function (5.15 eV) than Mo, but in the presence of Se at high temperatures, it is rapidly converted to NiSe.

$CuInSe_2$-based solar cells with efficiencies greater than 10% have been produced only by vacuum co-evaporation of the elements at high substrate temperatures ($T_{sub} \cong 500$ °C), or by reacting pre-deposited elemental precursor layers at high temperatures [7]. A much

lower temperature deposition process would permit the use of a wider variety of substrate and contact materials.

The presence of sodium clearly has a significant influence on the $CuInSe_2$ films and solar cells. A recent study of rapid thermal processed stacked elemental precursor layers with controlled sodium incorporation [8] suggests that sodium promotes the formation of a CuSe phase which acts as a flux agent for the growth of larger grains of $CuInSe_2$. Since the beneficial effects of sodium were discovered accidentally as a consequence of the unintentional diffusion of sodium from a soda-lime glass substrate, systematic research should be undertaken to determine if there exists other impurities which promote the growth of good quality $CuInSe_2$ films.

An array of prototype thin film $Cu(In,Ga)Se_2$ modules with 340 W peak power has demonstrated stable operation for two years in outdoor tests and no intrinsic stability problems have been identified [9]. However, the additional surface area due to the grain boundaries, and the large density of intrinsic crystal defects, render a polycrystalline film more vulnerable to impurity diffusion and chemical attack than a single crystal. Thus, in order to obtain module lifetimes in excess of 20 years, even better encapsulation may be necessary for thin film polycrystalline solar cells, than is required for crystalline silicon modules.

Although $CuInSe_2$ based solar cells show considerable potential, it remains to be demonstrated that reliable, large area $CuInSe_2$ photovoltaic modules can be produced at costs competitive with silicon technology. It seems likely that silicon based solar cells (crystalline, multicrystalline and amorphous) will continue to dominate the terrestrial photovoltaics market for many years to come.

8.4 References

1 J. Parkes, R. D. Tomlinson, amd M. J. Hampshire, " Crystal data for $CuInSe_2$", J. Appl. Cryst. **6**, 414 (1973)

2 *Semiconductors: Other thanGroup IV Elements and III-V Compounds*, edited by O. Madelung (Springer-Verlag, Berlin, 1992).

3 H. Neumann and R.D. Tomlinson, "Band-gap narrowing in n-type $CuInSe_2$ single crystals", Solid State Communications, **57**, 591 (1986)

4 J.R. Tuttle, D. Albin, R.J. Matson, and R. Noufi, "A comprehensive study o the optical properties of thin-film $CuInSe_2$ as a function of composition and substrate temperature" J. Appl. Phys. **66**, 4408 (1989)

5 J. A. Groenink and P. H. Janse, "A generalized approach to the defect chemistry of ternary compounds", Z. Phys. Chem. N. F. **110**, 17 (1978)

6 A. Rockett and R.W. Birkmire, "$CuInSe_2$ for photovoltiac applications", J. Appl. Phys. 70, R81 (1991)

7 A. Catalano, "Polycrystalline thin-film technologies: Status and prospects", Sol. Energy Mater. Sol. Cells, **41/42**, 205 (1996)

8 V. Probst, F. Karg, J. Rimmasch, W. Reidl, W. Stetter, H. Harms, O. Eibl, "Advanced stacked elemental layer process for $Cu(In,Ga)Se_2$ thin film photovoltaic devices", Mat. Res. Soc. Symp. Proc.

9 T. Strand, B. Kroposki, and R. Hansen, "Siemens Solar CIS photovoltaic module and system performance at the national renewable energy laboratory", *Proc. 25th IEEE Photovoltaics Spec. Conf.*, p. 965 (IEEE, N.J., 1996)

Appendix A: $CuInSe_2$ Film Deposition Parameters, Thickness and Substrate Material

1	2	3	4	5	6	7	8	9	10	11	12	13	14	15
$CuInSe_2$ film (Y:M:D)	Cu rate (s^{-2})	In rate (s^{-2})	Se rate (s^{-2})	Cu T (C)	In T (C)	subs. T (C)	dep. time (min)	calc. layer thick (micron)	total meas. thick (micron)	layer deposit. ratio 'F'	average F for two layers	substrate details	matching CdS film #	general comments
// Manual temperature control, type (a) or (b) sources for Cu and In, type K thermocouples, contact substrate heater //														
910627	0.741	1.34	3.7	1361	1097	0	0	0.000		0.999		7059		aborted: no In rate detected
910730	0.741	1.34	3.7	1070	867	370	60	0.433		0.999		7059		manual control difficult
910814	0.741	1.34	3.7	1020	875	350	150	1.083		0.999		7059		base pressure !E-6 torr
910826	0.741	1.34	3.7	994	777	354	150	1.083		0.999		7059		
910930	0.741	1.34	5.5	1110	891	350	150	1.083		0.999		7059		
// Three source temperature controller designed, constructed and installed //														
920730	0.7	1.265	3.48	1032	782	350	146.6	1.000		1.000		7059		source controller tested
// Tungsten-rhenium thermocouple installed at Cu source, because type K thermocouple unstable at high T //														
920916	0.7	1.265	3.48	980	826	350	0	0.000		1.000		7059		aborted: Cu source failure
920917	0.7	1.265	3.48	931	0	350	0	0.000		1.000		7059		aborted: In source failure
920918	0.7	1.265	3.48	940	624	350	165	1.125		1.000		7059		innacurate In T measure
// Type (C) sources, for both Cu and In //														
921002	0.7	1.265	3.48	1054	837	350	170	1.159		1.000		7059		more accurate source T's
921113	0.7	1.265	3.48	1093	835	350	170	1.159		1.000		7059		insufficient Se
930219	0.7	1.265	3.48	1105	836	0	165	1.125		1.000		7059		100 eV ion beam assist
930508	0.7	1.265	3.48	1055	827	350				1.000		7059		100 eV ion beam assist
930715	0.7	1.265	3.48	1085	0	350	0	0.000		1.000		7059		aborted: Cu source failure
930719	0.7	1.265	3.48	1087	823	350				1.000		7059		try Cu current control
930806	0.7	1.265	3.48	1071	818	350	173	1.180		1.000		7059		
930909	0.7	1.265	3.48	1091	813	350				1.000		7059		P=1.1E-7 with LN2 + 2 days
// Type (d) Cu source //														
931021	0.7	1.265	3.48	1111	0	450	0	0.000		1.000		7059		aborted: unstable Cu T
Use 2.7 amps AC to keep Cu thermocouple wire hot and free of metal condensate //														
931111	0.7	1.265	3.48	1119	843	450	165	1.125		1.000		7059		fair source stability
940217	1.25	2.26	6.213	1145	850	450	195	2.375		0.999		Mo/7059		first solar cell attempt
940405	1.25	2.26	6.213	1149	845	450	164	1.998		0.999		Mo/7059		

940425	1.25	2.26	6.213	1148	851	450	80	0.974	0.999		Mo/7059		first cell photo-current
940516	1.25	2.26	6.213	1132	847	450	0	0.000	0.999		Mo/7059		aborted: forgot shutter
940524	1.25	2.259	6.213	1157	850	450	160	1.948	1.000		Mo/7059		
940623	1.25	2.259	6.213	1141	853	450	105	1.278	1.000		Au/Mo/7059		1/2 of substrate Au film
// Bakeout and cool down chamber before deposition start //													
940720b	1.25	2.259	6.213	1152	861	350	82	0.998	1.000				
940720t	0.75	2.259	6.213	1123	863	450	82	0.876	0.600	0.800	Mo/7059	940722	first 2 layer film
940803b	1.25	2.259	6.213	1143	847	350	82	0.998	1.000				
940803t	0.75	2.259	6.213	1119	844	450	82	0.876	0.600	0.800	Mo/7059	940803	
940923	1.25	2.259	6.213	1146	832	450	82	0.998	1.000		7059		100 eV ion beam assist
940930	1.5	2.259	6.213	1166	829	450			1.200		7059		100 eV ion beam assist
// Prototype type (e) Cu source //													
941017	1.375	2.259	6.213	1194	822	450			1.100		7059		100 eV ion beam assist
941021	1.45	2.259	6.213	1143	811	450			1.160		7059		100 eV ion beam assist
// Final design type (e) source for both Cu and In //													
941104	1.375	2.259	6.213	1106	871	0	93	1.167	1.100		7059		100 eV ion beam assist
941114	1.15	2.259	6.2	1198	868	300	86	1.021	0.920		Mo/7059	941115	500 eV ion etch Mo
941208b	1.375	2.259	7	1209	872	300	82	1.029	1.100				
941208t	0.625	2.259	7	1160	865	450	62	0.639	0.500	0.842	Mo/7059	941209	poor Mo adhesion
950106b	1.375	2.259	7	1210	887	300	81	1.016	1.100				
950106t	0.75	2.259	7	1163	865	450	60	0.641	0.600	0.887	Mo/7059	950109	200 eV ion etch Mo
// Substrate radiaion heater installed, to allow faster control //													
950118b	1.375	2.259	7	1205	863	300	82	1.029	1.100				
950118t	0.75	2.259	7	1171	863	450	60	0.641	0.600	0.889	Mo/7059	950119	substrate thermcple failure
// Indium-bonded substrate thermocouple //													
950126	1.25	2.259	7	1205	883	300			1.000		Mo/7059	950128	fast substrate cool-down
950207b	1.375	2.259	7	1213	884	300	90	1.129	1.100				
950207t	0.675	2.259	7	1174	884	450	46	0.481	0.540	0.910	Mo/7059	950208	
950331b	1.375	2.259	7	1206	868	300	93	1.167	1.100				
950331t	0.75	2.259	7	1170	868	450	47	0.502	0.600	0.932	Mo/7059	950403	poor Mo adhesion
950407b	1.375	2.259	7	1206	885	300			1.100				
950407t	0.875	2.259	7	1180	886	450			0.700		Mo/7059		total Mo adhesion failure
// Install data acquisition computer for recording deposition data //													
950508b	1.375	2.259	7	1208	884	300	96	1.205	1.100				
950508t	0.875	2.259	7	1181	884	450	40	0.442	0.700	0.982	Mo/7059	950509	first complete data record
// Disassemble and clean vacuum chamber to remove possible Cd, Zn and As contamination from previous users //													
// Discovered that diffusion pump stack output to foreline had been incorrrectly positioned away from foreline pipe //													

// Upper internal structure removed. Re-designed substrate holder, shutter, microbalance crystal holder, etc. installed.//
// Type (f) indium source installed. Source, substrate, crystal configuration as in figure 2. except Se at z = -26.3 cm //

950708b	1.408	2.259	7	1154	870	300	90.6	1.146	1.032				
950708t	0.768	2.259	7	1123	870	450	14	0.150	0.563	0.970	Mo/7059	950709	P=3.5E-8; insufficient Se
// z distance of Se source reduced by two times, to z= -10.7 cm, to allow higher rate with same Se mass //													
950719b	1.662	2.6	13.62	1182	872	300	67.2	0.987	1.059				
950719t	0.906	2.6	13.62	1149	872	450	37.5	0.466	0.577	0.886	Mo/7059	950720	increased Se rate
950816b	4.155	6.5	31.95	1230	918	300	46	1.688	1.059				increased Cu,In, Se rates
950816t	2.266	6.5	31.95	1201	918	450	23	0.714	0.577	0.898	Mo/7059	950817	50% $CuInSe_2$ adhesion
950824b	4.155	6.5	31.95	1240	918	375	46	1.688	1.059				
950824t	2.266	6.5	31.95	1206	918	475	23	0.714	0.577	0.898	Mo/7059		10% $CuInSe_2$ adhesion
950826b	4.155	6.5	31.95	1224	922	380	54.3	1.993	1.059				
950826t	2.266	6.5	31.95	1195	922	475	18.9	0.587	0.577	0.934	Ga/Mo/7059		sources splattered
// Type (f) copper source installed //													
950830b	4.155	6.5	31.95	1220	923	375	44.5	1.633	1.059				
950830t	2.266	6.5	31.95	1177	923	475	26.1	0.811	0.577	0.881	Ga/Mo/7059		20% $CuInSe_2$ adhesion
// Evaporate Se during substrate cool-down, to minimize Se loss from film //													
950901b	4.35	6.5	31.95	1216	917	375	50.7	1.890	1.108				300 eV ion etch Ga/Mo
950901t	2.374	6.5	31.95	1176	917	475	10.2	0.320	0.605	1.024	Ga/Mo/7059		50% $CuInSe_2$ adhesion
950905b	4.749	6.5	31.95	1226	910	375	51.2	1.970	1.210				
950905t	2.59	6.5	31.95	1181	910	475	17.97	0.576	0.660	1.067	Ga/Mo/7059		5% $CuInSe_2$ adhesion
950906b	4.749	6.5	31.95	1226	906	375	48.4	1.862	1.210				
950906t	2.59	6.5	31.95	1182	906	475	20.7	0.663	0.660	1.045	Mo/7059	950907	200 eV ion etch Mo
// Fused silica chimney at Cu source replaced with tantalum chimney //													
950909b	4.35	6.5	31.95	1210	916	365	49.1	1.831					200 eV ion etch Mo
950909t	2.374	6.5	31.95	1167	916	465	20	0.628	0.605	0.963	Mo/7059		10% $CuInSe_2$ adhesion
950913b	4.55	6.5	31.95	1220	909	365	46.1	1.746	1.159				200 eV ion etch Ga/Mo
950913t	2.48	6.5	31.95	1175	909	465	21.5	0.682	0.632	0.992	Ga/Mo/7059		30% $CuInSe_2$ adhesion
950915b	4.55	6.5	31.95	1217	904	365	46.3	1.754	1.159				200 eV ion etch Ga/Mo
950915t	2.48	6.5	31.95	1175	904	450	21.7	0.688	0.632	0.991	Ga/Mo/7059		0% $CuInSe_2$ adhesion
950916b	4.55	6.5	31.95	1212	907	350	51.8	1.962	1.159				damaged during CdS dep.
950916t	2.48	6.5	31.95	1175	907	450	14.2	0.450	0.632	1.046	Mo/7059		200 eV ion etch Mo
// Improved CdS deposition: no mask,radiation heater, better quality CdS (E.S.P.) //													
951003b	4.55	6.5	31.95	1222	908	350	46.6	1.765	1.159				
951003t	2.48	6.5	31.95	1182	908	450	15.5	0.491	0.632	1.028	Mo/7059	951011	70 eV ion etch Mo
951018b	4.749	6.5	31.95	1225	910	350	53.2	2.047	1.210				70 eV ion etch Mo
951018t	2.59	6.5	31.95	1183	910	450	17.8	0.570	0.660	1.072	Mo/7059		20% $CuInSe_2$ adhesion

951023b	4.749	6.5	31.95	1225	910	350	42.4	1.631		1.210				partially oxidized Mo top
951023t	2.59	6.5	31.95	1184	910	450	25.2	0.807		0.660	1.005	Mo/7059	951026	200 eV ion etch Mo
951025b	4.749	6.5	31.95	1228	909	360	35.4	1.362		1.210				
951025t	2.59	6.5	31.95	1186	909	460	30.7	0.983		0.660	0.955	Mo/7059	951101	partially oxidized Mo top
// Install Se source with increased holding capacity for longer deposition //														
951109b	4.53	6.5	31.95	1226	911	350	58.2	2.201		1.154				200 eV ion etch Mo
951109t	3.595	6.5	31.95	1209	911	450	18.4	0.645	3.366	0.916	1.097	Mo/7059	951114	slightly oxidized Mo top
951111b	4.57	6.5	31.95	1228	914	350	59.4	2.254		1.165				200 eV ion etch Mo
951111t	3.125	6.5	31.95	1201	914	450	22.5	0.757	3.700	0.796	1.063	Mo/7059	951115	slightly oxidized Mo top
951121b	4.57	6.5	31.95	1227	900	350	57.6	2.185		1.165				
951121t	3.125	6.5	31.95	1201	900	450	18.6	0.625		0.796	1.075	Mo/7059	951126	200 eV ion etch with Cu+Se
951124b	4.57	6.5	31.95	1223	908	350	57	2.163		1.165				
951124t	3.125	6.5	31.95	1195	908	450	20.9	0.703	3.088	0.796	1.066	Mo/7059	951128	200 eV ion etch with Cu+Se
951205b	4.748	6.5	31.95	1223	908	350	57.4	2.208		1.210				200 eV ion etch Mo
951205t	2.675	6.5	31.95	1189	908	525	22.1	0.714		0.682	1.063	Mo/sodalime	951212	poor Mo adhesion
// Preheat Cu and In sources to full temperature before calibration, to remove residual Se. //														
951207b	4.748	6.5	31.95	1231	913	350	56.7	2.181		1.210				
951207t	2.675	6.5	31.95	1191	913	450	21.7	0.701	3.410	0.682	1.064	Mo/sodalime	951213	poor Mo adhesion
951209b	4.748	6.5	31.95	1232	911	350	57.3	2.204		1.210				200 eV ion etch Mo
951209t	2.675	6.5	31.95	1192	911	450	21.6	0.697	3.266	0.682	1.065	Mo/sodalime	951215	poor Mo adhesion
960102b	4.748	6.5	31.95	1232	913	350	57	2.193		1.210				
960102t	2.675	6.5	31.95	1193	913	450	21.6	0.697	3.243	0.682	1.065	Mo/sodalime	960126	cracked substrate
960106b	4.748	6.5	31.95			350	59.2	2.277		1.210				200 eV ion etch with Cu+Se
960106t	2.675	6.5	31.95			450	21.4	0.691	2.455	0.682	1.070	Mo/sodalime		indium source T error
960113b	4.748	6.5	31.95	1246	953	350	56	2.154		1.210				1/2 of Mo dipped in NaOH
960113t	2.675	6.5	31.95	1204	953	450	22.3	0.720	3.266	0.682	1.059	Na/Mo/7059	960202	In thermocouple contacted
960116b	4.748	6.5	31.95	1238	912	350	58.7	2.258		1.210				
960116t	2.675	6.5	31.95	1197	912	450	22	0.710	3.777	0.682	1.066	Mo/sodalime	960127	200 eV ion etch with Cu+Se
960120b	4.748	6.5	31.95	1232	909	350	57.5	2.212		1.210				CuInSe2 adhesion only
960120t	2.675	6.5	31.95	1191	909	450	21.9	0.707		0.682	1.064	Na/Mo/7059	960131	on area with 4% NaOH
960123b	4.748	6.5	31.95	1230	907	350	58.2	2.239		1.210				
960123t	2.675	6.5	31.95	1190	907	450	22.5	0.726		0.682	1.063	Na/7059		zones 0, 0.2, 1, 5% NaOH
// Move Cu and In sources to positions of figure 2. //														
960218	4.289	7.75	31.95	1227	911	350	61	2.548	2.766	1.000		Na/7059		1/2 substrate 1% NaOH
960221	4.628	7.75	31.95	1233	910	350	58	2.482	2.744	1.079		Na/7059		1/2 substrate 1% NaOH
// Move Se source, so that all sources are in symmetrical configuration shown in figure 2. //														
960228	4.375	7.75	21.65	1229	908	350	44	1.849	1.988	1.020		7059		single layer In rich film

960229	4.5925	7.75	21.65	1231	907	350	56	2.390	2.566	1.071		7059		single layer stoichiometric
960302b	4.877	7.75	21.65	1247	912	350	52	2.264		1.137				1/2 substrate 1.5% NaOH
960302t	2.738	7.75	21.65	1204	912	450	29.5	1.096	4.088	0.638	0.957	Na/7059		poor adhesion NaOH 1/2
960308b	5	7.75	21.65	1237	902	350	51.5	2.261		1.166				
960308t	2.738	7.75	21.65	1194	902	450	21	0.780	2.950	0.638	1.013	7059		1/2 substrate 1% NaOH
960309	5	7.75	21.65	1237	900	350	52	2.283	2.288	1.166		7059		1/2 substrate 1% NaOH
960312	5	7.75	21.65	1234	901	350	52	2.283		1.166		7059		100 eV ion beam assist
960314b	5	7.75	21.65	1236	902	350	52	2.283		1.166				1/2 0.5% and 1/2 1% NaOH
960314t	2.738	7.75	21.65	1192	902	450	19	0.706	3.155	0.638	1.025	Na/Mo/7059	960608	30% CuInSe2 adh. on 1%
960316	4.78	7.75	21.65	1233	903	350	55	2.378	2.588	1.114		Na/Mo/7059	960610	1/2 substrate 1% NaOH

NOTES

Column 1 is the date of film deposition date given by year-month-day. Suffix "t" means top layer and "b" means bottom layer in the case of two layer films

Column 2, 3 and 4 are the elemental deposition rates of Cu In and Se, respectively, in s^{-2} or Hz/s measured at the microbalance crystal

Columns 5 and 6 are the Cu and In source temperatures, respectively, when calibrated to give the listed deposition rates

Column 7 is the substrate temperature used during the deposition of each layer

Column 8 is the time of deposition in minutes of each layer

Column 9 is the calculated layer thickness based on the deposition times and rates

Column 10 is the total film thickness determined by measuring the film mass

Column 11 is the nominal deposition ratio for each layer

Column 12 is the time average depostion ratio, as defined by equation 2.15

Column 13 specifies the substrate material, and additional films predeposited on substrate

Column 14 specifies the identifying number of the CdS film which is used for the window layer in solar cells.

Appendix B: CdS Film Deposition Parameters

1	2	3	4	5	6	7	8	9	10
CdS sample # (y,m,d)	CdS dep. time (min)	CdS evap. time (min)	evap. CdS mass (g)	CdS thick (um)	CdS type	CdS source T (C)	In source T (C)	hot wall T (C)	subs. T (C)
// no shutter, no thermocouple on CdS source, thermocouple bolted to indium //									
// doping source, substrate bonded to Al heater block with grease, heater //									
// wire wound directly on hot wall, substrate thermocouple bolted to heater block //									
940722	18	18	0.2				780	209	126
940803	14	14	0.2				780	228	180
941115	12	12	0.25				780	211	158
// installed crude shutter, operated by falling weight triggered by external magnet //									
941209		12	0.3					189	144
// nitrogen venting installed on vacuum chamber, for faster substrate cool-down //									
950109		9					765	198	170
950119							775	198	169
// argon venting system installed, attempt to repair sticking shutter //									
950128		7	0.6					209	170
950208		9	0.6				780	189	173
// CdS vacuum system disassembled, shutter with rotary feedthrough installed //									
// repair leak in liquid nitrogen cold trap, re-machine scratched vacuum seals //									
// clean system, design and install radiation heater for hot wall //									
950403		6.5	0.8				777	234	202
// type (f) source installed for CdS evaporation, start computer data acquisition //									
950420	36.3	37.0				837		229	170
950427	34.0	33.7		2.00		880	746	229	172
950501	102.0	108.0	0.13		ALFA	610		259	170
950502	34.8	33.0	0.42	20.00	ALFA	751		265	175
950503	10.2	15.0				851		268	175
950504	10.3	14.3	0.23	12.00		764		266	172
950505	17.8	19.5	0.22	5.00	ALFA	751		267	173
950509	17.8	20.8	0.31	9.00	ALFA	767	631	265	173
950709	14.0	20.2	0.33		ALFA	767	633	273	171
950720	12.6	18.6	0.34		ALFA	768	631	277	172
950817	12.2	15.8	0.26		ALFA	770	631	282	171
950907	15.4	19.8	0.33		ALFA	767	633	277	171

950920	9.2	12.2	0.32		ALFA	803	636	295	174
950928	11.6	15.0	0.34	3.80	E.S.P.	803		337	202
950928	15.2	18.0	0.25	3.30	E.S.P.	767		395	208
950929	20.0	23.0	0.35	2.05	E.S.P.	765		304	200
951002	30.0	32.6	0.5	2.00	E.S.P.	768	539	306	200
951004	20.0	23.0	0.5	1.00	E.S.P.	798		270	199
951005	22.4	26.0	0.43	15.80	ALFA	770		311	204
951005	30.2	35.8	0.22	9.95	ALFA	698		312	202
951006	20.4	24.2	0.38	3.81	ALFA	768		246	199
951006	32.6	36.4	0.76	4.49	E.S.P.	802		306	201
951011	29.8	33.8	0.8	5.58	E.S.P.	799	533	306	201
951026	23.0	26.8	0.62	3.84	E.S.P.	802	524	305	200
951101	23.0	28.0	0.66	3.83	E.S.P.	804	529	306	200
951114	24.0	27.4	0.58	4.30	E.S.P.	805	527	306	200
951115	24.2	27.6	0.53	4.00	E.S.P.	799	529	306	200
951126	24.2	27.6	0.64	4.19	E.S.P.	801	536	306	200
951128	24.2	27.8	0.65	4.49	E.S.P.	800	534	306	200
951212	23.8	27.4	0.64	5.00	E.S.P.	803	534	306	201
951213	22.2	25.8	0.49	3.94	E.S.P.	802	534	305	200
951215	24.6	27.8	0.59	3.66	E.S.P.	801	536	306	200
960126	23.6	27.4	0.58	4.25	E.S.P.	804	534	308	204
960127	22.6	26.4	0.62	4.39	E.S.P.	805	536	308	201
960131	22.6	26.2	0.6	4.41	E.S.P.	803	535	308	201
960202	22.4	26.2	0.55	3.95	E.S.P.	802	536	307	202
960608	22.4	26.2	0.59	3.96	E.S.P.	801	550	308	202
960610	22.6	27.2			E.S.P.	804	554	308	202

NOTES

Column 1 is the date of deposition in year-month-day, also sample number

Column 2 is the time (minutes) during which the shutter is open

Column 3 is the time during which the source is at operating temperature

Column 4 is the total mass of CdS evaporated from the source

Column 5 is the film thickness in microns

Column 6 is the CdS manufacturer: Alfa inorganics or Electr. Space Products

Column 8 is the indium doping source temperature

Appendix C: Solar Cell Performance Data

1 device number [a]	2 total area [b] (cm^2)	3 Isc (mA)	4 Jsc (mA/cm^2)	5 Voc (mV)	6 fill factor	7 energy efficiency (%)	8 light source [c]	9 substrate [d]
940425	1	0.9	0.9	106	0.25	0.025		
950623	1.66	2.0	1.2	57	0.25	0.018		
940720	1.66	2.4	1.4	106	0.25	0.040		
940803	0.5	0.8	1.7	74	0.25	0.033		
941114	0.5	0.8	1.6	64	0.25	0.027		
// first shutter installed in CdS system //								
941208	0.5	3.0	6.0	170	0.25	0.268		
950106	0.5	1.8	3.6	121	0.25	0.115		
950118	0.5	6.0	12.0	160	0.25	0.505		
950126	0.5	2.4	4.8	90	0.25	0.114		
950207	0.5	4.4	8.7	203	0.25	0.466		
950508	0.5	7.0	14.0	190	0.3	0.840		
950708	0.5	7.0	14.0	155	0.314	0.715		
950719	0.5	6.1	12.1	207	0.29	0.765		
950816	0.5	0.8	1.6	100	0.3	0.051		
950906	0.5	0.2	0.4	75	0.25	0.008		
// change CdS supplier from ALFA to E.S.P. //								
951003	15.1	267.3	17.7	186	0.368	1.275	sunlight	
951023	15	20.0	1.3	100	0.25	0.035		
951025	15	53.0	3.5	115	0.3	0.128		
951109	15	15.0	1.0	30	0.25	0.008		
951111	15	55.0	3.7	130	0.3	0.151		
951121	15	130.0	8.7	170	0.352	0.546		
951124	15	190.5	12.7	147	0.335	0.658	sunlight	
951207	14.36	347.5	24.2	333	0.569	4.827	sunlight	sodalime
951209	14.36	210.0	14.6	195	0.38	1.141		sodalime
960102	11	120.0	10.9	200	0.31	0.712		sodalime
960113	10	155.0	15.5	245	0.462	1.847		Na doped
960116	15	195.0	13.0	170	0.38	0.884	sunlight	sodalime
960120	3.666	59.8	16.3	293	0.495	2.488	sunlight	Na doped
960314	11.11	193.2	17.39	223	0.3859	1.575	sunlight	Na doped
960316	15	74.0	4.9	100		0.000		Na doped

Notes:
[a] device number is the same as the $CuInSe_2$ absorber film number used in the solar cell
[b] about 13% of total area is covered by front contact grid
[c]light source is solar simulator is 75 W tungsten halogen lamp with 3 cm water filter or sunlight
sunlight is midday sun on clear dry summer day: assumed equal to AM1: 95.62 $mWcm^{-2}$
[d] substrate is Mo/7059 glass unless specified as sodalime (Mo/sodalime glass)